Simulation schemes of a non-miscible three-phase flow model for vapor explosion applications

Hamza Boukili

UNIVERSITÉ AIX-MARSEILLE

U.F.R. des Sciences

École doctorale de mathématiques et informatique (E.D. 184)

THÈSE

présentée pour obtenir le grade de

Docteur de l'université Aix-Marseille

Spécialité : Mathématiques appliquées

par

Hamza BOUKILI

Schémas de simulation d'un modèle à trois phases immiscibles pour application à l'explosion vapeur

---

soutenue publiquement à Marseille le 9 mars 2020

devant le jury composé de

Enrique Fernandez-Nieto	Université de Séville	Rapporteur
Jacques Sainte-Marie	INRIA	Rapporteur
Gloria Faccanoni	Université de Toulon	Examinatrice
Thierry Gallouët	Université Aix-Marseille	Examinateur
Sergey Gavrilyuk	Université Aix-Marseille	Examinateur
Jean-Marc Hérard	EDF Lab Chatou	Directeur de thèse
Jean-Claude Latché	IRSN Cadarache	Examinateur
Maria-Giovanna Rodio	CEA Saclay	Examinatrice

Remerciements

Ce travail de thèse est le fruit de trois années laborieuses passées au sein du département *MFEE* d'*EDF Lab Chatou*. Si cela a pu bien se passer, c'est avant tout grâce à celles et ceux qui ont fait en sorte que ce soit une expérience agréable. J'essaierai dans cet intermède de leur rendre hommage, en espérant que la mémoire ne me trahisse pas et que je n'y oublie aucune personne.

Tout d'abord, je commence par remercier les collègues du *LAMSID*. Bien que ce laboratoire n'ait pas de lien direct avec ma thèse, le stage de césure que j'y ai effectué a eu le plus grand impact sur ma décision de rejoindre *EDF Lab* pour ma thèse. Je souhaite donc en particulier citer Patrick M., Alexandre M., Matthieu L.-C., Zouhair A., Tianyi L. et Abdallah M..

Concernant l'aventure de thèse elle-même, j'aimerais rendre hommage en premier lieu à Jean-Marc Hérard, mon directeur de thèse et encadrant principal. Le côtoyer de près était une source d'apprentissage continu, grâce à ses qualités scientifiques mais aussi humaines. Jean-Marc n'hésitait pas à s'assurer que tout allait bien au travail et en dehors, en proposant volontairement son aide dès qu'il sentait un semblant de difficulté. Cette bienveillance est certainement l'une des raisons principales du succès de cette thèse.

Merci également à Olivier H. et Érik D.-M., collègues proches qui sont intervenus plusieurs fois au court de ce travail. Ils m'ont, chacun dans son domaine d'expertise, fait des propositions utiles et apporté des contributions pertinentes.

Merci à Fatiha N., elle était volontairement accueillante, disponible, taquine par moment, mais surtout bienveillante. Autant de qualités qui ont fait d'elle beaucoup plus qu'une simple collègue.

Merci à Lucie Q. avec qui j'ai partagé le bureau et qui me permettait de casser la routine du travail à travers diverses conversations et pauses improvisées au milieu de batailles multiphasiques.

Merci à Li M. qui m'a permis de satisfaire grandement ma curiosité à l'égard de ma passion pour la langue et la culture chinoise, d'apprendre plein d'anecdotes, et surtout de faire mes devoirs de mandarin quelques instants à peine avant d'aller en cours du soir !

Merci à Nasser N., un des rares collègues à survivre dans les couloirs au-delà de 19h. L'occasion s'offrait à nous de faire le point sur les actualités du groupe, du département, de l'entreprise, du pays et même du monde. Il faut dire que c'était une heure propice aux conversations sur des sujets profonds !

Merci à l'ensemble des collègues du groupe I8D, et aux collègues de l'équipe Neptune. Les moments conviviaux aux pauses cafés, à la pause déjeuner (et surtout au babyfoot qui la suit) vont rester longtemps dans la mémoire. Que ceux qui ne voient pas leurs noms figurer explicitement me trouvent excuse. Plus d'une page est nécessaire pour leur exprimer ma gratitude.

Enfin, je remercie papa et maman, Abderrahman et Latifa, ainsi que ma sœur et mon frère, Khaoula et Saad, et le reste de ma famille. La thèse a demandé beaucoup d'intérêt pour la science, de motivation et de persévérance, et la majeure partie de cela je le dois à ma famille.

Table des matières

Chapitre 0

Introduction

Ce travail de thèse a eu lieu dans le cadre du contrat CIFRE numéro 2016/0611. Il s'est déroulé au sein du département MFEE d'EDF Lab Chatou, en partenariat avec l'Institut de Mathématiques de Marseille (I2M, Aix-Marseille Université). Les ressources informatiques qui ont aidé à la réalisation de ce travail ont été fournies par le groupe EDF.

0.1 Contexte industriel

Plusieurs types de réacteurs nucléaires sont utilisés dans le monde pour la production de l'électricité, leur fonctionnement fait appel à différents types de combustible nucléaire tels que l'uranium naturel, l'uranium enrichi ou le plutonium, ils utilisent aussi différents modérateurs de la réaction en chaîne (graphite, eau ordinaire, eau lourde, etc.) ainsi que différents fluides caloporteurs, dont la fonction est le transport de chaleur produite par la réaction de fission.

En France, le choix qui a été adopté consiste à utiliser de l'uranium enrichi comme combustible nucléaire, et de l'eau ordinaire comme fluide caloporteur. Cette eau est mise sous haute pression pour rester à l'état liquide à haute température. Ce type de réacteurs porte donc le nom de *Réacteur à Eau Pressurisée* (REP). Une des particularités du design des REP est la présence de trois circuits d'eau, étanches entre eux, qui gèrent le transport de chaleur depuis le cœur du réacteur jusqu'aux systèmes de refroidissement :

— Circuit primaire :
C'est le circuit d'eau qui évacue la chaleur dégagée lors de la fission du combustible nucléaire. L'eau est mise sous pression d'environ 155 bars afin de rester à l'état liquide dans tout le circuit, sous des températures qui peuvent dépasser 300 °C. L'eau parcourt le cœur du réacteur du bas vers le haut, elle récupère la chaleur résultant de la réaction de fission et passe ensuite dans les *Générateurs de Vapeur* (GV). Ces derniers sont des échangeurs thermiques destinés à produire de la vapeur. L'eau primaire en passant dans le GV perd sa chaleur, refroidit et repart ensuite dans le cœur du réacteur.

— Circuit secondaire :
Ce circuit est constitué d'eau liquide qui passe dans le GV et se transforme en vapeur, suite au transfert de chaleur qui a lieu avec l'eau (chaude) du circuit primaire. Cette vapeur est mise sous pression et envoyée ensuite pour faire tourner la turbine, qui à son

tour entraîne l'alternateur pour générer l'électricité. A la sortie de la turbine, la vapeur passe dans le condenseur où elle revient à l'état liquide, et repart au générateur de vapeur. Le circuit secondaire est aussi un circuit fermé, le changement d'état liquide-vapeur qui y est prévu constitue une différence majeure avec le circuit primaire. Il faut noter aussi que chaque cœur de réacteur nucléaire est lié à trois ou quatre circuits secondaires, au nombre des générateurs de vapeur installés.

— Circuit tertiaire :

Appelé encore circuit de refroidissement, ce circuit a pour but de refroidir la vapeur du circuit secondaire afin de la condenser. De l'eau froide en provenance de la mer ou d'un fleuve est envoyée dans le condenseur, une fois le refroidissement de la vapeur secondaire fait, l'eau tertiaire a elle même besoin d'être refroidie. Cela est réalisé dans de grandes tours appelées aéroréfrigérants. Ces derniers constituent la partie la plus visible d'une centrale nucléaire, de par leur dimension et aussi de par le panache de vapeur d'eau qu'ils dégagent dans l'atmosphère.

La mécanique des fluides occupe donc une place importante dans la gestion des installations nucléaires. En effet, pour le dimensionnement correct des composants de chacun des circuits d'un REP, et pour la compréhension précise de leurs comportements lors de différents scénarios de fonctionnement, on a besoin de mener un large spectre d'études afin de justifier de la sécurité permanente et infaillible des installations. Dans cette perspective, la mécanique des fluides occupe une place centrale, compte tenu de l'importance des échanges thermiques entre fluides dans le fonctionnement des REP.

En particulier, la mécanique des fluides multiphasique est fortement mise en jeu, notamment quand il s'agit des scénarios d'écoulement accidentel tels que la *crise d'ébullition* (DNB) [73], la *perte de réfrigérant primaire* (PRP) [72] ou l'*accident d'insertion de réactivité* (RIA) [59].

L'*explosion vapeur* fait partie des phénomènes pouvant survenir en cas d'accident grave impliquant une fusion du cœur. Il s'agit de ce qui se passe quand un fluide chaud rentre en contact avec un fluide froid (typiquement lors d'une éruption volcanique, avec l'entrée en contact du magma chaud avec l'eau liquide). Il y a donc échange thermique qui transforme l'eau en vapeur. Si l'écart de température est important, l'évaporation de l'eau peut se produire de façon tellement rapide et intense que cela conduit à la formation d'ondes de choc accompagnant l'expansion de la vapeur, d'où le mot explosion. En effet, si le cœur du réacteur -suite à une défaillance majeure de refroidissement- venait à entrer en fusion totale ou partielle, le combustible nucléaire fondrait, et entraînerait avec lui la fusion des gaines métalliques qui l'entourent, ce qui conduirait à la formation d'un mélange de métaux fondus, à la fois chaud et radioactif, appelé *corium*. Cela représente le fluide chaud. L'eau présente dans le circuit primaire, ou éventuellement autour de la cuve (comme solution de refroidissement dans certains scénarios), représente le fluide froid qui, en rentrant en contact avec le *corium*, s'évapore et présente ainsi un risque d'occurrence d'*explosion vapeur*. Des ondes de choc pourraient se développer dans le bâtiment réacteur, et endommager ses structures internes.

Ce phénomène d'e*xplosion vapeur* constitue le cadre général de ce travail de thèse. En effet, compte tenu du risque qu'il présente pour l'installation nucléaire, on souhaite disposer d'outils de simulation, qui nous aideraient à estimer les ondes de pression potentiellement

résultantes d'une *explosion vapeur*.

L'ambition ultime de ce travail est ainsi décrite. Le phénomène auquel on s'intéresse est à dynamique rapide, et met en jeu de forts échanges mécaniques et thermiques. Cela fait de sa modélisation et simulation un véritable défi scientifique.

0.2 Modélisation multiphasique pour la représentation des écoulements industriels

La mécanique des fluides multiphasique est la branche de la mécanique des fluides qui étudie ce qui se passe lorsque l'on a affaire à plusieurs fluides qui s'écoulent ensemble. Cela peut consister en un même composant présent sous différentes phases (de l'eau liquide et vapeur par exemple), ou encore un mélange de fluides différents (mélange d'eau, gaz et huile par exemple). Le comportement global de l'écoulement à plusieurs phases se retrouve nettement modifié par rapport à l'écoulement monophasique, c'est actuellement l'un des domaines les plus actifs dans la recherche en mécanique des fluides.

Avec le développement accéléré des moyens de calcul, la *simulation numérique directe* (DNS en anglais) a été de plus en plus mise en œuvre pour l'approximation numérique des équations de la mécanique des fluides, notamment en monophasique. Mais cela a profité aussi à la mécanique des fluides multiphasique, l'acronyme DNS a été adopté par la communauté multiphasique pour désigner l'étude de l'écoulement dans toutes ses échelles, même les plus petites, en tentant de simuler les différents phénomènes et interactions ayant lieu entre les fluides. La dernière cinquantaine d'années a témoigné d'une multiplication importante des travaux de recherche multiphasiques, mais cela concerne surtout le cadre diphasique.

Globalement, les travaux diphasiques en approche Eulérienne peuvent être répartis en deux classes distinctes : la représentation homogène ou bifluide.

L'approche homogène consiste à considérer le mélange diphasique comme étant un seul fluide, des équilibres de vitesse, de pression, de température et de potentiel chimique sont supposés entre les deux phases, cela permet de représenter l'écoulement moyennant un nombre réduit de variables. Une loi d'état du mélange peut aussi être proposée, par exemple par tabulation à partir des lois d'état des deux fluides concernés [34, 74]. Si une des contraintes d'équilibre présupposé est relâchée, il faut fermer le modèle en proposant une équation supplémentaire sur la grandeur en déséquilibre. Cela conduit à des modèles dérivés du modèle homogène comme par exemple : le modèle *homogène relaxé* (HRM en anglais) [7, 19] en cas de potentiels chimiques différents, ou encore modèle *de dérive* ("*drift-flux model*") en cas de déséquilibre de vitesse entre les deux phases [23, 32].

Il faut noter que parfois les hypothèses d'équilibre sur lesquelles le modèle homogène est construit ne sont pas toujours valables, certaines configurations d'écoulement peuvent les mettre entièrement, ou partiellement, à défaut. C'est ce qui a motivé le développement de la deuxième approche, dite bifluide, où aucun équilibre n'est présupposé entre les deux phases. Le point de départ de modélisation dans cette approche est que les lois de conservation sont vérifiées par chacune des phases. Ces lois sont pondérées d'une fonction couleur qui permet de savoir la répartition spatiale d'une phase donnée en fonction du temps. La dynamique de cette fonction couleur est elle aussi décrite par une équation de transport, qui fait intervenir une

vitesse de transport appelée *vitesse d'interface*. De plus, chaque phase dispose de sa propre équation d'état, les variables thermodynamiques évoluent en toute indépendance d'une phase à l'autre. Cela constitue un système d'équations avec de nombreuses inconnues. Afin de l'étudier, il est nécessaire de proposer des lois de fermeture, elles permettent notamment de caractériser ce qui se passe à l'interface entre les deux fluides, en décrivant chacun des échanges possibles : échange mécanique, thermique, chimique, etc.

Historiquement, le modèle à deux vitesses et deux pressions de Ransom et Hicks [61] a été l'un des premiers modèles bifluides proposés ; il vient dans la même période que le modèle de Baer et Nunziato [4], qui était destiné à l'étude des écoulements gaz-particules, et qui a été largement repris depuis pour le même type d'écoulements par Kapila et al. [50] ou encore pour les écoulements eau-gaz [30] ou eau-vapeur [28]. Si l'on souhaite établir une sorte de hiérarchie entre les différents modèles diphasiques, il est plutôt naturel de placer celui de Baer et Nunziato en haut de la pyramide. Ne supposant aucun équilibre à priori entre les phases, ce modèle peut bien constituer le modèle père d'une large famille diphasique. On peut notamment y trouver les modèles qui supposent équilibre de pression uniquement [26], ou vitesse uniquement [69], ou encore les modèles homogènes supposant à la fois équilibre de vitesse et pression [49]. Enfin, on trouve la classe de modèles homogènes HRM (pression, vitesse, et température) [7, 19], et le modèle homogène équilibré (HEM) [13].

Dans le domaine des écoulements multiphasiques à nombre de phases strictement supérieur à deux, il existe nettement moins de travaux de modélisation. En effet, la complexité des modèles diphasiques évoqués ci-dessus, et des écoulements que cela représente, encourage peu à aller au delà de deux phases. Une première possibilité pour parer à cette difficulté, et représenter un écoulement triphasique, est l'utilisation de méthodes numériques de suivi d'interface (type "Volume of Fluid" par exemple) sur la base d'un système d'équations diphasique ([52]). Une autre possibilité similaire consiste à l'utilisation d'un modèle diphasique pour un écoulement gaz-liquide, où la phase liquide elle-même est munie d'équations du type "*drift flux model*" afin de représenter deux liquides différents ([9, 67]). Une classe différente de modèles triphasiques considère un ensemble d'équations de bilan sur chaque phase (classiquement bilan de masse, quantité de mouvement et énergie), mais l'examen des propriétés mathématiques globales du modèle n'est généralement pas détaillé, et parfois la compressibilité n'est pas considérée. Plusieurs de ces modèles sont utilisés dans l'industrie pétrolière ([1]) ou nucléaire (par exemple, le code MC3D pour la simulation de l'explosion vapeur [56]).

Une difficulté cependant, lors de l'utilisation de ces modèles équilibrés en pression [48], est que les relations de saut ne sont pas définies clairement, du fait de la présence de produits non conservatifs actifs dans les champs *vraiment non linéaires* (VNL), ce qui rend impossible l'évaluation des ondes de pression lorsque des ondes de choc apparaissent dans l'écoulement. D'autre part, l'hyperbolicité conditionnelle peut interdire le calcul de transitoires rapides.

Ainsi, l'approche que nous considérons pour la modélisation des écoulements triphasiques compressibles consiste à repartir du système de Baer et Nunziato [4], et écrire une formulation générale d'un mélange à trois phases, qui ne suppose aucun équilibre préalable. Cela a fait l'objet de travaux comme [39], ou plus récemment [57, 35, 36]. Dans [40], une version barotrope du modèle [39] a été proposée. D'autres travaux du type approche homogène ont fait leur apparition, comme par exemple [60, 47] à un seul champ de vitesse.

Plusieurs arguments physiques sont avancés pour justifier le choix d'un modèle par rapport à l'autre, cependant il est important d'examiner également les propriétés mathématiques

de ces modèles. À ce propos, trois propriétés essentielles sont particulièrement examinées dans notre étude :

— Hyperbolicité du système convectif :

Cette condition a une conséquence importante sur le modèle, à la fois sur l'aspect théorique et numérique. En effet, en son absence, le caractère bien posé à condition initiale n'est plus garanti [51, 70]. Numériquement, cela se traduit par des explosions de solutions à temps fini tel que cela est montré dans [33, 41] et [27].

— Inégalité d'entropie sur le système global :

C'est la pierre angulaire de la formulation de notre modèle. D'une part, elle permet de sélectionner les solutions physiques du système. D'autre part, elle fournit une relation algébrique dont l'exploitation conduit à la détermination des pressions d'interface. Par ailleurs, elle nous permet de donner des formes admissibles pour les lois de fermeture des termes sources figurant dans notre système, et décrivant ainsi complètement les échanges entre les phases.

— Unicité des relations de saut à la traversée de chacune des ondes du système convectif :

Cette unicité n'est pas une question évidente pour les systèmes non-conservatifs dans le cas général. Cela est pourtant obtenu pour ces systèmes tels [39, 40] grâce à l'exploitation du caractère linéairement dégénéré de l'onde associée aux taux de présence. L'absence d'unicité des relations de saut conduit sinon à une conséquence négative majeure, puisque les solutions convergées (lorsque le pas de maillage tend vers zéro) diffèrent selon le schéma choisi en présence de chocs [33, 44].

0.3 Schémas pour la simulation numérique - Vérification et validation

Dans le domaine de la simulation des écoulements multiphasiques transitoires, de nombreux travaux ont été proposés au cours de la dernière vingtaine d'années, majoritairement dans le cadre diphasique. Notre regard ici porte sur les modèles déséquilibrés en pression, étant donné que les modèles mono-pression ne répondent pas aux exigences mathématiques détaillées dans le paragraphe précédent.

Les modèles diphasiques qui nous intéressent sont tous du type convection-source, où le système convectif est hyperbolique. L'utilisation de solveurs de Riemann avec la méthode des *Volumes Finis* paraît alors parfaitement adaptée pour des transitoires rapides. Dans ce sens, des solveurs de Riemann de type HLL [68] ou HLLC [25, 53, 71] peuvent être adaptés, d'autres types de schémas comme [2, 16] peuvent aussi être pertinents.

Les modèles triphasiques qui nous intéressent sont aussi du type convection-source, l'utilisation d'une méthode à pas fractionnaires semble également dès lors légitime. En effet, cette méthode nous permet de subdiviser le système d'équations aux dérivées partielles (EDP) de départ en plusieurs sous-systèmes relativement plus faciles à approximer. Cette subdivision est d'autant plus légitime qu'elle sépare les sous-systèmes en fonction de la physique qu'ils traduisent, tout en restant consistants avec l'équation d'entropie, qui constitue la pierre angulaire de la famille des modèles qu'on considère.

Le premier pas fractionnaire est celui qui concerne la convection. Le caractère hyperbolique du sous-système convectif est vérifié, cela permet de bénéficier du retour d'expérience des travaux sur les modèles diphasiques déséquilibrés en pression, afin de proposer des schémas à la fois précis et robustes. De notre part, on considérera dans un premier temps le schéma de Rusanov [64] afin d'approximer l'étape de convection. Ce schéma est certes diffusif, mais il est robuste et relativement simple à mettre en œuvre. Cela nous permet de ménager le temps et l'effort pour le travail sur l'approximation des termes sources, qui constitue la valeur ajoutée majeure de ce travail de thèse.

L'approximation des termes sources fait l'objet du deuxième pas fractionnaire. Dans l'esprit de [42], chacun des effets de relaxation (vitesse, pression, température et potentiel chimique) est traité séparément. Cela revient à dire que cette étape de relaxation est elle même divisée en quatre sous-étapes en fonction des effets physiques respectifs, la consistance de chaque sous-étape avec l'équation d'entropie étant ainsi vérifiée. Sur le plan discret, des schémas implicites sont proposés pour chaque sous-étape de relaxation, les termes sources pouvant être très raides, et l'usage de schémas explicites étant ainsi impossible, car le pas de temps est celui défini par l'étape de convection résolue de manière explicite. Les schémas implicites conduisent à l'écriture de systèmes d'équations non linéaires, des méthodes d'approximation sont alors proposées afin d'obtenir les solutions approchées.

Une attention particulière est portée au processus de vérification et validation lors du travail de simulation numérique dans cette thèse. En effet, le développement de méthodes numériques pour l'approximation de nouveaux systèmes d'équations est une tâche qui demande la plus grande prudence, surtout lorsqu'il s'agit du domaine de la sécurité nucléaire. La vérification consiste en la mise en place de cas tests où l'on dispose de solutions analytiques, et où on confronte les solutions approchées à la solution analytique. L'erreur doit tendre vers zéro au fur et à mesure que le maillage est raffiné, et la convergence doit se faire à la vitesse théoriquement attendue. Pour le système de convection, des cas tests de vérification sur base de problèmes de Riemann sont construits. Pour les étapes de relaxation, la construction se fait en adoptant des hypothèses sur les lois thermodynamiques et en introduisant des solutions exactes des ODE.

La validation consiste quand à elle à confronter les résultats de notre modèle complet (convection et sources) à des mesures expérimentales. La difficulté se pose au niveau du choix des résultats expérimentaux de référence. En effet, ce choix doit correspondre à la problématique physique qu'on se propose de simuler, qui -on le rappelle- est l'explosion vapeur. Ce phénomène est caractérisé par sa dynamique rapide et la violence des ondes de choc qu'il génère, sachant que les programmes expérimentaux associés sont rares. Face à ce problème, notre stratégie est de valider, dans un premier temps, partiellement les effets dynamiques (vitesse et pression) sur un cas test diphasique [12, 11]. Ensuite, une validation plus complète est proposée, sur la base de l'essai KROTOS-44 [45], l'un des rares essais d'explosion vapeur relativement bien documenté, qui présente des mesures de pression dans le cas d'un mélange entre métal fondu, eau liquide et vapeur d'eau.

Synthèse des travaux

0.4 Chapitre 1 : Relaxation and simulation of a barotropic three-phase flow model

Dans la perspective de l'objectif global de ce travail de thèse, à savoir la modélisation et simulation de l'*explosion vapeur*, ce premier chapitre constitue une étape nécessaire et fondatrice. En effet, il est consacré à l'étude d'un modèle à trois phases non miscibles où aucune hypothèse d'équilibre préalable n'est considérée. Un tel modèle est obtenu par l'application d'un opérateur de moyenne aux équations d'évolution de chaque phase, un système d'équations aux dérivées partielles (EDP) est ainsi formé, mais il est dit "*ouvert*" car il comporte plus de variables que d'équations, ce qui nécessite des lois de fermeture afin que le système soit bien posé. Les premiers éléments de cette modélisation ont été présentés dans [40], le choix de la configuration barotrope permet d'analyser le comportement dynamique des ondes de choc dans un milieu triphasique, ce qui est d'une pertinence notable au sujet de l'*explosion vapeur*, même si les effets de température n'y sont pas pris en compte.

Dans ce chapitre, le système d'EDP "*ouvert*" est présenté, il se compose d'une équation de taux de présence, d'un bilan de masse et d'un bilan de quantité de mouvement, tous indexés par l'indice de phase $k = 1, 2, 3$:

$$\begin{cases} \frac{\partial \alpha_k}{\partial t} + \mathcal{V}_\mathbf{i}(\mathbf{W}).\nabla \alpha_k = \phi_k(\mathbf{W}) \\ \\ \frac{\partial m_k}{\partial t} + \nabla.\left(m_k \mathbf{U_k}\right) = 0 \\ \\ \frac{\partial m_k \mathbf{U_k}}{\partial t} + \nabla.\left(m_k \mathbf{U_k} \times \mathbf{U_k} + \alpha_k P_k \mathbf{Id}\right) + \sum_{l=1, l\neq k}^{3} \Pi_{kl}(\mathbf{W}) \nabla \alpha_l = m_k \mathbf{S_k}(\mathbf{W}) \end{cases} \tag{0.1}$$

L'une des difficultés majeures liées à ce genre de modèles multi-phasiques est le choix des lois de fermeture, qui permettent de décrire ce qui se passe à l'interface entre les différents fluides. Ces lois doivent répondre à la fois à des exigences mathématiques (caractère *bien posé* du système à résoudre) et physiques concernant le comportement du mélange étudié.

Dans ce travail, des lois de fermeture sont proposées pour les termes d'interface (vitesse d'interface $\mathcal{V}_\mathbf{i}$ et pressions d'interface Π_{kl}) ainsi que les termes sources dits de relaxation (relaxation vitesse $\mathbf{S_k}$ et relaxation pression ϕ_k), le système *fermé* ainsi décrit respecte le cahier des charges détaillé en introduction, c'est-à-dire :

- L'hyperbolicité du système convectif ;
- Une inégalité d'entropie sur le système global ;
- L'unicité des relations de saut.

De plus, le système (0.1) est enrichi d'une équation d'aire interfaciale pour modéliser le processus de fragmentation sous l'effet d'une onde de choc : une phase présente sous forme de gouttes dispersées voit la taille de ses gouttes diminuer de plus en plus, sous l'effet d'une onde de choc se propageant dans le milieu fluide ambiant. Ce processus joue un rôle important dans la dynamique d'une *explosion vapeur* [6], d'où l'intérêt de le modéliser.

Après avoir présenté le modèle et ses différentes propriétés dans le cadre continu en section 2 du chapitre, dans la section 3 le cadre discret est étudié. La stratégie globale de résolution repose sur la méthode de *pas fractionnaires* [42], où le système global (0.1) est décomposé en plusieurs sous-systèmes qui représentent respectivement les effets de : convection, relaxation vitesse et relaxation pression.

Le sous-système convectif est à structure hyperbolique (hors cas de résonance), un schéma numérique de convection est donc choisi pour permettre le calcul des solutions approchées. Le schéma est ensuite vérifié sur deux cas-tests de problèmes de Riemann.

Les sous-systèmes de relaxation sont également examinés. On attire l'attention du lecteur sur le fait que se placer dans le cadre barotrope a pour conséquence importante le découplage total des deux étapes de relaxation : vitesse et pression. Cela simplifie de façon remarquable leur résolution. Les schémas adoptés pour chacune de ces étapes sont écrits sur la base des écarts de vitesse et de pression, et permettent de garantir le comportement de *relaxation*, ou retour en équilibre, qui se manifeste dans la décroissance des écarts en fonction du temps.

Enfin, un cas-test d'écoulement multiphasique est présenté. Il s'agit de la configuration correspondant au travail expérimental détaillé dans [12, 11]. Du point de vue numérique, ce cas est une illustration importante de l'effet de l'aire interfaciale sur l'évolution de l'écoulement. La fragmentation des gouttes dispersées dans une phase continue a un impact non négligeable, et retrouver sa trace sur les résultats numériques (notamment en pression) est l'une des conclusions significatives de ce chapitre.

Ce chapitre est complété d'une annexe qui fournit plusieurs résultats complémentaires concernant les cas-tests numériques réalisés.

0.5 Chapitre 2 : Simulation and validation of a three phase flow model with energy

Dans ce chapitre, on présente l'extension du modèle (0.1) au cadre non barotrope, cela se traduit par la prise en compte du bilan d'énergie dans le système d'EDP étudié, qui s'écrit pour $k = 1, 2, 3$:

$$\left\{\begin{array}{l} \frac{\partial \alpha_k}{\partial t} + \mathbf{V}_i(\mathbf{W}).\nabla \alpha_k = S_k^{\alpha}(\mathbf{W}) \\ \frac{\partial m_k}{\partial t} + \nabla.(m_k \mathbf{U}_k) = 0 \\ \frac{\partial m_k \mathbf{U}_k}{\partial t} + \nabla.(m_k \mathbf{U}_k \otimes \mathbf{U}_k + \alpha_k p_k \mathbf{Id}) + \sum_{l=1, l\neq k}^{3} \Pi_{kl}(\mathbf{W}) \nabla \alpha_l = \mathbf{S}_k^{U}(\mathbf{W}) \\ \frac{\partial \alpha_k E_k}{\partial t} + \nabla.(\alpha_k E_k \mathbf{U}_k + \alpha_k p_k \mathbf{U}_k) - \sum_{l=1, l\neq k}^{3} \Pi_{kl}(\mathbf{W}) \frac{\partial \alpha_l}{\partial t} = S_k^{E}(\mathbf{W}) \end{array}\right. \tag{0.2}$$

Ce système décrit donc un écoulement triphasique à trois champs de pression distincts, représentant ainsi une généralisation du modèle de Baer Nunziato [4]. Le modèle (0.2) s'inspire du formalisme présenté dans [39], notamment en ce qui concerne les lois de fermeture des termes interfaciaux : vitesse $\mathbf{V}_i(\mathbf{W})$ et pressions $\Pi_{kl}(\mathbf{W})$. En ce qui concerne les termes sources, des lois analogues à celles employées dans (0.1) sont proposées.

Dans le cadre continu, l'ensemble des propriétés du modèle (0.2) est vérifié : dans le formalisme général $3D$, les aspects mathématiques d'hyperbolicité et d'inégalité d'entropie sont démontrés, l'analyse est poussée dans le formalisme $1D$ en s'assurant que les solutions

régulières de (0.2) sont admissibles du point de vue thermodynamique, et également en étudiant le problème de Riemann $1D$, qui est d'une grande utilité pour l'étape de vérification numérique. S'agissant des termes sources, trois effets de relaxation sont considérés dans un premier temps : vitesse, pression et température. On s'assure que les lois de fermeture proposées pour ces termes sont conformes à l'inégalité d'entropie. Dans la suite du chapitre, seules la vitesse et la pression sont retenues, représentées par les termes $S_k^\alpha(\mathbf{W})$ et $\mathbf{S}_k^U(\mathbf{W})$ ainsi que leurs contributions respectives dans le bilan de l'énergie via $\Pi_{kl}(\mathbf{W})\frac{\partial \alpha_l}{\partial t}$ et $S_k^E(\mathbf{W})$.

Sur le plan discret, on reste dans le cadre de résolution par *pas fractionnaires* [42]. Un schéma de convection est choisi pour la résolution du sous-système convectif. Ce schéma est vérifié sur un cas test de problème de Riemann impliquant deux ondes : onde de couplage et onde de choc.

En ce qui concerne les sous-systèmes de relaxation, leur résolution est plus compliquée que dans le cadre barotrope. En effet, la prise en compte du bilan d'énergie a pour conséquence immédiate le couplage des deux effets de relaxation : vitesse et pression. De plus, le formalisme non barotrope induit plus d'interdépendances entre les variables du système, et donc plus de difficulté à les résoudre. En prenant compte de ces difficultés, des schémas d'approximation sont proposées pour chaque sous-système de relaxation, et des cas de vérification sont réalisés.

Enfin, on revient sur l'étude expérimentale [12, 11] déjà considérée dans le chapitre premier. Une comparaison est établie entre les résultats numériques et expérimentaux. On montre que la prise en compte des équations d'énergie permet une estimation plus *réaliste* des niveaux de pression résultant du passage d'une onde de choc dans le milieu diphasique étudié. On souligne également que, comme pour le modèle barotrope, l'effet de fragmentation des gouttes en milieu dispersé est retrouvé.

Plusieurs annexes sont présentées à la fin du chapitre, donnant des détails techniques sur les algorithmes considérés ou encore les cas-tests étudiés. En particulier, on y trouve l'algorithme de relaxation pression instantanée, des solutions analytiques pour les sous-systèmes de relaxation (vitesse et pression) qui sont indispensables pour les cas tests de vérification, et, en dernière annexe, l'examen de l'impact des temps de relaxation (en vitesse et pression) sur le comportement des solutions du modèle (0.2), dans une configuration de tube à choc triphasique.

0.6 Chapitre 3 : Simulation of a three-phase flow involving heat and mass transfer

Dans ce chapitre, on reprend le modèle (0.2) et on y apporte les dernières briques nécessaires pour la simulation d'un scénario d'*explosion vapeur* (EV).

En effet, en cas d'EV, lors du contact entre un fluide chaud (comme le corium) et un fluide de refroidissement (typiquement de l'eau), il y a non seulement des échanges mécaniques modélisés par les termes de relaxation vitesse et pression (déjà pris en compte dans (0.2)),

mais surtout des échanges thermiques forts, qui sont largement responsables de l'évaporation intense et rapide de l'eau, ce qui donne à l'EV son caractère explosif. La prise en compte du transfert thermique et l'échange de masse est donc indispensable.

Le système d'EDP qu'on considère est le suivant :

$$\begin{cases} \frac{\partial \alpha_k}{\partial t} + \mathbf{V}_i(\mathbf{W}).\nabla \alpha_k = S_k^{\alpha}(\mathbf{W}) \\ \frac{\partial m_k}{\partial t} + \nabla.(m_k \mathbf{U}_k) = S_k^{m}(\mathbf{W}) \\ \frac{\partial m_k \mathbf{U}_k}{\partial t} + \nabla.(m_k \mathbf{U}_k \otimes \mathbf{U}_k + \alpha_k p_k \mathbf{Id}) + \sum_{l=1,l\neq k}^{3} \Pi_{kl}(\mathbf{W}) \nabla \alpha_l = \mathbf{S}_k^{U}(\mathbf{W}) \\ \frac{\partial \alpha_k E_k}{\partial t} + \nabla.(\alpha_k E_k \mathbf{U}_k + \alpha_k p_k \mathbf{U}_k) - \sum_{l=1,l\neq k}^{3} \Pi_{kl}(\mathbf{W}) \frac{\partial \alpha_l}{\partial t} = S_k^{E}(\mathbf{W}) \end{cases} \tag{0.3}$$

La majeure différence avec (0.2) est la présence du terme source dans l'équation de bilan de masse. Ce terme a un impact significatif sur le reste du modèle, car sa contribution se voit sur les bilans de quantité de mouvement et d'énergie.

La partie convective de (0.3) est identique à celle de (0.2), notamment en ce qui concerne les fermetures des termes interfaciaux (vitesse $\mathbf{V}_i(\mathbf{W})$ et pressions $\Pi_{kl}(\mathbf{W})$). Les propriétés d'hyperbolicité, d'unicité de relations de saut et d'admissibilité des variables thermodynamiques (démontrées pour (0.2)) sont ainsi automatiquement préservées.

Quant aux termes sources, une loi de fermeture est proposée pour le terme de transfert de masse $S_k^m(\mathbf{W})$, ainsi que ses contributions dans $\mathbf{S}_k^U(\mathbf{W})$ et $S_k^E(\mathbf{W})$. On vérifie que le modèle ainsi formé reste conforme à l'inégalité d'entropie.

On examine ensuite de près les sous-systèmes de relaxation. Pour l'échange thermique, on s'assure que la loi de fermeture proposée permet le retour asymptotique à l'équilibre entre les températures des trois phases. Pour le transfert de masse, comme on s'intéresse aux applications EV où le mélange est composé de corium, eau liquide et vapeur d'eau, il ne peut y avoir transfert de masse qu'entre les deux phases de l'eau : liquide et vapeur. C'est donc un transfert de masse diphasique qu'on étudie.

Sur le plan discret, on adopte le schéma numérique de transfert de masse diphasique présenté dans [17, 46]. Pour l'échange thermique, un schéma écrit sur la base des écarts de température est mis en place, il permet notamment de préserver le comportement de relaxation mis en évidence dans le cadre continu.

Deux cas tests de vérification sont donnés, afin de démontrer la précision des schémas numériques adoptés pour l'échange thermique et le transfert de masse. Ensuite, deux autres cas tests d'*écoulement en boite* sont considérés pour illustrer l'effet combiné des différents termes de relaxation : le premier cas sert à valider la combinaison des effets de relaxation pression avec l'échange thermique, la solution analytique dans ce cas peut être calculée en fonction des lois d'état choisies ; et le deuxième cas prend en compte l'effet du transfert de masse, et permet notamment de mettre en évidence l'importance des rapports entre les temps caractéristiques d'échange de masse et transfert thermique.

Enfin, un cas test plus complet, représentatif d'un scénario d'EV, est étudié. Il s'agit de l'essai KROTOS-44 [45] où une masse de métal fondu est injectée dans un volume d'eau. Au contact de l'eau, de la vapeur est formée du fait de l'échange thermique qui a lieu entre

le métal et l'eau liquide. Au moment où le métal fondu est complétement immergé dans l'eau, une onde de choc est déclenchée dans le milieu, et une EV est ainsi provoquée. Cette expérience a fait l'objet d'un benchmark numérique (voir [58]), qui a notamment précisé les données d'initialisation à adopter, afin d'en faire une base de cas test numérique. En utilisant ces données d'initialisation, des calculs avec le modèle (0.3) sont réalisés. Une comparaison est dressée entre d'un côté le modèle (0.3) et les résultats expérimentaux, et d'un autre côté entre le modèle (0.3) et les résultats du code MC3D [56], code IRSN communément utilisé en France pour la simulation de l'EV.

0.7 Valorisation des travaux

Les travaux présentés dans ce manuscrit de thèse ont fait l'objet des publications suivantes :

1. Boukili H., Hérard JM. A splitting scheme for three-phase flow models. In : Cancès C., Omnes P. (eds) Finite Volumes for Complex Applications VIII - Hyperbolic, Elliptic and Parabolic Problems. FVCA 2017. Springer Proceedings in Mathematics & Statistics, vol 200. Springer, Cham.
2. Boukili H., Hérard JM. Relaxation and simulation of a barotropic three-phase flow model, ESAIM : M2AN, Volume 53, Number 3, Page(s) 1031-1059, May-June 2019.
3. Boukili H., Hérard JM. Simulation and preliminary validation of a three-phase flow model with energy. Soumis à Computers and Fluids.

Note importante : dans chaque chapitre « p » qui suit (p=1 à 3), la référence [N] appelée dans le texte du chapitre « p » figure en bibliographie de fin de chapitre « p ». Les références [L] appelées dans les chapitres 0 et 4 figurent dans la bibliographie générale pp. 147-151.

Chapitre 1

Relaxation and simulation of a barotropic three-phase flow model[1]

Hamza Boukili[2, 3], **Jean-Marc Hérard**[2, 3, 4]

Abstract. We focus here on a three-phase flow model in order to represent complex flows involving liquid metal droplets, liquid water, and its vapour. The governing equations and its main properties are given, and focus is given on the pressure-velocity relaxation process on the one hand, and on the structure of solutions of the one-dimensional Riemann problem associated with pure convective effects. A fractional step method that computes successively the convective part and the relaxation effects is used to obtain approximate solutions on unstructured meshes. Details of algorithms are provided, and it is shown that the numerical method preserves positive values of statistical fractions and partial masses. Verification and validation test cases are presented, and some perspectives are eventually drawn.

Mathematics Subject Classification. 76M12, 76T30, 35L60, 35Q35, 35L67.

Received March 20, 2018. Accepted December 28, 2018.

1. Boukili H., Hérard JM. Relaxation and simulation of a barotropic three-phase flow model, ESAIM : M2AN, Volume 53, Number 3, Page(s) 1031-1059, May-June 2019.

2. EDF Lab Chatou, 6, quai Watier, 78400 Chatou, France.

3. I2M, Aix Marseille Université, 39 rue Joliot Curie, 13453 Marseille, France.

4. Corresponding author : jean-marc.herard@edf.fr

1.1 Introduction

The modeling and the accurate simulation of steam explosion is actually an open topic ; it is indeed important for nuclear safety analysis, and it deserves relevant and meaningful models, and also appropriate numerical methods, to get decent approximations of pressure waves acting on solid structures. The steam explosion may occur when some very hot liquid metal flows down in a quiet liquid component such as water. In that case the heat transfer towards the water component depends on the local structure of liquid metal droplets. The liquid water surrounding the liquid metal droplet is suddenly changed into steam, and this, in turn, can modify the process, since the thin layer of steam in the vicinity of the metal droplet can inhibit the heat transfer between the two components. Afterwards, pressure waves may propagate, and change the topology of the flow, because droplets are sheared and dislocated when high relative velocities are involved. The break-up of liquid metal droplets thus increases the interfacial area between droplets and liquid water, so that the heat transfer may again develop and feed-up the whole chain. Different phenomenological scenarios have been proposed in the literature to predict these flow patterns. We refer the reader to [4] and references therein in order to have a better understanding of that problem, and also to the recent paper [27].

An important point to quote at once is that the sudden increase of vapour concentration results in huge pressure waves including shock and rarefaction waves. Another feature is that the three fields (liquid metal droplets, liquid water and steam) are immiscible ; moreover, mass transfer may only happen within the water component, more precisely between the liquid water and its vapour phase. Some multiphase flow models have been proposed in the past, which mainly rely on the instantaneous pressure relaxation assumption. However, as it is well known for standard two-phase flow models, one straightforward drawback is that associated sets of PDEs are not hyperbolic. Even more, jump relations through -expected- shock waves are not defined. This may not only result in several difficulties when tackling the steam explosion description, in order to estimate the amplitude of shock waves on wall boundaries, since we need to compute an initial-value problem, but it also renders the estimation of the pressure shock waves questionable.

Hence the work presented herein aims at providing some original preliminary results in the direction of steam explosion modeling. For that purpose, we first need to define adequate sets of PDEs, so that the following requirements arise :

— the whole model must comply with hyperbolicity requirements ;

— some physical entropy inequality is needed ;

— unique jump conditions are mandatory ;

and of course, schemes should provide convergent approximations of pressure shock waves.

Obviously, there are several difficulties on the way to such a correct and physically relevant description. In order to simplify a little bit the whole approach, we will focus in this work on barotropic situations, thus neglecting heat transfer. One basic reason is that one needs to get some estimation of the interfacial area, since this seems to be one of the key

points on the way to pave towards a correct modeling of steam explosion. However, we emphasize that extensions of the barotropic three-phase model that will be considered here [20] already exist (see [19]), which means that the sequel of the present framework is indeed clear, at least from a global point of view. In other words, the current barotropic model [20] may be seen as a rough version of model [19]. It is also worth noting that the latter models [20, 19] are actually quite similar to the classical two-phase flow models arising from [3, 5, 24, 15, 8].

Hence, the present paper will be organized as follows. We will first present the governing set of equations for the basic barotropic three-phase flow model, and then give a slight extension in order to account for the interfacial area. Afterwards, we will give the main properties of both of these, while focusing on solutions of the one-dimensional Riemann problem. This enables to extract meaningful analytical test cases including shock waves, rarefaction waves and contact discontinuities. Next, we will briefly discuss the inner pressure-velocity relaxation processes, and comment the whole. The second part will be devoted to the presentation of a fractional step method that treats separately convective effects and source terms. In this paper, we will only consider a rough Finite Volume scheme to cope with the convective part, and postpone the derivation of more accurate -though stable- approximate Riemann solvers to a future work ; this will enable us to concentrate on the numerical treatment of velocity and pressure relaxation effects. The first section in the last part will provide some approximate solutions of analytical test cases, including the measure of the L^1 norm of the error. Eventually, we will show some results corresponding to the propagation of a shock wave through a cloud of liquid droplets, which corresponds to the experimental setup of the paper [7]. One crucial point is that the latter configuration is very similar to what happens in the steam explosion setup, and meanwhile, this will give some good confidence with respect to the modeling of the break-up phenomenon. The conclusion will highlight the main directions of progress towards a complete simulation of steam explosion.

1.2 Governing equations and main properties of the two-dimensional three-phase flow model

1.2.1 Governing equations

Throughout the paper, $\alpha_k \in [0,1]$, ρ_k, $m_k = \alpha_k \rho_k$, $\mathbf{U_k}$, will denote the mean statistical fraction, the mean density, the partial mass and the mean velocity of phase k Statistical fractions are such that :

$$\alpha_1 + \alpha_2 + \alpha_3 = 1 \tag{1.1}$$

The mean pressure $P_k(\rho_k)$ is an increasing function which is such that :

$$\lim_{x\to\infty} P_k(x) = +\infty \qquad ; \qquad \lim_{x\to 0} P_k(x) = 0 \tag{1.2}$$

and we introduce the phasic speed of sound waves c_k such that : $c_k^2 = P_k'(\rho_k)$.

The state variable $\mathbf{W}$ will denote the following vector :

$$\mathbf{W} = (\alpha_2, \alpha_3, m_1, m_2, m_3, m_1\mathbf{U_1}, m_2\mathbf{U_2}, m_3\mathbf{U_3})^t$$

The set of governing equations for the three-phase flow model will read ([20]) :

$$\left\{\begin{array}{l} \frac{\partial \alpha_k}{\partial t} + \mathcal{V}_\mathbf{i}(\mathbf{W})\nabla\alpha_k = \phi_k(\mathbf{W}) \ ; \\ \\ \frac{\partial m_k}{\partial t} + \nabla.\left(m_k \mathbf{U_k}\right) = 0 \ ; \\ \\ \frac{\partial m_k \mathbf{U_k}}{\partial t} + \nabla.\left(m_k \mathbf{U_k} \times \mathbf{U_k} + \alpha_k P_k \mathbf{Id}\right) + \Sigma_{l=1,l\neq k}^{3} \Pi_{kl}(\mathbf{W})\nabla\alpha_l = m_k \mathbf{S_k}(\mathbf{W}) \ . \end{array}\right. \tag{1.3}$$

Source terms should be such that :

$$\Sigma_{k=1}^{3} m_k \mathbf{S_k}(\mathbf{W}) = \mathbf{0}$$

and :

$$\Sigma_{k=1}^{3} \phi_k(\mathbf{W}) = 0$$

since they only take into account transfers between the different phases.

Moreover, a similar constraint holds for the $\Pi_{kl}(\mathbf{W})$ since :

$$\Sigma_{k=1}^{3} \left(\Sigma_{l=1,l\neq k}^{3} \Pi_{kl}(\mathbf{W})\nabla\alpha_l\right) = \mathbf{0}$$

and of course, owing to (1.1), the three quantities $\nabla\alpha_l$ are in agreement with :

$$\Sigma_{k=1}^{3} \nabla\alpha_k = \mathbf{0}$$

The first and second equations provide the evolution of the statistical fraction and mass fraction within phase k, while the third equation stands for the momentum balance equation. The interface velocity $\mathcal{V}_\mathbf{i}(\mathbf{W})$ and the interfacial pressures $\Pi_{kl}(\mathbf{W})$ are not unknown. Actually the interface pressures are uniquely defined as functions of the interface velocity. More precisely, if $\mathcal{V}_\mathbf{i}(\mathbf{W})$ denotes a convex combination of the phasic velocities, that is :

$$\mathcal{V}_\mathbf{i}(\mathbf{W}) = a_1(\mathbf{W})\mathbf{U_1} + a_2(\mathbf{W})\mathbf{U_2} + a_3(\mathbf{W})\mathbf{U_3}$$

where all $a_k(\mathbf{W})$ lie in $[0,1]$, with the constraint : $a_1(\mathbf{W}) + a_2(\mathbf{W}) + a_3(\mathbf{W}) = 1$, then all interfacial pressures should be such that :

$$\left\{\begin{array}{l} \Pi_{12}(\mathbf{W}) = (1 - a_1(\mathbf{W}))P_1 + a_1(\mathbf{W})P_2 \ ; \\ \Pi_{21}(\mathbf{W}) = a_2(\mathbf{W})P_1 + (1 - a_2(\mathbf{W}))P_2 \ ; \\ \Pi_{13}(\mathbf{W}) = (1 - a_1(\mathbf{W}))P_1 + a_1(\mathbf{W})P_3 \ ; \\ \Pi_{31}(\mathbf{W}) = a_3(\mathbf{W})P_1 + (1 - a_3(\mathbf{W}))P_3 \ ; \\ \Pi_{23}(\mathbf{W}) = (1 - a_2(\mathbf{W}))P_2 + a_2(\mathbf{W})P_3 \ ; \\ \Pi_{32}(\mathbf{W}) = a_3(\mathbf{W})P_2 + (1 - a_3(\mathbf{W}))P_3 \ ; \end{array}\right. \tag{1.4}$$

These closure laws, together with a correct choice of the right hand side contributions $\phi_k(\mathbf{W})$ and $\mathbf{S_k}(\mathbf{W})$, will ensure that smooth solutions of system (1.3) would comply with a relevant entropy balance.

Closure laws to account for drag effects between phases k, l are simply chosen as :

$$m_k \mathbf{S_k}(\mathbf{W}) = \Sigma_{l=1}^{3} e_{kl}(\mathbf{W})(\mathbf{U_l} - \mathbf{U_k}) \tag{1.5}$$

where the symetric positive functions $e_{kl}(\mathbf{W}) = e_{lk}(\mathbf{W})$ are chosen in agreement with the two-phase flow literature.

Meanwhile, we define :

$$\phi_k(\mathbf{W}) = \Sigma_{l=1}^{3} d_{kl}(\mathbf{W})(P_k - P_l) \tag{1.6}$$

where the symetric positive functions $d_{kl}(\mathbf{W}) = d_{lk}(\mathbf{W})$, which involve presssure relaxation time scales, will be taken from [14].

1.2.2 Main properties of the three-phase flow model

We introduce $\psi_k(\rho_k)$ such that $\psi_k'(\rho_k) = \frac{P_k(\rho_k)}{\rho_k^2}$, and define the mixture entropy $\eta(\mathbf{W})$ and the entropy flux $\mathbf{f}_\eta(\mathbf{W})$ as :

$$\begin{cases} \eta(\mathbf{W}) = \Sigma_{k=1}^{3} m_k \left(|\mathbf{U_k}.\mathbf{U_k}|/2 + \psi_k(\rho_k) \right) \\ \mathbf{f}_\eta(\mathbf{W}) = \Sigma_{k=1}^{3} m_k \left(|\mathbf{U_k}.\mathbf{U_k}|/2 + \psi_k(\rho_k) + \frac{P_k}{\rho_k} \right) \mathbf{U_k} \end{cases} \tag{1.7}$$

Owing to the closure laws (1.5) and (1.6), the following property holds for smooth solutions of (1.3) :

Property 1 :
Smooth solutions of (1.3) *comply with the following entropy inequality :*

$$\frac{\partial \eta(\mathbf{W})}{\partial t} + \nabla . \left(\mathbf{f}_\eta(\mathbf{W}) \right) \leq 0. \tag{1.8}$$

(see [20]).

Now, using invariance under frame rotation of system (1.3), introducing two normal vectors $\mathbf{n} = (n_x, n_y)$ and $\tau = (-n_y, n_x)$ in $\mathcal{R}^2$, such that : $n_x^2 + n_y^2 = 1$, and rewriting (1.3) in the $(\mathbf{n}, \tau)$ frame, we may consider the one-dimensional homogeneous system in the $\mathbf{n}$ direction obtained by neglecting transverse variations $\frac{\partial g}{\partial \tau}$ with respect to τ, whatever g is. Thus we get :

$$\begin{cases} \frac{\partial \alpha_k}{\partial t} + \mathcal{V}_\mathbf{i}(\mathbf{W}).\mathbf{n} \frac{\partial \alpha_k}{\partial n} = 0 \ ; \\ \frac{\partial m_k}{\partial t} + \frac{\partial m_k \mathbf{U_k}.\mathbf{n}}{\partial n} = 0 \ ; \\ \frac{\partial m_k \mathbf{U_k}.\mathbf{n}}{\partial t} + \frac{\partial m_k (\mathbf{U_k}.\mathbf{n})^2 + \alpha_k P_k}{\partial n} + \Sigma_{l=1, l \neq k}^{3} \Pi_{kl}(\mathbf{W}) \frac{\partial \alpha_l}{\partial n} = 0 \ ; \\ \frac{\partial m_k \mathbf{U_k}.\tau}{\partial t} + \frac{\partial m_k (\mathbf{U_k}.\mathbf{n})(\mathbf{U_k}.\tau)}{\partial n} = 0 \ . \end{cases} \tag{1.9}$$

A straightforward consequence is the following :

Property 2 :
System (1.9) *is hyperbolic. It admits the following real eigenvalues :*

$$\lambda_{0,1}(\mathbf{W}) = \mathcal{V}_\mathbf{i}(\mathbf{W}).\mathbf{n} \quad ; \quad \lambda_{2-7}(\mathbf{W}) = \mathbf{U_k}.\mathbf{n} \pm c_k \quad ; \quad \lambda_{8-10}(\mathbf{W}) = \mathbf{U_k}.\mathbf{n} \tag{1.10}$$

and associated right-eigenvectors span the whole space IR^{11} *unless :*

$$(\mathcal{V}_\mathbf{i}(\mathbf{W}) - \mathbf{U_k}).\mathbf{n} = \pm c_k. \tag{1.11}$$

The proof is classical and left to the reader.

In the sequel of the paper, we will focus on the following closure law :

$$\mathcal{V}_\mathbf{i}(\mathbf{W}) = \mathbf{U_1}.$$

which implies :

$$\left\{ \begin{array}{l} \Pi_{12}(\mathbf{W}) = \Pi_{21}(\mathbf{W}) = \Pi_{23}(\mathbf{W}) = P_2 \ ; \\ \Pi_{13}(\mathbf{W}) = \Pi_{31}(\mathbf{W}) = \Pi_{32}(\mathbf{W}) = P_3 \ . \end{array} \right. \tag{1.12}$$

owing to (1.4). We note at a glance that this is in fact the straightforward counterpart of the Baer-Nunziato closure laws in a two-phase framework ([3]).

1.2.3 Some additional results in the one-dimensional framework

In a pure one-dimensional framework, we may focus on the structure of the latter fields. More precisely, if we consider :

$$\left\{ \begin{array}{l} \frac{\partial \alpha_k}{\partial t} + \mathcal{V}_i(W)\frac{\partial \alpha_k}{\partial x} = 0 \ ; \\ \\ \frac{\partial m_k}{\partial t} + \frac{\partial m_k u_k}{\partial x} = 0 \ ; \\ \\ \frac{\partial m_k u_k}{\partial t} + \frac{\partial m_k u_k^2 + \alpha_k P_k}{\partial x} + \Sigma_{l=1, l\neq k}^{3} \Pi_{kl}(\mathbf{W})\frac{\partial \alpha_l}{\partial x} = 0 \ . \end{array} \right. \tag{1.13}$$

we may set : $\mathbf{X} = (\alpha_2, \alpha_3, m_1, m_2, m_3, m_1u_1, m_2u_2, m_3u_3)$, and we get at once :

Property 3 :

— *The convective subset* (1.13) *admits eight real eigenvalues which read :*

$$\lambda_{0,1}(\mathbf{X}) = u_1 \quad ; \quad \lambda_{2-7}(\mathbf{X}) = u_k \pm c_k. \tag{1.14}$$

The field associated with eigenvalues $\lambda_{0,1}(\mathbf{X})$ *is linearly degenerate. Meanwhile, fields associated with* $\lambda_{2-7}(\mathbf{X})$ *are genuinely non linear.*

— *The six Riemann invariants in the* $0-1$ *coupling wave write :*

$$I^1_{0,1}(\mathbf{X}) = u_1 \quad ; \quad I^2_{0,1}(\mathbf{X}) = m_2(u_2-u_1) \quad ; \quad I^3_{0,1}(\mathbf{X}) = m_3(u_3-u_1);$$

$$I^4_{0,1}(\mathbf{X}) = \frac{(u_1-u_2)^2}{2} + \int_0^{\rho_2} \frac{c_2^2(x)}{x}dx \quad ; \quad I^5_{0,1}(\mathbf{X}) = \frac{(u_1-u_3)^2}{2} + \int_0^{\rho_3} \frac{c_3^2(x)}{x}dx;$$
$$I^6_{0,1}(\mathbf{X}) = \Sigma_{k=1}^3(\alpha_k P_k) + m_2(u_2-u_1)^2 + m_3(u_3-u_1)^2.$$

— *Within each isolated GNL wave, unique jump conditions between* $\mathbf{X}_l, \mathbf{X}_r$ *states arise :*

$$\begin{cases} [\alpha_k]_l^r = 0 \ ; \\ -\sigma[m_k]_l^r + [m_k u_k]_l^r = 0 \ ; \\ -\sigma[m_k u_k]_l^r + [m_k u_k^2 + \alpha_k P_k]_l^r = 0 \ ; \end{cases} \tag{1.15}$$

where σ denotes the speed of the discontinuity separating states $\mathbf{X}_l, \mathbf{X}_r$.

— *Within the GNL wave associated with* $\lambda_2(\mathbf{X}) = u_1 - c_1$ *(resp.* $\lambda_3(\mathbf{X}) = u_1 + c_1$*) , Riemann invariants connecting* $\mathbf{X}_l, \mathbf{X}_r$ *states are* $(\alpha_2, \alpha_3, \rho_2, \rho_3, u_2, u_3)$ *and :* $u_1 + \int \frac{c_1(\rho_1)}{\rho_1}d\rho_1$ *(resp.* $u_1 - \int \frac{c_1(\rho_1)}{\rho_1}d\rho_1$*). Similar results hold for* $4-5$ *and* $6-7$ *fields.*

The latter Riemann invariants and jump conditions will enable us to construct exact solutions in order to check the true convergence of algorithms (see for instance the first two test cases in section 4). Again, the latter property is the straightforward counterpart of what occurs when focusing on the two-phase barotropic Baer-Nunziato model (see [3]).

Actually, if $\mathbf{X}_l$ denotes the state on the left-hand side of the $0-1$ coupling wave, and if we assume that $(\alpha_2)_r, (\alpha_3)_r$ are also given, we may compute the right state $\mathbf{X}_r$ by enforcing :

$$I^m_{0,1}(\mathbf{X}_r) = I^m_{0,1}(\mathbf{X}_l)$$

where the left state is given. We only need to compute $x_2 = (\rho_2)_r$ solution of the scalar equation $g_2(x_2) = 0$ where :

$$g_2(x_2) = \frac{(I^2_{0,1}(\mathbf{X}_l))^2}{2((\alpha_2)_r x_2)^2} + \int_0^{x_2} \frac{c_2^2(x)}{x}dx - I^4_{0,1}(\mathbf{X}_l)$$

and in a similar way $x_3 = (\rho_3)_r$ solution of the scalar equation $g_3(x_3) = 0$ where :

$$g_3(x_3) = \frac{(I^3_{0,1}(\mathbf{X}_l))^2}{2((\alpha_3)_r x_3)^2} + \int_0^{x_3} \frac{c_3^2(x)}{x}dx - I^5_{0,1}(\mathbf{X}_l)$$

Once these two scalar quantities have been calculated, we may update $(u_2)_r$ and $(u_3)_r$ using the following equalities :

$$(u_2)_r = (u_1)_l + \frac{I^2_{0,1}(\mathbf{X}_l)}{(m_2)_r}$$

and also :

$$(u_3)_r = (u_1)_l + \frac{I^3_{0,1}(\mathbf{X}_l)}{(m_3)_r}$$

The last unknown $x_1 = (\rho_1)_r$ is found by solving :

$$I^6_{0,1}(x_1) = I^6_{0,1}(\mathbf{X}_l)$$

with some abuse of notation.
□
We also note that the form of the function $g_k(x)$ is similar to the one encountered in the shallow-water framework, when the "bottom of the lake" is not uniform. The latter results will be used in section 4.1. Other technical results on the convexity of the entropy and on the symmetric form of the system can be found in [22].

1.2.4 A slightly modified three-phase flow model

For some practical purposes, we will need some enrichment of the latter three-phase flow model (1.3), in order to account for interfacial area modeling. Actually this will be used in order to compute situations where droplets of liquid phase 1 are sheared and dislocated.

Hence, if A denotes some -positive- function standing for the interfacial area, we introduce some extension of the latter three-phase flow model (1.3), which reads :

$$\left\{ \begin{array}{l} \frac{\partial A}{\partial t} + \nabla.(A\mathbf{U_1}) = g(A,\mathbf{W}) \ ; \\ \\ \frac{\partial \alpha_k}{\partial t} + \mathcal{V}_\mathbf{i}(\mathbf{W})\nabla\alpha_k = \phi_k(\mathbf{W}) \ ; \\ \\ \frac{\partial m_k}{\partial t} + \nabla.(m_k\mathbf{U_k}) = 0 \ ; \\ \\ \frac{\partial m_k\mathbf{U_k}}{\partial t} + \nabla.(m_k\mathbf{U_k}\times\mathbf{U_k} + \alpha_k P_k\mathbf{Id}) + \Sigma^3_{l=1,l\neq k}\Pi_{kl}(\mathbf{W})\nabla\alpha_l = m_k\mathbf{S^A_k}(\mathbf{A},\mathbf{W}) \ . \end{array} \right. \tag{1.16}$$

or in a more condensed form :

$$\left\{ \begin{array}{l} \frac{\partial A}{\partial t} + \nabla.(A\mathbf{U_1}) = g(A,\mathbf{W}) \ ; \\ \\ \frac{\partial \mathbf{W}}{\partial t} + \nabla.(\mathbf{F}(\mathbf{W})) + \Sigma^3_{l=1}\mathbf{G_l}(\mathbf{W})\nabla\alpha_l = \mathbf{r}(\mathbf{A},\mathbf{W}) \ . \end{array} \right. \tag{1.17}$$

where the non-negative function $g(A,\mathbf{W})$, which takes dislocation effects of phase 1 droplets into account, will be described in detail afterwards. The first governing equation for A is taken from [27, 29]. Actually, the closure laws for $\Pi_{kl}(\mathbf{W})$ interfacial terms still agree with (1.4). Furthermore, we assume that we still have :

$$m_k\mathbf{S^A_k}(\mathbf{A},\mathbf{W}) = \Sigma^3_{l=1}e^A_{kl}(A,\mathbf{W})(\mathbf{U_l}-\mathbf{U_k}) \tag{1.18}$$

where the positive functions $e^A_{kl}(A,\mathbf{W}) = e^A_{lk}(A,\mathbf{W})$ are directly deduced from the latter $e_{kl}(\mathbf{W})$.

Then, if we choose the combination $a_1 = 1$, $a_2 = a_3 = 0$, we get the following result :

Proposition 1 :

— *The homogeneous convective part of system* (1.17) *admits real eigenvalues ; it is hyperbolic unless :*

$$|(\mathbf{U_1} - \mathbf{U_k}).\mathbf{n}| = c_k$$

— *Smooth solutions of* (1.17) *comply with :*

$$\frac{\partial \eta(\mathbf{W})}{\partial t} + \nabla.(\mathbf{f}_\eta(\mathbf{W})) = RHS_\eta(\mathbf{W}) \leq 0. \tag{1.19}$$

Proof : the computation of eigenvalues is classical. Turning to the entropy inequality, the only difference with the former three-phase flow model (1.3) in section 2.1 concerns the exact form of the right hand side, which reads now :

$$RHS_\eta(\mathbf{W}) = \nabla_W \eta(\mathbf{W}).\mathbf{r}(\mathbf{A}, \mathbf{W})$$

or :

$$RHS_\eta(\mathbf{W}) = -\Sigma_{k=1}^3 \Sigma_{l=1}^3 \left(e_{kl}^A(A, \mathbf{W})|\mathbf{U_l} - \mathbf{U_k}|^2 + d_{kl}(\mathbf{W})(P_k - P_l)^2 \right)/2$$

□

Remark 1 :

We may introduce $\psi_A = A/m_1$, and some positive function $h(\psi_A)$ such that $h'(\psi_A) \leq 0$ and $0 \leq h''(\psi_A)$. We also note :

$$\eta_A(A, \mathbf{W}) = \eta(\mathbf{W}) + m_1 k_0^2 h(\psi_A)$$

with $k_0 \in \mathcal{R}$, and :

$$\mathbf{f}_{\eta,\mathbf{A}}(\mathbf{A}, \mathbf{W}) = \mathbf{f}_\eta(\mathbf{W}) + m_1 k_0^2 h(\psi_A)\mathbf{U_1}$$

Then regular solutions of (1.17) *agree with*

$$\frac{\partial \eta_A(A, \mathbf{W})}{\partial t} + \nabla.(\mathbf{f}_{\eta,\mathbf{A}}(\mathbf{A}, \mathbf{W})) \leq 0.$$

Proof : starting from the balance equation for A and using the mass balance equation for phase 1, we get :

$$\frac{\partial \psi_A}{\partial t} + \mathbf{U_1}.\nabla \psi_A = g(A, \mathbf{W})/m_1 \tag{1.20}$$

Thus, using the mass balance equation of phase 1 once more :

$$\frac{\partial m_1 h(\psi_A)}{\partial t} + \nabla.(m_1 \mathbf{U_1} h(\psi_A)) = g(A, \mathbf{W})h'(\psi_A) \tag{1.21}$$

Meanwhile, we have :

$$\frac{\partial \eta(\mathbf{W})}{\partial t} + \nabla.(\mathbf{f}_\eta(\mathbf{W})) = \nabla_W \eta(\mathbf{W}).\mathbf{r}(\mathbf{A}, \mathbf{W}) \leq 0 \tag{1.22}$$

which, after summation, ends up with :

$$\frac{\partial \eta_A(A,\mathbf{W})}{\partial t} + \nabla.\left(\mathbf{f}_{\eta,\mathbf{A}}(\mathbf{A},\mathbf{W})\right) = \nabla_W \eta(\mathbf{W}).\mathbf{r}(\mathbf{A},\mathbf{W}) + k_0^2 g(A,\mathbf{W}) h'(\psi_A) \tag{1.23}$$

This enables to conclude since $h'(\psi_A) \leq 0$. $\square$

It is indeed useful to go back to the pure one-dimensional framework in order to examine some particularities of the modified three-phase flow model. Thus, if we focus on the pure $1D$ model that writes :

$$\left\{ \begin{array}{l} \frac{\partial m_1 \psi_A}{\partial t} + \frac{\partial m_1 u_1 \psi_A}{\partial x} = 0 \ ; \\ \\ \frac{\partial \alpha_k}{\partial t} + u_1 \frac{\partial \alpha_k}{\partial x} = 0 \ ; \\ \\ \frac{\partial m_k}{\partial t} + \frac{\partial m_k u_k}{\partial x} = 0 \ ; \\ \\ \frac{\partial m_k u_k}{\partial t} + \frac{\partial m_k u_k^2 + \alpha_k P_k}{\partial x} + \Sigma_{l=1, l\neq k}^{3} \Pi_{kl}(\mathbf{W}) \frac{\partial \alpha_l}{\partial x} = 0 \ . \end{array} \right. \tag{1.24}$$

We may introduce the non-conservative state vector $\mathbf{Y}$ such that :

$$\mathbf{Y}^T = (\psi_A, \mathbf{X^T})$$

Then, for regular solutions, the homogeneous convective part of system (1.24) reads :

$$\left\{ \begin{array}{l} \frac{\partial \psi_A}{\partial t} + u_1 \frac{\partial \psi_A}{\partial x} = 0 \ ; \\ \\ \frac{\partial \mathbf{X}}{\partial t} + \mathbf{C}(\mathbf{X}) \frac{\partial \mathbf{X}}{\partial x} = 0 \ ; \end{array} \right. \tag{1.25}$$

which may also be written in a more compact form :

$$\frac{\partial \mathbf{Y}}{\partial t} + \mathcal{C}(\mathbf{Y}) \frac{\partial \mathbf{Y}}{\partial x} = 0. \tag{1.26}$$

We get at once :

Proposition 2 :

— *The convective subset* (1.24) *admits nine real eigenvalues which read :*

$$\lambda_{0,1,2}(\mathbf{Y}) = u_1 \quad ; \quad \lambda_{3-8}(\mathbf{Y}) = u_k \pm c_k. \tag{1.27}$$

The field associated with eigenvalues $\lambda_{0,1,2}(\mathbf{Y})$ *is linearly degenerate. Fields associated with* $\lambda_{3-8}(\mathbf{Y})$ *are genuinely non linear.*

— ψ_A is a Riemann inavariant within each GNL field.

— *The structure of the coupling wave is unchanged, since the six Riemann invariants in the* $0-1-2$ *coupling wave write :*

$$I^1_{0,1,2}(\mathbf{Y}) = u_1 \quad ; \quad I^2_{0,1,2}(\mathbf{Y}) = m_2(u_2-u_1) \quad ; \quad I^3_{0,1,2}(\mathbf{Y}) = m_3(u_3-u_1);$$

$$I^4_{0,1,2}(\mathbf{Y}) = \frac{(u_1-u_2)^2}{2} + \int_0^{\rho_2}(\frac{c_2^2(x)}{x}dx) \quad ; \quad I^5_{0,1,2}(\mathbf{Y}) = \frac{(u_1-u_3)^2}{2} + \int_0^{\rho_3}(\frac{c_3^2(x)}{x}dx);$$
$$I^6_{0,1,2}(\mathbf{Y}) = \Sigma_{k=1}^3(\alpha_k P_k) + m_2(u_2-u_1)^2 + m_3(u_3-u_1)^2.$$

— *If* σ *denotes the speed of the discontinuity separating* $\mathbf{Y}_l, \mathbf{Y}_r$ *states in an isolated GNL wave, jump conditions between* $\mathbf{Y}_l, \mathbf{Y}_r$ *states are :*

$$\begin{cases} [\alpha_k]_l^r = [\psi_A]_l^r = 0 \ ; \\ \\ [\rho_k(u_k-\sigma)]_l^r = 0 \ ; \\ \\ [\rho_k(u_k-\sigma)^2 + P_k]_l^r = 0 \ ; \end{cases} \tag{1.28}$$

Proof : if $\mathbf{r_0}(\mathbf{X}), \mathbf{r_1}(\mathbf{X})$ denote the two right-eigenvectors associated with the double eigenvalue $\lambda_{0,1}(X) = u_1$ of matrix $\mathbf{C}(\mathbf{X})$, we define :

$$\mathbf{R_0}(\mathbf{Y})^T = (1, \mathbf{O}^T)$$

and, for $k = 1, 2$:

$$\mathbf{R_k}(\mathbf{Y})^T = (0, \mathbf{r_{k-1}}(\mathbf{X})^T)$$

Now, we may compute, for $m = 1-6$:

$$\nabla_Y(I^m_{0,1,2}(\mathbf{Y})).\mathbf{R_0}(\mathbf{Y}) = (0, \nabla_X(I^m_{0,1}(\mathbf{X}))^T).(1, \mathbf{O}^T)^T = 0$$

and, for $k = 1, 2$:

$$\nabla_Y(I^m_{0,1,2}(\mathbf{Y})).\mathbf{R_k}(\mathbf{Y}) = (0, \nabla_X(I^m_{0,1,2}(\mathbf{Y}))^T)(0, \mathbf{r_{k-1}}(\mathbf{X})^T)^T = \nabla_X(I^m_{0,1}(\mathbf{X}))).\mathbf{r_{k-1}}(\mathbf{X}) = 0$$

owing to property 3. Evenmore, defining $\mathbf{R_k}(\mathbf{Y})^T = (0, \mathbf{r_{k-1}}(\mathbf{X})^T)$, for $k = 3-8$, where $\mathbf{r_{k-1}}(\mathbf{X})$ stands for the $(k-1)$-th right-eigenvector of $\mathbf{C}(\mathbf{X})$, we end up with :

$$\nabla_Y(\psi_A).\mathbf{R_k}(\mathbf{Y}) = (1, \mathbf{0}^T)(0, \mathbf{r_{k-1}}(\mathbf{X})^T)^T = 0$$

Furthermore, if we turn to jump conditions within an isolated GNL field, we have :

$$\begin{cases} -\sigma[m_1\psi_A]_l^r + [m_1\psi_A u_1]_l^r = 0 \ ; \\ \\ -\sigma[m_1]_l^r + [m_1 u_1]_l^r = 0 \ ; \end{cases} \tag{1.29}$$

and thus :

$$\overline{m_1(u_1-\sigma)}_{lr}[\psi_A]_l^r = 0$$

with the classical notation $\overline{\psi}_{lr} = (\psi_l + \psi_r)/2$, or equivalently :

$$m_1(u_1 - \sigma)[\psi_A]_l^r = 0$$

□

Remark 2 :
Using the above jump conditions in the GNL field associated with eigenvalue $u_1 \pm c_1$ within phase 1 we note that :

$$[A]_l^r = [m_1\psi_A]_l^r = \psi_A[m_1]_l^r = \psi_A\alpha_1[\rho_1]_l^r$$

This means that for the weakly compressible liquid within phase 1, we may expect slight variations of the interfacial area A through phase 1 shock waves, though α_1 does not vary through the latter field.

Remark 3 :
The function $g(A, W)$ that will be used in practical computations will only take breakup phenomenum into account, and effects of coalescence will be neglected, which means that A will always be non-decreasing. Of course other forms are available in the litterature, in order to account for coalescence (see [16, 30, 31, 36] among others, and also numerous references therein), and alternative closure laws for the breakup can also be found in the latter references. We emphasize that other convective patterns are also proposed in [23, 36] for the interfacial area A, which are not under conservative form. This of course would raise the problem of how to close jump conditions associated with A.

1.2.5 Some comments on the pressure-velocity relaxation process

We turn now to some aspects related to the pressure-velocity relaxation process involved in the latter three-phase flow models. For readers interested in theoretical aspects in relaxation processes occuring in two phase flow models, we refer for instance to [13]. Now, some specificities immediately arise for three-phase flows, which are mainly due to the fact that three one-to-one connections are present in the whole interfacial transfer. In [20], a few results were given when restricting to "isotropic" relaxation time scales. Hence the system of interest is :

$$\begin{cases} \frac{\partial \alpha_k}{\partial t} = \phi_k(\mathbf{W}) \ ; \\ \\ \frac{\partial m_k}{\partial t} = 0 \ ; \\ \\ \frac{\partial m_k \mathbf{U_k}}{\partial t} = m_k \mathbf{S_k}(\mathbf{W}) \ . \end{cases} \tag{1.30}$$

and we define the quantities : $a_k = \rho_k c_k^2/\alpha_k$. We also introduce :

$$\Delta P_{21} = P_2 - P_1 \quad ; \quad \Delta P_{23} = P_2 - P_3$$

and :

$$\mathbf{Y_p} = (\Delta P_{21}, \Delta P_{23})^T \ . \tag{1.31}$$

Owing to the fact that the partial mass remains constant, we get first :

$$\frac{\partial P_k}{\partial t} = -a_k \frac{\partial \alpha_k}{\partial t}$$

Thus it comes :

$$\frac{\partial \mathbf{Y_p}}{\partial t} = -\mathcal{U}_\mathbf{a} \frac{\partial (\alpha_2, \alpha_3)^T}{\partial t}$$

The 2×2 matrix $\mathcal{U}_\mathbf{a}$ has real coefficients :

$$(\mathcal{U}_\mathbf{a})_{11} = a_1 + a_2; \quad (\mathcal{U}_\mathbf{a})_{12} = a_1; \quad (\mathcal{U}_\mathbf{a})_{21} = a_2; \quad (\mathcal{U}_\mathbf{a})_{22} = -a_3$$

Its determinant reads :

$$\delta_a = -(a_1 a_3 + a_2 a_3 + a_1 a_2) < 0$$

Now we may also get the evolution of α_2 and α_3, so that :

$$\frac{\partial (\alpha_2, \alpha_3)^T}{\partial t} = \mathcal{U}_\mathbf{b} \mathbf{Y_p}$$

where the 2×2 matrix $\mathcal{U}_\mathbf{b}$ is such that :

$$(\mathcal{U}_\mathbf{b})_{11} = d_{12}; \quad (\mathcal{U}_\mathbf{b})_{12} = d_{23}; \quad (\mathcal{U}_\mathbf{b})_{21} = d_{13}; \quad (\mathcal{U}_\mathbf{b})_{22} = -d_{13} - d_{23}$$

$\mathcal{U}_\mathbf{b}$ determinant is :

$$\delta_b = -(d_{12} d_{13} + d_{12} d_{23} + d_{13} d_{23}) < 0$$

Hence we get :

$$\frac{\partial \mathbf{Y_p}}{\partial t} = -\mathcal{U}_\mathbf{a} \mathcal{U}_\mathbf{b} \mathbf{Y_p} = -\mathcal{U} \mathbf{Y_p} \tag{1.32}$$

If μ_1, μ_2 denote the two eigenvalues of $\mathcal{U}$, straightforward calculations give :

$$\begin{cases} \mu_1 \mu_2 = det(\mathcal{U}) = \delta_a \delta_b > 0 \ ; \\ \\ \mu_1 + \mu_2 = trace(\mathcal{U}) = d_{12}(a_1 + a_2) + d_{13}(a_1 + a_3) + d_{23}(a_2 + a_3) > 0 \ . \end{cases} \tag{1.33}$$

If we note $\Delta_\mathcal{U} = (trace(\mathcal{U}))^2 - 4 det(\mathcal{U})$, we end up with :

$$\mu_{1,2} = \left(trace(\mathcal{U}) \pm (\Delta_\mathcal{U})^{1/2} \right) / 2$$

We may conclude now that, unlike in the two-phase flow framework, the decay in the pressure relaxation process is not necessarily uniform, since the sign of $\Delta_\mathcal{U}$ is unknown in the general case. This means in practice that some oscillations might arise in some regions. The algorithm used in the next section will take advantage of the present analysis.

Though not detailed here, the velocity relaxation process is quite similar to the pressure relaxation process, but it is indeed more straightforward. If :

$$\mathbf{Y_u} = (\Delta U_{21}, \Delta U_{23})^T \tag{1.34}$$

denotes the two independent relative velocities, setting :

$$\Delta U_{21} = U_2 - U_1 \quad ; \quad \Delta U_{23} = U_2 - U_3$$

then the following holds :

$$\frac{\partial \mathbf{Y_u}}{\partial t} = -\mathcal{V}\mathbf{Y_u} \tag{1.35}$$

where the 2×2 matrix $\mathcal{V}$ is given by :

$$\left\{ \begin{array}{l} (\mathcal{V})_{11} = E_{12} + E_{21} + E_{13} \ ; \quad (\mathcal{V})_{12} = E_{23} - E_{13} \ ; \\ \quad (\mathcal{V})_{21} = E_{21} - E_{31} \ ; \quad (\mathcal{V})_{22} = E_{23} + E_{31} + E_{32} \ . \end{array} \right. \tag{1.36}$$

where :

$$\left\{ \begin{array}{l} m_1 E_{12} = m_2 E_{21} = e_{12} \ ; \\ m_1 E_{13} = m_3 E_{31} = e_{13} \ ; \\ m_2 E_{23} = m_3 E_{32} = e_{23} \ . \end{array} \right. \tag{1.37}$$

The trace and the determinant of matrix $\mathcal{V}$ respectively read :

$$trace(\mathcal{V}) = e_{12}(\frac{1}{m_1} + \frac{1}{m_2}) + e_{13}(\frac{1}{m_1} + \frac{1}{m_3}) + e_{23}(\frac{1}{m_2} + \frac{1}{m_3}) > 0$$

and :

$$det(\mathcal{V}) = (e_{12}e_{13} + e_{12}e_{23} + e_{13}e_{23})(\frac{1}{m_1 m_2} + \frac{1}{m_1 m_3} + \frac{1}{m_2 m_3}) > 0$$

Hence we have the same kind of behaviour : the velocity relaxation process may be monotone if : $\Delta_{\mathcal{V}} = (trace(\mathcal{V}))^2 - 4det(\mathcal{V})$ is positive, whereas it is not when $\Delta_{\mathcal{V}}$ is negative.

The numerical method that will be used for computational applications is presented and discussed below. It is actually the straightforward counterpart of the one used in [21, 10] for two-phase flow models.

1.3 Numerical method

Owing to the former results, the temptation is great to introduce a fractional step method in order to compute approximate solutions of (1.3). Actually this one will guarantee positive values of discrete statistical fractions and partial masses, given a classical constraint on the time step. Moreover, by construction, it will be in agreement with the inner pressure-velocity relaxation processes. We will explain at the end of the section how to account for the additional interfacial area A.

We consider a classical Finite Volume formulation. The computational domain is meshed using unstructured cells Ω_i, the surface of which is noted ω_i ; S_{ij} stands for the length of the ij interface. At each interface separating cells Ω_i and Ω_j, we define the unit outward normal vector n_{ij} pointing from cell Ω_i towards Ω_j. We define Δt_n the time step at time such that : $t_{n+1} = t_n + \Delta t_n$. More over, $V(i)$ will refer to the neighbouring cells of Ω_i.

1.3.1 Fractional step method

The time scheme is the following :

— **Step 1 : Evolution step :**
For a given initial condition $\mathbf{W}_i^n$, compute an approximate solution of $\mathbf{W}$ at time t_{n+1}^-, namely $\mathbf{W}^{n+1,-}$, by solving :

$$\begin{cases} \frac{\partial \alpha_k}{\partial t} + \mathcal{V}_\mathbf{i}(\mathbf{W}) \nabla \alpha_k = 0 \ ; \\ \\ \frac{\partial m_k}{\partial t} + \nabla . \left(m_k \mathbf{U_k} \right) = 0 \ ; \\ \\ \frac{\partial m_k \mathbf{U_k}}{\partial t} + \nabla . \left(m_k \mathbf{U_k} \times \mathbf{U_k} + \alpha_k P_k \mathbf{Id} \right) + \Sigma_{l=1, l \neq k}^3 \Pi_{kl}(\mathbf{W}) \nabla \alpha_l = 0 \ . \end{cases} \tag{1.38}$$

— **Step 2 : Relaxation step :**
Starting with $\mathbf{W}^{n+1,-}$, compute an approximation $\mathbf{W}^{n+1}$ of the solution of :

$$\begin{cases} \frac{\partial \alpha_k}{\partial t} = \phi_k(\mathbf{W}) \ ; \\ \\ \frac{\partial m_k}{\partial t} = 0 \ ; \\ \\ \frac{\partial m_k \mathbf{U_k}}{\partial t} = m_k \mathbf{S_k}(\mathbf{W}) \ . \end{cases} \tag{1.39}$$

1.3.2 Computing the relaxation step

1.3.2.1 Pressure relaxation

Within each cell Ω_i, starting with $\mathbf{W_i^*}$, we compute the following sequence :

— Initialize : $\mathbf{y_p^n} = \mathbf{Y_p}(\mathbf{W_i^*})$, where $\mathbf{Y_p}$ is defined in (1.31) ;

— Compute the exact solution $\mathbf{y_p^{n+1}}$ of the linear ODE :

$$\frac{\partial \mathbf{y_p}}{\partial t} = -\mathcal{U}(\mathbf{W_i^*}) \mathbf{y_p} \tag{1.40}$$

at time $t = \Delta t_n$, using the initial condition $\mathbf{y_p^n}$, where the 2×2 matrix $\mathcal{U}$ is defined in (1.32) ;

— Find the pressure $x = (P_1)_i^{n+1}$ solution of the scalar equation $g_p(x) = 1$:

$$g_p(x) = \frac{(m_1)_i^*}{\rho_1(x)} + \frac{(m_2)_i^*}{\rho_2(x + (\Delta P)_{21}^{n+1})} + \frac{(m_3)_i^*}{\rho_3(x + (\Delta P)_{21}^{n+1} - (\Delta P)_{23}^{n+1})} \tag{1.41}$$

— Update $(P_2)_i^{n+1}$ and $(P_3)_i^{n+1}$, setting :

$$(P_2)_i^{n+1} = x + (\Delta P)_{21}^{n+1} \ ; \quad (P_3)_i^{n+1} = x + (\Delta P)_{21}^{n+1} - (\Delta P)_{23}^{n+1}$$

— Update $(\alpha_k)_i^{n+1}$ for : $k \in 1, 2, 3$, setting :

$$(\alpha_k)_i^{n+1} = \frac{(m_k)_i^*}{\rho_k((P_k)_i^{n+1})}$$

We now have the following result :

Proposition 3 :

— We assume that EOS comply with the constraints (1.2). Then there exists a unique solution x of (1.41) in the admissible range.

— Statistical fractions $(\alpha_k)_i^{n+1}$ lie in $[0,1]$, and partial masses remain positive.

Proof : we define $x_{min} = max(0, -(\Delta P)_{21}^{n+1}, (\Delta P)_{23}^{n+1} - (\Delta P)_{21}^{n+1})$. Since $c_k^2 > 0$, the function $g_p(x)$ is decreasing for $x \in [x_{min}, +\infty[$. Moreover :

$$\lim_{x \to +\infty} g_p(x) = 0, \quad and: \quad \lim_{x \to x_{min}} g_p(x) = +\infty.$$

Thus there exists a unique solution to $g_p(x) = 1$. Evenmore, this equation perfectly matches the condition :

$$(\alpha_1)_i^{n+1} + (\alpha_2)_i^{n+1} + (\alpha_3)_i^{n+1} = 1$$

since $(m_k)_i^* = (m_k)_i^{n+1}$. This completes the proof.

□

By the way, we note that for long time behaviours, the solution x to $g_p(x) = 1$ will exactly coincide with the equilibrium pressure. We may now examine the velocity relaxation step.

We also note that another implicit scheme, which is based on the initial algorithm [21], might also be used (see **appendix A**).

1.3.2.2 Velocity relaxation

Again, in each cell Ω_i, starting with $\mathbf{W_i^*}$, we compute the sequence :

— Initialize : $\mathbf{y_u^n} = \mathbf{Y_u}(\mathbf{W_i^*})$, where $\mathbf{Y_u}$ is defined in (1.34) ;

— Compute the exact solution $\mathbf{y_u^{n+1}}$ of the linear ODE :

$$\frac{\partial \mathbf{y_u}}{\partial t} = -\mathcal{V}(\mathbf{W_i^*})\mathbf{y_u} \tag{1.42}$$

at time $t = \Delta t_n$, using the initial condition $\mathbf{y_u^n}$, where the 2×2 matrix $\mathcal{V}$ is defined in (1.35) ;

— Compute : $(\mathbf{U_1})_i^{n+1}$ as follows :

$$(\mathbf{U_1})_i^{n+1} = (\mathbf{U}_{eq})_i^{n+1} - \frac{((m_2)_i^* + (m_3)_i^*)(\Delta \mathbf{U})_{21}^{n+1} - (m_3)_i^*(\Delta \mathbf{U})_{23}^{n+1}}{(m_1)_i^* + (m_2)_i^* + (m_3)_i^*} \tag{1.43}$$

where $(\mathbf{U}_{eq})_i^{n+1}$ denotes the equilibrium velocity :

$$(\mathbf{U}_{eq})_i^{n+1} = \frac{(m_1)_i^*(\mathbf{U}_1)_i^* + (m_2)_i^*(\mathbf{U}_2)_i^* + (m_3)_i^*(\mathbf{U}_3)_i^*}{(m_1)_i^* + (m_2)_i^* + (m_3)_i^*}$$

— Update : $(\mathbf{U}_2)_i^{n+1}$ and $(\mathbf{U}_3)_i^{n+1}$, while setting :

$$(\mathbf{U}_2)_i^{n+1} = (\mathbf{U}_1)_i^{n+1} + (\Delta \mathbf{U})_{21}^{n+1} \; ; \quad (\mathbf{U}_3)_i^{n+1} = (\mathbf{U}_1)_i^{n+1} + (\Delta \mathbf{U})_{21}^{n+1} - (\Delta \mathbf{U})_{23}^{n+1}$$

Again, we note that for large time steps, the three updated velocities will tend towards $(\mathbf{U}_{eq})_i^{n+1}$. By construction, this scheme preserves the conservation of the total momentum.

1.3.3 Computing the evolution step

The scheme that is used in the sequel in order to compute the evolution step is nothing but the Rusanov scheme [34]. Thus, at each interface ij separating cells Ω_i and Ω_j, we define numerical normal fluxes :

$$\left\{ \begin{array}{l} \mathcal{F}_n^{\alpha_k}(\mathbf{W}, \mathbf{n_{ij}}) = 0 \ ; \\ \mathcal{F}_n^{m_k}(\mathbf{W}, \mathbf{n_{ij}}) = m_k \mathbf{U_k}.\mathbf{n_{ij}} \ ; \\ \mathcal{F}_{\mathbf{n}}^{\mathbf{Q_k}}(\mathbf{W}, \mathbf{n_{ij}}) = m_k \mathbf{U_k}.\mathbf{n_{ij}} \mathbf{U_k} + \alpha_k P_k \mathbf{n_{ij}} \ ; \end{array} \right. \tag{1.44}$$

and :

$$\left\{ \begin{array}{l} 2\mathcal{G}_n^{\alpha_k}(\mathbf{W_i}, \mathbf{W_j}, \mathbf{n_{ij}}) = -r_{ij}((\alpha_k)_j - (\alpha_k)_i) \ ; \\ \\ 2\mathcal{G}_n^{m_k}(\mathbf{W_i}, \mathbf{W_j}, \mathbf{n_{ij}}) = \mathcal{F}_n^{m_k}(\mathbf{W_i}, \mathbf{n_{ij}}) + \mathcal{F}_n^{m_k}(\mathbf{W_j}, \mathbf{n_{ij}}) - r_{ij}((m_k)_j - (m_k)_i) \ ; \\ \\ 2\mathcal{G}_{\mathbf{n}}^{\mathbf{Q_k}}(\mathbf{W_i}, \mathbf{W_j}, \mathbf{n_{ij}}) = \mathcal{F}_{\mathbf{n}}^{\mathbf{Q_k}}(\mathbf{W_i}, \mathbf{n_{ij}}) + \mathcal{F}_{\mathbf{n}}^{\mathbf{Q_k}}(\mathbf{W_j}, \mathbf{n_{ij}}) - r_{ij}((m_k \mathbf{U_k})_j - (m_k \mathbf{U_k})_i) \end{array} \right. \tag{1.45}$$

where the quantity r_{ij} is defined by :

$$r_{ij} = max_{k=1-3} \left((|\mathbf{U_k}.\mathbf{n_{ij}}| + c_k)_i, (|\mathbf{U_k}.\mathbf{n_{ij}}| + c_k)_j \right)$$

Whatever ϕ is, we also use the standard notation :

$$\overline{\phi}_{ij} = (\phi_i + \phi_j)/2$$

Hence the solution is updated through the evolution step computing :

$$\left\{ \begin{array}{l} \omega_i((\alpha_k)_i^{n+1,-} - (\alpha_k)_i^n) + \Delta t^n \left(\Sigma_{j \in V(i)} \mathcal{G}_n^{\alpha_k}(\mathbf{W_i^n}, \mathbf{W_j^n}, \mathbf{n_{ij}}) S_{ij} \right) \\ \qquad + \Delta t^n (\mathbf{U_1})_i^n . \left(\Sigma_{j \in V(i)} (\overline{\alpha}_k)_{ij}^n \mathbf{n_{ij}} S_{ij} \right) = 0 \ ; \\ \\ \omega_i((m_k)_i^{n+1,-} - (m_k)_i^n) + \Delta t^n \left(\Sigma_{j \in V(i)} \mathcal{G}_n^{m_k}(\mathbf{W_i^n}, \mathbf{W_j^n}, \mathbf{n_{ij}}) S_{ij} \right) = 0 \ ; \\ \\ \omega_i((m_k \mathbf{U_k})_i^{n+1,-} - (m_k \mathbf{U_k})_i^n) + \Delta t^n \left(\Sigma_{j \in V(i)} \mathcal{G}_{\mathbf{n}}^{\mathbf{Q_k}}(\mathbf{W_i^n}, \mathbf{W_j^n}, \mathbf{n_{ij}}) S_{ij} \right) \\ \qquad + \Delta t^n \Sigma_{l=1, l \neq k}^3 \Pi_{kl}(\mathbf{W})_i^n \left(\Sigma_{j \in V(i)} (\overline{\alpha}_l)_{ij}^n \mathbf{n_{ij}} S_{ij} \right) = 0 \end{array} \right. \tag{1.46}$$

and we have the expected result :

Proposition 4 :
The evolution step guarantees positive values of partial masses and statistical fractions if the time step complies with the constraint :

$$\Delta t^n \left(\Sigma_{j \in V(i)} r_{ij} S_{ij} \right) \leq 2 \omega_i \tag{1.47}$$

Proof : it is classical and omitted. Actually, the condition (1.47) is necessary and sufficient in order to rewrite $(\alpha_k)_i^{n+1,-}$ (respectively $(m_k)_i^{n+1,-}$) as a convex combination of the $(\alpha_k)_j^n$ (respectively $(m_k)_j^n$) for $j \in V(i)$.

1.3.4 Computing the interfacial area

We take the interfacial area into account in a very simple manner. Owing to the particular form of its governing equation :

$$\frac{\partial A}{\partial t} + \nabla.\left(A\mathbf{U_1}\right) = g(A, \mathbf{W})$$

we compute convective fluxes in the evolution step :

$$\frac{\partial A}{\partial t} + \nabla.\left(A\mathbf{U_1}\right) = 0$$

and then update A by computing approximate solutions of the ODE :

$$\frac{\partial A}{\partial t} = g(A, \mathbf{W})$$

Before going further on, we detail the form of $g(A, \mathbf{W})$, which reads :

$$g(A, \mathbf{W}) = C_0 \frac{A^2}{6\alpha_1} \left(\frac{\rho_p}{\rho_1}\right)^{1/2} ||U_1 - U_p|| f(We)$$

where p (resp. 1) stands for the index of the liquid water (resp. liquid metal droplets), $C_0 = 0.245$, $We = \rho_1 ||U_1 - U_p||^2 d_1/\sigma$ denotes the Weber number, and the function $f(We)$ is null unless :

$$f(We) = 1 \quad \textit{if :} \quad We > We_{crit}$$

d_1 and σ respectively denote the diameter of liquid metal droplets and the surface tension. In practice, the critical Weber number We_{crit} needs to be given ; the value $We_{crit} = 12$ will be used in the computations below.

Thus, if we define $\mathcal{F}_n^A(\mathbf{W}, \mathbf{n_{ij}}) = A\mathbf{U_1}.\mathbf{n_{ij}}$ and :

$$2\mathcal{G}_n^A(\mathbf{W_i}, \mathbf{W_j}, \mathbf{n_{ij}}) = \mathcal{F}_n^A(\mathbf{W_i}, \mathbf{n_{ij}}) + \mathcal{F}_n^A(\mathbf{W_j}, \mathbf{n_{ij}}) - r_{ij}(A_j - A_i)$$

the approximate solution is advanced in time as follows :

$$\omega_i(A_i^{n+1,-} - A_i^n) + \Delta t^n \left(\Sigma_{j\in V(i)} \mathcal{G}_n^A(\mathbf{W_i^n}, \mathbf{W_j^n}, \mathbf{n_{ij}}) S_{ij}\right) = 0.$$

Then it is updated in order to account for the dislocation term $g(A, \mathbf{W})$. Starting with cell values $A_i^{n+1,-}$, we compute :

$$A_i^{n+1} = A_i^{n+1,-} exp(\Delta t h(A_i^{n+1,-}, \mathbf{W}^{n+1}))$$

where : $h(A, \mathbf{W}) = C_0 \frac{A}{6\alpha_1} \left(\frac{\rho_p}{\rho_1}\right)^{1/2} ||U_1 - U_p|| f(We)$.

Starting with positive values for the A_j^n in all cells, then positive values of A_i^{n+1} are guaranteed, using the above algorithm, as soon as the time step complies with (1.47).

1.4 Numerical Results

In the first subsection, we will examine three different Riemann problems in order to verify the numerical schemes. A first test case will correspond to the computation of a pure $0-1-2$ coupling wave (contact discontinuity), thus using results of proposition 2 ; afterwards a second Riemann problem involving a shock wave in phase 1 and the $0-1-2$ coupling wave will be investigated. The last one will be a classical shock tube problem. We restrict here to the classical three-phase flow model (1.3).

The second subsection will focus on the experimental set-up proposed in [7]. As mentioned briefly in the introduction, a shock tube apparatus will generate a shock wave propagating towards the right hand side, which will hit a cloud of spherical particles and interact with it. Two situations will be examined : in the first one, particles in the bed will be assumed to be rigid, whereas in the second one these particles will be liquid droplets that will be sheared by the hinting gas shock wave, and break up ; this will strongly modify the structure of the flow, and the computation will take advantage of the fact that the interfacial area is estimated by the modified three-phase flow model introduced in section 2.4. Hence we compute here approximate solutions of system (1.16).

We use uniform meshes, and set for all cases : $CFL = 1/2$, which in turn enables to define the time step Δt_n.

1.4.1 Verification test cases based on Riemann problems

We consider simple EOS such that :

$$P_k(\rho_k) = P_k^0(\rho_k)^{\gamma_k}$$

where we set for all cases : $P_k^0 = 1.10^5$. Several values of polytropic exponents γ_k will be used. As usual, the initial discontinuity separating states W_L and W_R is located at $x = 1/2$, and the one-dimensional computational domain is $[0, 1]$.

We neglect here relaxation terms, thus setting : $d_{kl}(W) = 0$ and $e_{kl}(W) = 0$, whatever k, l are.

1.4.1.1 Pure coupling wave

For the first two test cases, EOS are chosen such that :

$$\gamma_1 = 3/2 \ , \quad \gamma_2 = 2 \ , \quad \gamma_3 = 5/2.$$

The left state is such that $(U_k)_L = k$, $(V_k)_L = 0$ and :

$$(\alpha_2)_L = 4/10 \quad ; \quad (\alpha_3)_L = 1/2;$$

$$(\rho_1)_L = 1/3 \quad ; \quad (\rho_2)_L = 1/4 \quad ; \quad (\rho_3)_L = 1.$$

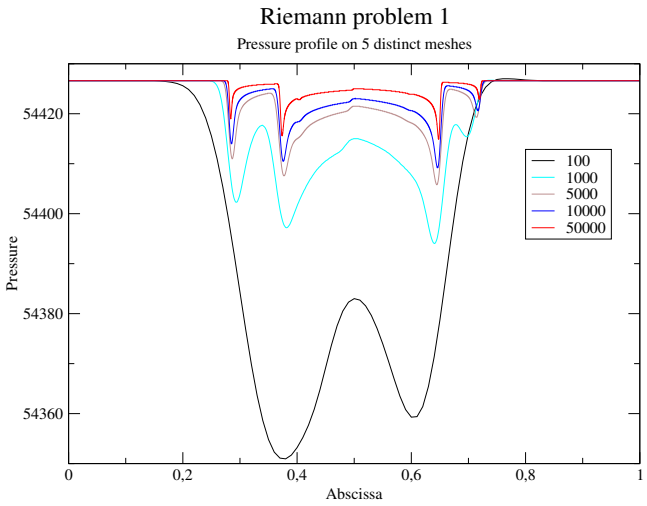

FIGURE 1.1 – Riemann problem 1. Pressure profiles for $I^6_{0,1}(W)$ on five distinct meshes. Coarser mesh : 100 cells, finer mesh : 50000 cells.

The right state labeled W_r is defined setting $(V_k)_r = 0$, but also :

$$(\alpha_2)_r = 2/10 \quad ; \quad (\alpha_3)_r = 3/10;$$

and computing the six unknowns $(\rho_k)_r, (U_k)_r$ in such a way that :

$$I^m_{0,1}(W_L) = I^m_{0,1}(W_r)$$

for $m = 1 \to 6$ (see section 2.3 for details).

Thus we obtain :

$$(\rho_1)_r = 0.598903, \quad ; \quad (\rho_2)_r = 0.249992, \quad ; \quad (\rho_3)_r = 0.999986,$$

and :

$$(U_1)_r = 1.0, \quad ; \quad (U_2)_r = 3.000060, \quad ; \quad (U_3)_r = 4.333381.$$

We may thus compute the L^1 norm for the six independent variables $I^m_{0,1}(W)$. The coarser and finer regular meshes contain 100 and 50000 cells respectively. We retrieve as expected the 1/2 rate of convergence for all variables (see Figure 1.2). Approximate values of the invariant $I^6_{0,1}(W)$ can be observed in Figure 1.1, while considering various meshes.

1.4.1.2 Phase 1 shock wave coupled with the coupling wave

This second Riemann problem relies on similar initial conditions W_L on the left hand side. However, the right state W_R is now taken equal to W_r, except for the two components $(\rho_1)_R$ and $(U_1)_R$ which read now :

$$(\rho_1)_R = 0.19963439 \ , \qquad (u_1)_R = -352,54023$$

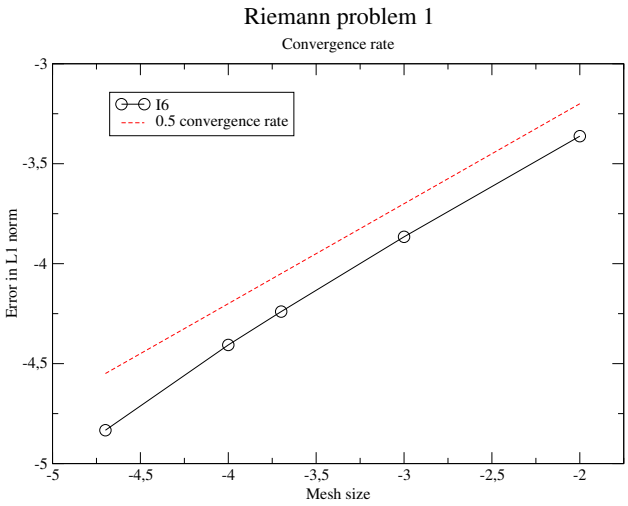

FIGURE 1.2 – Riemann problem 1. L^1 norm of the error for $I^6_{0,1}(W)$ wrt the mesh size h.

The exact solution is composed of a right-going coupling contact wave travelling at speed $(u_1)_L$ behind a 1-shock wave travelling at speed σ_1. More exactly we have :

$$\begin{cases} \mathbf{w}(x,t) = \mathbf{w}_L \qquad if: \qquad \frac{x}{t} < (u_1)_L \ ; \\ \mathbf{w}(x,t) = \mathbf{w}_r \qquad if: \qquad (u_1)_L < \frac{x}{t} < (\sigma_1) \ ; \\ \mathbf{w}(x,t) = \mathbf{w}_R \qquad if: \qquad \frac{x}{t} > (\sigma_1) \ ; \end{cases} \tag{1.48}$$

Using the same kind of meshes as before, we plot the L^1 norm of the error on figures 1.3, 1.4. Again we retrieve a convergence behaviour as $h^{1/2}$ for fine enough meshes. The finer mesh here involves two hundred thousand cells. This hudge refinement is mandatory, owing to the competition between the asymptotic $h^{1/2}$ (respectively h^1) rates of convergence in the contact (respectively shock) waves.

1.4.1.3 Pure shock tube problem

Herein, EOS are such that :

$$\gamma_1 = 7/5 \ , \quad \gamma_2 = 1.005 \ , \quad \gamma_3 = 1.001$$

We use here a fine mesh including 80000 regular cells. The initial data are such that velocities are null everywhere at the beginning of the computation, thus, for $k = 1, 2, 3$:

$$(U_k)_L = (U_k)_R = (V_k)_L = (V_k)_R = 0;$$

In addition we choose left and right states $(\alpha_k)_{L,R}$ and $(\rho_k)_{L,R}$ such that :

$$(\alpha_2)_L = 0.4 \quad ; \quad (\alpha_3)_L = 0.5 \quad ; \quad (\alpha_2)_R = 0.2 \quad ; \quad (\alpha_3)_R = 0.3;$$

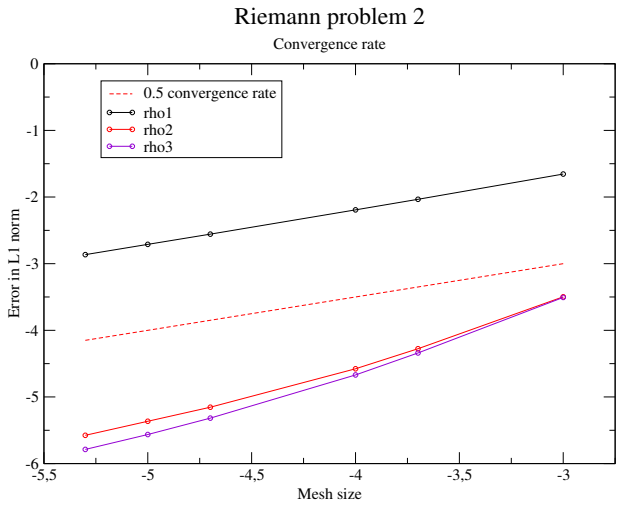

FIGURE 1.3 – Riemann problem 2. L^1 norm of the error (densities) wrt the mesh size h.

$$(\rho_k)_L = 1. \quad ; \quad (\rho_k)_R = 1/8.$$

for $k = 1to3$. Phasic pressures P_k have been plotted on Figure 1.5. Approximations of the sixth Riemann invariant : $\mathcal{P} = I^6_{0-1}(W)$ of the the $0-1$ coupling wave, and of the mean pressure :

$$P_{wall} = \Sigma_{k=1\to 3}\alpha_k P_k$$

are given in Figure 1.6, while velocity profiles are drawn in Figure 1.7. We may check the numerical invariance of $\mathcal{P} = I^6_{0-1}(W)$ through the $0-1$ coupling wave.

1.4.2 Shock tube apparatus : interaction of a gas shock wave with a lid of droplets

The main objectives of this section are two-fold. We wish first to validate the numerical method built in order to provide approximate solutions of the barotropic three-phase flow model, with one vanishing phase (phase labeled 3 here). Moreover, we aim at investigating the two solutions associated with :

1. the standard three-phase flow model (1.3),
2. the modified system (1.17) that accounts for the interfacial area A.

The first one will enable us to compute approximate solutions of an incoming gas shock wave hitting a cloud of spherical **rigid** particles, whereas the second one will generate similar approximations when a lid of **deformable** liquid droplets is considered instead.

For that purpose, we consider here the experimental setup discussed in [6, 7]. This one is indeed interesting and well documented. It is well suited for our basic goal : mechanical effects alone are at stake, which corresponds to our situation where the sole barotropic model is considered, rather than its full form [19] including partial differential equations for the total energies. Hence we may expect to retrieve the main flow patterns pointed out in [6, 7] ;

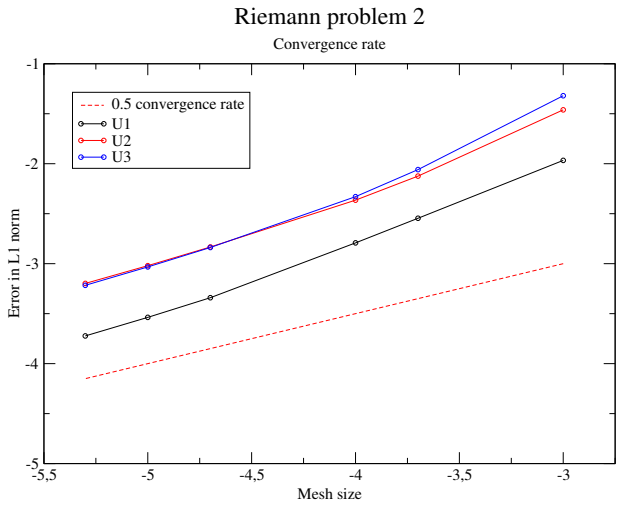

FIGURE 1.4 – Riemann problem 2. L^1 norm of the error (velocities) wrt the mesh size h.

more precisely, pressure transducers reveal that, after the first instants of interaction of the incoming shock wave with the cloud of liquid droplets, a pressure decrease occurs until some new pressure equilibrium is retrieved ; it thus clearly reduces the intensity of the shock wave.

A sketch of the shock tube apparatus is given in figure 1.8. Four pressure transducers are located at stations S_p (for $p = 1-4$). The length of the computational domain is $L = 3.75m$, and the tube is closed at both ends. The cloud of (rigid or liquid) droplets lies between $x_1 = 2.97m$ and $x_2 = 3.37m$ (hence the bed width is $400.mm$). The gas phase (with label 2) and the liquid-water droplet phase (with label 1) are at rest at the beginning of the computation, and all pressure fields are assumed to be in equilibrium with the gas phase everywhere, thus, for $k = 1, 3$:

$$P_k(x, t = 0) = P_2(x, t = 0).$$

The position of the initial pressure disequilibrium is $x_0 = 0.75$, and the mean gas pressure is given by ([6]) :

$$P_2(x < x_0, t = 0) = P_L = 7. \times 10^5, \qquad P_2(x > x_0, t = 0) = P_R = 1. \times 10^5,$$

on each side of the initial membrane.

The statistical fraction for the evanescent phase 3 is set to $\alpha_3 = 10^{-10}$ everywhere before the experiment starts.

Liquid water droplets in the cloud are spherical, identical and their initial diameter is $d(x, t = 0) = 0.5mm$.

Eventually, the amount of droplets (or rigid droplets) within the lid is equal to :

$$\alpha_1(x, t = 0) = 0.0104 \quad for: \quad x \in [x_1, x_2], \qquad \alpha_1(x, t = 0) = 10^{-10}. \quad elsewhere.$$

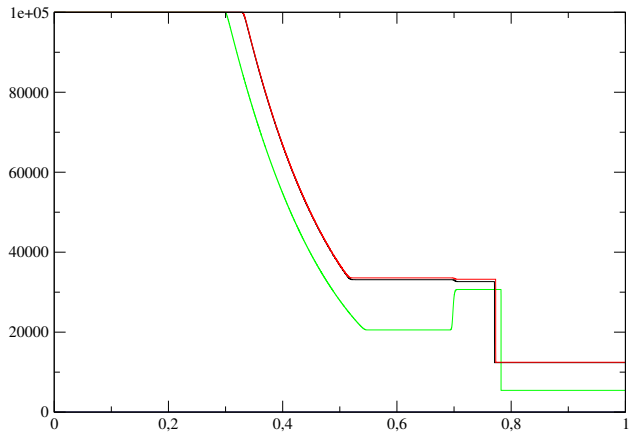

FIGURE 1.5 – Riemann problem 3. Pressure profiles on a fine mesh : P_1 (green), P_2 (black), P_3 (red).

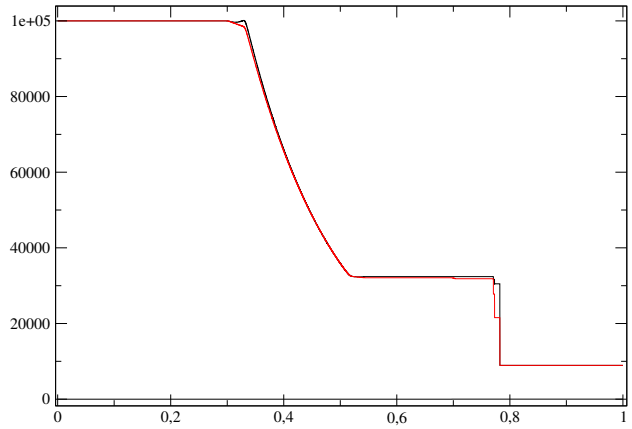

FIGURE 1.6 – Riemann problem 3. Pressure profiles on a fine mesh : $\mathcal{P} = I^6_{0,1}(W)$ (black), P_{wall} (red).

The EOS for the liquid water droplet phase 1 is chosen as follows :

$$P_1(\rho_1) = c^2_{1,0}\rho_1 + P_{ref}$$

where : $c_{1,0} = 1500$, and P_{ref} is such that : $P_1(10^3) = 10^5$, whereas for the gas phase we choose :

$$P_2(\rho_2) = 10^5 \times (\rho_2/\rho_{2,ref})^{7/5}, \qquad with : \rho_{2,ref} = 1.27.$$

The same EOS is chosen for the vanishing phase 3.

The drag force between gas and liquid water droplets (or undeformable droplets) is obtained using the following closure law :

$$e_{12} = 0.125 \times A\rho_2 C_{12}|u_1 - u_2|$$

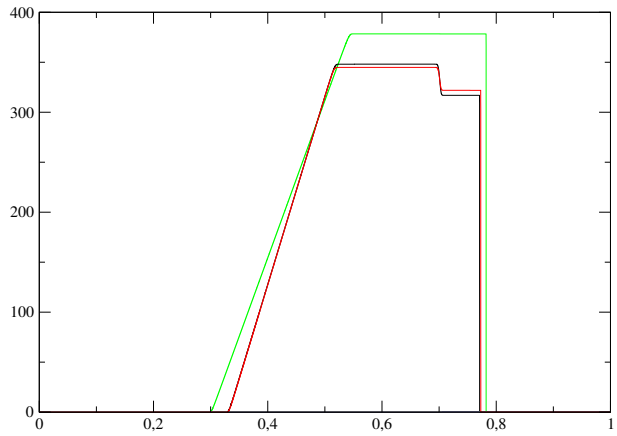

FIGURE 1.7 – Riemann problem 3. Velocity profiles on a fine mesh : U_1 (green), U_2 (black), U_3 (red).

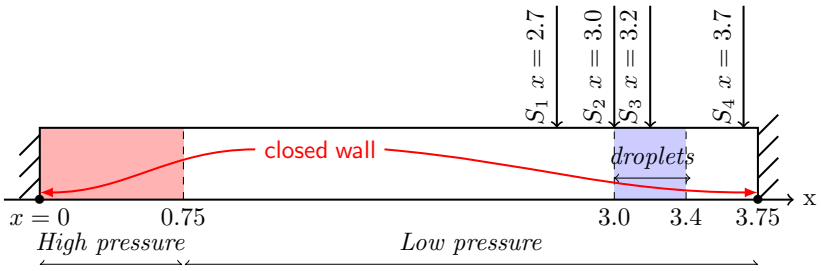

FIGURE 1.8 – Sketch of the experimental shock tube apparatus.

where : $C_{12} = 0.42$. Eventually we set in these computations : $d_{12} = 10^{10}$. Unless otherwise specified, computations have been performed using regular meshes including 10^4, $5. \times 10^4$ and 10^5 cells, and the time step in chosen in order to comply with the $CFL = 1/2$ constraint.

1.5 Discussion

1.5.1 Single phase reference experiment

As a reference case, we may first compute the **single phase** case of a pure gas shock tube apparatus, by removing the initial cloud of particles (hence setting the above value $\alpha_1 = 0.014$ to $\alpha_1 = 10^{-10}$). The total pressure is noted :

$$P = \Sigma_{k=1}^{3}(\alpha_k P_k).$$

The pressure records at station 1 and station 4 during the first ten milliseconds are shown in figure 1.9 and 1.10. For this single phase case, we may define the mean pressure P^* just behind the right going shock wave, and also the mean pressure P^{**} after the reflection of this

shock wave on the right wall boundary. We may compute exact values P^*, P^{**} , assuming that the gas phase is governed by :

1. the **barotropic** Euler equations, using notation $P^{*,Eulerbaro}, P^{**,Eulerbaro}$,
2. the **full** Euler equations, using notation $P^{*,Euler}, P^{**,Euler}$,

and we may compare these values with the experimental values $P^{*,exp}, P^{**,exp}$. The latter two values can be found in [6, 7], which are approximately :

$$P^{*,exp} = 2.4 \times 10^5, \qquad P^{**,exp} = 5.0 \times 10^5;$$

whereas exact values obtained with the (Euler and barotropic Euler) models are respectively :

$$P^{*,Euler} = 2.46 \times 10^5, \qquad P^{**,Euler} = 5.42 \times 10^5;$$

and :

$$P^{*,Eulerbaro} = 2.78 \times 10^5, \qquad P^{**,Eulerbaro} = 6.85 \times 10^5.$$

Hence, we note that the full Euler equations provide a fair appoximation of the experimental results, whereas the barotropic Euler equations over estimate the latter. Obviously, the former exact values of $P^{*,Eulerbaro}, P^{**,Eulerbaro}$ are retrieved by the three-phase barotropic code on sufficiently fine meshes (see figure 1.10), which was expected of course (and mandatory).

Looking at figure 1.10, one can also note at station 4 that when $t > t_1 = 7.7ms$, the second plateau value $P^{**,Eulerbaro}$ is followed by a regular decrease, due to the reflection of the initial left-going $1-$rarefaction wave that has reflected on the left wall boundary.

A straightforward consequence of the previous comparison in the single-phase framework is that we can hardly expect an accurate approximation of experimental results with the current barotropic three-phase flow model when turning to two-phase or three-phase flow experiments.

1.5.2 Two-phase experiment with rigid droplets

We turn now to the case of a lid of **rigid** droplets, setting $\alpha_1 = 0.0104$ in the range $[x_1, x_2]$ at the beginning of the computation.

Thus we compute approximate solutions of the three-phase flow model (1.3), getting rid of the interfacial area equation for A, and using the initial diameter $d(x,t) = d_0$ everywhere throughout the computation.

Hence, we focus now on figure 1.11. At station 1, the pressure first jumps up to the same value $P^{*,Eulerbaro} = 2.78 \times 10^5$, and it then remains steady until the reflection of the left-going rarefaction wave meets that position (around time $t = 5.91ms$), as it occured in the single phase experiment (see figure 1.9). The latter plateau value is thus followed by a decrease of the pressure due the interaction with the reflection of the left going rarefaction wave, and

then we note a second jump (around time $t = 6.4ms$), which is due to the reflection of the right-going gas shock wave that has hit the cloud of droplets, again followed by a smooth decrease of the pressure. The latter jump obviously cannot be observed on signals recorded at stations 2 and 3 since these are located on the right hand side of the bottom of the cloud.

If we turn to station 2 , we may observe the first jump of the pressure which is slightly lower than the value $P^{*,Eulerbaro} = 2.78 \times 10^5$. Once the gas has penetrated the cloud of droplets, the pressure smoothly increases (the lid of solid particles acts as a convergent nozzle) until $t = 6.4ms$. This is again followed by a decrease of the pressure, owing to the reflected rarefaction wave, and again by a sudden compression due to the reflection of the initial right going shock wave on the right wall boundary.

Similar comments hold for the pressure signal at station 3, with a small delay, as shown on figure 1.11.

1.5.3 Two-phase experiment with deformable liquid droplets

The last test corresponds to the interaction of the gas shock wave with a lid of **deformable** liquid droplets. Hence we compute now approximate solutions of the modified three-phase flow model (1.17), including the governing equation for the interfacial area A.

Figures 1.12 and 1.13 provide numerical approximations of the mean pressure $P = \Sigma_{k=1}^{3}(\alpha_k P_k)$ obtained with the code at stations 2 and 3 in that case; meanwhile figures 1.14 and 1.15 respectively show the behaviour of the interfacial area A and of the void fraction α_1 within the liquid phase.

At the beginning, we still note the same kind of flow pattern, and we retrieve a value of the mean pressure which is close to $P^{*,Eulerbaro}$. Nonetheless, and unlike in the previous case involving rigid droplets, it must emphasized that the mean pressure suddenly decreases just after the impact of the incoming gas shock wave with the lid of droplets. This behaviour is typical of what happens in a medium involving deformable droplets with a high breakup phenomenon (see [16]). This is actually well detailed in reference [7]. The present numerical simulation enables us to retrieve this specific behaviour, and this is indeed a very encouraging point. Afterwards, we note that the pressure P increases again until it reaches some maximum value close to 4.8×10^5 (respectively 3.1×10^5) at station 2 (respectively at station 3). The experimental counterparts arising from [6, 7] for the latter two values are respectively 3.2×10^5 and 3.25×10^5.

Thus, as expected within the light of our preliminary single phase flow computations, the barotropic model provides a rather good qualitative agreement with experiment, and it enables to retrieve the sudden experimental decrease of the pressure in the lid of droplets once the transmitted incoming shock wave has hit the cloud, as soon as the breakup of droplets is accounted for in the model. However, the whole obviously requires further investigation and improvements in order to achieve a better matching with experimental results. Eventually,

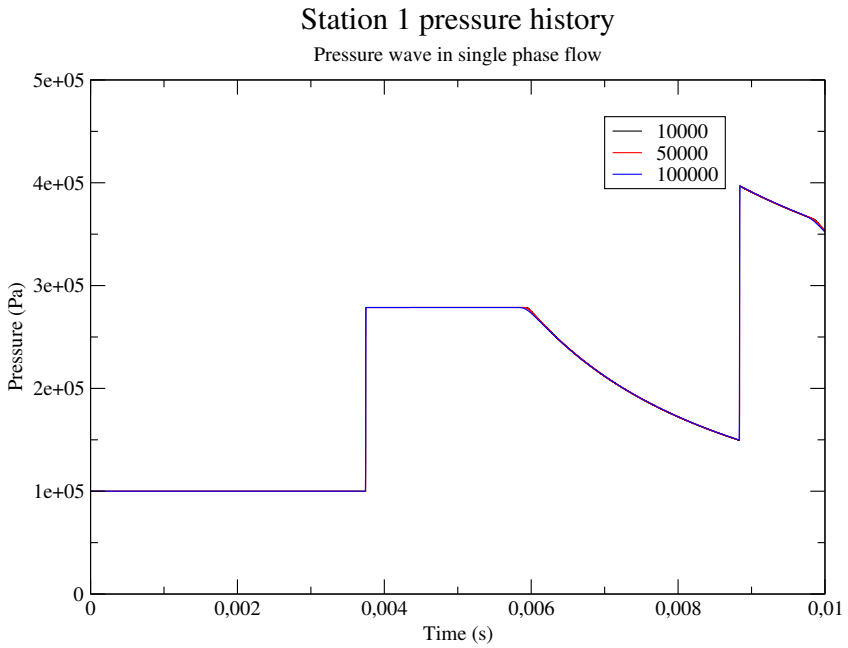

FIGURE 1.9 – Single phase shock tube apparatus. Pressure signal at station 1. Meshes : 10^4 cells (black), $5. \times 10^4$ cells (red) and 10^5 cells (blue).

figure 1.16 shows the influence of the drag coefficient on the computations, hence comparing results associated to $C_{12} = 0.42$ with those obtained with :

$$C_{12} = \frac{24}{Re}\left(1 + 0.15(Re)^{0.687}\right) + 0.42\left(1 + 42500(Re)^{-1.16}\right)^{-1}$$

1.6 Conclusion

We have discussed in this paper the main properties of a three-phase flow barotropic model, and we gave special focus on the pressure and velocity relaxation process involved in the source terms. The fractional step method enables to comply with the entropy inequality at the continuous level, and it provides satisfactory results on fine meshes, as expected. It would be worth investigating alternative schemes in the pressure relaxation step in order to get a fully discrete entropy inequality. The comparison with the results of the experimental set-up of [7] is indeed encouraging. Applications to different situations such as those encountered in solid-gas-liquid flows in pipelines also seem quite appealing.

However, this work must also be understood as a first step in the direction of steam explosion modeling. Though the list below is not exhaustive, we detail afterwards some items that are still missing in order to obtain a complete and accurate enough approximation of that kind of flow.

Actually the following points immediately arise :

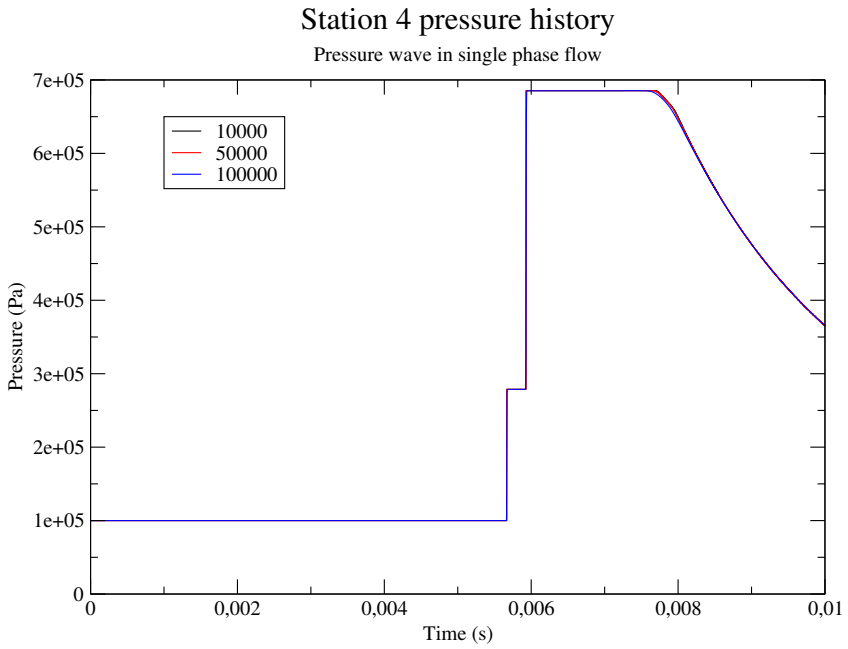

FIGURE 1.10 – Single phase shock tube apparatus. Pressure signal at station 4. Meshes : 10^4 cells (black), $5. \times 10^4$ cells (red)and 10^5 cells (blue)

— First of all, the present work suggests that reliable and accurate enough $2D$ or evenmore $3D$ simulations will urge the development of approximate Riemann solvers dedicated to three phase flow models. An extension of the relaxation solvers introduced in [1, 2, 10, 9] seems promising for that purpose (see [35]) ;

— As underlined before, the barotropic approach provides a rather fair qualitative agreement with experimental results, but one obvious way to improve quantitative results requires the introduction of energy balance equations within each phase. Actually, the non-barotropic models provided in [19, 28] are two possible candidates in order to take heat transfer into account, while being ensured that the barotropic part lies in the same hierarchy of models. One should nonetheless be aware that pressure relaxation processes are even more complex than those involved in the current barotropic model ;

— A comparison of results obtained with the present model with extensions of the homogeneous models [12, 17, 18] (involving a sole velocity field) would be worth being achieved ;

— Eventually, the modification of the classical framework, which is due to the introduction of interfacial area equation, might certainly be improved. Possible ways in that direction are implicitly suggested in papers [26, 11, 23, 36], among others.

1.7 acknowledgement

The first author receives financial support by ANRT and EDF through an EDF/CIFRE grant number 2016/0611. Computational facilities were provided by EDF. Both authors

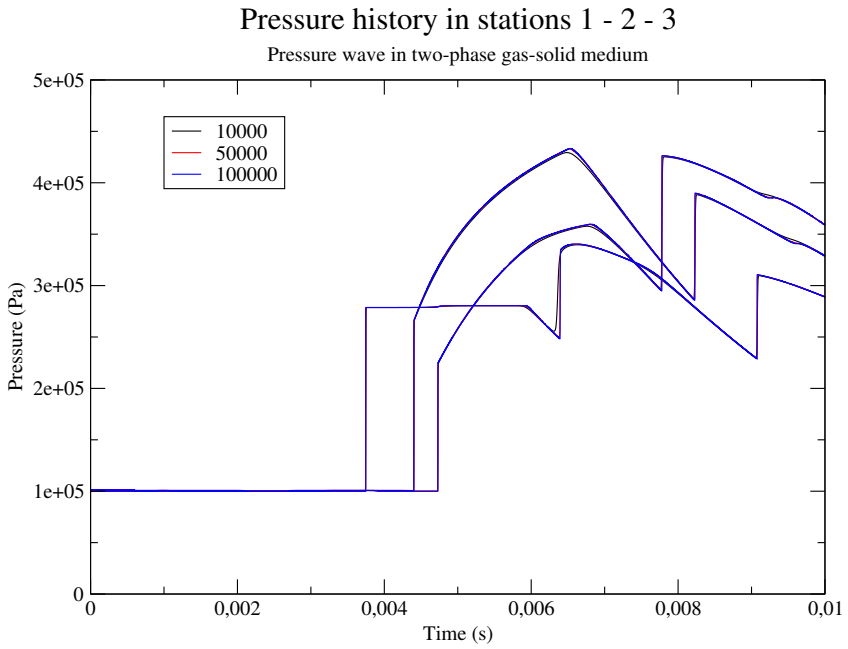

FIGURE 1.11 – Two-phase shock tube apparatus with solid particles. Mean pressure signal at stations $1-2-3$. Meshes : 10^4 cells (black), $5.\times 10^4$ cells (red)and 10^5 cells (blue)

would like to thank Thierry Gallouët, Sergey Gavrilyuk, Olivier Hurisse, Georges Jourdan, Jean-Claude Latché, Khaled Saleh and Nicolas Seguin for their help and for various useful discussions on the subject.

1.8 Appendix A : an alternative pressure relaxation scheme

An implicit Euler scheme might be used to compute pressures and statistical fractions in the pressure relaxation step, thus seeking solutions of :

$$\left\{\begin{array}{l} (\alpha_2)_i^{n+1} - (\alpha_2)_i^* = \Delta t^n \left(\Sigma_k(d_{2k})(P_2(\frac{m_2^*}{\alpha_2^{n+1}}) - P_k(\frac{m_k^*}{\alpha_k^{n+1}}))\right) \ ; \\ (\alpha_3)_i^{n+1} - (\alpha_3)_i^* = \Delta t^n \left(\Sigma_k(d_{3k})(P_3(\frac{m_3^*}{\alpha_3^{n+1}}) - P_k(\frac{m_k^*}{\alpha_k^{n+1}}))\right) \ ; \end{array}\right. \tag{1.49}$$

where of course : $(\alpha_1)_i^{n+1,*} = 1 - (\alpha_2)_i^{n+1,*} - (\alpha_3)_i^{n+1,*}$, with some abuse of notation.

Hence we have the result :

Property :
Assume that $(\alpha_k)_i^*$ *and* $(m_k)_i^*$ *are positive. Then the previous discrete pressure relaxation scheme* (1.49) *computes a unique set of positive values* $(\alpha_k)_i^{n+1}$.

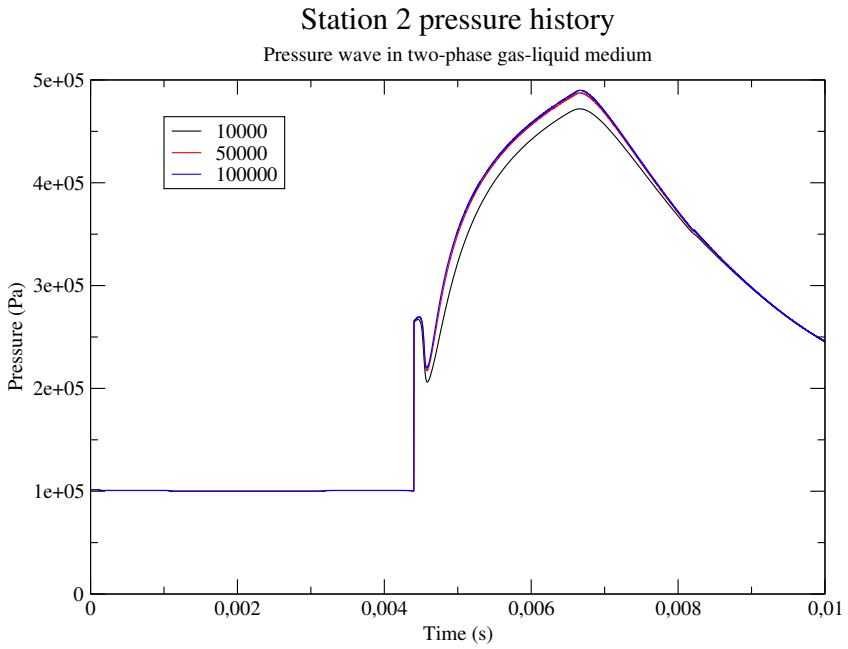

FIGURE 1.12 – Two-phase shock tube apparatus with liquid water droplets. Mean pressure signal at station 2. Meshes : 10^4 cells (black), $5. \times 10^4$ cells (red)and 10^5 cells (blue)

One drawback of the latter scheme is that the discrete solution may be hard to find in practice, especially when statistical fractions are close to the boundary of the admissible domain ; some cure should be found in order to use the latter algorithm for practical computations. We underline that the latter scheme is the straightforward extension of the one used for two-phase flow models in [21].

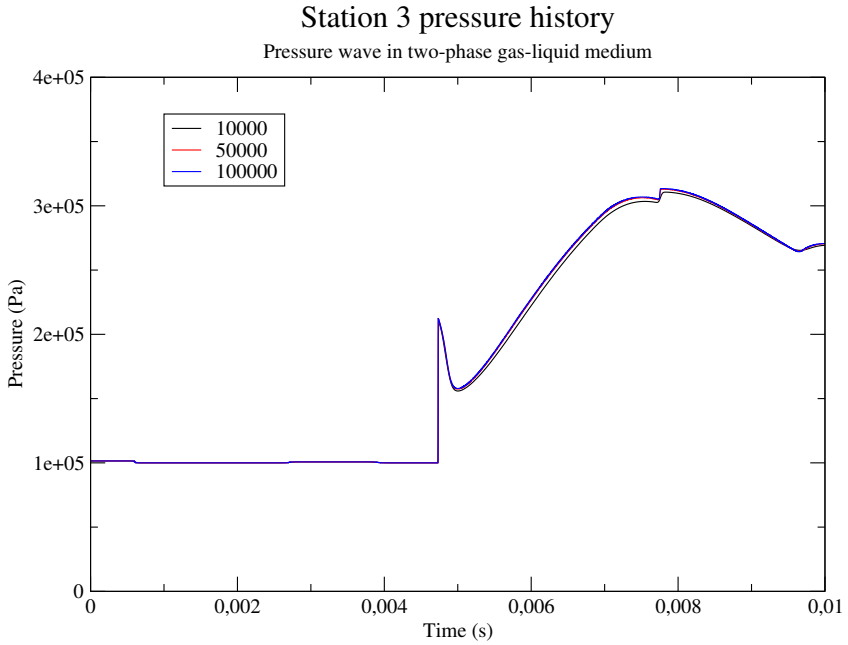

FIGURE 1.13 – Two-phase shock tube apparatus with liquid water droplets. Mean pressure signal at station 3. Meshes : 10^4 cells (black), $5. \times 10^4$ cells (red)and 10^5 cells (blue)

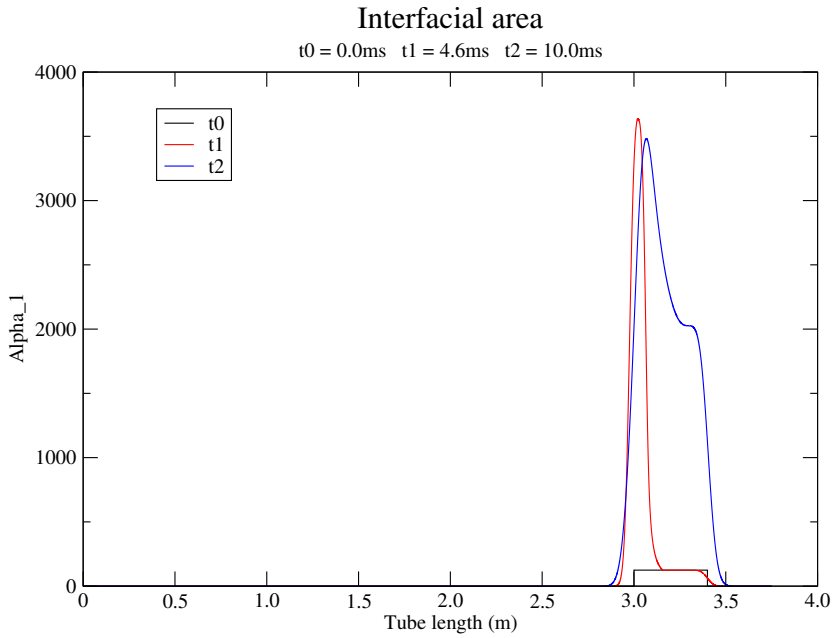

FIGURE 1.14 – Two-phase shock tube apparatus with liquid water droplets. Liquid water interfacial aerea profiles at three distinct instants.

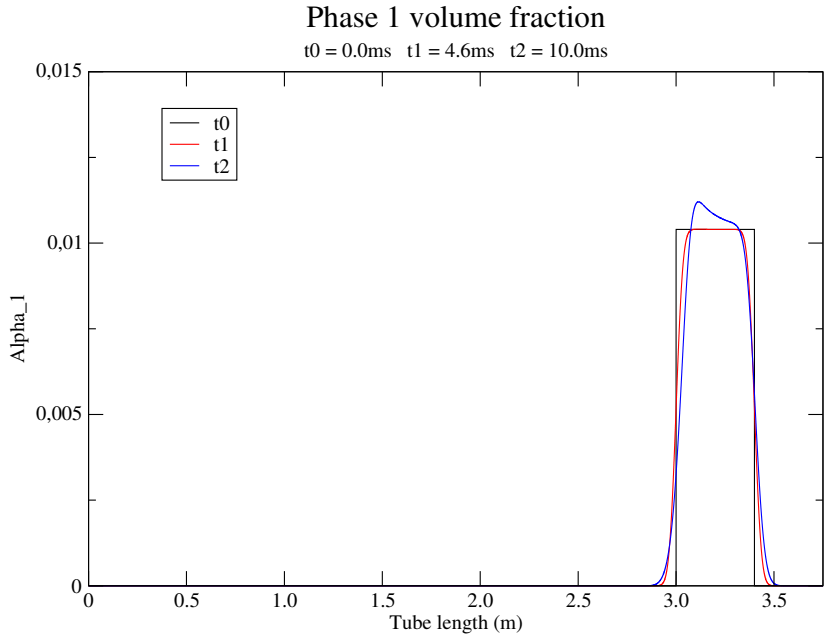

FIGURE 1.15 – Two-phase shock tube apparatus with liquid water droplets. Liquid water statistical fraction profiles at three distinct instants.

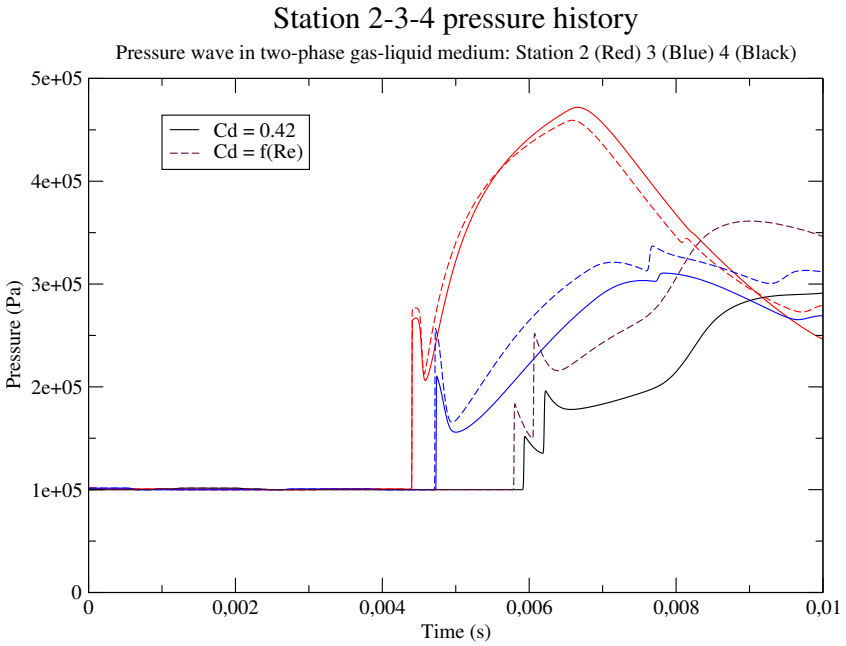

FIGURE 1.16 – Two-phase shock tube apparatus with liquid water droplets. Influence of the drag coefficient C_{12} on the mean pressure profiles at stations $2-3-4$.

Bibliographie

[1] A. Ambroso , C. Chalons, F. Coquel and T. Galié, Relaxation and numerical approximation of a two-fluid two-pressure diphasic model, *ESAIM : Mathematical Modelling and Numerical Analysis*, vol. 43, pp. 1063-1097, 2009.

[2] A. Ambroso , C. Chalons and P.A.Raviart, A Godunov type method for the seven-equation model of compressible two-phase flow, *Computers and Fluids*, vol. 54 , pp. 67-91, 2012.

[3] M.R. Baer and J.W. Nunziato, A two phase mixture theory for the deflagration to detonation transition (DDT) in reactive granular materials, *Int. J. Multiphase Flow*, vol. 12-6, pp. 861–889, 1986.

[4] G. Berthoud, Vapor explosions, *Annual Review of Fluid Mechanics*, vol. 32, pp. 573–611, 2000.

[5] W. Bo, H. Jin, D. Kim, X. Liu, H. Lee, N. Pestiau, Y. Yu, J. Glimm and J.W. Grove, Comparison and validation of multiphase closure models, *Computers and Mathematics with Applications*, vol. 56, pp. 1291-1302, 2008.

[6] A. Chauvin, Etude expérimentale de l'atténuation d'une onde de choc par un nuage de gouttes et validation numérique, *PhD thesis*, Université Aix Marseille, 2012.

[7] A. Chauvin, G. Jourdan, E. Daniel, L. Houas and R. Tosello, Experimental investigation of the propagation of a planar shock wave through a two-phase gas-liquid medium, *Physcis of Fluids*, vol.23,113301, 2011.

[8] F. Coquel, T. Gallouët, J.M. Hérard and N. Seguin, Closure laws for a two fluid two-pressure model, *C. R. Acad. Sci. Paris*, vol. I-332, pp. 927–932, 2002.

[9] F. Coquel, J.M. Hérard, K. Saleh and N. Seguin, A robust entropy-satisfying finite volume scheme for the isentropic Baer Nunziato model, *ESAIM : Mathematical Modelling and Numerical Analysis*, vol. 48, pp. 165-206, 2014.

[10] F. Coquel, J.M. Hérard and K. Saleh, A positive and entropy-satisfying finite volume scheme for the Baer Nunziato model, *Journal of Computational Physics*, vol. 330, pp. 401-435, 2017.

[11] M. Essadki, Contribution to a unified modelling of fuel injection : from dense liquid to polydisperse evaporating spray, *PhD thesis*, Ecole polytechnique, february 13, 2018.

[12] G. Faccanoni, S. Kokh and G. Allaire, Modelling and simulation of liquid-vapor phase transition in compressible flows based on thermodynamical equilibrium, *ESAIM : Mathematical Modelling and Numerical Analysis*, vol. 46, pp.1029-1054, 2012.

[13] T. Flätten and H. Lund, Relaxation two-phase flow models and the subcharacteristic condition. *Mathematical Models and Methods in Applied Sciences*, vol. 21(12), 2011.

[14] S. Gavrilyuk, The structure of pressure relaxation terms : the one-velocity case, *EDF report H-I83-2014-0276-EN*, 2014 .

[15] S. Gavrilyuk and R. Saurel, Mathematical and numerical modelling of two-phase compressible flows with micro inertia, *Journal of Computational Physics*, vol. 175, pp. 326-360, 2002 .

[16] B.E Gelfand, Droplet breakup phenomena in flows with velocity lag, *Progress in Energy and Combustion Science*, vol.22 , pp.201-265 , 1996.

[17] P. Helluy and H. Mathis, Pressure laws and fast Legendre transform, *Mathematical Models and Methods in Applied Sciences*, vol. 21, pp.745-775, 2011.

[18] P. Helluy and N. Seguin, Relaxation models of phase transition flows, *ESAIM : Mathematical Modelling and Numerical Analysis*, vol. 40, pp.331-352, 2006.

[19] J.M. Hérard, A three-phase flow model, *Mathematical and Computer Modelling*, vol. 45, pp. 732-755, 2007.

[20] J.M. Hérard, A class of compressible multiphase flow models, *Comptes Rendus Mathématique*, vol. 354, pp. 954-959, 2016.

[21] J.M. Hérard and O. Hurisse, A fractional step method to compute a class of compressible gas-liquid flows, *Computers and Fluids*, vol. 55, pp.57-69, 2012.

[22] J.M. Hérard, K. Saleh and N. Seguin, Some mathematical properties of a hyperbolic multiphase flow model, *HAL preprint available on : https ://hal.archives-ouvertes.fr/hal-01921027v1*, 2018.

[23] T. Hibiki and M. Ishii, One-group interfacial area transport of bubbly flows in vertical round tubes, *Int. J. of Heat and Mass Transfer*, vol. 43, pp. 2711-2726, 2000.

[24] A.K. Kapila, S.F. Son, J.B. Bdzil, R. Menikoff and D.S. Stewart, Two phase flow modeling of deflagration to detonation transition : srtucture of the velocity relaxation zone, *Physics of Fluids*, vol. 9(12), 1997.

[25] H. Mathis, A thermodynamically consistent model of a liquid-vapor fluid with a gas, *ESAIM : Mathematical Modelling and Numerical Analysis*, HAL preprint available on https ://hal.archives-ouvertes.fr/hal-01615591v2, 2018.

[26] M. Massot, F. Laurent, D. Kah and S. de Chaisemartin, A robust moment method for evaluation of the disappearance rate of evaporating sprays, *SIAM Journal of Applied Mathematics*, vol. 70, pp.3203-3234, 2010.

[27] R. Meignen, B. Raverdy, S. Picchi and J. Lamome, The challenge of modelling fuel-coolant interaction. Part II : steam explosion, *Nuclear Engineering and Design*, vol. 280, pp.528-541, 2014.

[28] S. Müller, M. Hantke and P. Richter, Closure conditions for non-equilibrium multicomponent models, *Continuum Mechanics and Thermodynamics*, vol. 28, pp. 1157-1190, 2016.

[29] S. Picchi, MC3D version 3.9. Description of the physical models of the premixing application, *IRSN internal report PSN-RES/SAG/2017-0073*, 2017.

[30] M. Pilch, Acceleration induced fragmentation of liquid drops, *PhD thesis*, University of Virginia, 1981.

[31] M. Pilch and C.A. Erdman, Use of breakup time data and velocity history data to predict the maximum size of stable fragments for acceleration induced breakup of a liquid drop, *Int. J. Multiphase Flow*, vol. 28, pp. 741-757, 1987.

[32] X. Rogue, G. Rodriguez, J.F. Haas and R. Saurel, Experimental and numerical investigation of the shock induced fluidization of a particles bed, *Shock Waves*, vol. 8, pp.29-46, 2014.

[33] E. Romenski, A. A. Belozerov and I. M. Peshkov, Conservative formulation for compressible multiphase flows, *http ://arxiv.org/abs/1405.3456*, pp. 1-21, 2014.

[34] E. Rusanov, Calculation of interaction of non steady shock waves with obstacles, *Journal of Computational Mathematics and Physics*, vol. 1, pp. 267-279, 1961.

[35] K. Saleh, A relaxation scheme for a hyperbolic multiphase flow model. Part I : barotropic EOS, *HAL preprint available on https : https ://hal.archives-ouvertes.fr/hal-01737681v1*, 2018.

[36] W. Yao and C. Morel, Volumetric interfacial area prediction in upward bubbly two-phase flow, *Int. J. of Heat and Mass Transfer*, vol. 47, pp. 307-328, 2004.

Appendix B

1.9 Appendix B - Introduction

This appendix aims at presenting different numerical simulations that were conducted using the three-phase flow barotropic model. The simulations concern the propagation of pressure shock waves in single phase or two-phase medium, they were described in Chapter 1 [BH19] [5]. The present appendix gives more numerical results in order to better understand the considered model, and its numerical applications.

The concerned set of partial differential equations (PDEs) is the following :

$$\begin{cases} \partial_t A + \partial_x(AU_1) = f_A A^2/\alpha_1 \\ \partial_t \alpha_k + U_1 \partial_x \alpha_k = \Sigma_{l=1}^3 d_{kl}(P_k - P_l) \\ \partial_t m_k + \partial_x(m_k U_k) = 0 \\ \partial_t(m_k U_k) + \partial_x(m_k U_k^2 + \alpha_k P_k) + \Sigma_{l\neq k}\Pi_{kl}\partial_x\alpha_l = \Sigma_{l=1}^3 e_{kl}(U_l - U_k) \end{cases} \tag{1.50}$$

Where :

— $k = 1, 2, 3$ is the phase index ;

— α_k, $m_k = \alpha_k \rho_k$, P_k and U_k denote respectively statistical fraction, partial mass, pressure and velocity of phase k ;

— interfacial pressures Π_{kl} are given by : $\Pi_{12} = \Pi_{21} = \Pi_{23} = P_2$ and $\Pi_{13} = \Pi_{31} = \Pi_{32} = P_3$;

— $f_A = \frac{C_0}{6}\left(\frac{\rho_2}{\rho_1}\right)^{1/2} |U_1 - U_2| f(We)$ with $C_0 = 0.245$;

— $f(We) = 0$ if $We < 12$ and 1 if not ;

— $d_{kl} = 10^{10}$ for all $k, l = 1, 2, 3$ with $k \neq l$;

— $e_{12} = \frac{C_{d12}}{8} A \rho_2 |U_2 - U_1|$ with $C_{d12} = 0.42$, $e_{13} = 10^{-10} e_{12}$ and $e_{23} = 10^{-10}$;

In practice we investigated a series of Riemann problems where the initial condition is such that the total pressure is discontinuous and all velocities are set to 0. In order to observe the gas shock wave behaviour across the domain, four pressure stations (S_p, $p = 1..4$) were placed in the low-pressure side of the tube. Stations distribution is chosen, as shown in Fig.1.17, in order to give a clear understanding of pressure map throughout shock tube and water liquid droplets (for two-phase simulations). The switch between single phase and

5. [BH19] H. Boukili, J.M. Hérard. Relaxation and Simulation of a Three-Phase Flow Model. ESAIM Mathematical Modelling and Numerical Analysis, vol. 53, pp. 1031-1059, 2019.

two-phase flows is achieved by acting on volume fractions α_k, which are set to 10^{-10} for vanishing phases.

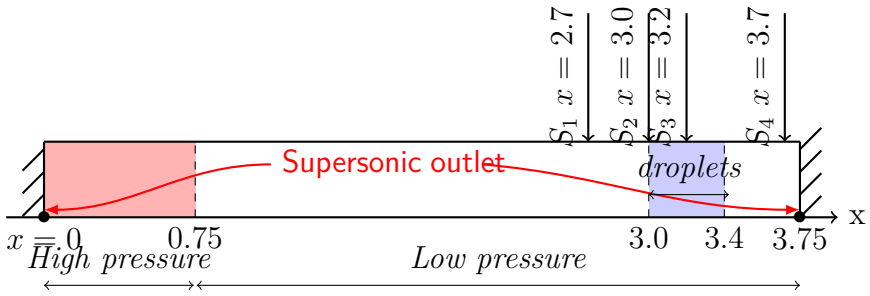

FIGURE 1.17 – Shock tube with closed wall boundary condition

The simulation time step is enforced by a classical CFL condition, which results from the convection numerical scheme (Rusanov scheme). We chose in practice $CFL = 1/2$ for all test cases. Furthermore, the considered meshes are regular and 3-dimensional, with 1 element in y/z directions and various elements number in x direction, so that only the 1D effects will be taken into account. Boundary conditions were chosen in order to take into account the effect of a "closed" shock tube, which is representative of experimental configurations, wave reflections on both sides of the shock tube are possible.

An *ideal gas* equation of state *EOS* was chosen for phases indexed by 2 and 3, with the same coefficient $\gamma = 7/5 : p_k(\rho_k) = 10^5(\rho_k/\rho_{ref})^{7/5}$ for $k = 2, 3$, where $\rho_{ref} = 1.27$. Phase 1 *EOS* is set to : $p_1(\rho_1) = c_1^2\rho_1 + p_{ref}$, where $c_1 = 1500$ and p_{ref} such that $p_1(10^3) = 10^5$.

1.10 Appendix B - Single phase flow

This first test case was carried out with two vanishing phases to simulate the case of homogeneous gaseous medium. The Riemann problem was initialised as follows :

	Left $(x < 0.75)$	Right $(0.75 < x)$
p_k	$= 7\ bar\ for\ k = 1, 2, 3$	$= 1\ bar\ for\ k = 1, 2, 3$
u_k	$= 0\ for\ k = 1, 2, 3$	$= 0\ for\ k = 1, 2, 3$
$\alpha_1 = \alpha_3$	$= 10^{-10}$	$= 10^{-10}$
α_2	$= 1 - \alpha_1 - \alpha_3$	$= 1 - \alpha_1 - \alpha_3$

Fig.1.18 presents the pressure histories obtained in the station 4 for different meshes. As explained in [BH19], we can observe the typical uniform pressure jump induced by the shock wave around $t = 5.7ms$, which is followed by a constant pressure level then by a second pressure jump due to reflection on the right wall boundary. We can also notice that mesh convergence is quickly obtained, the difference between the

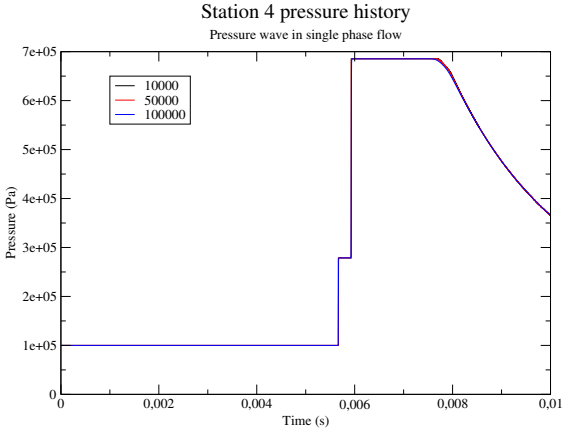

FIGURE 1.18 – Single phase flow

last two calculations (mesh sizes 1/50000 and 1/100000) is almost invisible.

These numerical results are consistent with Euler equations for barotropic gas dynamics. In fact, the initial data of our 1D Riemann problem satisfies the condition (1.51), which ensures existence and uniqueness of the solution :

$$u_R - u_L < \frac{2}{\gamma - 1}(c_L + c_R) \tag{1.51}$$

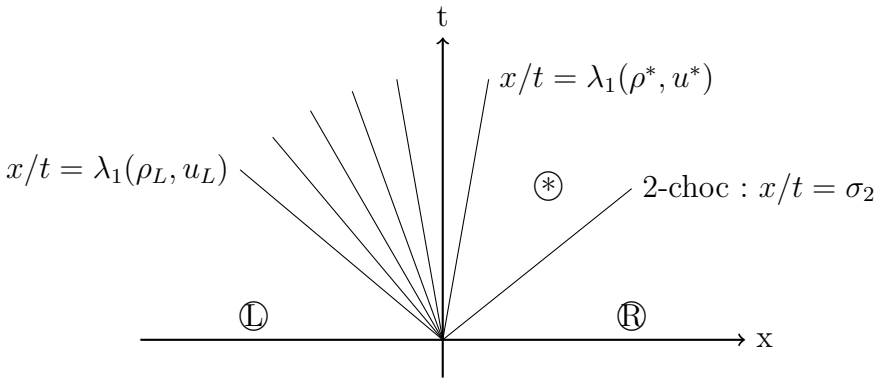

FIGURE 1.19 – Solution of the Riemann problem : 1-rarefaction and 2-chock

Moreover, the actual calculation of intermediate states (Fig.1.19) gives the next numerical results :

— **Intermediate state** ⊛ : this corresponds to the state that immediately follows the shock wave observed in all stations shortly after calculation starts. Given the right and left states : (ρ_R, u_R) and (ρ_L, u_L), the question is to evaluate the state (ρ^*, u^*).

The 2-shock relation gives : $u^* - u_R = \sqrt{-(p^* - p_R)\left(\frac{1}{\rho^*} - \frac{1}{\rho_R}\right)}$

The 1-rarefaction relation implies : $u^* - u_L = \frac{-2}{\gamma-1}(c^* - c_L)$

Combining these two equations gives :

$$\frac{2}{\gamma - 1}(c(\rho^*) - c_L) + \sqrt{-(p(\rho^*) - p_R)\left(\frac{1}{\rho^*} - \frac{1}{\rho_R}\right)} = u_L - u_R \tag{1.52}$$

We solve the equation (1.52) with respect to ρ^* to obtain the constant pressure value $p^* = p(\rho^*)$ that follows immediately the 2-shock : $p^* = 2.78 \times 10^5$, which is the observed value on Fig.1.18.

— **Intermediate state** ⊛⊛ this corresponds to the shock wave reflected on the right side boundary. It is determined by solving :

$$\begin{cases} u^* - u^{**} = \sqrt{-(p(\rho^{**}) - p^*)\left(\frac{1}{\rho^{**}} - \frac{1}{\rho^*}\right)} \\ u^{**} = 0 \end{cases} \tag{1.53}$$

The numerical resolution gives : $p^{**} = p(\rho^{**}) = 6.85 \times 10^5$.

As expected, the numerical values confirm then that our three-phase barotropic model is consistent with barotropic Euler equations for gas dynamics, when executed in the 2 vanishing phases configuration.

1.11 Appendix B - Two-phase gas-solid flow

This configuration concerns the case of a two-phase flow where the pressure wave is in interaction with **solid** spherical particles. The Riemann problem is initialised as follows :

Left $(x < 0.75)$	Right $(0.75 < x)$
$P_k = 7\ bar\ for\ k = 1,2,3$	$P_k = 1\ bar\ for\ k = 1,2,3$
$u_k = 0\ for\ k = 1,2,3$	$u_k = 0\ for\ k = 1,2,3$
$\alpha_3 = 10^{-10}$	$\alpha_3 = 10^{-10}$
$\alpha_2 = 1 - \alpha_1 - \alpha_3$	$\alpha_2 = 1 - \alpha_1 - \alpha_3$
$\alpha_1 = 10^{-10}$	$\alpha_1 = 0.0104$ if $[2.97 < x < 3.37]$ and 10^{-10} if not

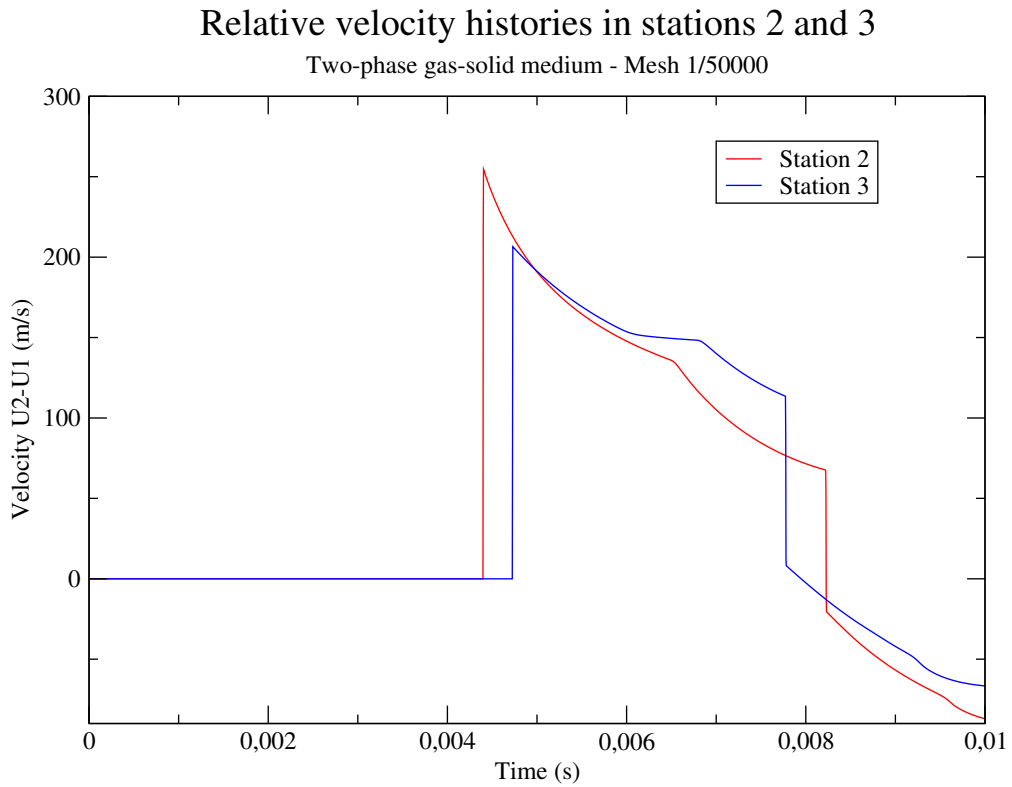

FIGURE 1.20 – Gas-solid flow - Relative velocity

Fig.1.20 shows the evolution of the relative velocity $U_2 - U_1$ over stations 2 and 3, situated respectively in the front and middle of particles lid. We can see the arrival of the incident

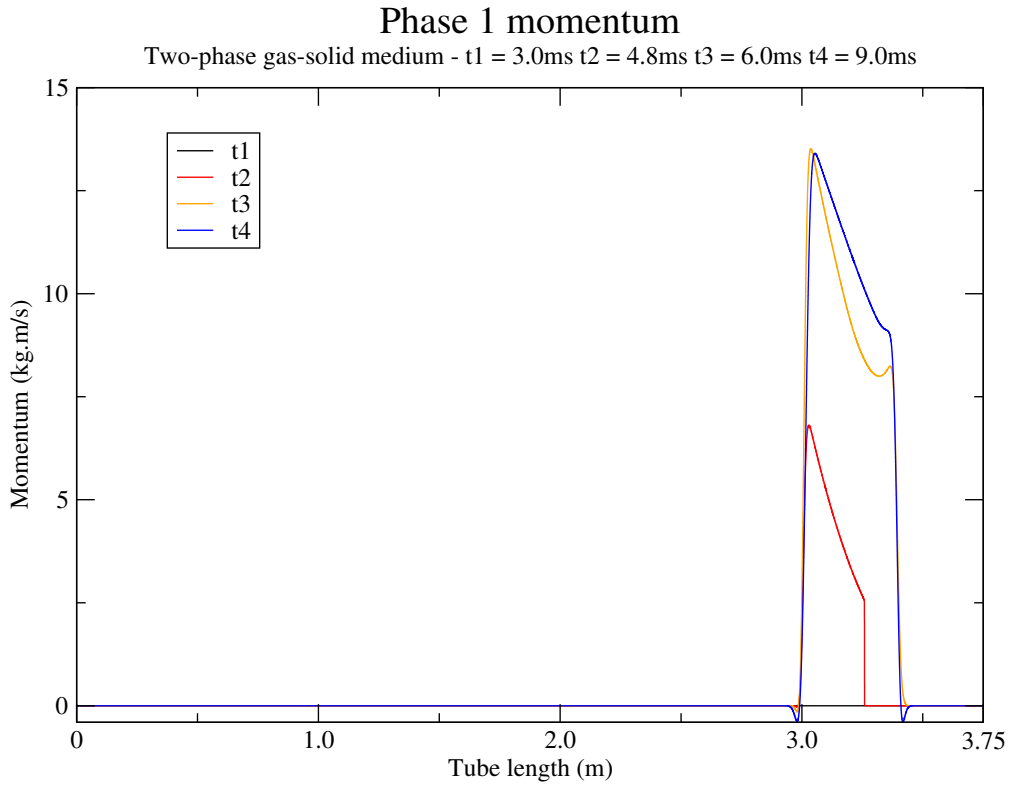

FIGURE 1.21 – Gas-solid flow - Phase 1 momentum

shock wave around $t = 4.5ms$, which strikes first the station 2 and leads to an important relative velocity jump. It strikes then station 3 with a decreasing jump, due to the fact that the shock wave lost some energy while travelling inside the particles lid.

The relative velocity decreases afterwards until the reflected shock wave on the tube right wall boundary hits back the two stations around $t = 8ms$, station 3 is hit first since it's closer to the tube right end.

The next two figures present a different perspective to visualize computational results ; instead of the history records shown on stations $S_p, p = 1..4$, here we observe the evolution of variables along the shock tube at different time instants.

Fig.1.21 gives the evolution of phase 1 momentum m_1U_1 at 4 chosen time instants. At $t_1 = 3.0ms$ (black) m_1U_1 is almost null everywhere, this is due to the fact that the shock wave at t_1 didn't hit the droplets cloud yet. At $t_2 = 4.8ms$ (red), the shock wave moving inside the droplet cloud, we can clearly see the discontinuity around $x = 3.26$ corresponding to the front of the shock wave. Phase 1 momentum keeps increasing as seen at $t_3 = 6.0ms$ (orange), at this moment the shock wave has not hit the tube end wall yet. At $t_4 = 9.0ms$ (blue) the reflected shock wave had enough time to cross back the droplet cloud and to progress towards the left side of the tube. This increases slightly m_1U_1.

Fig.1.22 gives the same representation for m_2U_2. Phase 2 is the shock wave carrying phase, so the observed momentum values are significantly greater than those of phase 1. The same qualitative patterns are observed :

— $t_1 = 3.0ms$ (black) : incident shock wave located at $x = 2.33$ and progressing towards

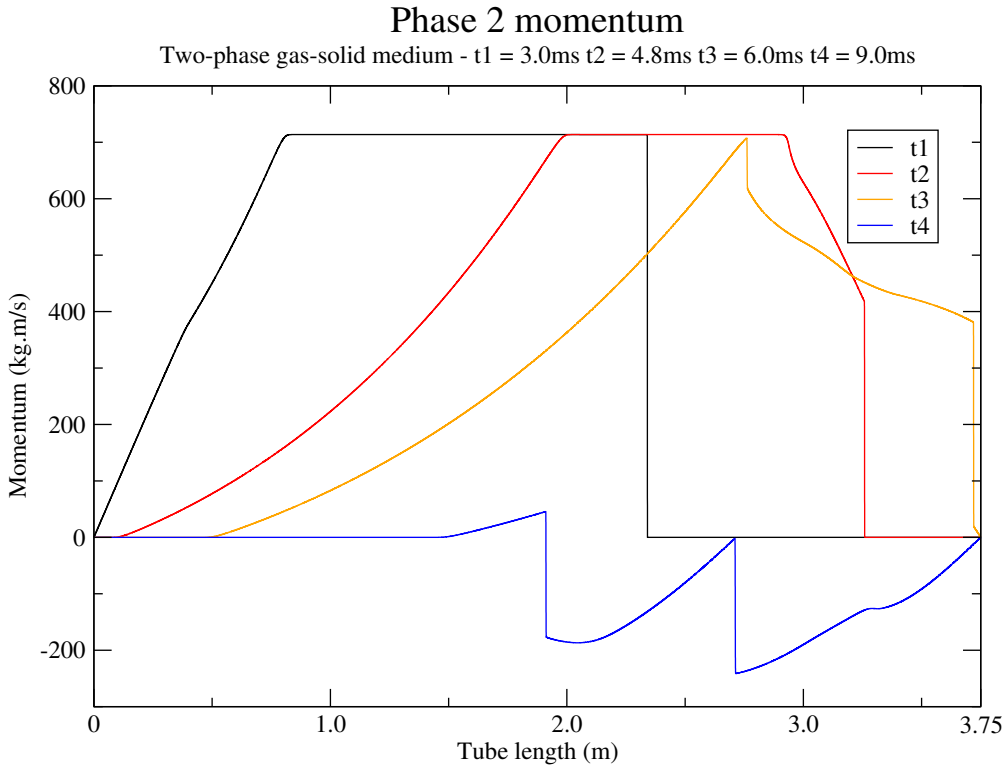

FIGURE 1.22 – Gas-solid flow - Phase 2 momentum

the particles cloud situated between $x = 2.97$ and $x = 3.37$.

— $t_2 = 4.8ms$ (red) : shock wave progressing inside the particles cloud.

— $t_3 = 6.0ms$ (orange) : after crossing the particles cloud, the shock wave is arriving at the tube's end wall.

— $t_4 = 9.0ms$ (blue) : reflected shock wave ($x = 2.7$) crossed back the whole particles cloud and arrived at the position of station S_1. An other discontinuity is observed in $x = 1.9$, it corresponds to the left-travelling reflected wave on the front of particles could, it's only observed in station S_1 since stations S_2 and S_3 are located inside the particles cloud (See [BH19] Fig. 11).

1.12 Appendix B - Two-phase gas-liquid flow

The two-phase flow simulation of the previous section is modified in order to take into account the **fragmentation** of particles. In fact, as the shock wave reaches the droplets cloud, each droplet deforms and is split into smaller droplets ; this leads to an increase of the global exchange surface between gas (phase 2) and **liquid** (phase 1). In practice, we use the same Riemann problem initialization as in the precedent section.

Fig.1.23 gives the relative velocity $U_2 - U_1$ over stations 2 and 3. We observe the arrival of the incident shock wave, leading to a relative velocity jump of the same order as in the gas-solid case for station S_2. This is followed by a sudden decrease specific to the gas-liquid case

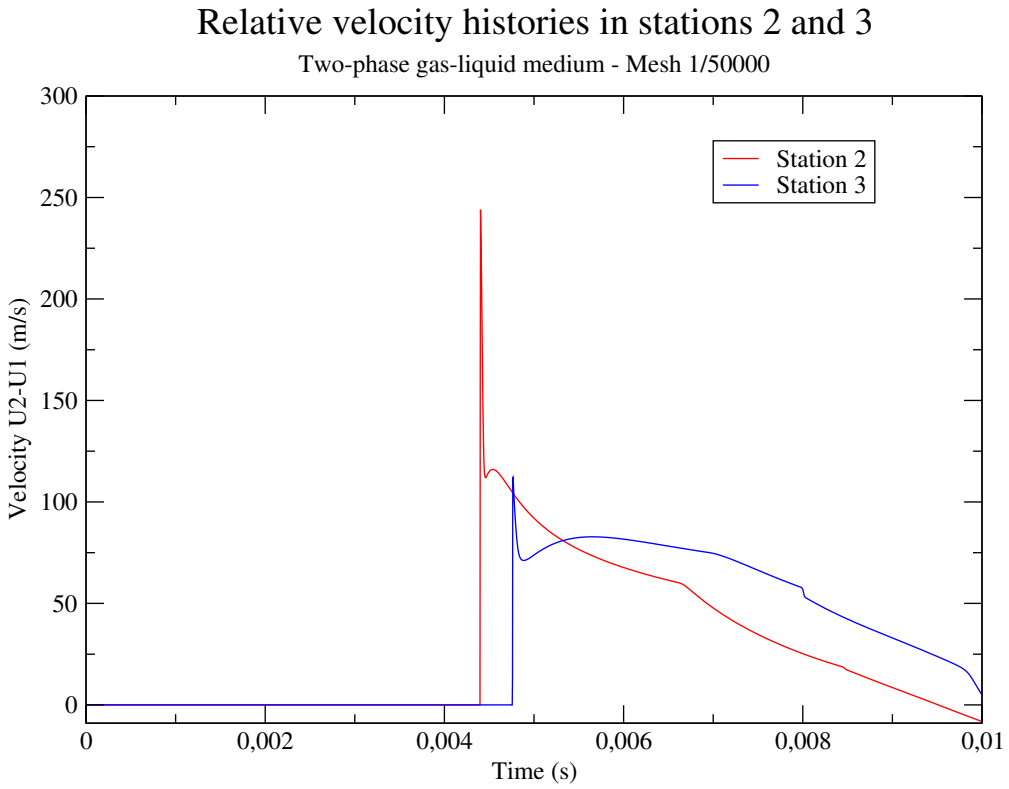

FIGURE 1.23 – Gas-liquid flow - Relative velocity

and corresponding to the fragmentation of particles happening just after the impact of the incoming shock wave. The relative velocity jump of station S_3 is significantly smaller than the jump observed in the gas-solid case, this is due to the fact that the fragmentation phenomenon absorbs a significant part of energy and shock wave gets more and more attenuated as it travels inside the deformable particle cloud.

As in the previous section, Fig.1.24 gives the spacial representation of m_1U_1 at 4 time instants. The same patterns are retrieved, but the numerical values reached in this gas-liquid case are significantly higher than in the gas-solid case. It shows that the fragmentation phenomenon leads to an important exchange of kinetic energy between phases 1 and 2. Concretely, this means that after fragmentation the droplets start to move towards the right side of the tube, following the movement of the incoming shock wave.

Fig.1.25 shows the results of m_2U_2 at the same 4 time instants. Here again we retrieve the same qualitative patterns as the previous section, but with two main differences :

— At $t_2 = 4.8ms$ the front of the shock wave is moving inside the droplet cloud, followed immediately by a sudden decrease, which is characteristic of the fragmentation process. This obviously does not appear in the previous case since no fragmentation is happening in gas-solid medium.

— At $t_4 = 9.0ms$ we observe in $x = 1.5$ the jump corresponding to the reflected shock wave on the front of the particle cloud ; however, unlike the gas-solid case we are not able to clearly distinguish the reflected shock wave on the right wall boundary of the tube. This could be a consequence of dissipation effects due to fragmentation. Once

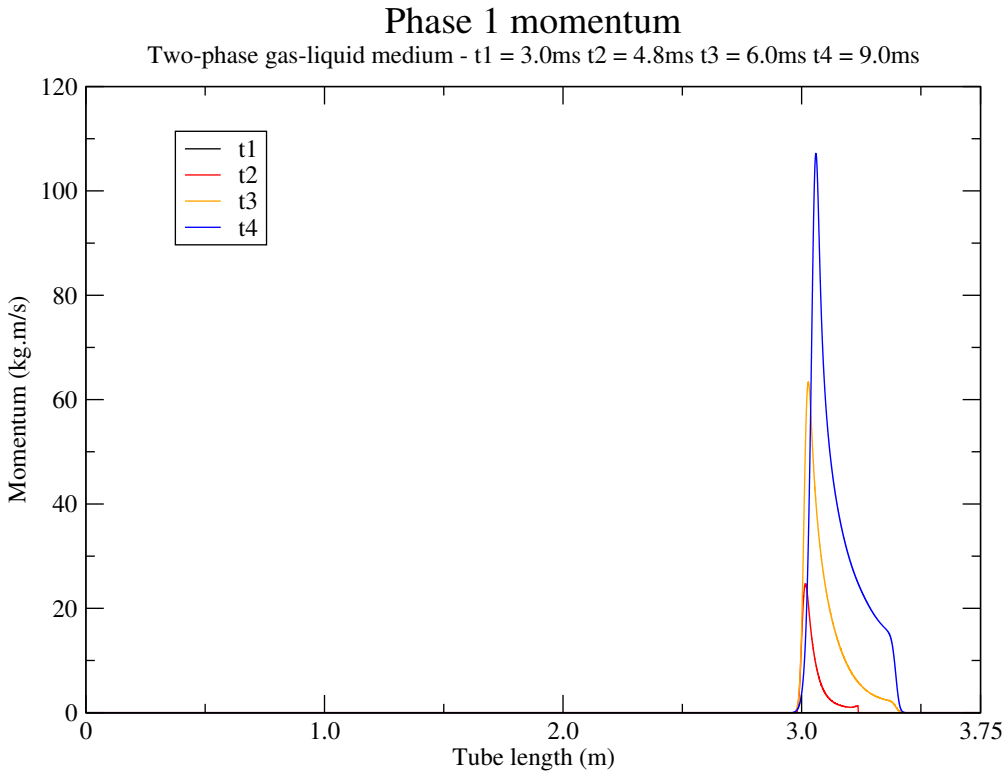

FIGURE 1.24 – Gas-liquid flow - Phase 1 momentum

the incident shock wave has crossed the particles cloud it is significantly attenuated, after reflection and crossing back the particles cloud it is almost invisible, at least at the level of the considered 1/50000 mesh.

1.13 Appendix B - Influence of the drag coefficient

As described in the section 4.2 of the paper [BH19] and references therein, several parameters are involved in the construction of our three-phase flow model, in particular the drag coefficient C_{d12} between phases 1 and 2. We compared the results obtained with two different drag coefficients :

— A constant value $C_{d12} = 0.42$;

— A function of the relative Reynolds number :
$C_{d12} = \frac{24}{Re}\left(1 + 0.15(Re)^{0.687}\right) + 0.42\left(1 + 42500(Re)^{-1.16}\right)^{-1}$

Fig.1.26 shows the impact of C_{d12} on the relative velocity $U_2 - U_1$. We can observe that choosing the drag coefficient as function of Re leads globally to an increase of relative velocity, which remains true until the arrival of the reflected shock wave around $t = 8.0ms$ (which is easier to identify on the $C_{d12} = f(Re)$ computations).

Fig.1.27 shows the impact of C_{d12} on the momentum of phase 1. We can see that taking $C_{d12} = f(Re)$ gives lower momentum peaks than the constant value $C_{d12} = 0.42$. This is

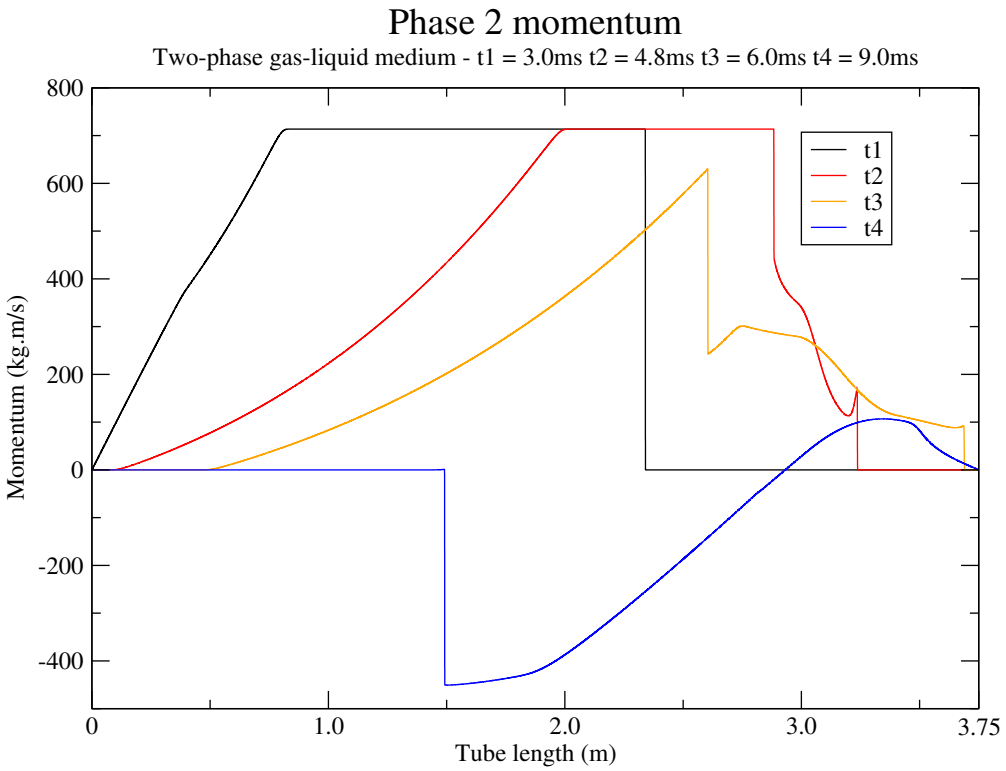

FIGURE 1.25 – Gas-liquid flow - Phase 2 momentum

consistent with the fact that relative velocity peaks are higher for the case $C_{d12} = f(Re)$. In fact, assuming that U_2 remains at the same level (because the incident pressure shock wave is the same), higher relative velocity means lower values for U_1, and then lower momentum of phase 1.

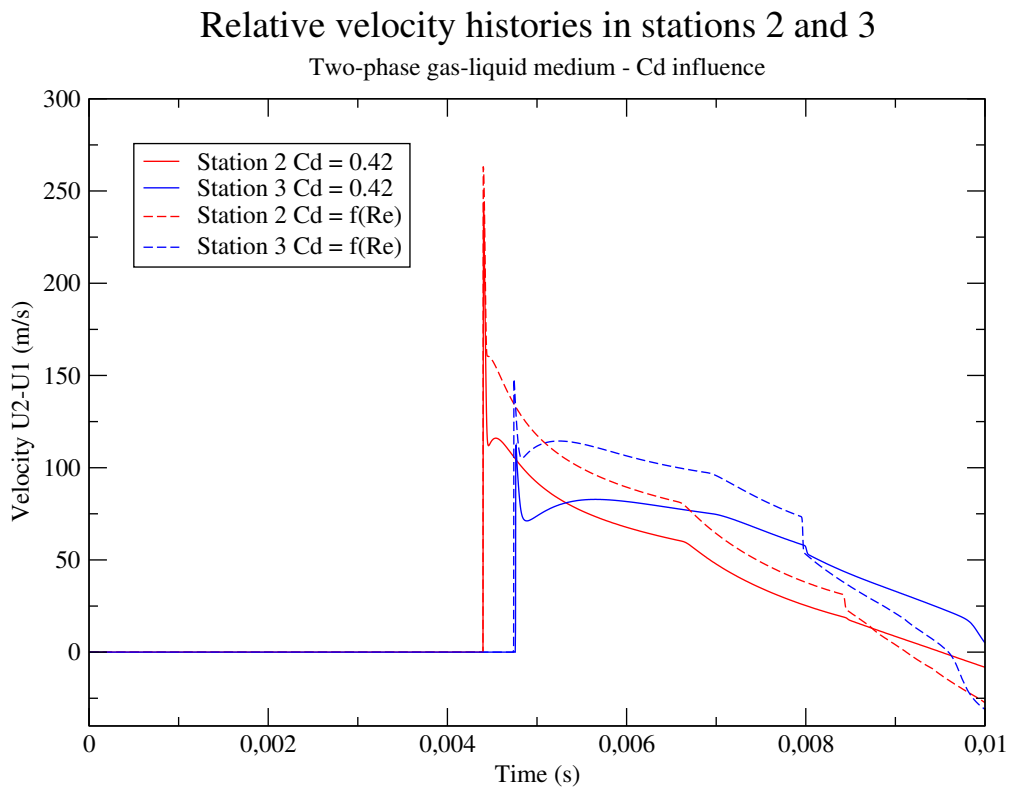

FIGURE 1.26 – Gas-liquid flow - Impact of drag coefficient on relative velocity

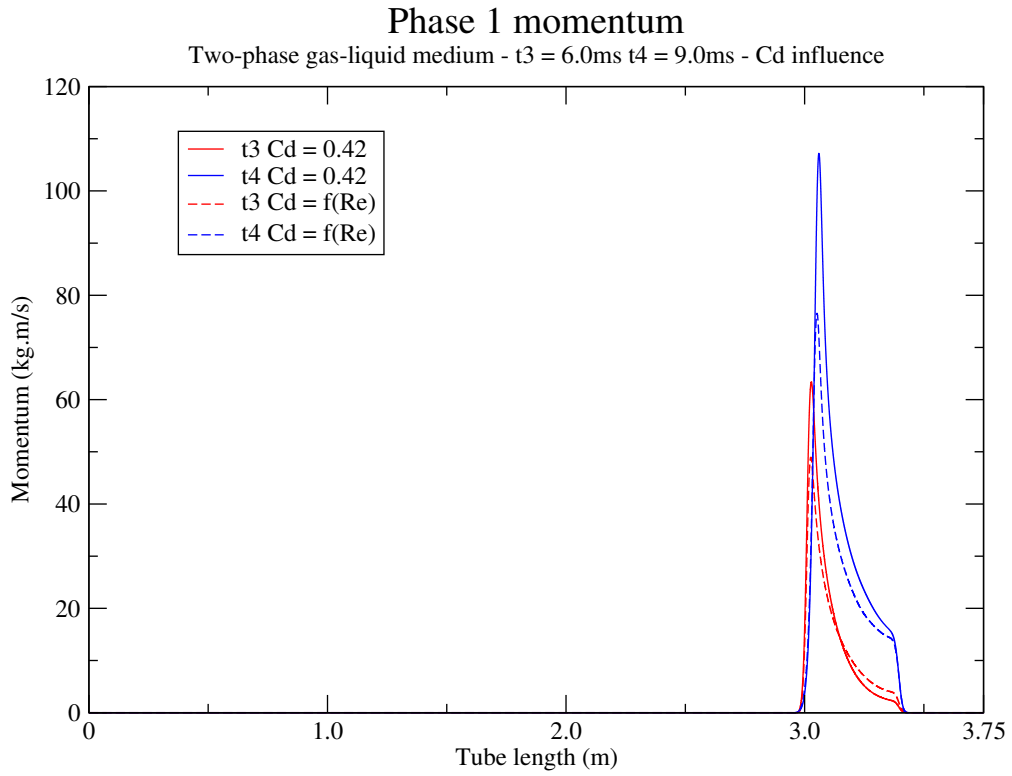

FIGURE 1.27 – Gas-liquid flow - Impact of drag coefficient on phase 1 momentum

Chapitre 2

Simulation and validation of a three-phase flow model with energy [1]

Hamza Boukili [2, 3], **Jean-Marc Hérard**[2, 3]

Abstract. This paper is devoted to the simulation of the three-phase flow model [18], in order to account for immiscible components. The whole model is first recalled, and the main properties of the closed set are given, with particular focus on the Riemann problem associated with the convective subset that contains non-conservative terms, and also on the relaxation process. The model is hyperbolic, far from resonance occurrence, and a physically relevant entropy inequality holds for smooth solutions of the whole system. Owing to the uniqueness of jump conditions, specific solutions of the one-dimensional Riemann problem can be built, and these are useful (and mandatory) for the verification procedure. The fractional step method proposed herein complies with the continuous entropy inequality, and implicit schemes that are considered to account for relaxation terms take their roots on the true relaxation process. Once verification tests have been achieved, focus is given on the simulation of the experimental set-up [7, 8], in order to simulate a cloud of droplets that is hit by an incoming gas shock-wave.

1. Les travaux de ce chapitre sont inclus dans :
Boukili H., Hérard JM. Simulation and preliminary validation of a three-phase flow model with energy. Soumis à Computers and Fluids.

2. EDF Lab Chatou, 6, quai Watier, 78400 Chatou, France.
3. I2M, Aix Marseille Université, 39 rue Joliot Curie, 13453 Marseille, France.

2.1 Introduction

In fluid dynamics, a multiphase flow is a simultaneous flow of two or more components in the same media, or the flow of one single component but with different chemical properties or thermodynamic states. It has a wide range of applications in the modern industry that cover different flow configurations, for instance : gas-liquid-solid mixtures, non miscible liquid-liquid mixtures, change of state liquid-gas mixtures, etc.

In the nuclear industry, many configurations of multiphase flows arise, either in the normal operation (for instance in the *steam generator* : liquid water - water vapor flow) or the accidental operation (for instance : *Loss of Coolant Accident* [32] or *Reactivity Initiated Accident* [29]). *Vapor Explosion* arises as one of the multiphase flows that could take place in an accidental scenario. It happens in the case of a meltdown of the reactor core, where the *corium* (i.e. mixture of molten nuclear fuel, fission products, control rods, reactor vessel structure materials, etc.) gets in touch with liquid water used to cool down the reactor core. The contact between these two fluids is generally characterized by an intense and rapid heat transfer that leads to a strong evaporation of the liquid water. During the expansion of water vapor, pressure shock waves may be formed, which might damage the surrounding structures [5]. In view of this risk, the modeling and the numerical simulation of *Vapor Explosion* is a completely relevant and highly challenging task to undertake.

Many efforts have been devoted to the modeling and simulation of *Vapor Explosion*. This requires at least a three-phase flow model to account for the *corium* phase, the liquid water phase, and the water vapor phase. Some models consider more than three phases, this could be useful for instance to take into account the different gaseous phases or fission products (see for instance [27]). However, this kind of models generally suffers from typical mathematical short-comings, one of which is the loss of hyperbolicity, or the violation of energy conservation.

For the sake of the correct representation of shock and rarefaction waves, compressible multiphase flow models with hyperbolicity criterion and unique jump conditions are required. The hyperbolicity provides an assurance of the well-posedness of the initial-value problem, while the uniqueness of jump conditions is mandatory, for non conservative systems, otherwise computed shock patterns totally depend on the chosen scheme, which of course does not make sense (see [4, 22, 15]).

In the two-phase flow framework, Baer and Nunziato [3] proposed a rather appealing model that allows to describe the strong shock and rarefaction waves, and also the compressible effects, while preserving the hyperbolicity condition. This model has been studied in [11] and extended by A.K. Kapila et al. [26] and S. Gavrilyuk and R. Saurel [13] among others. Another category of models exists in the two-phase flow literature [10, 25], it consists of considering one pressure field for the two fluids, or in other words with instantaneous pressure equilibrium between all phases, but this approach does not ensure the preservation of the mathematical properties we mentioned above, namely the hyperbolicity and the existence and uniqueness of jump conditions.

In [18] an extension of Baer-Nunziato model to the three-phase flow framework was suggested. The main difficulty that arises is the description of what happens at the interface between the three phases. In fact, in the two-phase mixture there is only one interface velocity and one interface pressure that need to be defined, whereas in the three-phase mixture more

closure laws need to be introduced at the statistical interface. The paper [18] addresses the main modeling choices that allow to guarantee a relevant entropy inequality, and also the uniqueness of jump conditions. Other recent works have allowed to get more results considering the same class of two or three-phase flow models [28, 21, 17, 20].

In the present work, we consider the same class of three-phase flow model as in [18], and we especially take a deeper look at the source terms that account of the relaxation processes between the three phases. The present paper is organized as follows. In Section 2, we present the set of equations of the three phase flow model, as well as the different closure laws and the mathematical properties of the closed model. In this section, we also discuss the properties of the velocity and pressure relaxation processes. These two distinct relaxation effects indeed have a significant impact on the dynamics of the three-phase mixture. In Section 3, we focus on the discrete framework, the global resolution strategy actually consists of the fractional step method [19]. We give the details of the numerical scheme that was considered to take the convective subset into account, since the latter includes non conservative terms. We also present the numerical schemes for the relaxation effects. In Section 4, we present the different numerical results that consist of :

— Verification of the convective subset : pure convection test cases, which involve a Riemann problem ;

— Verification of the velocity and pressure relaxation subsets ;

— Validation of the whole solver on a shock tube apparatus [7, 8].

Six appendices devoted to technical details complete the whole.

2.2 Governing equations and main properties of the three-dimensional three-phase flow model

2.2.1 Governing equations

We consider the following system of partial differential equations for the modeling of a three-phase flow with two non miscible components (water, liquid metal), assuming that water may be present under two distinct states : liquid or vapor phase. For $k = 1, .., 3$ and $t > 0$:

$$\left\{ \begin{array}{l} \frac{\partial \alpha_k}{\partial t} + \mathbf{V}_i(\mathbf{W}).\nabla \alpha_k = S_k^{\alpha}(\mathbf{W}) \\ \frac{\partial m_k}{\partial t} + \nabla.(m_k \mathbf{U}_k) = 0 \\ \frac{\partial m_k \mathbf{U}_k}{\partial t} + \nabla.(m_k \mathbf{U}_k \otimes \mathbf{U}_k + \alpha_k p_k \mathbf{Id}) + \sum_{l=1, l\neq k}^{3} \Pi_{kl}(\mathbf{W}) \nabla \alpha_l = \mathbf{S}_k^U(\mathbf{W}) \\ \frac{\partial \alpha_k E_k}{\partial t} + \nabla.(\alpha_k E_k \mathbf{U}_k + \alpha_k p_k \mathbf{U}_k) - \sum_{l=1, l\neq k}^{3} \Pi_{kl}(\mathbf{W}) \frac{\partial \alpha_l}{\partial t} = S_k^E(\mathbf{W}) \end{array} \right. \tag{2.1}$$

The quantities $\alpha_k \in [0, 1]$, ρ_k, $m_k = \alpha_k \rho_k$, $\mathbf{U}_k$, p_k, $e_k(p_k, \rho_k)$ and E_k represent respectively the statistical fraction, the mean density, the partial mass, the mean velocity, the mean pressure, the mean internal energy and the mean total energy of phase k, $k = 1, 2, 3$, where :

$$E_k = \frac{1}{2} \rho_k \mathbf{U}_k.\mathbf{U}_k + \rho_k e_k(p_k, \rho_k) \tag{2.2}$$

Since the liquid water, water vapor and liquid metal are not miscible, we have the following constraint on statistical fractions :

$$\alpha_1 + \alpha_2 + \alpha_3 = 1 \tag{2.3}$$

The state variable $\mathbf{W} \in \mathbb{R}^{17}$ denotes the following vector :

$$\mathbf{W} = (\alpha_2, \alpha_3, m_1, m_2, m_3, m_1\mathbf{U}_1, m_2\mathbf{U}_2, m_3\mathbf{U}_3, \alpha_1 E_1, \alpha_2 E_2, \alpha_3 E_3)^t \tag{2.4}$$

The first and second equations of (2.1) give the evolution of statistical fractions and partial masses, while the third and fourth equation stand for the momentum balance and energy balance equations.

In this work, the interface velocity is defined by :

$$\mathbf{V}_i(\mathbf{W}) = \mathbf{U}_1 \tag{2.5}$$

Thus, following [18], the interface pressures are given by :

$$\begin{cases} \Pi_{12}(\mathbf{W}) = \Pi_{21}(\mathbf{W}) = \Pi_{23}(\mathbf{W}) = p_2 \\ \Pi_{13}(\mathbf{W}) = \Pi_{31}(\mathbf{W}) = \Pi_{32}(\mathbf{W}) = p_3 \end{cases} \tag{2.6}$$

Remark 1 :
The choice made in (2.5) *is not unique. In fact, an other possibility consists of considering* $\boldsymbol{V}_i(\boldsymbol{W})$ *as a convex combination of velocities* $\boldsymbol{U}_k$, $k = 1, 2, 3$ *:*

$$\boldsymbol{V}_i(\boldsymbol{W}) = \sum_{k=1}^{3} m_k \boldsymbol{U}_k / \sum_{k=1}^{3} m_k$$

This leads to a different set of interface pressures $\Pi_{kl}(\boldsymbol{W})$ *which is uniquely defined, and in agreement with the entropy inequality (see paragraph 2.2.2.1 and Appendix G of [18]).* □

Source terms should be such that :

$$\sum_{k=1}^{3} S_k^{\alpha}(\mathbf{W}) = \sum_{k=1}^{3} S_k^{E}(\mathbf{W}) = 0$$

and :

$$\sum_{k=1}^{3} \mathbf{S}_k^{U}(\mathbf{W}) = \mathbf{0}$$

since they only take into account the internal transfers between phases.

Closure laws to account for pressure-relaxation effects are chosen as :

$$S_k^{\alpha}(\mathbf{W}) = \sum_{l=1, l\neq k}^{3} \frac{\alpha_k \alpha_l}{\tau_{kl}^{P}(\mathbf{W})\Pi_0}(p_k - p_l) \tag{2.7}$$

where, for $k, l \in \{1, 2, 3\}$, the symmetric positive function $\tau_{kl}^P(\mathbf{W}) = \tau_{lk}^P(\mathbf{W})$ represents the pressure-relaxation time scale between phases k and l, it will be taken from [12], and Π_0 is a positive reference pressure.

Moreover, for drag effects we will rely on standard closures of the form :

$$\mathbf{S}_k^U(\mathbf{W}) = \sum_{l=1, l\neq k}^{3} \mathbf{D}_{kl}(\mathbf{W}) \tag{2.8}$$

where :

$$\mathbf{D}_{kl}(\mathbf{W}) = e_{kl}(\mathbf{W})(\mathbf{U}_l - \mathbf{U}_k) \tag{2.9}$$

and the symmetric positive functions $e_{kl}(\mathbf{W}) = e_{lk}(\mathbf{W})$ involve the velocity-relaxation time scales, which are chosen in agreement with the two-phase flow literature [25].

The contribution of velocity relaxation terms to the energy balance is such that :

$$S_k^E(\mathbf{W}) = \sum_{l=1, l\neq k}^{3} \mathbf{V}_{kl}(\mathbf{W}).\mathbf{D}_{kl}(\mathbf{W}) + \sum_{l=1, l\neq k}^{3} \psi_{kl} \tag{2.10}$$

where :

$$\mathbf{V}_{kl} = \frac{1}{2}(\mathbf{U}_k + \mathbf{U}_l) \tag{2.11}$$

and ψ_{kl}, which accounts for the heat transfer between phases k and l, will be defined in the next paragraph (2.2.2.1), in order to comply with the entropy inequality.

2.2.2 Main properties of the three-phase flow model

2.2.2.1 Entropy

We set the following notations :

$$(c_k(p_k, \rho_k))^2 = \left(\frac{p_k}{\rho_k^2} - \frac{\partial e_k(p_k, \rho_k)}{\partial \rho_k}\right)\left(\frac{\partial e_k(p_k, \rho_k)}{\partial p_k}\right)^{-1} \tag{2.12}$$

$$a_k = \left(\frac{\partial s_k(p_k, \rho_k)}{\partial p_k}\right)\left(\frac{\partial e_k(p_k, \rho_k)}{\partial p_k}\right)^{-1} \tag{2.13}$$

We assume $a_k > 0$, and we define $s_k(p_k, \rho_k)$, the specific entropy of phase k, such that :

$$c_k^2 \frac{\partial s_k(p_k, \rho_k)}{\partial p_k} + \frac{\partial s_k(p_k, \rho_k)}{\partial \rho_k} = 0 \tag{2.14}$$

We define also $\eta(\mathbf{W})$, the mixture entropy, and $\mathbf{F}_\eta(\mathbf{W})$, the mixture entropy flux, such that :

$$\begin{cases} \eta(\mathbf{W}) = -\sum_{k=1}^{3} m_k Log(s_k) \\ \mathbf{F}_\eta(\mathbf{W}) = -\sum_{k=1}^{3} m_k Log(s_k)\mathbf{U}_k \end{cases} \tag{2.15}$$

Finally, we consider the following closure of the heat transfer term ψ_{kl} :

$$\psi_{kl} = \frac{a_k - a_l}{\tau^{\psi}_{kl}\kappa_0} \tag{2.16}$$

where the positive function $\tau^{\psi}_{kl} = \tau^{\psi}_{lk}$ is the characteristic time of heat transfer between phases k and l, and κ_0 a positive constant.

Property 1 :

Considering closure laws (2.5-2.11) and (2.16)*, the following entropy inequality holds for smooth solutions of system* (2.1) *:*

$$\frac{\partial \eta(\mathbf{W})}{\partial t} + \nabla.\mathbf{F}_{\eta}(\mathbf{W}) \leq 0 \tag{2.17}$$

Proof :

For regular solutions of the system (2.1), the governing equation of $\eta(\mathbf{W})$ reads :

$$\begin{aligned} \frac{\partial \eta(\mathbf{W})}{\partial t} + \nabla.\mathbf{F}_{\eta}(\mathbf{W}) = &- \sum_{k=1}^{3} a_k \left(p_k S^{\alpha}_k(\mathbf{W}) + \sum_{l \neq k} \Pi_{kl}(\mathbf{W}) S^{\alpha}_l(\mathbf{W}) \right) \\ &- \sum_{k=1}^{3} a_k \left(S^{E}_k(\mathbf{W}) - \mathbf{U}_k.\mathbf{S}^{U}_k(\mathbf{W}) \right) \end{aligned} \tag{2.18}$$

Now, on the basis of the interface pressure definitions (2.6) and the closure laws presented in (2.7), (2.8), (2.9), (2.10), (2.11), and (2.16), a straightforward calculus provides :

$$\begin{aligned} \sum_{k=1}^{3} a_k \left(p_k S^{\alpha}_k(\mathbf{W}) + \sum_{l \neq k} \Pi_{kl}(\mathbf{W}) S^{\alpha}_l(\mathbf{W}) \right) =& a_1 \sum_{k=1}^{3} p_k S^{\alpha}_k(\mathbf{W}) \\ =& a_1 \sum_{k,l=1,k\neq l}^{3} \frac{\alpha_k \alpha_l}{\tau^{P}_{kl}\Pi_0} (p_k - p_l)^2 \end{aligned} \tag{2.19}$$

and :

$$\begin{aligned} \sum_{k=1}^{3} a_k \left(S^{E}_k(\mathbf{W}) - \mathbf{U}_k.\mathbf{S}^{U}_k(\mathbf{W}) \right) =& \sum_{k=1}^{3} \left[a_k \sum_{l \neq k} \left(\mathbf{V}_{kl}(\mathbf{W}).\mathbf{D}_{kl}(\mathbf{W}) - \mathbf{U}_k.\mathbf{D}_{kl}(\mathbf{W}) \right) \right] \\ &+ \sum_{k=1}^{3} a_k \sum_{l \neq k} \psi_{kl} \\ =& \frac{1}{2} \sum_{k=1}^{3} \left[a_k \sum_{l \neq k} e_{kl}(\mathbf{W}) (\mathbf{U}_l - \mathbf{U}_k)^2 \right] \\ &+ \sum_{1 \leq l < k \leq 3}^{3} \frac{(a_k - a_l)^2}{\tau^{\psi}_{kl}\kappa_0} \end{aligned} \tag{2.20}$$

It obviously follows that the regular solutions of system (2.1) comply with the inequality (2.17). □

We also note that the right-hand side of (2.18) vanishes as soon as pressure, velocity and temperature equilibria are reached.

2.2.2.2 Hyperbolicity and structure of fields

We focus here on the convective subset -left hand side- of (2.1). Let $\mathbf{n}$ be a unit vector, and τ_1,τ_2 such that $(\mathbf{n}, \tau_1, \tau_2)$ defines an orthonormal basis of the $3D$ space. Considering the invariance of equations (2.1) under frame rotation, and neglecting transverse derivatives of all components, the associated one-dimensional problem in the $\mathbf{n}$ direction writes :

$$\left\{\begin{array}{l} \partial_t \alpha_k + (\mathbf{U}_1.\mathbf{n})\partial_{x_n}\alpha_k = 0 \\ \partial_t m_k + \partial_{x_n}(m_k(\mathbf{U}_k.\mathbf{n})) = 0 \\ \partial_t(m_k(\mathbf{U}_k.\mathbf{n})) + \partial_{x_n}(m_k(\mathbf{U}_k.\mathbf{n})^2 + \alpha_k p_k) + \sum_{l=1,l\neq k}^{3} \Pi_{kl}(\mathbf{W})\partial_{x_n}\alpha_l = 0 \\ \partial_t(\alpha_k E_k) + \partial_{x_n}(\alpha_k(E_k + p_k)(\mathbf{U}_k.\mathbf{n})) - \sum_{l=1,l\neq k}^{3} \Pi_{kl}(\mathbf{W})\partial_t\alpha_l = 0 \\ \partial_t(m_k(\mathbf{U}_k.\tau_1)) + \partial_{x_n}(m_k(\mathbf{U}_k.\mathbf{n})(\mathbf{U}_k.\tau_1)) = 0 \\ \partial_t(m_k(\mathbf{U}_k.\tau_2)) + \partial_{x_n}(m_k(\mathbf{U}_k.\mathbf{n})(\mathbf{U}_k.\tau_2)) = 0 \end{array}\right. \tag{2.21}$$

Property 2 :
2.1 The system (2.21) *admits the following real eigenvalues :*

$$\begin{array}{c} \lambda_{1,2,3,4,5}(\mathbf{W}) = \mathbf{U}_1.\mathbf{n}\ ;\ \lambda_{6,7,8}(\mathbf{W}) = \mathbf{U}_2.\mathbf{n}\ ;\ \lambda_{9,10,11}(\mathbf{W}) = \mathbf{U}_3.\mathbf{n} \\ \lambda_{12,13}(\mathbf{W}) = \mathbf{U}_1.\mathbf{n} \pm c_1\ ;\ \lambda_{14,15}(\mathbf{W}) = \mathbf{U}_2.\mathbf{n} \pm c_2\ ;\ \lambda_{16,17}(\mathbf{W}) = \mathbf{U}_3.\mathbf{n} \pm c_3 \end{array} \tag{2.22}$$

Associated right eigenvectors span the whole space $\mathbb{R}^{17}$ *if :*

$$(\mathbf{U}_1 - \mathbf{U}_k).\mathbf{n} \neq \pm c_k \tag{2.23}$$

2.2 Fields λ_k *for* $k \in 1,..,11$ *are Linearly Degenerated ; other fields are Genuinely Non Linear.*

Proof :
For smooth solutions the system (2.21) can be written as :

$$\partial_t \mathbf{Z} + A(\mathbf{Z})\partial_{x_n}\mathbf{Z} = 0 \tag{2.24}$$

The computation of eigenvalues of the matrix A is rather easy when choosing the variable :

$$\begin{array}{rl} \mathbf{Z} = (\alpha_2, \alpha_3, s_1, s_2, s_3, & \mathbf{U}_1.\mathbf{n}, \mathbf{U}_1.\tau_1, \mathbf{U}_1.\tau_2, \\ & \mathbf{U}_2.\mathbf{n}, \mathbf{U}_2.\tau_1, \mathbf{U}_2.\tau_2, \\ & \mathbf{U}_3.\mathbf{n}, \mathbf{U}_3.\tau_1, \mathbf{U}_3.\tau_2, p_1, p_2, p_3)^t \end{array} \tag{2.25}$$

(See more detailed calculations in the one-dimensional framework in [18] Appendix A).

We also check that : $\frac{\partial \lambda_k(\mathbf{Z})}{\partial \mathbf{Z}}.\mathbf{r}_k(\mathbf{Z}) = 0$ for $k \in 1,..,11$, and $\frac{\partial \lambda_k(\mathbf{Z})}{\partial \mathbf{Z}}.\mathbf{r}_k(\mathbf{Z}) \neq 0$ otherwise. □

2.2.2.3 Additional properties in the one-dimensional framework

We consider a pure one-dimensional problem, thus system (2.21) can be written as :

$$\left\{\begin{array}{l} \partial_t \alpha_k + u_1\partial_x\alpha_k = 0 \\ \partial_t m_k + \partial_{x_n}(m_k u_k) = 0 \\ \partial_t(m_k u_k) + \partial_x(m_k u_k^2 + \alpha_k p_k) + \sum_{l=1,l\neq k}^{3} \Pi_{kl}(\mathbf{w})\partial_x\alpha_l = 0 \\ \partial_t(\alpha_k E_k) + \partial_{x_n}(\alpha_k(E_k + p_k)u_k) - \sum_{l=1,l\neq k}^{3} \Pi_{kl}(\mathbf{w})\partial_t\alpha_l = 0 \end{array}\right. \tag{2.26}$$

where the $1D$ state variable is denoted $\mathbf{w} \in \mathbb{R}^{11}$:

$$\mathbf{w} = (\alpha_2, \alpha_3, m_1, m_2, m_3, m_1u_1, m_2u_2, m_3u_3, \alpha_1E_1, \alpha_2E_2, \alpha_3E_3)^t \tag{2.27}$$

Property 3 :

— *The convective system* (2.26) *admits eleven real eigenvalues which read :*

$$\begin{array}{c} \lambda_{1,2,3}(\mathbf{w}) = u_1 \ ; \ \lambda_4(\mathbf{w}) = u_2 \ ; \ \lambda_5(\mathbf{w}) = u_3 \\ \lambda_{6,7}(\mathbf{w}) = u_1 \pm c_1 \ ; \ \lambda_{8,9}(\mathbf{w}) = u_2 \pm c_2 \ ; \ \lambda_{10,11}(\mathbf{w}) = u_3 \pm c_3 \end{array} \tag{2.28}$$

The field associated with $\lambda_k(\mathbf{w})$ for $k \in \{1, .., 5\}$ is Linearly Degenerated, while fields associated with $\lambda_{6-11}(\mathbf{w})$ are Genuinely Non Linear.

— *Regarding the 1D Riemann problem associated with* (2.26)*, the LD field $\lambda_{1,2,3}(\mathbf{w})$ admits the following eight Riemann invariants :*

$$\begin{array}{c} I^1_{1,2,3}(\mathbf{w}) = m_2(u_2 - u_1) \quad ; \quad I^2_{1,2,3}(\mathbf{w}) = m_3(u_3 - u_1) \\ I^3_{1,2,3}(\mathbf{w}) = s_2 \quad ; \quad I^4_{1,2,3}(\mathbf{w}) = s_3 \quad ; \quad I^5_{1,2,3}(\mathbf{w}) = u_1 \\ I^6_{1,2,3}(\mathbf{w}) = \sum_{k=1}^3 \alpha_k p_k + m_2(u_2 - u_1)^2 + m_3(u_3 - u_1)^2 \\ I^7_{1,2,3}(\mathbf{w}) = e_2 + \frac{p_2}{\rho_2} + \frac{1}{2}(u_2 - u_1)^2 \ ; \ I^8_{1,2,3}(\mathbf{w}) = e_3 + \frac{p_3}{\rho_3} + \frac{1}{2}(u_3 - u_1)^2 \end{array} \tag{2.29}$$

— *We note $\Delta(\phi) = \phi_r - \phi_l$. For each isolated GNL wave, the following exact jump conditions hold for phase index $k = 1, 2, 3$, through any discontinuity separating states l, r and moving with speed σ :*

$$\left\{ \begin{array}{l} \Delta(\alpha_k) = 0 \\ \Delta(\rho_k(u_k - \sigma)) = 0 \\ \Delta(\rho_k u_k(u_k - \sigma) + p_k) = 0 \\ \Delta(E_k(u_k - \sigma) + p_k u_k) = 0 \end{array} \right. \tag{2.30}$$

Proof :
The proof of these properties is classical and left to the reader. □

The latter Riemann invariants and jump conditions are particularly important because they will enable us to build exact solutions of the $1D$ Riemann problem for the system (2.26), and verify the convergence of algorithms (see paragraph 2.4.1). We mention that these properties are the exact counterpart of the two-phase Baer-Nunziato model [3].

2.2.2.4 Admissibility of thermodynamic quantities

In this subsection, we study the admissibility of thermodynamic variables in the one-dimensional framework. We consider smooth solutions of the system (2.26), and we make the following assumptions :

Assumption 1 :

For $k = 1, 2, 3$ we assume admissible initial and boundary conditions, i.e. :

$$\forall x \in \Omega : \left\{ \begin{array}{l} 0 \leq \alpha_k(x,0) \\ 0 \leq m_k(x,0) \\ 0 \leq s_k(x,0) \end{array} \right. \quad and \quad \forall t \in [0,T] : \left\{ \begin{array}{l} 0 \leq \alpha_k(x_\Gamma,t) \\ 0 \leq m_k(x_\Gamma,t) \\ 0 \leq s_k(x_\Gamma,t) \end{array} \right. \tag{2.31}$$

where Γ denotes the boundary of the domain Ω, and T is the simulation final time.

Assumption 2 :
We also assume that functions a_k (defined in (2.13)), u_k and $\frac{\partial u_k}{\partial x}$ remain in $L^\infty(\Omega \times [0,T])$.

We have then the following result :

Property 4 :
The regular solutions of the system (2.26) *are consistent with the physical requirements :*

$$\forall (x,t) \in (\Omega \times [0,T]) : \left\{ \begin{array}{l} 0 \leq \alpha_k(x,t) \\ 0 \leq m_k(x,t) \\ 0 \leq s_k(x,t) \end{array} \right. \tag{2.32}$$

Proof :
It is classical, and based on building the evolution equations of the α_k, m_k and s_k as smooth solutions of the system (2.26) (See [18] for some more details).□

We can prove that a similar admissibility result holds for pressure variables p_k, when we consider the specific case of Stiffened Gas equations of state (EOS). In that case, for each phase $k = 1, 2, 3$:

$$p_k + \gamma_k \Pi_k = (\gamma_k - 1)\rho_k e_k \tag{2.33}$$

where $\gamma_k > 1$ and $\Pi_k > 0$ are thermodynamic constants of phase k. We denote also :

$$\mathcal{P}_k = \alpha_k(p_k + \Pi_k)/(\gamma_k - 1) \tag{2.34}$$

For regular solutions of the system (2.26), the evolution equations of $\mathcal{P}_k$ read :

$$\left\{ \begin{array}{l} \partial_t \mathcal{P}_1 + \partial_x(u_1 \mathcal{P}_1) + (\gamma_1 - 1)\mathcal{P}_1 \partial_x u_1 = 0 \\ \partial_t \mathcal{P}_2 + \partial_x(u_2 \mathcal{P}_2) + (\gamma_2 - 1)\mathcal{P}_2(\partial_x u_2 + (u_2 - u_1)\partial_x Log(\alpha_2)) = 0 \\ \partial_t \mathcal{P}_3 + \partial_x(u_3 \mathcal{P}_3) + (\gamma_3 - 1)\mathcal{P}_3(\partial_x u_3 + (u_3 - u_1)\partial_x Log(\alpha_3)) = 0 \end{array} \right. \tag{2.35}$$

Based on the same type of arguments as those invoked in the proof of **Property 4**, we conclude that $\forall (x,t) \in (\Omega \times [0,T]) : 0 \leq \mathcal{P}_k(x,t)$, provided that, in addition, $(u_k - u_1)\partial_x Log(\alpha_k))$ remains bounded.

Of course, the latter results can easily be extended to the $3D$ framework.

2.2.2.5 Velocity relaxation

In this subsection, we focus on the relaxation mechanisms embedded in our PDE system. More particularly, we study what happens in a continuous framework, considering an homogeneous flow such that the spatial derivatives are null. Thus, only time derivatives and source terms are taken into account. The studied system is :

$$\begin{cases} \partial_t \alpha_k = S_k^{\alpha}(\mathbf{W}) \\ \partial_t m_k = 0 \\ \partial_t (m_k \mathbf{U}_k) = \mathbf{S}_k^{U}(\mathbf{W}) \\ \partial_t (\alpha_k E_k) - \sum_{l=1, l\neq k}^{3} \Pi_{kl}(\mathbf{W}) \frac{\partial \alpha_l}{\partial t} = S_k^{E}(\mathbf{W}) \end{cases} \tag{2.36}$$

The system (2.36) is itself split into two subsystems, in order to study separately the velocity relaxation, and the pressure relaxation. In this paragraph, we study the velocity relaxation effects, the corresponding PDE system is obtained from (2.36) by considering only the velocity-related source terms. The velocity relaxation system then writes :

$$\begin{cases} \partial_t \alpha_k = 0 & \text{(2.37a)} \\ \partial_t m_k = 0 & \text{(2.37b)} \\ \partial_t (m_k \mathbf{U}_k) = \sum_{l=1, l\neq k}^{3} \mathbf{D}_{kl}(\mathbf{W}) & \text{(2.37c)} \\ \partial_t (\alpha_k E_k) = \sum_{l=1, l\neq k}^{3} \mathbf{V}_{kl}(\mathbf{W}).\mathbf{D}_{kl}(\mathbf{W}) & \text{(2.37d)} \end{cases}$$

We have the following noteworthy property :

Property 5 :
The velocity relaxation step is consistent with the admissibility of the internal energy, i.e. this step keeps the internal energy e_k in the admissible range.

Proof :
Starting with : $\alpha_k E_k = m_k e_k + \frac{1}{2} m_k \mathbf{U}_k^2$, using the closures (2.9) - (2.11) and combining (2.37c) - (2.37d) we obtain :

$$m_k \partial_t e_k = \frac{1}{2} \sum_{l=1, l\neq k}^{3} e_{kl}(\mathbf{W})(\mathbf{U}_l - \mathbf{U}_k)^2 \geq 0 \tag{2.38}$$

This means that the internal energy is non-decreasing, regardless of the chosen EOS.□

Thus, the integration method we adopt consists, first, of obtaining the velocity variation over time, and then using the result to update the energy. The velocity variation over time is obtained by studying the velocity differences, as shown in what follows.

Let $(\mathbf{n}, \tau_1, \tau_2)$ be an orthonormal basis of the $3D$ space. If we set $X_{12}^{\mathbf{n}} = \mathbf{U}_1.\mathbf{n} - \mathbf{U}_2.\mathbf{n}$, $X_{13}^{\mathbf{n}} = \mathbf{U}_1.\mathbf{n} - \mathbf{U}_3.\mathbf{n}$, and $\mathbf{X}^{\mathbf{n}} = (X_{12}^{\mathbf{n}}, X_{13}^{\mathbf{n}})^t$, the momentum equation of (2.37) could be

written as :

$$\partial_t \mathbf{X^n} = -A(\mathbf{W})\mathbf{X^n} \tag{2.39}$$

where :

$$A(\mathbf{W}) = \begin{pmatrix} a_{11} & a_{12} \\ a_{21} & a_{22} \end{pmatrix} \tag{2.40a}$$

$$\begin{cases} a_{11} = e_{12}(\frac{1}{m_1} + \frac{1}{m_2}) + \frac{e_{23}}{m_2} \\ a_{12} = \frac{e_{13}}{m_1} - \frac{e_{23}}{m_2} \\ a_{21} = \frac{e_{12}}{m_1} - \frac{e_{23}}{m_3} \\ a_{22} = e_{13}(\frac{1}{m_1} + \frac{1}{m_3}) + \frac{e_{23}}{m_3} \end{cases} \tag{2.40b}$$

A similar result stands for $\mathbf{X}^{\tau_1}$ and $\mathbf{X}^{\tau_2}$, when considering the normal velocities in the directions τ_1 and τ_2, with the same matrix $A(\mathbf{W})$. This comes from the structure of (2.37c), which remains unchanged regardless of the projection direction.

This velocity variation mechanism (2.39) is identical to what happens in the barotropic framework, which has been studied in a previous work [6]. Equation (2.39) gives then the evolution of velocity differences, the total kinetic energy conservation allows, *formally* also, to retrieve the variation over time of velocities $\mathbf{U}_k$.

Details are given in the numerical scheme subsection 2.3.3.1.

2.2.2.6 Pressure relaxation

In this paragraph, we focus on the pressure relaxation effects. The concerned PDE system, extracted from (2.36), writes :

$$\begin{cases} \partial_t \alpha_k = S_k^{\alpha}(\mathbf{W}) & \text{(2.41a)} \\ \partial_t m_k = 0 & \text{(2.41b)} \\ \partial_t (m_k \mathbf{U}_k) = \mathbf{0} & \text{(2.41c)} \\ \partial_t (\alpha_k E_k) - \sum_{l=1, l\neq k}^{3} \Pi_{kl}(\mathbf{W}) \partial_t \alpha_l = 0 & \text{(2.41d)} \end{cases}$$

In order to understand the underlying relaxation mechanism, we study, in this sub-step, the evolution of the pressure differences. To do so, we define the following notations :

— The coefficients : $A_k = \frac{\rho_k c_k^2}{\alpha_k}$ and $b_1 = \frac{1}{\rho_1}\left(\frac{\partial e_1}{\partial p_1}\right)^{-1}$;

— The pressure differences : $y_{12} = p_1 - p_2$, $y_{13} = p_1 - p_3$, $y_{23} = -y_{32} = y_{13} - y_{12}$ and $\mathbf{Y} = (y_{12}, y_{13})^t$.

We have the following result :

Property 6 :
The evolution of the pressure differences writes :

$$\partial_t \mathbf{Y} = -\frac{1}{\Pi_0} B(\mathbf{W})\mathbf{Y} \tag{2.42}$$

where the matrix $B(\mathbf{W}) = \begin{pmatrix} b_{11} & b_{12} \\ b_{21} & b_{22} \end{pmatrix}$ *is given by :*

$$\left\{ \begin{array}{l} b_{11} = \left(A_1 + A_2 - \frac{b_1}{\alpha_1} y_{12}\right) \frac{\alpha_1\alpha_2}{\tau_{12}} + \left(A_2 - \frac{b_1}{\alpha_1} y_{32}\right) \frac{\alpha_2\alpha_3}{\tau_{23}} \\ b_{12} = \left(A_1 - \frac{b_1}{\alpha_1} y_{13}\right) \frac{\alpha_1\alpha_3}{\tau_{13}} - \left(A_2 - \frac{b_1}{\alpha_1} y_{32}\right) \frac{\alpha_2\alpha_3}{\tau_{23}} \\ b_{21} = \left(A_1 - \frac{b_1}{\alpha_1} y_{12}\right) \frac{\alpha_1\alpha_2}{\tau_{12}} - \left(A_3 - \frac{b_1}{\alpha_1} y_{23}\right) \frac{\alpha_2\alpha_3}{\tau_{23}} \\ b_{22} = \left(A_1 + A_3 - \frac{b_1}{\alpha_1} y_{13}\right) \frac{\alpha_1\alpha_3}{\tau_{13}} + \left(A_3 - \frac{b_1}{\alpha_1} y_{23}\right) \frac{\alpha_2\alpha_3}{\tau_{23}} \end{array} \right. \tag{2.43}$$

Proof :
On the one hand, equation (2.41b) yields :

$$\partial_t \rho_k = -\frac{\rho_k}{\alpha_k} \partial_t \alpha_k = -\frac{\rho_k}{\alpha_k} S_k^\alpha(\mathbf{W})$$

On the other hand, combining (2.41c) and (2.41d) gives :

$$m_k \partial_t e_k = \sum_{l=1, l\neq k}^{3} \Pi_{kl}(\mathbf{W}) \partial_t \alpha_l = \sum_{l=1, l\neq k}^{3} \Pi_{kl}(\mathbf{W}) S_l^\alpha(\mathbf{W})$$

Knowing that $\partial_t e_k = \frac{\partial e_k}{\partial p_k} \partial_t p_k + \frac{\partial e_k}{\partial \rho_k} \partial_t \rho_k$, we can write :

$$\frac{\partial e_k}{\partial p_k} \partial_t p_k + \frac{\partial e_k}{\partial \rho_k} \partial_t \rho_k = \frac{1}{m_k} \sum_{l=1, l\neq k}^{3} \Pi_{kl}(\mathbf{W}) S_l^\alpha(\mathbf{W})$$

By using the evolution equation of ρ_k above we get :

$$\partial_t p_k = \left(\frac{\partial e_k}{\partial p_k}\right)^{-1} \left[\frac{1}{m_k} \sum_{l=1, l\neq k}^{3} \Pi_{kl}(\mathbf{W}) S_l^\alpha(\mathbf{W}) + \frac{\rho_k}{\alpha_k} \frac{\partial e_k}{\partial \rho_k} S_k^\alpha(\mathbf{W}) \right]$$

By expliciting the interface pressures $\Pi_{kl}(\mathbf{W})$, given in (3.10), we obtain :

$$\left\{ \begin{array}{l} \partial_t p_1 = -A_1 S_1^\alpha(\mathbf{W}) + \frac{b_1}{\alpha_1} \sum_{k=1}^{3} p_k S_k^\alpha(\mathbf{W}) \\ \partial_t p_2 = -A_2 S_2^\alpha(\mathbf{W}) \\ \partial_t p_3 = -A_3 S_3^\alpha(\mathbf{W}) \end{array} \right.$$

Finally, a straightforward, though cumbersome, calculation gives (2.42) and (2.43), using the closure of $S_k^\alpha(\mathbf{W})$ given in (2.7).□

Remark 2 :
The matrix $B(\boldsymbol{W})$ *defined in* (2.42)-(2.43) *depends in particular of the pressure differences themselves. Actually, as shown in* (2.43)*, each coefficient of* $B(\boldsymbol{W})$ *contains a first degree polynomial wrt* $\boldsymbol{Y}$*. Thus, a threshold effect may arise, as detailed in Appendix 2 while focusing on two-phase flows. We emphasize that this effect does not exist in the barotropic framework.*

Turning to the three-phase flow model (2.1)*, a necessary condition to be verified for initial conditions is that the trace of* $B(\boldsymbol{W})$ *should be strictly positive (whatever* $B(\boldsymbol{W})$ *admits real or complex eigenvalues). Otherwise the return to the pressure equilibrium cannot be guaranteed.*

Since the trance of B reads :

$$\begin{aligned} tr(B(\mathbf{W})) = b_{11} + b_{22} = & \frac{1}{\tau_{12}^P \Pi_0} \left(\alpha_2 \rho_1 c_1^2 + \alpha_1 \rho_2 c_2^2 - \alpha_2 b_1 y_{12} \right) \\ & + \frac{1}{\tau_{13}^P \Pi_0} \left(\alpha_3 \rho_1 c_1^2 + \alpha_1 \rho_3 c_3^2 - \alpha_3 b_1 y_{13} \right) \\ & + \frac{1}{\tau_{23}^P \Pi_0} \left(\alpha_2 \rho_3 c_3^2 + \alpha_3 \rho_2 c_2^2 \right) \end{aligned}$$

We may set :

$$|y| = max(|y_{12}|, |y_{13}|)$$

Hence, a sufficient condition on $|y|$ to ensure a positive trace will be :

$$|y| < \left[\frac{1}{b_1} \left(\frac{\alpha_2}{\tau_{12}^P} + \frac{\alpha_3}{\tau_{13}^P} \right)^{-1} \left(\sum_{k<l} \frac{1}{\tau_{kl}^P} (\alpha_k \rho_l c_l^2 + \alpha_l \rho_k c_k^2) \right) \right] (t = 0) \tag{2.44}$$

Eventually, when assuming vanishing phase $k = 3$, this allows to retrieve the result of Appendix 2 for two-phase flows.

Moreover, as emphasized in [6], stable oscillations wrt time may occur in three-phase flow models, owing to the structure of $B(\boldsymbol{W})$.$\square$

From a practical point of view, the **Property 6** allows to retrieve the pressure differences, yet this is not sufficient to fully compute the pressure relaxation step. For this purpose, we need to define the evolution equations through the pressure relaxation step for more variables :

Property 7 :

In the pressure relaxation step (2.41)*, we have :*

— *The specific entropies evolution is governed by :*

$$\begin{cases} \partial_t s_1 = \frac{a_1}{m_1} \sum_{k=1}^3 p_k S_k^\alpha(\mathbf{W}) \\ \partial_t s_2 = 0 \\ \partial_t s_3 = 0 \end{cases} \tag{2.45}$$

and specific entropies s_k remain in the admissible range.

— *We set $\Pi = \alpha_1 \alpha_2 \alpha_3$, $\delta_{kl} = \alpha_k \alpha_l$, we have :*

$$\begin{cases} \partial_t \Pi = (a(\alpha_2 - \alpha_1) + b(\alpha_3 - \alpha_2) + c(\alpha_1 - \alpha_3))\, \Pi \\ \partial_t \delta_{12} = (a(\alpha_2 - \alpha_1) + (b - c)\alpha_3)\, \delta_{12} \\ \partial_t \delta_{13} = (c(\alpha_1 - \alpha_3) + (a - b)\alpha_2)\, \delta_{13} \\ \partial_t \delta_{23} = (b(\alpha_3 - \alpha_2) + (c - a)\alpha_1)\, \delta_{23} \end{cases} \tag{2.46}$$

where : $a = \frac{p_1 - p_2}{\tau_{12}^P \Pi_0}$ $b = \frac{p_2 - p_3}{\tau_{23}^P \Pi_0}$ $c = \frac{p_3 - p_1}{\tau_{13}^P \Pi_0}$.

Sketch of proof :

We have : $s_k = s_k(p_k, \rho_k)$, this gives : $\partial_t s_k = \frac{\partial s_k}{\partial p_k}\partial_t p_k + \frac{\partial s_k}{\partial \rho_k}\partial_t \rho_k$. We use then the evolution equations of p_k and ρ_k to obtain the result (2.45).

Assuming that the initial data is admissible, it is obvious that s_2 and s_3 are in the admissible range. For s_1, we use (2.7) and get :

$$\partial_t s_1 = \frac{a_1}{m_1} \sum_{1 \leq l < k \leq 3} \frac{\alpha_k \alpha_l}{\tau_{kl}^P \Pi_0} (p_k - p_l)^2 \geq 0$$

s_1 is then, as well, admissible. Eventually, (2.46) is obtained from (2.41a), through direct computations. □

Therefore, numerical schemes is built in order to preserve the previous properties, more details are given in the numerical scheme subsection 2.3.3.2.

As shown in the subsection 2.2.2.1, an entropy inequality exists for the global PDE system (2.1). It is notable that a similar entropy result holds for each one of the studied subsystems, namely :

— *the convective subsystem* (2.21) *;*

— *the velocity relaxation subsystem* (2.37) *;*

— *the pressure relaxation subsystem* (2.41)*.*

Moreover, each one of the subsystems (2.37) and (2.41) guarantees the conservation of the mass, the total momentum and the total energy. This conservation is a substantial point of the relaxation processes, and will be used to build the approximation algorithms detailed in the next section.

The heat transfer, represented by the terms ψ_{kl}, is not considered in the applications of the present chapter.

2.3 Numerical method

We consider a classical Finite Volume formulation, where the computational domain is meshed using unstructured $3D$ cells denoted Ω_i, the volume of which is denoted ω_i. S_{ij} stands for the surface of the interface between cells Ω_i and Ω_j, $\mathbf{n}_{ij}$ is the normal vector pointing from Ω_i towards Ω_j. We define Δt_n the time step such that : $t_{n+1} = t_n + \Delta t_n$.

2.3.1 Fractional step method

In the spirit of [19], the time scheme is the following :

— **Step 1 : Evolution step**

For a given initial condition $\mathbf{W}_i^n$ we compute an approximate solution of $\mathbf{W}$ at time t_{n+1}, namely $\mathbf{W}_i^{n+1,-}$, by solving the homogeneous part of the system (2.1) :

$$\left\{\begin{array}{l} \frac{\partial \alpha_k}{\partial t} + \mathbf{V}_i(\mathbf{W}).\nabla \alpha_k = 0 \\ \frac{\partial m_k}{\partial t} + \nabla.(m_k \mathbf{U}_k) = 0 \\ \frac{\partial m_k \mathbf{U}_k}{\partial t} + \nabla.(m_k \mathbf{U}_k \otimes \mathbf{U}_k + \alpha_k p_k \mathbf{Id}) + \sum_{l=1,l\neq k}^{3} \Pi_{kl}(\mathbf{W}) \nabla \alpha_l = \mathbf{0} \\ \frac{\partial \alpha_k E_k}{\partial t} + \nabla.(\alpha_k E_k \mathbf{U}_k + \alpha_k p_k \mathbf{U}_k) + \mathbf{V}_i(\mathbf{W}). \sum_{l=1,l\neq k}^{3} \Pi_{kl}(\mathbf{W}) \nabla \alpha_l = 0 \end{array}\right. \tag{2.47}$$

— **Step 2 : Relaxation step**

Taking $\mathbf{W}_i^{n+1,-}$ as initial data, we compute $\mathbf{W}_i^{n+1}$ an approximate solution of the subsystem (2.36).

2.3.2 Computing the evolution step

The scheme we consider in order to compute the evolution step is the Rusanov scheme [30]. Thus, at each interface i, j separating cells Ω_i and Ω_j we define the numerical normal fluxes :

$$\left\{\begin{array}{l} \mathcal{F}_n^{\alpha_k}(\mathbf{W}, \mathbf{n}_{ij}) = 0 \\ \mathcal{F}_n^{m_k}(\mathbf{W}, \mathbf{n}_{ij}) = m_k \mathbf{U}_k.\mathbf{n}_{ij} \\ \mathcal{F}_n^{U_k}(\mathbf{W}, \mathbf{n}_{ij}) = \mathbf{U}_k.\mathbf{n}_{ij} m_k \mathbf{U}_k + \alpha_k p_k \mathbf{n}_{ij} \\ \mathcal{F}_n^{E_k}(\mathbf{W}, \mathbf{n}_{ij}) = \alpha_k (E_k + p_k) \mathbf{U}_k.\mathbf{n}_{ij} \end{array}\right. \tag{2.48}$$

and :

$$\left\{\begin{array}{l} 2\mathcal{G}_n^{\alpha_k}(\mathbf{W}_i, \mathbf{W}_j, \mathbf{n}_{ij}) = -r_{ij}((\alpha_k)_j - (\alpha_k)_i) \\ 2\mathcal{G}_n^{m_k}(\mathbf{W}_i, \mathbf{W}_j, \mathbf{n}_{ij}) = \mathcal{F}_n^{m_k}(\mathbf{W}_i, \mathbf{n}_{ij}) + \mathcal{F}_n^{m_k}(\mathbf{W}_j, \mathbf{n}_{ij}) - r_{ij}((m_k)_j - (m_k)_i) \\ 2\mathcal{G}_n^{U_k}(\mathbf{W}_i, \mathbf{W}_j, \mathbf{n}_{ij}) = \mathcal{F}_n^{U_k}(\mathbf{W}_i, \mathbf{n}_{ij}) + \mathcal{F}_n^{U_k}(\mathbf{W}_j, \mathbf{n}_{ij}) - r_{ij}((m_k \mathbf{U}_k)_j - (m_k \mathbf{U}_k)_i) \\ 2\mathcal{G}_n^{E_k}(\mathbf{W}_i, \mathbf{W}_j, \mathbf{n}_{ij}) = \mathcal{F}_n^{E_k}(\mathbf{W}_i, \mathbf{n}_{ij}) + \mathcal{F}_n^{E_k}(\mathbf{W}_j, \mathbf{n}_{ij}) - r_{ij}((\alpha_k E_k)_j - (\alpha_k E_k)_i) \end{array}\right. \tag{2.49}$$

where r_{ij} is defined by :

$$r_{ij} = max_{k=1,2,3} \left((|\mathbf{U}_k.\mathbf{n}_{ij}| + c_k)_i, (|\mathbf{U}_k.\mathbf{n}_{ij}| + c_k)_j \right) \tag{2.50}$$

Hence, using the standard notation $\overline{\phi}_{ij} = (\phi_i + \phi_j)/2$ whatever ϕ is, the solution of the

evolution step is obtained in each cell Ω_i by the following update :

$$\left\{\begin{array}{l}
\omega_i\left((\alpha_k)_i^{n+1,-}-(\alpha_k)_i^n\right)+\Delta t_n\left(\sum_{j\in V(i)}\mathcal{G}_n^{\alpha_k}(\mathbf{W}_i,\mathbf{W}_j,\mathbf{n}_{ij})S_{ij}\right)\\
\qquad\qquad+\Delta t_n(\mathbf{U}_1)_i^n.\left(\sum_{j\in V(i)}(\overline{\alpha}_k)_{ij}^n\mathbf{n}_{ij}S_{ij}\right)=0\\
\omega_i\left((m_k)_i^{n+1,-}-(m_k)_i^n\right)+\Delta t_n\left(\sum_{j\in V(i)}\mathcal{G}_n^{m_k}(\mathbf{W}_i,\mathbf{W}_j,\mathbf{n}_{ij})S_{ij}\right)=0\\
\omega_i\left((m_k\mathbf{U}_k)_i^{n+1,-}-(m_k\mathbf{U}_k)_i^n\right)+\Delta t_n\left(\sum_{j\in V(i)}\mathcal{G}_n^{U_k}(\mathbf{W}_i,\mathbf{W}_j,\mathbf{n}_{ij})S_{ij}\right)\\
\qquad\qquad+\Delta t_n\sum_{l=1,l\neq k}^{3}\Pi_{kl}(\mathbf{W})_i^n\left(\sum_{j\in V(i)}(\overline{\alpha}_l)_{ij}^n\mathbf{n}_{ij}S_{ij}\right)=0\\
\omega_i\left((\alpha_kE_k)_i^{n+1,-}-(\alpha_kE_k)_i^n\right)+\Delta t_n\left(\sum_{j\in V(i)}\mathcal{G}_n^{E_k}(\mathbf{W}_i,\mathbf{W}_j,\mathbf{n}_{ij})S_{ij}\right)\\
\qquad\qquad+\Delta t_n(\mathbf{U}_1)_i^n.\sum_{l=1,l\neq k}^{3}\Pi_{kl}(\mathbf{W})_i^n\left(\sum_{j\in V(i)}(\overline{\alpha}_l)_{ij}^n\mathbf{n}_{ij}S_{ij}\right)=0
\end{array}\right. \tag{2.51}$$

and we have the expected result :

Property 7 :
The evolution step guarantees positive values of partial masses and statistical fractions if the time step complies with the constraint :

$$\Delta t_n\left(\sum_{j\in V(i)}r_{ij}S_{ij}\right)\leq 2\omega_i \tag{2.52}$$

Proof : It is classical and omitted. □

2.3.3 Computing the relaxation step

In this step, we compute approximate solutions of the relaxation step (2.36), which is itself split into two sub-steps : the velocity relaxation step and the pressure relaxation step. It is important to note that these two relaxation effects are interconnected via the energy balance. However, the numerical method we adopt consists in treating separately the velocity relaxation (2.37) and then the pressure relaxation (2.41).

In what follows, we give the concrete details of the algorithms used for the velocity and the pressure relaxation sub-steps.

2.3.3.1 Velocity relaxation : approximate solutions of (2.37)

Two algorithms were considered. The difference between them lays in the approximation of the equation (2.39). The first algorithm uses an exact approximation of a linearised form

of (2.39), while the second considers an implicit Euler approximation. The other algorithm steps are identical.

In what follows we present the details of each algorithm :

Algorithm 3.3.1.1

In each cell Ω_i, starting with $\mathbf{W}_i^{n+1,-}$, we compute $\mathbf{W}_i^*$ by following the sequence :

a) Initialize the velocity differences : $\mathbf{X^n}$ with $(X_{12}^{\mathbf{n}}, X_{13}^{\mathbf{n}})_i^{n+1,-}$ where :

$$X_{1k}^{\mathbf{n}} = (\mathbf{U}_1 - \mathbf{U}_k).\mathbf{n}$$

Initialize also the velocity relaxation matrix defined in (2.40) : $A(\mathbf{W}_i^{n+1,-})$;

b) Compute the exact solution $(\mathbf{X^n})_i^*$ of the linear ODE :

$$\partial_t \mathbf{X^n} = -A(\mathbf{W}_i^{n+1,-})\mathbf{X^n} \tag{2.53}$$

at time $t = t_n + \Delta t_n$, using the initial condition defined in a) ;

c) Compute $(\mathbf{X}^{\tau_1})_i^* = (X_{12}^{\tau_1}, X_{13}^{\tau_1})_i^*$ and $(\mathbf{X}^{\tau_2})_i^* = (X_{12}^{\tau_2}, X_{13}^{\tau_2})_i^*$ by solving the same EDO (2.53), using the initial conditions $(X_{12}^{\tau_1}, X_{13}^{\tau_1})_i^{n+1,-}$ and $(X_{12}^{\tau_2}, X_{13}^{\tau_2})_i^{n+1,-}$ respectively ;

d) Compute $(\mathbf{U}_1)_i^*$ by the total momentum conservation :

$$(\mathbf{U}_1)_i^* = \frac{\sum_{k=1}^3 (m_k \mathbf{U}_k)_i^{n+1,-} + (m_2)_i^{n+1,-}(\mathbf{X}_{12})_i^* + (m_3)_i^{n+1,-}(\mathbf{X}_{13})_i^*}{(m_1 + m_2 + m_3)_i^{n+1,-}} \tag{2.54}$$

where :

$$(\mathbf{X}_{kl})_i^* = (X_{kl}^{\mathbf{n}})_i^* \mathbf{n} + (X_{kl}^{\tau_1})_i^* \tau_1 + (X_{kl}^{\tau_2})_i^* \tau_2$$

e) Update $(\mathbf{U}_2)_i^*$ and $(\mathbf{U}_3)_i^*$:

$$(\mathbf{U}_2)_i^* = (\mathbf{U}_1)_i^* - (\mathbf{X}_{12})_i^* \quad ; \quad (\mathbf{U}_2)_i^* = (\mathbf{U}_1)_i^* - (\mathbf{X}_{13})_i^* \tag{2.55}$$

f) Finally, update the energies by the discrete counterpart of (2.37d) :

$$(\alpha_k E_k)_i^* = (\alpha_k E_k)_i^{n+1,-} + \Delta t_n \sum_{l=1, l\neq k}^{3} \frac{e_{kl}(\mathbf{W}_i^{n+1,-})}{2} \left(((\mathbf{U}_l)_i^*)^2 - ((\mathbf{U}_k)_i^*)^2 \right) \tag{2.56}$$

Algorithm 3.3.1.2

In each cell Ω_i, starting with $\mathbf{W}_i^{n+1,-}$, we compute $\mathbf{W}_i^*$ by following the sequence :

a) Initialize the velocity differences : $\mathbf{X^n}$ with $(X_{12}^{\mathbf{n}}, X_{13}^{\mathbf{n}})_i^{n+1,-}$, and the velocity relaxation matrix defined in (2.40) : $A(\mathbf{W}_i^{n+1,-})$;

b) Compute $(\mathbf{X^n})_i^*$ such that :

$$(\mathbf{Id} + \Delta t_n A(\mathbf{W}_i^{n+1,-}))(\mathbf{X^n})_i^* = (\mathbf{X^n})_i^{n+1,-} \tag{2.57}$$

(2.57) is nothing but the implicit Euler discretization of (2.39) ;

c) Compute $(\mathbf{X}^{\tau_1})_i^*$ and $(\mathbf{X}^{\tau_2})_i^*$ by solving the same equation (2.57), using the initial conditions $(X_{12}^{\tau_1}, X_{13}^{\tau_1})_i^{n+1,-}$ and $(X_{12}^{\tau_2}, X_{13}^{\tau_2})_i^{n+1,-}$ respectively ;

d) Compute $(\mathbf{U}_1)_i^*$ by the total momentum conservation (2.54) (step (d) of *Algorithm 3.3.1.1*) ;

e) Update $(\mathbf{U}_2)_i^*$ and $(\mathbf{U}_3)_i^*$ following (2.55) (step (e) of *Algorithm 3.3.1.1*) ;

f) Finally, update the energies by (2.56) (step (f) of *Algorithm 3.3.1.1*).

Remark 3 :

This numerical scheme is consistent with the mass conservation, the total momentum conservation and the total energy conservation.□

Remark 4 :

Obviously, when considering instantaneous velocity relaxation, (2.53)/(2.57)-(2.54)-(2.55)-(2.56) *degenerates into :*

$$(\mathbf{U}_k)_i^* = \frac{\sum_{l=1}^3 (m_l \mathbf{U}_l)_i^{n+1,-}}{\sum_{l=1}^3 (m_l)_i^{n+1,-}} \tag{2.58}$$

□

2.3.3.2 Pressure relaxation : approximate solutions of (2.41)

Here we present two different algorithms that were implemented, in order to compute approximate solutions of (2.41). The basic unknown is $(\alpha_1, \alpha_2, p_1, p_2, p_3)$.

Algorithm 3.3.2.1

In each cell Ω_i, starting with $\mathbf{W}_i^*$ we compute $\mathbf{W}_i^{n+1}$ by following the sequence :

a) Initialize the pressure differences $\mathbf{Y}_i^* = \mathbf{Y}(\mathbf{W}_i^*)$ and the pressure relaxation matrix defined in (2.43) : $B(\mathbf{W}_i^*)$;

b) Compute $\mathbf{Y}_i^{n+1}$, the exact solution of the ODE :

$$\partial_t \mathbf{Y} = -\frac{1}{\Pi_0} B(\mathbf{W}_i^*)\mathbf{Y} \tag{2.59}$$

at time $t = t_n + \Delta t_n$, using the initial condition $\mathbf{Y}_i^*$.

c) Update the partial entropies with respect to (2.45), i.e. $(s_2)_i^{n+1}$ and $(s_3)_i^{n+1}$ by :

$$\begin{cases} (s_2)_i^{n+1} = (s_2)_i^* \\ (s_3)_i^{n+1} = (s_3)_i^* \end{cases} \tag{2.60}$$

and $(s_1)_i^{n+1}$ as approximate solution at time $t = t_n + \Delta t_n$ of the ODE :

$$\partial_t s_1 = \left[\frac{(a_1)_i^*}{(m_1)_i^*} \sum_{1 \le l < k \le 3} \left(\frac{\alpha_k \alpha_l}{\tau_{kl}^P \Pi_0} \right)_i^* \left((p_k - p_l)_i^{n+1} \right)^2 \right] \tag{2.61}$$

using Euler scheme.

d) Compute the pressure $(p_1)_i^{n+1}$ solution of $g(x) = 1$, where :

$$g(x) = \frac{(m_1)_i^*}{\rho_1(x, (s_1)_i^{n+1})} + \frac{(m_2)_i^*}{\rho_2(x - (y_{12})_i^{n+1}, (s_2)_i^{n+1})} + \frac{(m_3)_i^*}{\rho_3(x - (y_{13})_i^{n+1}, (s_3)_i^{n+1})} \quad (2.62)$$

The equation $g(x) = 1$ is nothing but the saturation condition of the statistical fractions (2.3) ;

e) Update the pressures of phases, for $k = 2, 3$ compute :

$$(p_k)_i^{n+1} = (p_1)_i^{n+1} - (y_{1k})_i^{n+1} \quad (2.63)$$

f) Update the statistical fractions, for $k = 1, 2, 3$ compute :

$$(\alpha_k)_i^{n+1} = \frac{(m_k)_i^*}{\rho_k((p_k)_i^{n+1}, (s_k)_i^{n+1})} \quad (2.64)$$

g) Finally, update the total energies by combining (2.41a) and (2.41d) :

$$(\alpha_k E_k)_i^{n+1} = (\alpha_k E_k)_i^* + \Delta t_n \sum_{l=1, l\neq k}^{3} (\Pi_{kl}(\mathbf{W}))_i^{n+1} (S_l^\alpha(\mathbf{W}))_i^{n+1} \quad (2.65)$$

where $(\Pi_{kl}(\mathbf{W}))_i^{n+1}$ and $(S_l^\alpha(\mathbf{W}))_i^{n+1}$ are expressed, owing to (2.6) and (2.7), in terms of $(p_k)_i^{n+1}$ and $(\alpha_k)_i^{n+1}$.

We note that :

$$\begin{aligned} \sum_k \Big((m_k e_k)^{n+1} - (m_k e_k)^* \Big) &= \Delta t_n (p_2 + p_3)^{n+1} ((S_1^\alpha)^{n+1} + (S_2^\alpha)^{n+1} + (S_3^\alpha)^{n+1}) \\ &= 0 \end{aligned}$$

The well-posedness of this algorithm relies on the following property :

Property 8 :
The equation $g(x) = 1$ is well-posed and admits a unique solution in the admissible range.

Proof :
Let $\mathcal{D}_k$ be the definition domain of the density $\rho_k(p_k, s_k)$ wrt its first parameter p_k. Thus, if we denote $\mathcal{D}_g$ the definition domain of the function g we have :

$$\mathcal{D}_g = \{x \ / \ x \in \mathcal{D}_1 \ and \ x - (y_{12})_i^{n+1} \in \mathcal{D}_2 \ and \ x - (y_{13})_i^{n+1} \in \mathcal{D}_3\}$$

For any type of EOS, and for any $x \in \mathcal{D}_g$ we have :

$$g'(x) = -\sum_{k=1}^{3} \frac{m_k}{\rho_k^2} \left(\frac{\partial \rho_k}{\partial p_k} \right)_{s_k}$$

We assume that the EOS complies with the following constraints :

— Positive derivative wrt the pressure :

$$\left(\frac{\partial \rho_k}{\partial p_k}\right)_{s_k} > 0$$

— Asymptotic limit :

$$\lim_{p_k \to +\infty} \rho_k(p_k, s_k) = +\infty$$

— Null density :

$$\exists p_k^0 \in \mathcal{D}_k / \rho_k(p_k^0, s_k) = 0$$

Thus we have on the one hand :

$$\forall x \in \mathcal{D}_g : g'(x) < 0$$

On the other hand :

$$\lim_{x \to +\infty} g(x) = 0$$

And :

$$\lim_{x \to x_0^+} g(x) = +\infty$$

where $x_0 = max\{p_1^0, p_2^0 + (y_{12})_i^{n+1}, p_3^0 + (y_{13})_i^{n+1}\}$.

This allows to conclude that the equation $g(x) = 1$ admits a unique solution in $\mathcal{D}_g$. □

Algorithm 3.3.2.2

Again, in each cell Ω_i, starting with $\mathbf{W}_i^*$ we compute $\mathbf{W}_i^{n+1}$ by following the sequence :

a) Initialize the pressure differences $\mathbf{Y}_i^* = \mathbf{Y}(\mathbf{W}_i^*)$ and the pressure relaxation matrix defined in (2.43) : $B(\mathbf{W}_i^*)$;

b) Compute $\mathbf{Y}_i^{n+1}$, the exact solution of the ODE :

$$\partial_t \mathbf{Y} = -\frac{1}{\Pi_0} B(\mathbf{W}_i^*)\mathbf{Y} \tag{2.66}$$

at time $t = t_n + \Delta t_n$, using the initial condition $\mathbf{Y}_i^*$.

c) Compute the volume fraction variables Π and δ_{kl} with respect to (2.46), i.e. Π_i^{n+1} and $(\delta_{kl})_i^{n+1}$ as the exact solutions at time $t = t_n + \Delta t_n$ of the ODEs :

$$\begin{cases} \partial_t \Pi = \left[a((\alpha_2)_i^* - (\alpha_1)_i^*) + b((\alpha_3)_i^* - (\alpha_2)_i^*) + c((\alpha_1)_i^* - (\alpha_3)_i^*)\right] \Pi \\ \partial_t \delta_{12} = \left[a((\alpha_2)_i^* - (\alpha_1)_i^*) + (b-c)(\alpha_3)_i^*\right] \delta_{12} \\ \partial_t \delta_{13} = \left[c((\alpha_1)_i^* - (\alpha_3)_i^*) + (a-b)(\alpha_2)_i^*\right] \delta_{13} \\ \partial_t \delta_{23} = \left[b((\alpha_3)_i^* - (\alpha_2)_i^*) + (c-a)(\alpha_1)_i^*\right] \delta_{23} \end{cases} \tag{2.67}$$

where : $a = \frac{(y_{12})_i^{n+1}}{\tau_{12}^P \Pi_0}$ $\quad b = \frac{(y_{13})_i^{n+1} - (y_{12})_i^{n+1}}{\tau_{23}^P \Pi_0}$ $\quad c = \frac{-(y_{13})_i^{n+1}}{\tau_{13}^P \Pi_0}$

d) Update the volume fractions $(\alpha_k)_i^{n+1}$ and the densities $(\rho_k)_i^{n+1}$:

$$(\alpha_k)_i^{n+1} = \frac{\Pi_i^{n+1}}{(\delta_{jl})_i^{n+1}} \quad j,l \neq k \tag{2.68}$$

$$(\rho_k)_i^{n+1} = \frac{(m_k)_i^*}{(\alpha_k)_i^{n+1}} \tag{2.69}$$

e) Compute the pressure $(p_1)_i^{n+1}$ solution of $h(x) = 0$ where :

$$\begin{aligned} h(x) =& (m_1)_i^* e_1(x, (\rho_1)_i^{n+1}) + (m_2)_i^* e_2(x - (y_{12})_i^{n+1}, (\rho_2)_i^{n+1}) \\ &+ (m_3)_i^* e_3(x - (y_{13})_i^{n+1}, (\rho_3)_i^{n+1}) - \sum_{k=1}^{3} (m_k)_i^* (e_k)_i^* \end{aligned} \tag{2.70}$$

The equation $h(x) = 0$ is nothing but the conservation of the total internal energy during the pressure relaxation sub-step ;

f) Update the pressures of phases, for $k = 2, 3$ compute :

$$(p_k)_i^{n+1} = (p_1)_i^{n+1} - (y_{1k})_i^{n+1} \tag{2.71}$$

g) Finally, update the total energies by combining (2.41a) and (2.41d) :

$$(\alpha_k E_k)_i^{n+1} = (\alpha_k E_k)_i^* + \Delta t_n \sum_{l=1, l\neq k}^{3} (\Pi_{kl}(\mathbf{W}))_i^{n+1} (S_l^{\alpha}(\mathbf{W}))_i^{n+1} \tag{2.72}$$

where $(\Pi_{kl}(\mathbf{W}))_i^{n+1}$ and $(S_l^{\alpha}(\mathbf{W}))_i^{n+1}$ are expressed, owing to (2.6) and (2.7), in terms of $(p_k)_i^{n+1}$ and $(\alpha_k)_i^{n+1}$.

Remark 5 :
Algorithms 3.3.2.1 and 3.3.2.2. are consistent with the mass conservation, the total momentum conservation and the total energy conservation.□

Remark 6 :
In the asymptotic situation where the user would assume infinite drag effects between phases, thus neglecting relative velocities ($\boldsymbol{U}_1 = \boldsymbol{U}_2 = \boldsymbol{U}_3 = \mathcal{U}$ where $\mathcal{U}$ is defined in (2.58)), we may consider the limit case where $p_1 = p_2 = p_3 = \mathcal{P}$ where $\mathcal{P}$ is given in appendix A1.□

2.4 Numerical results

This section is dedicated to the presentation of the different numerical test-cases that were conducted using the three-phase flow model presented in Section 2.2 and the numerical schemes and algorithms given in Section 2.3.

In the first subsection, we present a verification test-case where we examine the computation of the evolution step, this consists in studying the convergence rates in terms of

the mesh size on a Riemann problem. In the second subsection, we focus on the relaxation step and we present, first, a series of verification cases of the velocity relaxation step, and then we focus on the pressure relaxation subsystem. In subsection 2.4.4, we analyse a more complete shock-tube test-case, which studies the impact of a planar shock wave on a cloud of deformable droplets.

2.4.1 Verification of the evolution step

This subsection is devoted to the verification of the convective subset of (2.1) using the numerical scheme (2.51). We consider a Riemann problem where two waves are at stake : the contact discontinuity associated with the eigenvalue $\lambda_{1,2,3}(\mathbf{w}) = u_1$ and a right-going shock wave of phase 1.

In order to initialize the Riemann problem, we start with a given left state $\mathbf{w}^L$, then we use the Riemann invariants introduced in (2.29) to build the intermediate state $\mathbf{w}^{int}$ such that : $I^i_{1,2,3}(\mathbf{w}^L) = I^i_{1,2,3}(\mathbf{w}^{int})$ for $i = 1, .., 8$. After that, we consider the phase 1 right-going shock wave such that $\rho_1^R/\rho_1^{int} = 1/2$, and use the exact connections through shock waves to determine the state $\mathbf{w}^R$. The following table gives the adopted numerical values :

	Left state $\mathbf{w}^L$	Intermediate state $\mathbf{w}^{int}$	Right state $\mathbf{w}^R$
α_1	3/10	3/5	3/5
α_2	7/20	1/5	1/5
α_3	7/20	1/5	1/5
ρ_1	1/4	1/10	5/100
ρ_2	0.14675324	0.14368748	0.14368748
ρ_3	0.16666666	0.14535470	0.14535470
p_1	1.00×10^4	1.0597086×10^4	3.8534858×10^3
p_2	1.13×10^4	1.0901632×10^4	1.0901632×10^4
p_3	1.20×10^4	9.6407273×10^3	9.6407273×10^3
u_1	300.0	300.0	40.315571
u_2	350.0	389.36692	389.36692
u_3	400.0	560.65856	560.65856

We emphasize that for this test case, all three phase EOS are chosen to be *Ideal Gas* EOS with the following thermodynamic parameters :

	Phase 1	Phase 2	Phase 3
γ_k	1.4	1.7	1.6

Calculations are run with 6 different mesh sizes h : 1/5000, 1/10000, 1/25000, 1/50000, 1/100000 and 1/200000. The computational domain is the unit cell $[0, 1]$ and the Riemann problem is initialized in $x = 0.5$.

Fig.2.1 gives the error in L^1 norm measured on the system's principal variables. We note that for coarse meshes, the u_1 curve shows a high convergence rate close to h^1, which is the asymptotic rate for shock waves. As the mesh is refined, the convergence rate tends towards $h^{1/2}$. That is the rate corresponding to the contact discontinuity associated with the coupling wave $\lambda = u_1$. For the other variables, the $h^{1/2}$ rate is obtained more quickly.

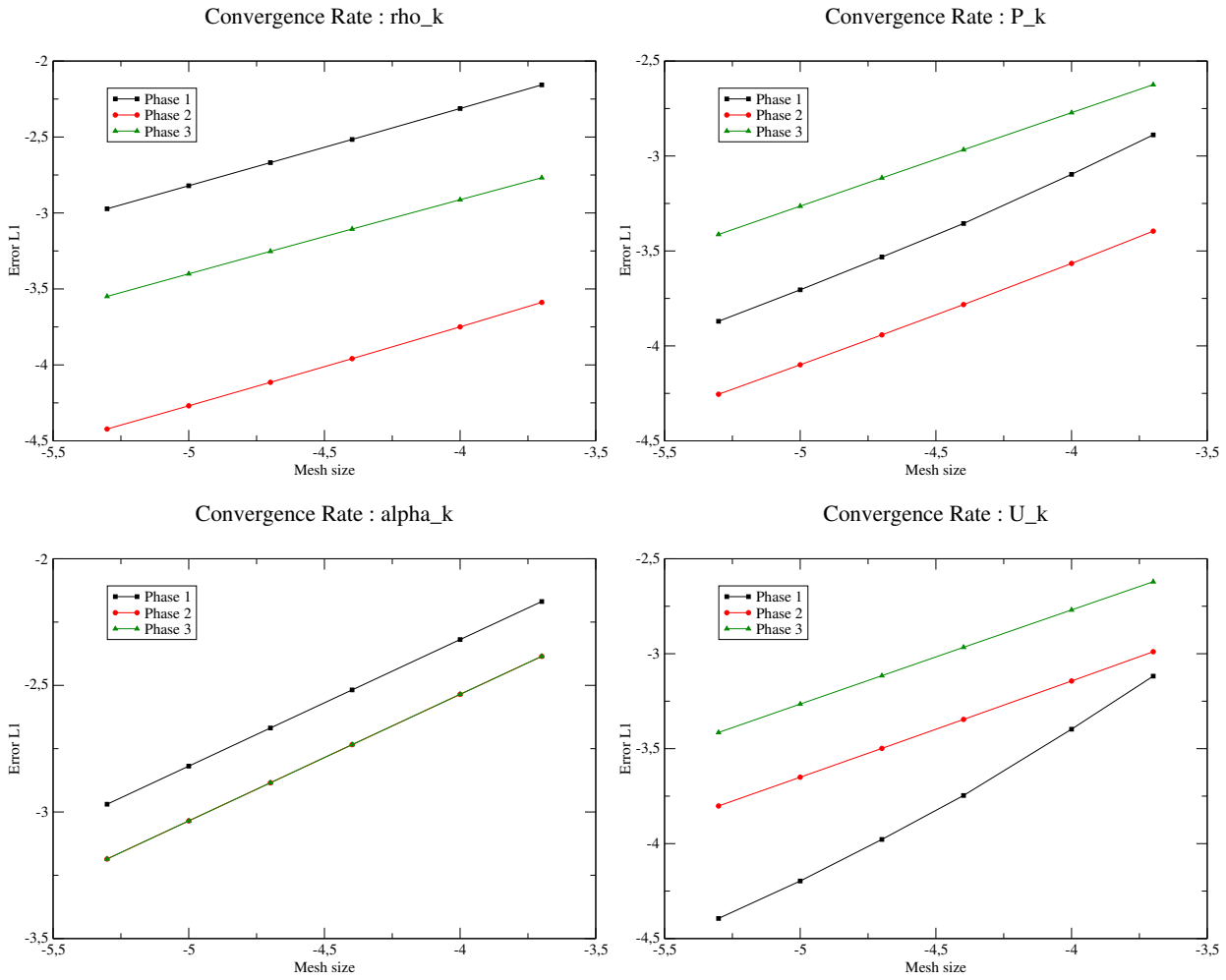

FIGURE 2.1 – L^1 *of the error for* ρ_k, p_k, α_k *and* u_k *wrt the mesh size* h

In order to get a better understanding of the structure of fields involved in this test case, Fig.2.2 gives the spacial representation of state variables at the final time of the simulation $T = 0.8ms$, while focusing on the 1/50000 mesh results.

We can observe the two jumps related to :

— **The contact discontinuity** located around $x_{contact} = 0.74$. In fact, considering the initial data, the coupling wave speed is :

$$\sigma_{contact} = u_1^L = 300.0 \ m/S \tag{2.73}$$

Knowing that the Riemann problem was initialized at $x_{Riemann} = 0.5$, the observed jump's position $x_{contact}$ is in agreement with the theoretically expected result : $x_{contact} = x_{Riemann} + T\sigma_{contact}$;

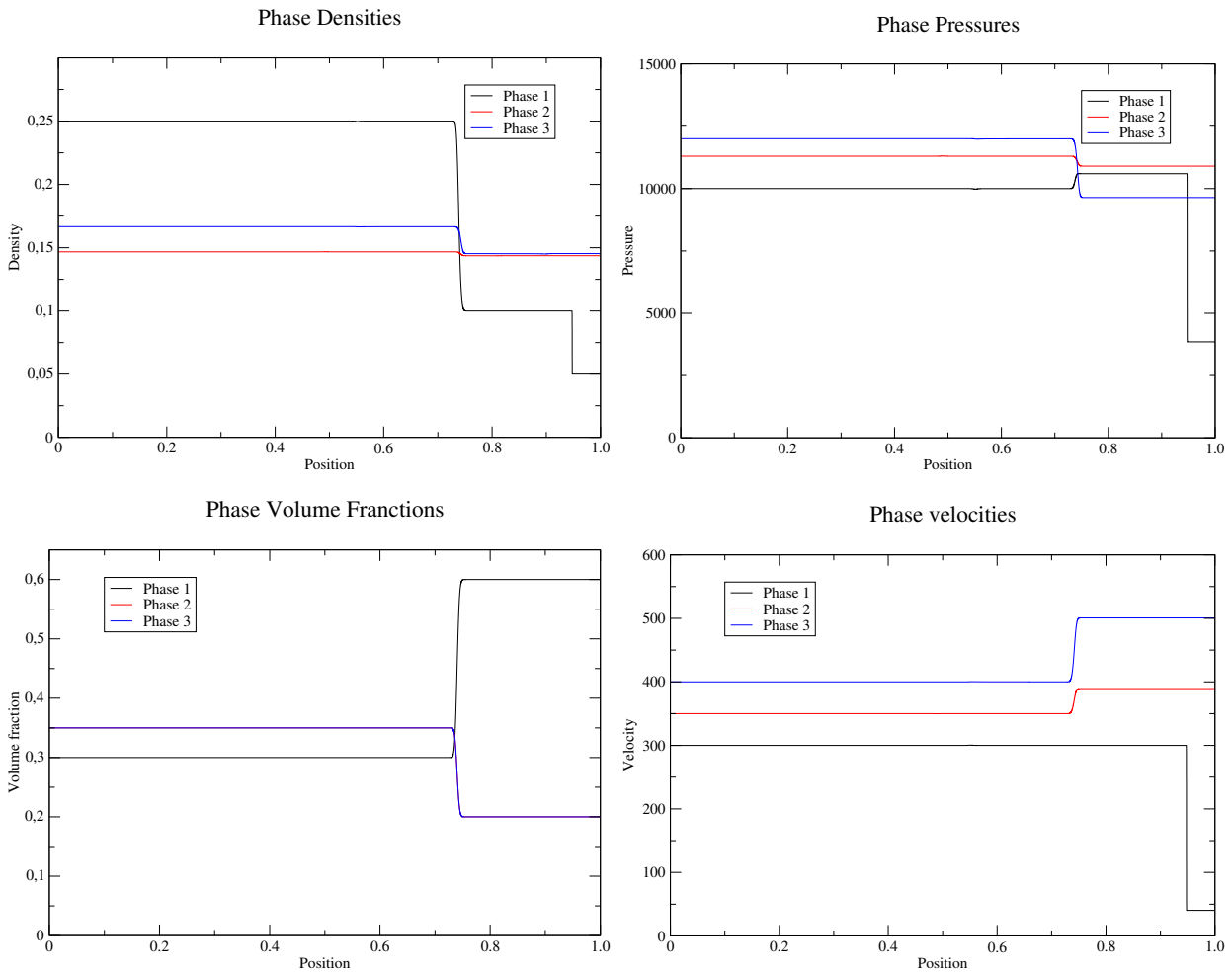

FIGURE 2.2 – *Spatial representation of variables at the final simulation time* $T = 0.8\ ms$

— **The phase 1 shock wave** observed around $x_{shock} = 0.95$. Actually, the initial data give a right-going shock the speed of which is :

$$\sigma_{shock} = \frac{(\rho_1 u_1)^R - (\rho_1 u_1)^{int}}{\rho_1^R - \rho_1^{int}} = 559.68442\ m/s \tag{2.74}$$

We check that all variables of phases 2 and 3 do not jump at this position, which is in agreement with shock relations. Of course, the statistical fraction α_1 does not jump, as expected.

2.4.2 Velocity relaxation verification test cases

This paragraph provides the results of two verification test cases of the velocity relaxation sub-step. It consists in verifying the algorithms introduced in the subsection (2.3.3.1), to find approximate solutions of (2.37). Appendix A3 gives the details of the analytical solution in each case.

— **Test-case A3.1** (see Fig.2.3)

The analytical solution in this case is in the discrete approximation space of *Algorithm 3.3.1.1*. In fact, by choosing the coefficients e_{kl} (introduced in (2.9)) constants, the approximation (2.53) becomes an exact counterpart of (2.92), which means that *Algorithm 3.3.1.1* in this case computes the exact analytical solution. The error is at its least when the mesh is coarse, here its value is around 10^{-16} (round-off error). Then, the error starts to increase progressively as the mesh is refined. This is due to the cumulation of the rounding errors throughout the different algorithm steps.

Turning then to *Algorithm 3.3.1.2*, an expected convergence at the rate h^1 is observed.

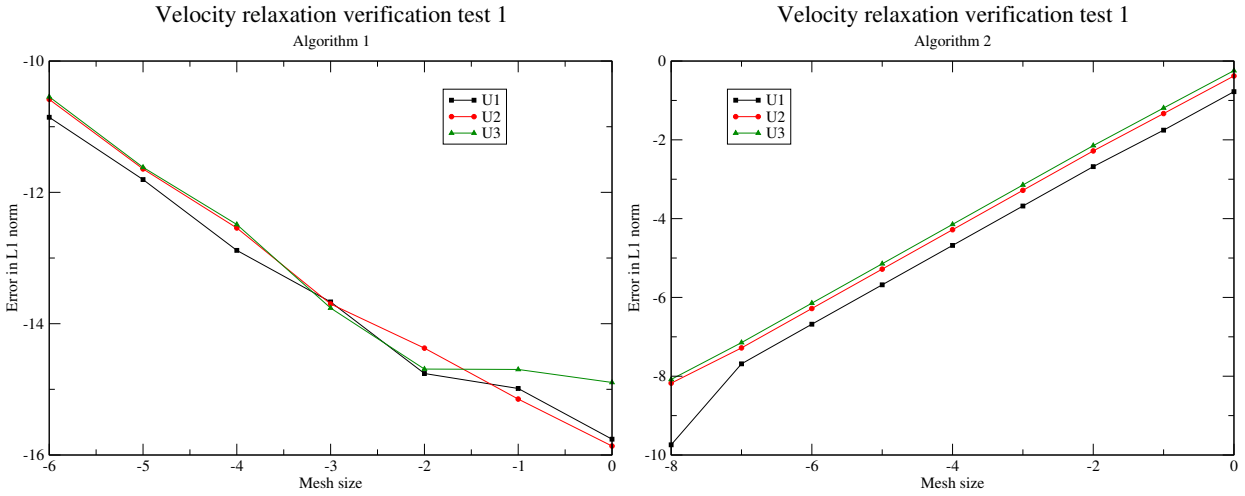

FIGURE 2.3 – *Test-case A3.1 convergence rates for the algorithms 3.3.1.1 (left) and 3.3.1.2 (right)*

— **Test-case A3.2** (see Fig.2.4)
In this case, the coefficients e_{kl} are chosen to be time-dependent. This means that none of the two algorithms computes the exact solution, both compute approximations, thus the error is decreasing as the mesh is refined. Once more, the convergence rate tends towards the expected h^1 rate.

2.4.3 Pressure relaxation verification test case

We turn in this paragraph to the verification of the schemes introduced in (2.3.3.2), to obtain approximate solutions of the pressure relaxation sub-system (2.41). In appendix A4 we present the analytical solution that was considered, and in Figure 2.5 we give the obtained numerical results with both algorithms (3.3.2.1) and (3.3.2.2).

We note that the *Algorithm 3.3.2.2* shows a convergent behaviour, starting by a constant error level for coarse meshes, then it arrives at a point where the mesh gets sufficiently refined (mesh size $dt \approx 10^{-4}$) and thus the convergence could be observed. This computational result was obtained with $\tilde{\tau}_0 = 10^2$ ($\tilde{\tau}_0$ is defined in (2.103)), which corresponds to :

$$\frac{dt}{\tilde{\tau}_0/(\gamma K_1)} \approx 1 \tag{2.75}$$

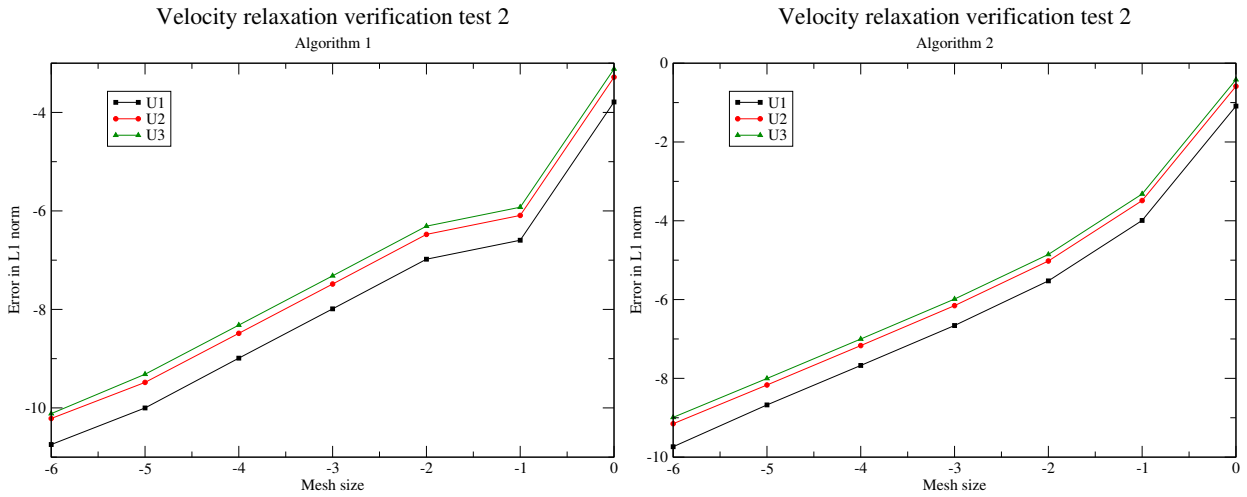

FIGURE 2.4 – *Test-case A3.2 convergence rates for the algorithms 3.3.1.1 (left) and 3.3.1.2 (right)*

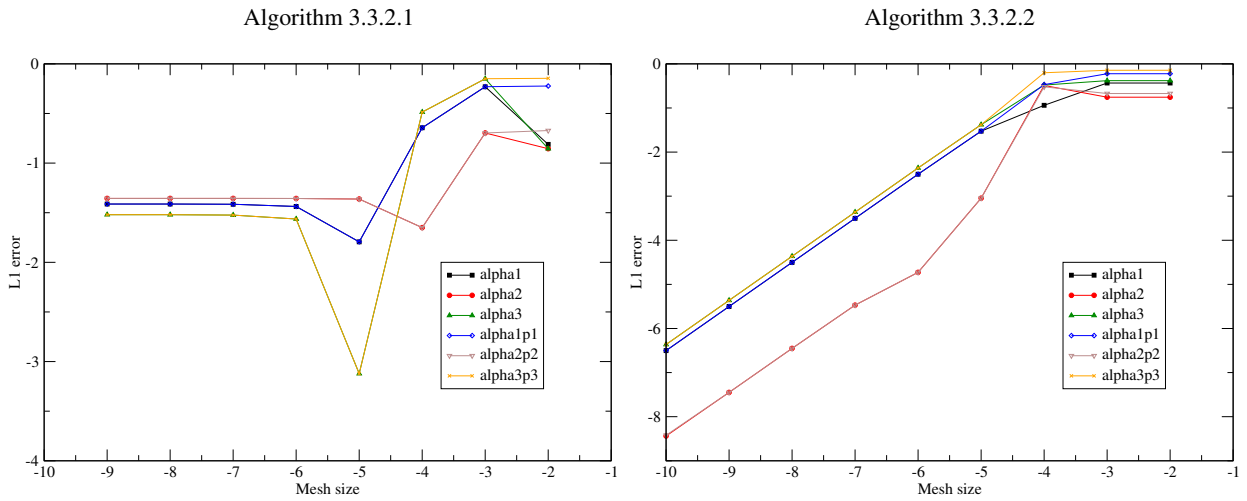

FIGURE 2.5 – *Convergence rates for the pressure relaxation algorithms 3.3.2.1 (left) and 3.3.2.2 (right). The error is measured at time* $t = 1.0\ s$

(See the property A4.1 of Appendix A4 for the definition of K_1).

Other numerical simulations were run with different $\tilde{\tau}_0$, γ and K_1 values, we noticed that (2.75) hold for all of them, this means that the convergence start to be observable when the mesh size dt becomes small enough compared to the pressure relaxation characteristic time included in $\frac{\tilde{\tau}_0}{\gamma K_1}$.

2.4.4 Validation test case

In this subsection we focus on the shock-tube experiment presented in [7, 8]. It consists in the analysis of the effects of a planar air shock wave on a cloud of water droplets. A high-pressure chamber filled with air generates the planar shock wave, which moves rightwards

into the air at atmospheric pressure. The cloud of droplets is placed in the low-pressure chamber and undergoes the impact of the incident shock wave.

In order to get a correct understanding of the shock wave / droplets interaction, several pressure sensors have been placed in the low-pressure chamber. This allows to record the pressure histories in different tube positions, and therefore highlight the undergoing physical mechanisms. Fig.2.6 gives the geometrical details of the shock-tube apparatus, as well as the droplets and the pressure sensors' positions.

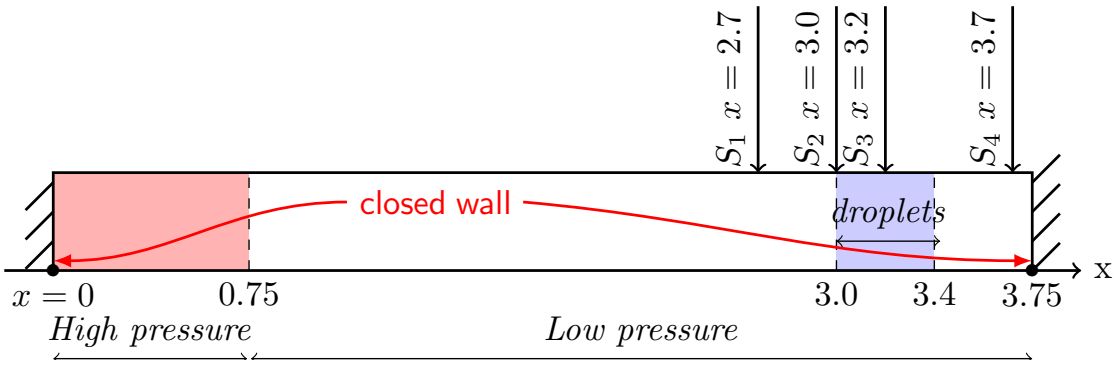

FIGURE 2.6 – *Shock-tube apparatus (bed hight* $400mm$*)*

In [7, 8], many experimental settings have been presented : a single-phase shock-tube without droplets, and three different two-phase gas-liquid mixtures where different cloud sizes were considered. It should be noted that the thermal effects don't play the primary role in this experiment, instead it is the dynamics (including velocity and pressure effects) that have the most important influence. Therefore, our present model (that does not include mass transfer) is fairly appropriate.

In fact, when put together, the convective system, the velocity and the pressure relaxation effects allow to get an adequate simulation of the experiment's dynamics. In addition to that, an *interfacial area* equation was included in order to take into account the atomization effect. The details of the *interfactial area* equation can be found in [6]. In the continuity of the latter work, we adopt the same initialization of the numerical test-cases (namely for the pressures, the velocities and the statistical fractions). The difference meanwhile concerns the EOS : while [6] focuses on the *barotropic* framework, in the present work we adopt a *non-barotropic EOS*. Appendix A5 presents the different EOS as well as the test-case initialization datasets.

In the sequel, we discuss the comparison between the experimental and the obtained numerical results :

— **Single-phase flow configuration :**

This is a reference test-case where we consider a single-phase shock tube configuration. No particle lid is included (α_1 is set to 10^{-10} in all the computational domain) and the mean pressure is denoted :

$$P = \sum_{k=1}^{3} \alpha_k P_k$$

One-phase flow	Experimental results	Euler model (exact solution)		Euler model (numerical simulation)	
		Barotropic	With energy	Barotropic	With energy
P^* (bar)	≈ 2.4	2.78	2.46	2.78	2.46
P^{**} (bar)	≈ 5.0	6.85	5.42	6.85	5.42
Celerity σ (m/s)	≈ 466		497		497

TABLE 2.1 – *Single-phase flow experimental, analytical and numerical results*

Figure 2.7 gives the pressure history recorded at station 4. We denote P^* the pressure level just behind the right-going shock wave observed around $t = 3.7\ ms$, and P^{**} the pressure level after the reflection of this shock wave on the right wall boundary of the tube.

In Table 2.1 we give the comparison between the different experimental, analytical and numerical results, including the barotropic case that was presented in [6]. We note, on the one hand, that the numerical results on a sufficiently refined mesh (50000 cells per meter here) are in agreement with the analytical solutions, both for the *barotropic* and the *full* Euler model (*full* here means the model with energy equations), which is expected and mandatory. On the other hand, we note that the *full* Euler model enables to obtain a better approximation of the experimental results. This has been already mentioned in [6], in Figure 2.7 we give the corresponding numerical result when using the model with energy.

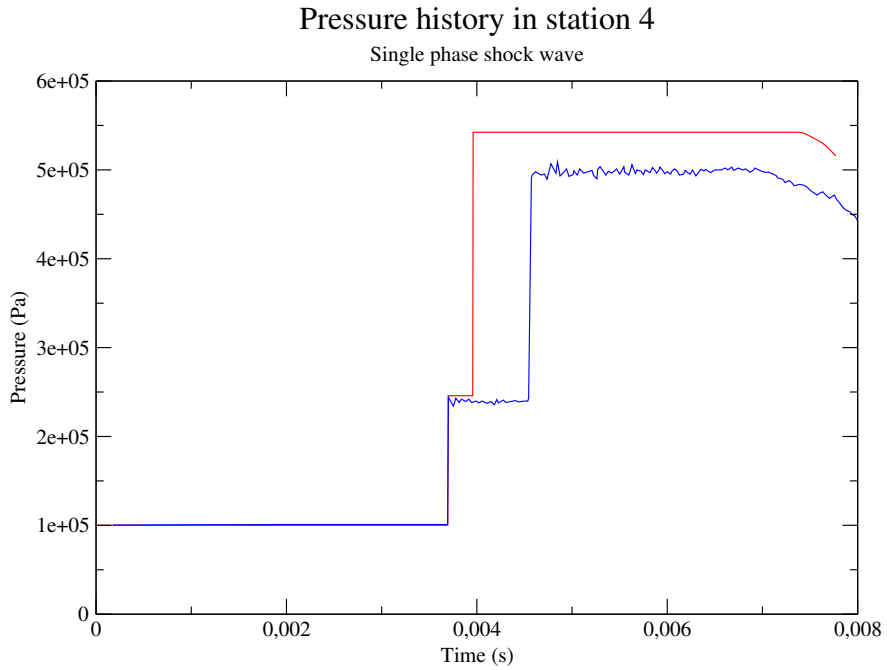

FIGURE 2.7 – *Shock wave in a single-phase medium : experimental data (blue) and numerical results with the energy equations (red)*

The shock wave celerity is also an interesting aspect to observe. In Table 2.1 we note that the experimental and the numerical (or exact) values display a 6% difference. Nonetheless, it is not sufficient to explain the gap shown in Figure 2.7, where the

numerical reflected wave returns back more quickly than the experimental wave, more than what could correspond to the latter 6% celerity discrepancy. This delay of the experimental reflected wave could be partially justified by the friction on the tube's sidewall and end-wall, which is not taken into account in our model. It could also be the consequence of a geometric difference, between the numerical computational domain (Figure 2.6) and the real tube used in the experimental set-up [7, 8].

Another notable conclusion of this single-phase comparison is the fact that the full Euler model provides results that are already slightly different from the experimental observations. Hence, we may expect some greater discrepancies when we run two-phase or three-phase simulations.

— **Gas-solid two-phase flow configuration :**

In this case, a 400 mm particle bed height is considered ($\alpha_1 = 0.0104$ for $2.97 \leq x \leq 3.37$), and the particle diameter is set to $d_0 = 500\mu m$ everywhere throughout the computation. This corresponds to a solid particle situation, where no particle deformation occurs. The retrieved pressure's pattern is shown in Figure 2.8.

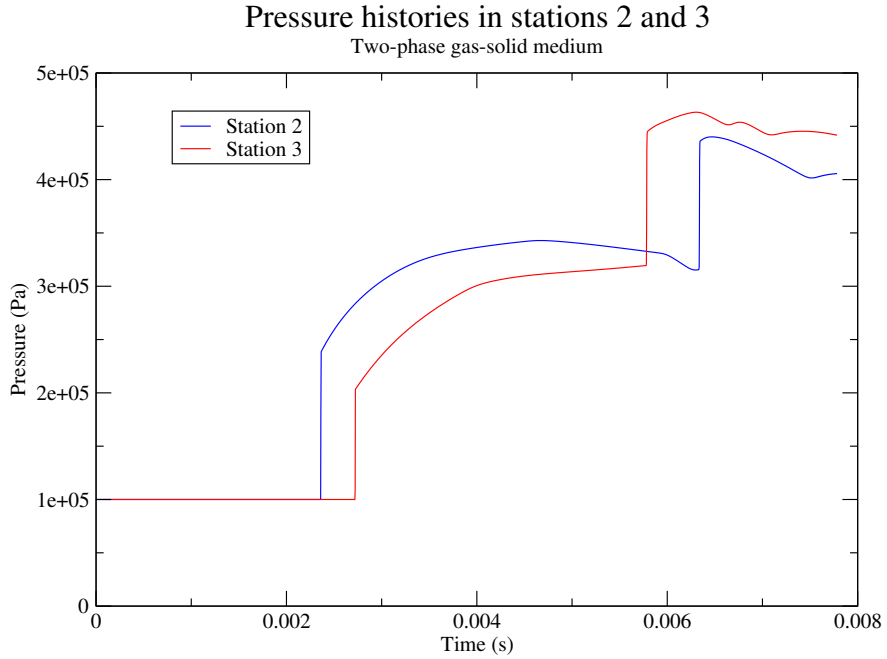

FIGURE 2.8 – *Shock wave through gas-solid two-phase medium - Stations 2 & 3*

In each station, we observe a sudden pressure jump that corresponds to the incident shock wave, followed by a smooth pressure increase until the arrival of a second pressure jump representing the reflected shock wave on the tube's end-wall. We can also note a difference in the amplitude of the incident shock wave between stations 2 and 3 : it starts by a value around 2.4 *bar* for station 2 which is equal to the single-phase pressure jump (see Table 2.1), and gets attenuated when getting closer to station 3. This is due

to the dissipation of the shock's energy as it travels inside the particle lid. The observed behaviour matches the qualitative description of the gas-solid configuration presented in [7, 8].

— **Gas-liquid two-phase flow configuration :**

This test corresponds to the interaction of a shock wave with a lid of liquid deformable droplets. The initialization is identical to the gas-solid case, but we take into account the interfacial area equation A as presented in [6].
Figure 2.9 gives the numerical results as well as the experimental data. We note that, at the beginning, the numerical simulations show a similar pattern to the gas-solid case, with an incident shock wave of 2.4 *bar* amplitude on station 2, and a smaller amplitude on station 3. But the major difference comes from the sudden decrease that follows the arrival of the incident shock, which is clearly visible on station 3. This is the characteristic signature of the droplets atomization [14] under the effect of the incoming shock wave : each droplet breaks into smaller droplets until reaching a certain diameter, where the particle cloud reaches an equilibrium with the incident shock wave. Afterwards, the pressure starts to build up and a compression is observed once more.
On station 2, the fragmentation signature can hardly be observed, and the compression following the incident shock occurs quickly : rapidly a pressure plateau is observed from $t \approx 2.8\ ms$ to $t \approx 6\ ms$. The end of the plateau is marked by a pressure decrease due the arrival from the left wall boundary of the reflected rarefaction wave.

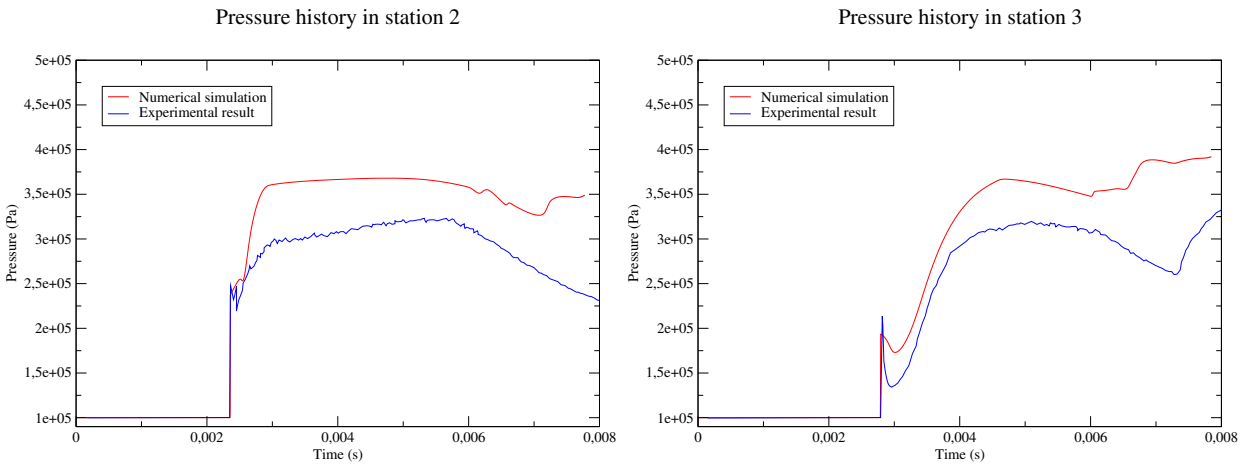

FIGURE 2.9 – *Shock wave through gas-liquid two-phase medium - Mean pressure at stations 2 & 3 - Comparison of experimental and numerical results*

As expected from the single-phase comparison, the numerical pressure levels are greater than the measured experimental results. Nevertheless, it seems to be remarkable that the qualitative pressure behaviour is rather good, as it takes into account the major dynamical phenomena that occur in this fragmentation experiment. The pressure levels also are closer to the experimentally measured values than those arising from the barotropic model computation (as observed in [6]).

In order to get a more complete view on this fragmentation test-case, we provide here some additional numerical results, though the comparison with experimental data is not available. Figure 2.10 gives the evolution of the relative velocity wrt time at stations 2 and 3. We can notice that the relative velocity jumps and it reaches a maximum value right at the arrival of the incident shock wave, which in turn activates the fragmentation process. After that, it decreases rather quickly. In both stations, the relative velocity decrease could be put in match with the pressure build-up after the incident shock wave. Both the pressure and the relative velocity reflect the nature of the fragmentation.

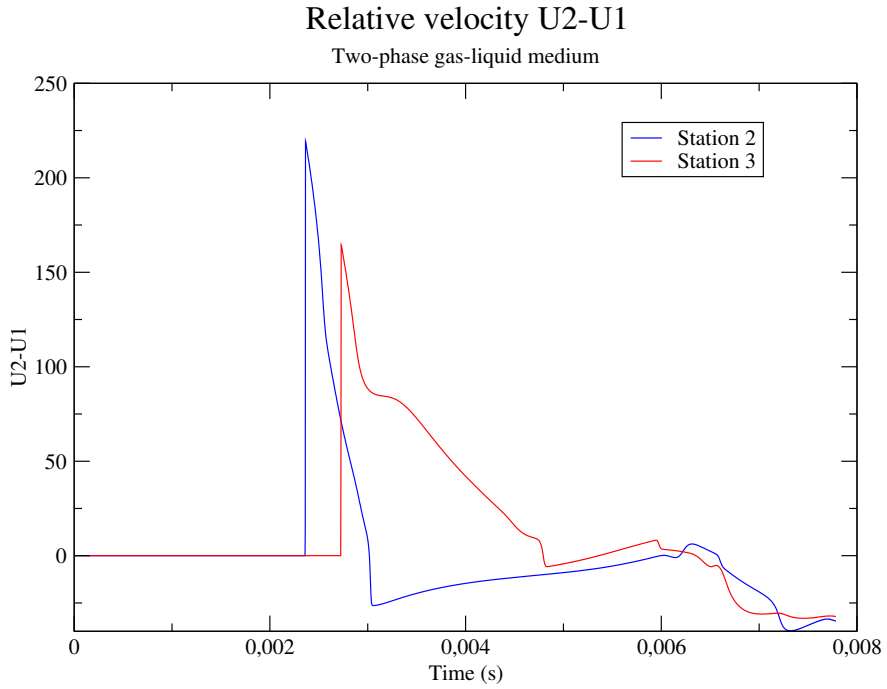

FIGURE 2.10 – *The relative velocity $u_2 - u_1$ in the stations 2 and 3*

In Figures 2.11 and 2.12 we give a spacial representation of the velocity and the momentum at four distinct time instants. Taking into account the fact that the phase 2 is the carrier of the shock wave, one can observe u_2 and $m_2 u_2$ and notice the different progress stages of the shock wave.

It is worth to be noted that the phase 1 momentum behaviour is consistent with the evolution of α_1 and A, as shown in Figure 2.13. This allows to understand that the particle cloud, in addition to the fragmentation, tends to move rightwards under the effect of the incident right-going shock wave. This movement is not uniform, the left side of the cloud (located initially around $x = 3.0$) undergoes a more significant shifting than the right side (initially at $x = 3.4$).

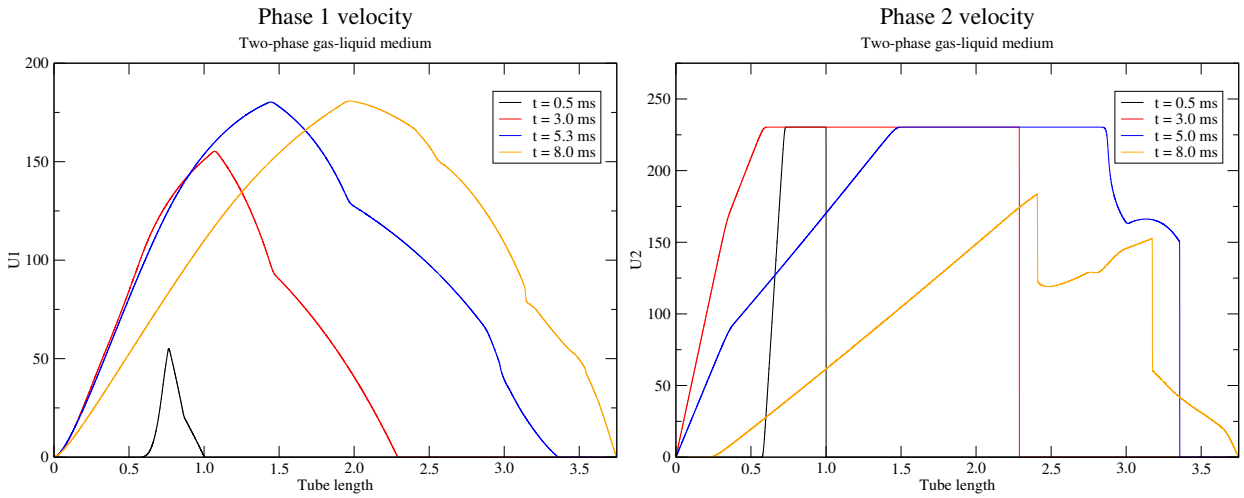

FIGURE 2.11 – *Phase 1 and 2 velocities at four distinct instants*

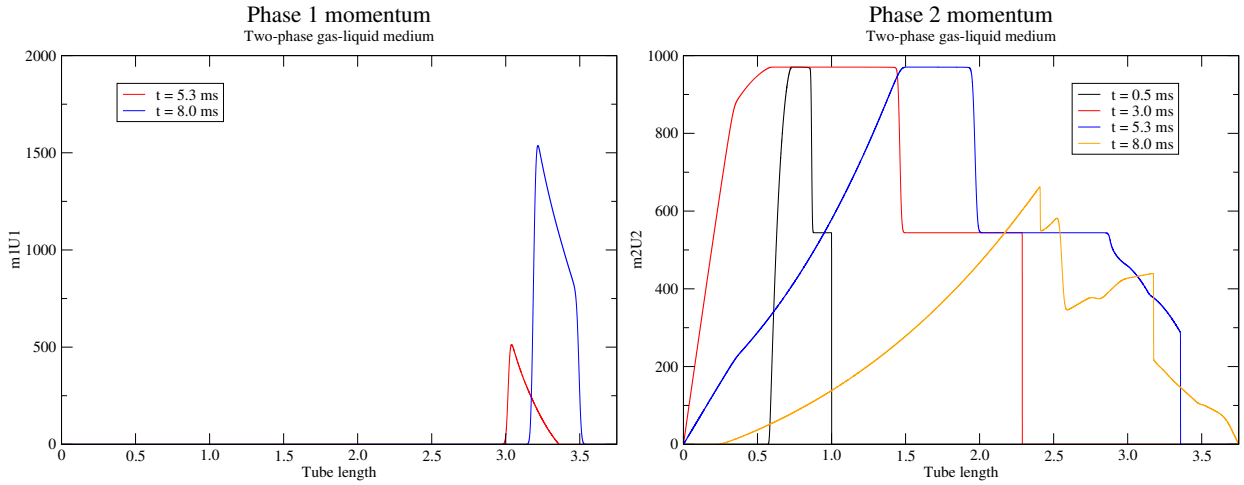

FIGURE 2.12 – *Phase 1 and 2 momentums at four distinct instants*

Finally, Figure 2.14 gives the comparison between the numerical results obtained on different meshes. We notice that the gap between the results gets smaller and smaller as the mesh is refined. Therefore, the discussed 1/50000 mesh size results above are reasonably representative of the model solution.

2.5 Conclusion

This paper is the continuation of research efforts concerning the modeling and the simulation of vapour explosion (*VE*). A previous study of a barotropic three-phase flow model was presented in [6]. In the present paper, we have discussed a three-phase flow model inclu-

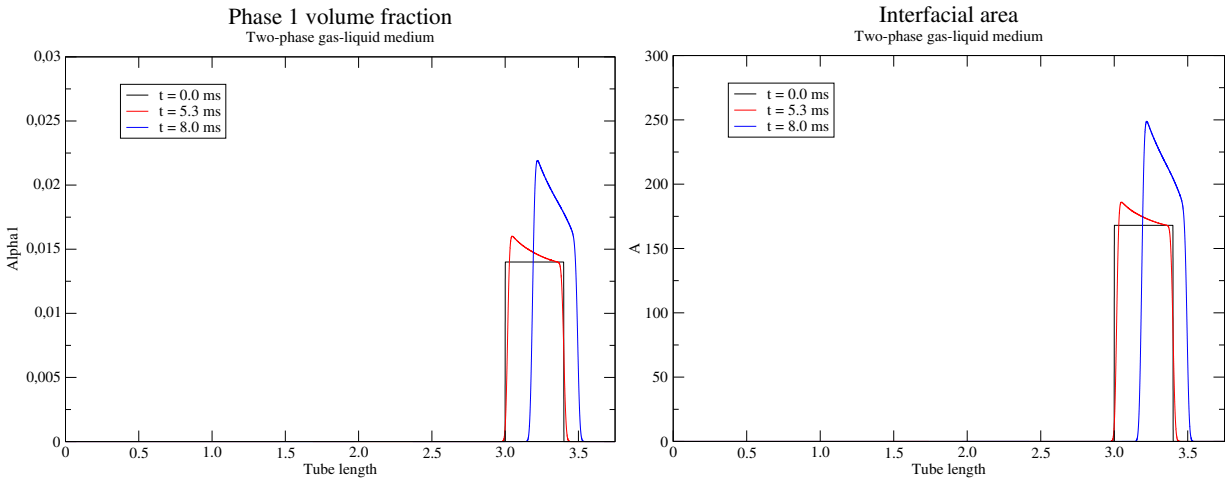

FIGURE 2.13 – *Phase 1 statistical fraction and interfactial area at three distinct instants*

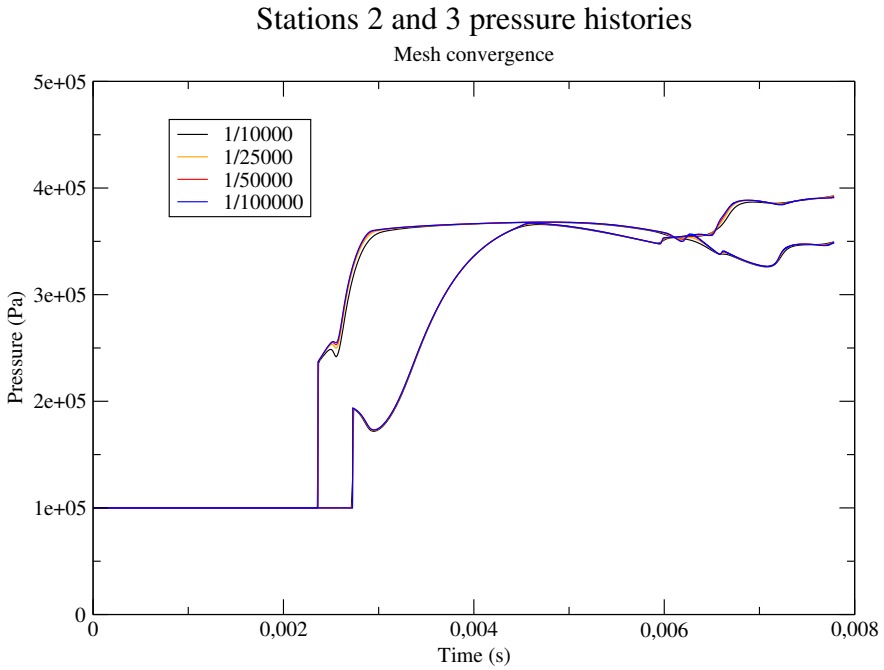

FIGURE 2.14 – *Stations 2 and 3 pressure histories for different meshes*

ding the energy balance. The model properties were highlighted, with special focus on the hyperbolicity, the entropy inequality and the jump conditions. A fractional step method was considered, we have shown that on the continuous level it allows to remain consistent with the entropy equation, and in the discrete framework it enables to get satisfactory results on fine enough meshes. The comparison with the results of the experimental set-up presented in [7, 8] is satisfactory, which means that the model is fairly able to account for the mechanical effects that take place in such gas-droplet flow configurations.

Nevertheless, there are still some points that require more work in order to progress towards a better three-phase flow *VE* oriented model :

— There is a need for more accurate and robust Riemann solvers (see for instance [1, 2, 9, 31] in that direction) ;

— The simulation of vapour explosion [23] requires to take into account mass transfer and heat exchange between components (see Chapter 3).

2.6 Acknowledgements

The first author receives financial support by ANRT and EDF through an EDF/CIFRE grant number 2016/0611. Computational facilities were provided by EDF. Both authors would like to thank Olivier Hurisse for his help and for various useful discussions on the subject.

Bibliographie

[1] A. Ambroso , C. Chalons, F. Coquel and T. Galié, Relaxation and numerical approximation of a two-fluid two-pressure diphasic model, *ESAIM : Mathematical Modelling and Numerical Analysis*, vol. 43, pp. 1063-1097, 2009.

[2] A. Ambroso , C. Chalons and P.-A. Raviart, A Godunov-type method for the seven-equation model of compressible two-phase flow *Comput. and Fluids*, vol. 54, pp. 67-91, 2012.

[3] M.R. Baer and J.W. Nunziato, A two phase mixture theory for the deflagration to detonation transition (DDT) in reactive granular materials, *Int. J. Multiphase Flow*, vol. 12-6, pp. 861-889, 1986.

[4] C. Berthon, Contribution à l'analyse numérique des equations de Navier-Stokes compressibles à deux entropies spécifiques. Applications à la turbulence compressible, *PhD thesis*, Université Paris 6, 1999.

[5] G. Berthoud, Vapor explosions, *Annual Review of Fluid Mechanics*, vol. 32, pp. 573-611, 2000.

[6] H. Boukili and J.M. Hérard, Relaxation and simulation of a barotropic three-phase flow model, *ESAIM : Mathematical Modelling and Numerical Analysis*, vol. 53, pp. 1031-1059, 2019.

[7] A. Chauvin, Étude expérimentale de l'atténuation d'une onde de choc par un nuage de gouttes et validation numérique, *PhD thesis*, Université Aix Marseille, https ://www.theses.fr/2012AIXM4732.pdf, 2012.

[8] A. Chauvin, G. Jourdan, E. Daniel, L. Houas and R. Tosello, Experimental investigation of the propagation of a planar shock wave through a two-phase gas-liquid medium, *Physcis of Fluids*, vol. 23, 113301, 2011.

[9] F. Coquel, J.M. Hérard and K. Saleh, A positive and entropy-satisfying finite volume scheme for the Baer Nunziato model, *Journal of Computational Physics*, vol. 330, pp. 401-435, 2017.

[10] D. A. Drew and S. L. Passman Theory of Multicomponent Fluids, *Springer Verlag*, 1999.

[11] P. Embid and M. Baer, Mathematical analysis of a two-phase continuum mixture theory, *Continuum Mech. Thermodyn*, vol. 4, pp. 279-312, 1992.

[12] S. Gavrilyuk, The structure of pressure relaxation terms : the one-velocity case, *EDF report H-I83-2014-0276-EN*, 2014.

[13] S. Gavrilyuk and R. Saurel, Mathematical and numerical modelling of two-phase compressible flows with micro inertia, *Journal of Computational Physics*, vol. 175, pp. 326-360, 2002.

[14] B. E. Gelfand, Droplet breakup phenomena in flows with velocity lag. *Progr. Energy Combust. Sci.*, vol. 22, pp. 201-265, 1996.

[15] V. Guillemaud, Modélisation et simulation numérique des écoulements diphasiques par une approche bifluide à deux pressions, *Ph.D. thesis*, Université de Provence - Aix-Marseille I, https ://tel.archives-ouvertes.fr/tel-00169178/document, 2007.

[16] E. Han, M. Hantke and S. Müller, Efficient and robust relaxation procedures for multi-component mixtures including phase transition, *Journal of Computational Physics*, vol. 338, pp. 217-239, March 2017.

[17] M. Hantke and S. Müller, Closure conditions for a one temperature non-equilibrium multi-component model of Baer-Nunziato type, *ESAIM proceedings*, vol. 66, pp. 42-60, 2019

[18] J.M. Hérard, A three-phase flow model, *Mathematical and Computer Modelling*, vol. 45, pp. 732-755, 2007.

[19] J.M. Hérard and O. Hurisse, A fractional step method to compute a class of compressible gas-liquid flows, *Computers and Fluids*, vol. 55, pp. 57-69, 2012.

[20] J.M. Hérard, H. Mathis, A three-phase flow model with two miscible phases, *ESAIM : Mathematical Modelling and Numerical Analysis*, vol. 53, pp. 1373-1389, 2019,

[21] J.M. Hérard, K. Saleh, N. Seguin, Some mathematical properties of a hyperbolic multiphase flow model, *HAL preprint available on https : https ://hal.archives-ouvertes.fr/hal-01921027*, 2018.

[22] T.Y. Hou and P.G. LeFoch, Why nonconservative schemes converge to wrong solutions : error analysis, *Mathematics of computation*, vol. 62(206), pp. 497-530, 1994.

[23] I. Huhtiniemi, H. Hohmann, R. Faraoni, M. Field, R. Gambaretti and K. Klein, KROTOS 38 to KROTOS 44 : Data Report, *Technical Note No. I.96.37, Joint Research Centre Ispra*, February 1996.

[24] O. Hurisse, L. Quibel, A homogeneous model for compressible three-phase flows involving heat and mass transfer, *ESAIM proceedings*, vol. 66, pp. 84-108, 2019.

[25] M. Ishii, Thermo-fluid dynamic theory of two-phase flows, *Eyrolles - Collection de la Direction des Etudes et Recherches d'Electricité de France*, 1975.

[26] A.K. Kapila, S.F. Son, J.B. Bdzil, R. Menikoff and D.S. Stewart, Two phase modeling of deflagration to detonation transition : srtucture of the velocity relaxation zone, *Physics of Fluids*, vol. 9(12), pp. 3885-3897, 1997.

[27] R. Meignen, B. Raverdy, S. Picchi and J. Lamome, The challenge of modelling fuel-coolant interaction. Part II : steam explosion, *Nuclear Engineering and Design*, vol. 280, pp. 528-541, 2014.

[28] S. Müller, M. Hantke and P. Richter, Closure conditions for non-equilibrium multi-component models, *Continuum Mechanics and Thermodynamics*, vol. 28, pp. 1157-1189, 2016.

[29] Nuclear Energy Agency Committee on the Safety of Nuclear Installations, Reactivity Initiated Accident (RIA) Fuel Codes Benchmark Phase-II, https ://www.oecd-nea.org/nsd/docs/2016/csni-r2016-6-vol1.pdf.

[30] E. Rusanov, Calculation of interaction of non steady shock waves with obstacles, *Journal of Computational Mathematics and Physics*, vol. 1, pp. 267-279, 1961.

[31] K. Saleh, A relaxation scheme for a hyperbolic multiphase flow model. Part I : barotropic EOS, *ESAIM : M2AN*, DOI : https ://doi.org/10.1051/m2an/2019034, vol. 53, pp. 1763-1795, 2019.

[32] U.S. NRC Glossary, Loss of coolant accident (LOCA), https ://www.nrc.gov/reading-rm/basic-ref/glossary/loss-of-coolant-accident-loca.html.

2.7 Appendix A1 - Instantaneous pressure relaxation

Here in this appendix, we consider the case of a pressure relaxation system where the pressures differences $p_k - p_l$ are neglected. In this case, we get at once :

$$\begin{cases} p_1 = p_2 = p_3 = \mathcal{P} & \text{(2.76a)} \\ \partial_t m_k = 0 & \text{(2.76b)} \\ \partial_t (m_k \mathbf{U}_k) = \mathbf{0} & \text{(2.76c)} \\ \partial_t (\alpha_k E_k) + \mathcal{P} \partial_t \alpha_k = 0 & \text{(2.76d)} \end{cases}$$

The energy balance (2.76d) can be rewritten as :

$$\partial_t (m_k e_k) + \mathcal{P} \partial_t \alpha_k = 0$$

In order to compute a discrete approximate solution, we apply an implicit Euler scheme :

$$\frac{(m_k e_k) - (m_k e_k)^*}{\Delta t} + \mathcal{P} \frac{\alpha_k - \alpha_k^*}{\Delta t} = \frac{1}{\Delta t} \left[(m_k e_k) - (m_k e_k)^* + \mathcal{P}(\alpha_k - \alpha_k^*) \right] = 0 \tag{2.77}$$

where the $*$ exponent indicates the given initial data.

For further development, we consider a Stiffened Gas EOS :

$$(\gamma_k - 1) m_k e_k = \alpha_k p_k + \alpha_k \gamma_k \Pi_k \tag{2.78}$$

This gives :

$$(\alpha_k \mathcal{P} + \alpha_k \gamma_k \Pi_k) - (\alpha_k p_k + \alpha_k \gamma_k \Pi_k)^* + (\gamma_k - 1) \mathcal{P} (\alpha_k - \alpha_k^*) = 0 \tag{2.79}$$

By denoting $\mathcal{P}_k^* = (\alpha_k p_k + \alpha_k \gamma_k \Pi_k)^*$, we express the statistical fractions in function of the pressure :

$$\alpha_k = \frac{\mathcal{P}_k^* + (\gamma_k - 1) \alpha_k^* \mathcal{P}}{\gamma_k (\mathcal{P} + \Pi_k)} \tag{2.80}$$

Now, to obtain the pressure $\mathcal{P}$, we solve the saturation condition :

$$\sum_{k=1}^{3} \alpha_k = 1 \tag{2.81}$$

Thus, we consider the function :

$$h(\mathcal{P}) = \sum_{k=1}^{3} \frac{\mathcal{P}_k^* + (\gamma_k - 1)\alpha_k^* \mathcal{P}}{\gamma_k(\mathcal{P} + \Pi_k)} \tag{2.82}$$

which definition domain is $\mathcal{D} =]-x_0, +\infty[$, where $x_0 = \Pi_{k_0} = min_{k=1,2,3}(\Pi_k)$. We have the following key property :

Property :
The equation $h(\mathcal{P}) = 1$ admits a unique solution in the domain $\mathcal{D}$.

Proof :
For any $x \in \mathcal{D}$ we have :

$$h'(x) = -\sum_{k=1}^{3} \frac{\alpha_k^*(p_k^* + \Pi_k)}{\gamma_k(x + \Pi_k)^2} < 0$$

Moreover, we have :

$$\lim_{x \to +\infty} h(x) = \sum_{k=1}^{3} \frac{\alpha_k^*(\gamma_k - 1)}{\gamma_k} = 1 - \sum_{k=1}^{3} \frac{\alpha_k^*}{\gamma_k} < 1$$

and :

$$\lim_{x \to -x_0+} h(x) = \lim_{x \to -x_0+} \left[\sum_{k=1, k \neq k_0}^{3} \frac{\mathcal{P}_k^* + (\gamma_k - 1)\alpha_k^*(-\Pi_{k_0})}{\gamma_k(-\Pi_{k_0} + \Pi_k)} + \frac{\mathcal{P}_{k_0}^* + (\gamma_{k_0} - 1)\alpha_{k_0}^* x}{\gamma_{k_0}(x + \Pi_{k_0})} \right]$$

A straightforward computation gives :

$$\mathcal{P}_{k_0}^* + (\gamma_{k_0} - 1)\alpha_{k_0}^*(-\Pi_{k_0}) = \alpha_{k_0}^*(p_{k_0}^* + \Pi_{k_0}) > 0$$

This allows to obtain the limit :

$$\lim_{x \to -x_0+} h(x) = +\infty$$

and therefore the desired result. □

Remark :

— *The statistical fractions defined by* (2.80) *are in the admissible range* $[0, 1]$. *In fact,* (2.80) *ensures that* $\alpha_k \geq 0$, *moreover,* $\mathcal{P}$ *satisfies* (2.81), *hence* $0 \leq \alpha_k \leq 1$.

— *This instantaneous pressure relaxation algorithm can be defined for a N-phase flow where* $N > 3$. *The fractions* α_k *and the pressure* $\mathcal{P}$ *are defined in the same way in the Stiffened Gas EOS case.*□

2.8 Appendix A2 - Threshold effect

In the two-phase framework, we consider the counterpart of (2.41), which represents the pressure relaxation sub-step :

$$\begin{cases} \partial_t \alpha_2 = \dfrac{\alpha_1 \alpha_2}{\tau_{12}^P(\mathbf{W})\Pi_0}(p_2 - p_1) & \text{(2.83a)} \\ \partial_t(m_1 e_1) + p_2 \partial_t \alpha_1 = 0 & \text{(2.83b)} \\ \partial_t(m_2 e_2) + p_2 \partial_t \alpha_2 = 0 & \text{(2.83c)} \end{cases}$$

with : $\partial_t m_k = 0$ and $\partial_t(m_k \mathbf{U}_k) = \mathbf{0}$ for $k = 1, 2$.

We denote :

$$A_k = \frac{\rho_k c_k^2}{\alpha_k} \quad ; \quad b_1 = \left(\rho_1 \frac{\partial e_1}{\partial p_1}\right)^{-1} > 0 \quad ; \quad \tau_{12}^P(\mathbf{W}) > 0$$

Using the same method of the paragraph 2.2.2.6, we prove that the pressure difference $y_{12} = p_1 - p_2$ satisfies the equation :

$$\partial_t y_{12} + (A_1 + A_2)\frac{\alpha_1 \alpha_2}{\tau_{12}^P \Pi_0} y_{12} - b_1 \frac{\alpha_2}{\tau_{12}^P \Pi_0} y_{12}^2 = 0$$

In order to simplify the analysis of the equation, we denote :

$$a(t) = (A_1 + A_2)\frac{\alpha_1 \alpha_2}{\tau_{12}^P \Pi_0} \quad ; \quad b(t) = b_1 \frac{\alpha_2}{\tau_{12}^P \Pi_0}$$

We have then :

$$\partial_t y_{12} = -a(t) y_{12} + b(t) y_{12}^2 \tag{2.84}$$

We denote :

$$\mu(t) = \int_0^t a(s)\,\mathrm{d}s \geq 0 \quad ; \quad x_{12} = e^{\mu(t)} y_{12}$$

We notice that the differential equation verified by x_{12} is :

$$\partial_t x_{12} = b(t) e^{-\mu(t)} x_{12}^2$$

By solving this equation, we have the general solution of (2.84) :

$$y_{12}(t) = \frac{y_{12}^0 e^{-\mu(t)}}{1 - y_{12}^0 \int_0^t b(s) e^{-\mu(s)}\,\mathrm{d}s} \tag{2.85}$$

The behaviour of $y_{12}(t)$ therefore depends on the initial condition $y_{12}^0 = y_{12}(0)$:

— If $y_{12}^0 < 0$:
The solution $y_{12}(t)$ is defined on $\mathbb{R}^+$, and we can check that it is decreasing, which ensures the relaxation behaviour.

— If $y_{12}^0 > 0$ and $y_{12}^0 < y_{12}^*$ where y_{12}^* is such that : $1 = y_{12}^* \int_0^\infty b(s) e^{-\mu(s)}\,\mathrm{d}s$:
$y_{12}(t)$ is defined on $\mathbb{R}^+$, and we can prove in the case $a(t) = a_0$ and $b(t) = b_0$ that the relaxation behaviour is ensured : $\lim_{t\to\infty} y_{12}(t) = 0$.

— If $y_{12}^0 > y_{12}^*$:

In this case there exists a certain $t_0 \in \mathbb{R}^{*+}$ such that :

$$1 - y_{12}^0 \int_0^{t_0} b(s) e^{-\mu(s)} \, \mathrm{d}s = 0$$

The function y_{12} is then not well defined on $\mathbb{R}^+$ and the relaxation can't be ensured.

2.9 Appendix A3 - Two particular analytical solutions of the velocity relaxation system

In the velocity relaxation sub-step, we recall that the concerned PDE system is (2.37). In the pure $1D$ framework it can be rewritten as :

$$\left\{ \begin{array}{l} \partial_t \alpha_k = 0 \\ \partial_t m_k = 0 \\ \partial_t (m_k u_k) = \sum_{l=1, l \neq k}^{3} e_{kl}(\mathbf{w})(u_l - u_k) \\ \partial_t (\alpha_k E_k) = \sum_{l=1, l \neq k}^{3} \frac{e_{kl}(\mathbf{w})}{2}(u_l^2 - u_k^2) \end{array} \right.$$

The three momentum equations are equivalent to :

$$\left\{ \begin{array}{l} m_1 \partial_t u_1 = e_{12}(\mathbf{w})(u_2 - u_1) + e_{13}(\mathbf{w})(u_3 - u_1) \\ m_2 \partial_t u_2 = e_{12}(\mathbf{w})(u_1 - u_2) + e_{23}(\mathbf{w})(u_3 - u_2) \\ \partial_t (m_1 u_1 + m_2 u_2 + m_3 u_3) = 0 \end{array} \right. \tag{2.86}$$

where the phase 3 equation has been replaced by the total momentum conservation equation.

If we denote $Q_0 = m_1 u_1(t=0) + m_2 u_2(t=0) + m_3 u_3(t=0)$ the total momentum in the velocity relaxation sub-step, we can integrate the phase 3 equation and write :

$$u_3(t) = \frac{1}{m_3}(Q_0 - m_1 u_1(t) - m_2 u_2(t)) \tag{2.87}$$

We use (2.87) to replace $u_3(t)$ in (2.86), this gives :

$$\left\{ \begin{array}{l} \partial_t u_1 + \left(\frac{e_{12}(\mathbf{w})}{m_1} + \frac{e_{13}(\mathbf{w})}{m_1} + \frac{e_{13}(\mathbf{w})}{m_3} \right) u_1 - \left(\frac{e_{12}(\mathbf{w})}{m_1} - \frac{m_2 e_{13}(\mathbf{w})}{m_1 m_3} \right) u_2 = \frac{e_{13}(\mathbf{w})}{m_1 m_3} Q_0 \\ \partial_t u_2 + \left(\frac{e_{12}(\mathbf{w})}{m_2} + \frac{e_{23}(\mathbf{w})}{m_2} + \frac{e_{23}(\mathbf{w})}{m_3} \right) u_2 - \left(\frac{e_{12}(\mathbf{w})}{m_2} - \frac{m_1 e_{23}(\mathbf{w})}{m_2 m_3} \right) u_1 = \frac{e_{23}(\mathbf{w})}{m_2 m_3} Q_0 \end{array} \right. \tag{2.88}$$

We assume that the coefficients e_{kl} comply with :

$$m_1 e_{23}(\mathbf{w}) = m_2 e_{13}(\mathbf{w}) = m_3 e_{12}(\mathbf{w}) \tag{2.89}$$

This allows to decouple u_1 and u_2 equations, which become :

$$\left\{ \begin{array}{l} \partial_t u_1 + \left(\frac{e_{12}(\mathbf{w})}{m_1} + \frac{e_{13}(\mathbf{w})}{m_1} + \frac{e_{13}(\mathbf{w})}{m_3} \right) u_1 = \frac{e_{13}(\mathbf{w})}{m_1 m_3} Q_0 \\ \partial_t u_2 + \left(\frac{e_{12}(\mathbf{w})}{m_2} + \frac{e_{23}(\mathbf{w})}{m_2} + \frac{e_{23}(\mathbf{w})}{m_3} \right) u_2 = \frac{e_{23}(\mathbf{w})}{m_2 m_3} Q_0 \end{array} \right. \tag{2.90}$$

Many choices are then possible to fully explicit the analytical solution, depending on the choice of e_{kl}, as far as the constraint (2.89) is respected.

Here we consider two different configurations :

	Phase $k=1$	Phase $k=2$	Phase $k=3$
u_k	10.00	150.0	200.0
p_k	7.10^5	7.10^5	4.10^5
ρ_k	10.00	1.00	1.50
α_k	0.30	0.50	0.20
γ_k	27.07	3.00	2.00
Π_k	$8.06\ 10^7$	0.00	0.00

TABLE 2.2 – *Velocity relaxation initialisation dataset*

— **Test-case A3.1 : constant** e_{kl}

We take $e_{12} = 1$ (or any other constant), and we compute e_{13} and e_{23} with respect to (2.89). We denote :

$$\left\{ \begin{array}{ll} A_1 = \frac{e_{12}(\mathbf{w})}{m_1} + \frac{e_{13}(\mathbf{w})}{m_1} + \frac{e_{13}(\mathbf{w})}{m_3} & Q_1 = \frac{e_{13}(\mathbf{w})}{m_1 m_3} Q_0 \\ A_2 = \frac{e_{12}(\mathbf{w})}{m_2} + \frac{e_{23}(\mathbf{w})}{m_2} + \frac{e_{23}(\mathbf{w})}{m_3} & Q_2 = \frac{e_{23}(\mathbf{w})}{m_2 m_3} Q_0 \end{array} \right. \tag{2.91}$$

A_1, A_2, Q_1 and Q_2 are time-independent constants, we can then integrate (2.90) as :

$$\left\{ \begin{array}{l} u_1(t) = \frac{Q_1}{A_1} + \left(u_1(t=0) - \frac{Q_1}{A_1} \right) exp(-A_1 t) \\ u_2(t) = \frac{Q_2}{A_2} + \left(u_2(t=0) - \frac{Q_2}{A_2} \right) exp(-A_2 t) \end{array} \right. \tag{2.92}$$

where $\frac{Q_1}{A_1} = \frac{Q_2}{A_2}$.
The velocity u_3 is given by (2.87), and the energies are obtained by direct integration of the energy balance of (2.86).

The initial dataset that was considered for this case is given in Table 2.2. The time relaxation scales are chosen such that :

$$e_{12} = 1.00 \quad ; \quad e_{13} = \frac{m_3}{m_2} e_{12} \quad ; \quad e_{23} = \frac{m_3}{m_1} e_{12} \tag{2.93}$$

— **Test-case A3.2 : time-dependent** e_{kl}

In this case we choose the coefficients e_{kl} such that :

$$m_1 e_{23}(\mathbf{w}) = m_2 e_{13}(\mathbf{w}) = m_3 e_{12}(\mathbf{w}) = t + 1 \tag{2.94}$$

This gives :

$$\left\{ \begin{array}{l} \partial_t u_1 + \alpha(t+1) u_1 = \beta(t+1) \\ \partial_t u_2 + \alpha(t+1) u_2 = \beta(t+1) \end{array} \right. \tag{2.95}$$

where α and β are time-independent constants :

$$\left\{ \begin{array}{l} \alpha = \frac{1}{m_1 m_2} + \frac{1}{m_1 m_3} + \frac{1}{m_2 m_3} \\ \beta = \frac{Q_0}{m_1 m_2 m_3} \end{array} \right. \tag{2.96}$$

This gives :

$$\left\{ \begin{array}{l} u_1(t) = \frac{\beta}{\alpha} + \left(u_1(t=0) - \frac{\beta}{\alpha}\right) exp(-\alpha(t^2/2+t)) \\ u_2(t) = \frac{\beta}{\alpha} + \left(u_2(t=0) - \frac{\beta}{\alpha}\right) exp(-\alpha(t^2/2+t)) \end{array} \right. \tag{2.97}$$

The velocity u_3 and the energies are obtained similarly to the first case.

Practically, for this case, the initial dataset is identical to the test-case *A3.1* (see Table 2.2).

2.10 Appendix A4 - A particular analytical solution of the pressure relaxation system

We recall that the considered PDE system in the pressure relaxation sub-step is (2.41) :

$$\left\{ \begin{array}{l} \partial_t \alpha_k = S_k^{\alpha}(\mathbf{W}) \\ \partial_t m_k = 0 \\ \partial_t (m_k \mathbf{U}_k) = \mathbf{0} \\ \partial_t (\alpha_k E_k) - \sum_{l=1, l\neq k}^{3} \Pi_{kl}(\mathbf{W}) \partial_t \alpha_l = 0 \end{array} \right.$$

This system is equivalent to :

$$\left\{ \begin{array}{ll} \partial_t \alpha_2 = \displaystyle\sum_{l=1, l\neq 2}^{3} \frac{\alpha_2 \alpha_l}{\tau_{2l}^P(\mathbf{W})\Pi_0}(p_2 - p_l) & \text{(2.98a)} \\ \partial_t \alpha_3 = \displaystyle\sum_{l=1, l\neq 3}^{3} \frac{\alpha_3 \alpha_l}{\tau_{3l}^P(\mathbf{W})\Pi_0}(p_3 - p_l) & \text{(2.98b)} \\ \partial_t (m_1 e_1) - p_2 \partial_t \alpha_2 - p_3 \partial_t \alpha_3 = 0 & \text{(2.98c)} \\ \partial_t (m_2 e_2) + p_2 \partial_t \alpha_2 = 0 & \text{(2.98d)} \\ \partial_t (m_3 e_3) + p_3 \partial_t \alpha_3 = 0 & \text{(2.98e)} \end{array} \right.$$

where the partial masses and momentums are constants : $\partial_t m_k = 0$, $\partial_t (m_k \mathbf{U}_k) = \mathbf{0}$. Thus, the variables are : $(\alpha_2, \alpha_3, \alpha_1 p_1, \alpha_2 p_2, \alpha_3 p_3)$.

In order to build analytical solution for the system (2.98), we consider the case of the *Ideal Gas* EOS :

$$m_k e_k = \frac{\alpha_k p_k}{\gamma_k - 1} \tag{2.99}$$

Property A4.1 :
Under the assumption (2.99), we have the following result :

$$\left\{ \begin{array}{ll} p_2 \alpha_2^{\gamma_2} = K_2 & \text{(2.100a)} \\ p_3 \alpha_3^{\gamma_3} = K_3 & \text{(2.100b)} \\ \alpha_1 p_1 = K_1 - \dfrac{\gamma_1 - 1}{\gamma_2 - 1} \alpha_2 p_2 - \dfrac{\gamma_1 - 1}{\gamma_3 - 1} \alpha_3 p_3 & \text{(2.100c)} \end{array} \right.$$

where K_1, K_2 and K_3 are positive integration constants :

$$\begin{cases} K_2 = (p_2\alpha_2^{\gamma_2})(t=0) \\ K_3 = (p_3\alpha_3^{\gamma_3})(t=0) \\ K_1 = (\gamma_1 - 1)\left(\sum_{k=1}^{3} \frac{\alpha_k p_k}{\gamma_k - 1}\right)(t=0) \end{cases}$$

We have also :

$$\begin{cases} \Pi_0 \partial_t \alpha_2 = -\dfrac{K_1}{\tau_{12}^P}\alpha_2 + \dfrac{\gamma_1 - \gamma_2}{\gamma_2 - 1}\dfrac{K_2}{\tau_{12}^P}\alpha_2^{2-\gamma_2} + \dfrac{K_2}{\tau_{12}^P}\alpha_2^{1-\gamma_2} \\ \qquad\qquad + \left(\dfrac{1}{\tau_{23}^P} - \dfrac{1}{\tau_{12}^P}\right) K_2 \alpha_2^{1-\gamma_2}\alpha_3 + \left(\dfrac{\gamma_1 - 1}{\gamma_3 - 1}\dfrac{1}{\tau_{12}^P} - \dfrac{1}{\tau_{23}^P}\right) K_3 \alpha_2 \alpha_3^{1-\gamma_3} \\ \Pi_0 \partial_t \alpha_3 = -\dfrac{K_1}{\tau_{13}^P}\alpha_3 + \dfrac{\gamma_1 - \gamma_3}{\gamma_3 - 1}\dfrac{K_3}{\tau_{13}^P}\alpha_3^{2-\gamma_3} + \dfrac{K_3}{\tau_{13}^P}\alpha_3^{1-\gamma_3} \\ \qquad\qquad + \left(\dfrac{1}{\tau_{23}^P} - \dfrac{1}{\tau_{13}^P}\right) K_3 \alpha_3^{1-\gamma_3}\alpha_2 + \left(\dfrac{\gamma_1 - 1}{\gamma_2 - 1}\dfrac{1}{\tau_{13}^P} - \dfrac{1}{\tau_{23}^P}\right) K_2 \alpha_3 \alpha_2^{1-\gamma_2} \end{cases} \tag{2.101}$$

Proof :

(2.100a) and (2.100b) are nothing but the conservation of the specific entropies of phases 2 and 3. In fact, we have seen in (2.45) that :

$$\partial_t s_2 = \partial_t s_3 = 0$$

This means that :

$$\partial_t(p_2\rho_2^{-\gamma_2}) = \partial_t(p_3\rho_3^{-\gamma_3}) = 0$$

Knowing that $m_k = \alpha_k\rho_k$ and $\partial_t m_k = 0$ in the pressure relaxation step, we conclude that (2.100a) and (2.100b) hold.

(2.100c) is simply obtained by writing the conservation of the total energy :

$$\partial_t(m_1 e_1 + m_2 e_2 + m_3 e_3) = 0$$

Therefore, we use the latter results (2.100) to develop (2.98a) and (2.98b), this allows to obtain (2.101) through direct calculations. □

In order to explicitly develop the analytical solution, we add more assumptions :

— The three phases have an identical EOS :

$$\gamma_1 = \gamma_2 = \gamma_3 := \gamma > 1 \tag{2.102}$$

— The pressure relaxation time scales are all equal to the same *constant* value :

$$\forall k, l : \tau_{kl}(\mathbf{W}) := \tau_0^P$$

and we denote :

$$\tilde{\tau}_0 = \tau_0^P \Pi_0 \tag{2.103}$$

Under these assumptions, we have :

Property A4.2 :
The solution of (2.98) with assumptions (2.102) *and* (2.103) *reads :*

$$\begin{cases} \alpha_2(t) = \left[(\alpha_2^0)^\gamma exp\left(-\gamma\frac{K_1}{\tilde{\tau}_0}t\right) + A_2\left(1 - exp\left(-\gamma\frac{K_1}{\tilde{\tau}_0}t\right)\right)\right]^{1/\gamma} & \text{(2.104a)} \\ \alpha_3(t) = \left[(\alpha_3^0)^\gamma exp\left(-\gamma\frac{K_1}{\tilde{\tau}_0}t\right) + A_3\left(1 - exp\left(-\gamma\frac{K_1}{\tilde{\tau}_0}t\right)\right)\right]^{1/\gamma} & \text{(2.104b)} \\ (\alpha_2 p_2)(t) = K_2(\alpha_2(t))^{1-\gamma} & \text{(2.104c)} \\ (\alpha_3 p_3)(t) = K_3(\alpha_3(t))^{1-\gamma} & \text{(2.104d)} \\ (\alpha_1 p_1)(t) = K_1 - K_2(\alpha_2(t))^{1-\gamma} - K_3(\alpha_3(t))^{1-\gamma} & \text{(2.104e)} \end{cases}$$

where $A_k = \frac{K_k}{K_1}$, α_2^0 *and* α_3^0 *are the initial values.*

Proof :
Under the assumptions (2.102) and (2.103), the system (2.101) becomes :

$$\begin{cases} \tilde{\tau}_0\partial_t\alpha_2 = -K_1\alpha_2 + \frac{K_2}{\alpha_2^{\gamma-1}} \\ \\ \tilde{\tau}_0\partial_t\alpha_3 = -K_1\alpha_3 + \frac{K_3}{\alpha_3^{\gamma-1}} \end{cases}$$

To integrate these ODEs we denote for $k = 2, 3$:

$$\Psi_k = \alpha_k^\gamma$$

The equation verified by Ψ_k is :

$$\partial_t\Psi_k + \gamma\frac{K_1}{\tilde{\tau}_0}\Psi_k = \gamma\frac{K_1}{\tilde{\tau}_0}A_k$$

By solving this equation we obtain :

$$\Psi_k(t) = \Psi_k(t=0)exp\left(-\gamma\frac{K_1}{\tilde{\tau}_0}t\right) + A_k\left(1 - exp\left(-\gamma\frac{K_1}{\tilde{\tau}_0}t\right)\right)$$

This allows to retrieve the result (2.104). □

In Table 2.3 we give the initial dataset that was used for the pressure relaxation verification computations :

	Phase $k=1$	Phase $k=2$	Phase $k=3$
u_k	0.00	0.0	0.0
p_k	1.10^5	5.10^5	1.10^6
ρ_k	100.00	200.00	300.00
α_k	0.65	0.15	0.20
γ_k	2.00	2.00	2.00
Π_k	0.00	0.00	0.00

TABLE 2.3 – *Pressure relaxation initialisation dataset*

2.11 Appendix A5 - Initial data of the shock tube test-cases

In this appendix, we present the initial datasets that were considered in the shock tube numerical simulations.

Single-phase flow configuration :

$$\begin{array}{rl} \underline{\text{Left } (x<0.75)} & \underline{\text{Right } (0.75<x)} \\ p_k = 7.10^5 \ for \ k=1,2,3 & p_k = 1.10^5 \ for \ k=1,2,3 \\ u_k = 0 \ for \ k=1,2,3 & u_k = 0 \ for \ k=1,2,3 \\ \alpha_1 = \alpha_3 = 10^{-10} & \alpha_1 = \alpha_3 = 10^{-10} \\ \alpha_2 = 1-\alpha_1-\alpha_3 & \alpha_2 = 1-\alpha_1-\alpha_3 \end{array}$$

Gas-solid and gas-liquid two-phase flow configurations :

$$\begin{array}{rl} \underline{\text{Left } (x<0.75)} & \underline{\text{Right } (0.75<x)} \\ P_k = 7.10^5 \ for \ k=1,2,3 & P_k = 1.10^5 \ for \ k=1,2,3 \\ u_k = 0 \ for \ k=1,2,3 & u_k = 0 \ for \ k=1,2,3 \\ \alpha_3 = 10^{-10} & \alpha_3 = 10^{-10} \\ \alpha_2 = 1-\alpha_1-\alpha_3 & \alpha_2 = 1-\alpha_1-\alpha_3 \\ \alpha_1 = 10^{-10} & \alpha_1 = 0.0104 \text{ if } [2.97<x<3.37] \text{ and } 10^{-10} \text{ if not} \end{array}$$

The EOS were chosen such that :

— Phase 1 : *Stiffened Gas* EOS (liquid water)

$$p_1 + \gamma_1 \Pi_1 = (\gamma_1 - 1)\rho_1 \epsilon_1$$

with :

$$\left\{ \begin{array}{l} \gamma_1 = 27.07619047 \\ \Pi_1 = 8.06358480 \ x10^7 \end{array} \right.$$

— Phase 2 : *Perfect Gas* EOS (air)

$$p_2 = (\gamma_2 - 1)\rho_2 \epsilon_2$$

with $\gamma_2 = 1.40$;

— Phase 3 : identical to phase 2.

2.12 Appendix A6 - Study of the pressure-velocity relaxation effects

In this appendix, we focus on the pressure-velocity relaxation effects embedded in the global PDE system (2.1). In Section 2.3, different pressure-velocity relaxation algorithms were presented, and a two-phase flow test case was given in Section 2.4. Here we consider a three-phase shock-tube configuration (see Figure 2.15), where a shock-wave carried by the phase 2 travels along the low-pressure side of the tube. It crosses two distinct domains where phases 1 and 3 are present at different proportions.

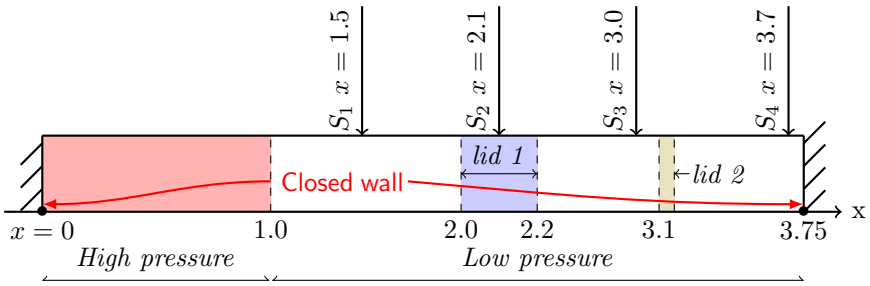

FIGURE 2.15 – *Scheme of the three-phase shock tube*

Numerically speaking, the shock-tube was initialized as follows :

	Left $(x < 1.0)$	Right $(1.0 < x)$
$P_k = 15.10^5$	$for\ k = 1, 2, 3$	$P_k = 1.10^5\ for\ k = 1, 2, 3$
	$\rho_1 = 998.1$	$\rho_1 = 998.1$
	$\rho_2 = \rho_3 = 8.89$	$\rho_2 = \rho_3 = 1.27$
	$\alpha_3 = 10^{-10}$	α_3 function of x
	$\alpha_1 = 10^{-10}$	α_1 function of x
	$\alpha_2 = 1 - \alpha_1 - \alpha_3$	$\alpha_2 = 1 - \alpha_1 - \alpha_3$
$u_k = 0\ for\ k = 1, 2, 3$		$u_k = 0\ for\ k = 1, 2, 3$

With : $\alpha_1 = 0.01$ for $x \in [2.0, 2.2]$ and $\alpha_1 = 10^{-10}$ elsewhere. For $k = 3$, $\alpha_3 = 0.01$ for both $x \in [2.0, 2.2]$ and $x \in [3.08, 3.12]$, and $\alpha_3 = 10^{-10}$ elsewhere. The chosen EOS are a mix of *Stiffened Gas* and *Perfect Gas* EOS, as shown below in Table 2.4.

Phase k	γ_k	Π_k	q'_k	$C_{V,k}$
1	22.83859097	8063584.804	2116.625872	10.58283017
2	1.655128030	37258761.46	1000.000000	1395.286166
3	1.401153242	0.00	-1836.098569	713.1396320

TABLE 2.4 – EOS parameters for the three-phase pressure-velocity relaxations test case

As presented in subsection 2.3.3, we have many simulation possibilities considering the different pressure and velocity relaxation algorithms, as well as the parameters that are not given by the mathematical modelling, notably the relaxation characteristic times. Thus, we focus on the following three configurations :

— *Configuration 1* :
We consider *Algorithm 3.3.1.1* for the velocity relaxation, with :

$$\begin{cases} e_{12}(\mathbf{W}) = \frac{1}{8} A \rho_2 C_{12} |U_1 - U_2| \\ e_{13}(\mathbf{W}) = \frac{m_3}{m_2} e_{12}(\mathbf{W}) \\ e_{23}(\mathbf{W}) = \frac{m_3}{m_1} e_{12}(\mathbf{W}) \end{cases} \tag{2.105}$$

The Closure of e_{12} (see Chapter 1 subsection 4.2) gives an implicit definition of the velocity relaxation time scale τ_{12}^U, the chosen e_{13} and e_{23} allow to retrieve the same relaxation time scale $\tau_{12}^U = \tau_{13}^U = \tau_{23}^U = \tau^U$ while being consistent with the general form :

$$e_{kl}(\mathbf{W}) = \frac{1}{\tau_{kl}^U} \frac{m_k m_l}{m_1 + m_2 + m_3} \tag{2.106}$$

For the pressure relaxation, we consider *Algorithm 3.3.2.1* with the same relaxation time scale for all the phases :

$$\tau_{kl}^P(\mathbf{W}) \Pi_0 = \tilde{\tau}_0^P = 10^{-5} \tag{2.107}$$

— *Configuration 2* :
Here we consider the same relaxations algorithms of the *Configuration 1*, but with the characteristic times :

$$\begin{cases} \tau_{Config.2}^U = \tau_{kl}^U / 10^N \\ \tau_{Config.2}^P = \tau_{kl}^P / 10^N \end{cases} \tag{2.108}$$

Several values of N were tested in order to understand the impact of these relaxation time scales on the relaxation procedure, the value we present in this *Configuration 2* is $N = 10$.

— *Configuration 3* :
For this configuration, we consider the instantaneous relaxation algorithms, both for the pressure and the velocity.

In order to comment the computational results, we restrict the scope of the analysis to the following three aspects : the mesh convergence, the comparison of *Configuration 1* and *Configuration 2*, and the comparison of *Configuration 2* and *Configuration 3*.

(i) **Mesh convergence**
Figure 2.16 gives the comparison in terms of velocity of the results on different meshes for the three configurations. Four meshes were tested, from 1000 elements per meter up

to 100000. The conclusion that stands for the three configurations is, while the 1000 element mesh allows to get the correct order of magnitude of the velocity, it is not fine enough to catch all the intermediate states, at it can be seen on *Configuration 1* velocity U_3 figure. When the mesh is refined, the intermediate states are well retrieved, the shocks are straight, and the gap between the the meshes gets reduced with each refinement.

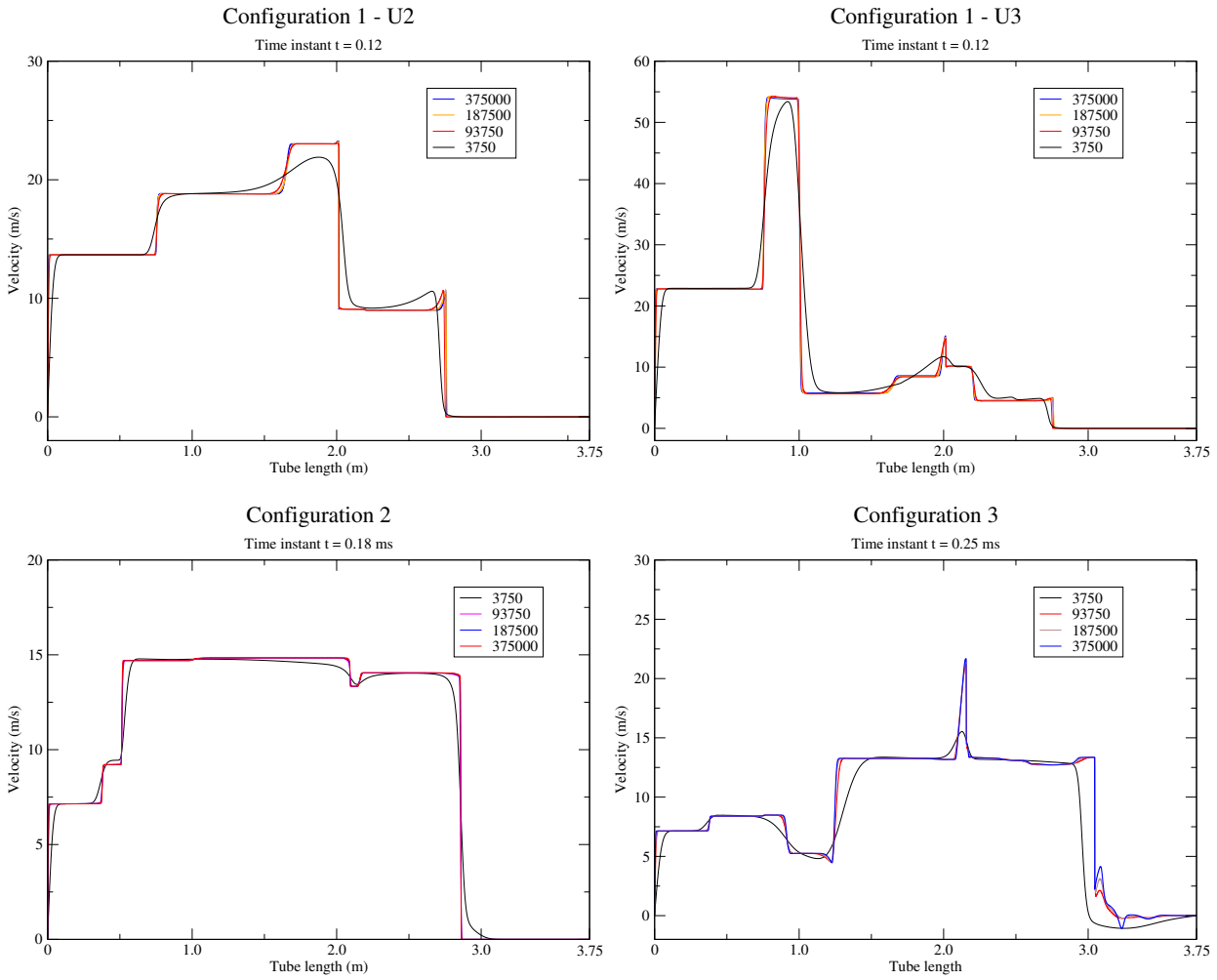

FIGURE 2.16 – *Velocities on different meshes for the three configurations at different time instants*

A noteworthy observation lays in the fact that we have shown two distinct velocities for *Configuration 1*, we can see that the profiles of U_2 and U_3 are quite different, and this is not surprising since the PDE model is built on the basis of distinct velocity fields, and the numerical scheme behind respects this set-up. For *Configuration 2* though, we did not mention in Figure 2.16 which velocity was represented, because the three of them are superimposed. This will be analysed with more details in the next point (comparison between *Configuration 1* and *Configuration 2*). For *Configuration 3*, only

one velocity profile is shown, since we used the instantaneous relaxation algorithm, which ensures that at the end of each time step the velocities (and the pressures) are equal.

In the following comparisons, we consider the 50000 element per meter mesh. Owing to the results presented in Figure 2.16, this mesh gives fair approximation of the model's solutions.

(ii) Comparison of *Configuration 1* and *Configuration 2*

Figure 2.17 presents the comparison of the pressure and the velocity profiles of *Configuration 1* and *Configuration 2* at the time instant $t = 1.2\ ms$.
For the velocities, we can notice that *Configuration 1*'s U_1 is not visible in the figure, this is due to the fact that the values taken by U_1 are significantly smaller than those of U_2 and U_3, and therefore they could not be put in the same scale. Meanwhile, *Configuration 2*'s three velocity fields are overlapped at the scale of the figure. This means that dividing the relaxation time scales τ^U by 10^N with $N = 10$ makes the velocities relax *almost instantaneously*, in a way such that the differences $\Delta U_{kl} = U_k - U_l$ are almost null at the end of each time step. This is a significant point, its importance relies in the fact that it shows how these relaxation time scales drive the relaxation process's speed. The different intermediate values of N that were tested (and are not shown here) confirm this relaxation behaviour : the larger N is, the smaller ΔU_{kl} relative velocities are at the end of each time step.

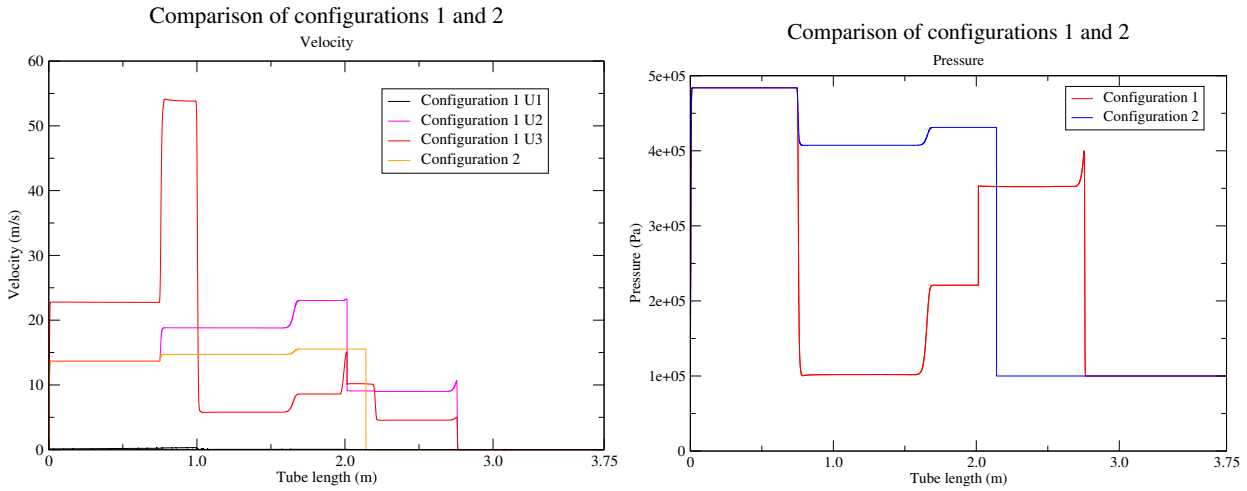

FIGURE 2.17 – *Comparison of* Configurations *1 and 2 - Velocity (left) and pressure (right) profiles at* $t = 1.2\ ms$

In Figure 2.17's pressure profile, no difference between the pressures of *Configuration 1* is visible. This suggests that this case's set-up do not allow to bring to light the pressures differences, even if there are visible on the velocities level.

Finally, we turn the reader's attention to the fact that the change in the relaxation time scales did not affect only the velocity differences, it has also impacted the position of the shock waves. Indeed, at $t = 1.2\ ms$ while the right-going shock wave is observed around $x = 2.75$ for *Configuration 1*, it is located around $x = 2.15$ for *Configuration 2*.

(iii) Comparison of *Configuration 2* and *Configuration 3*

In Figure 2.18 we give the comparison of *Configuration 2* and *Configuration 3* results at $t = 1.6\ ms$. As previously indicated, for *Configuration 2* there is no need to specify which velocity or pressure field is represented, because all the three are overlapped. For *Configuration 3* this is an obvious result, considering the involved instantaneous relaxations.

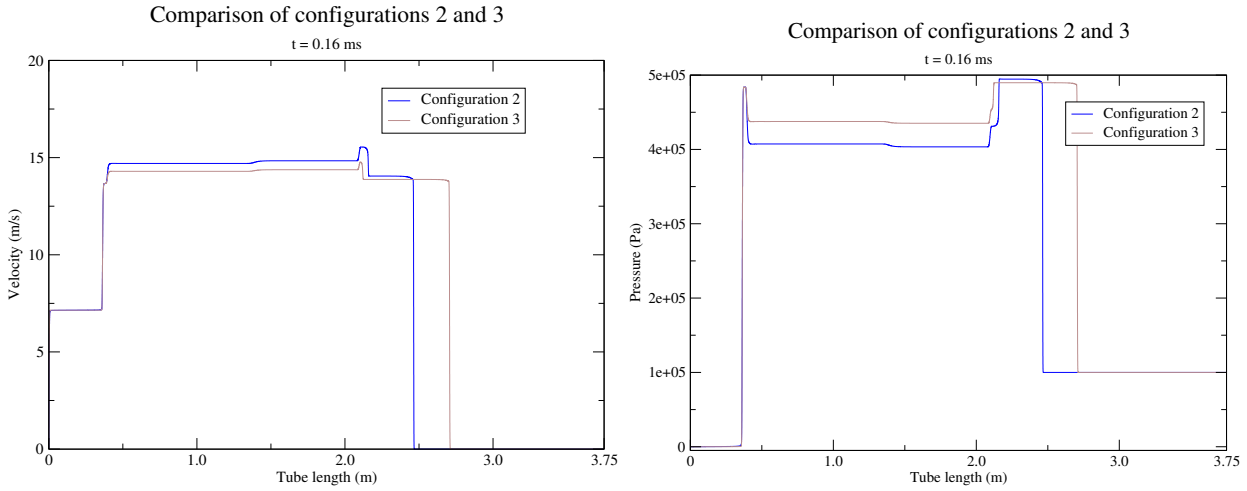

FIGURE 2.18 – *Comparison of* Configurations *2 and 3 - Velocity (left) and pressure (right) profiles at* $t = 1.6\ ms$

The notable point in Figure 2.18 though is the fact that there is a persistent lag between the results of the two configurations. In other words, this means that the general relaxation procedures (employed in *Configuration 1*) do not *converge* to the instantaneous relaxation algorithms used in *Configuration 3*, even if the relaxation time scales τ^P and τ^U are significantly small, such is the case of *Configuration 2*.

Chapitre 3

Simulation of a three-phase flow involving heat and mass transfer[1]

Hamza Boukili[2, 3], **Jean-Marc Hérard**[2, 3]

1. Les travaux de ce chapitre sont inclus dans :
Boukili H., Hérard JM. Simulation and preliminary validation of a three-phase flow model with energy. Soumis à Computers and Fluids.

2. EDF Lab Chatou, 6, quai Watier, 78400 Chatou, France.
3. I2M, Aix Marseille Université, 39 rue Joliot Curie, 13453 Marseille, France.

3.1 Introduction

In the domain of *fuel-coolant interactions*, *vapour explosion* (VE) is a phenomenon which still represents a challenge for modeling and numerical simulation. One part of the challenge lays in the fact that VE occurrence takes place in multi-phase flows, which are in general not obvious to model. An other challenging aspect is represented by the exchanges that happen between the different phases, which can accelerate, stress, or at the opposite limit the explosion's consequences [1].

There are mainly two different kinds of exchanges that happen in a FCI mixture : mechanical and thermal exchanges. Thermal aspects are related to the fact that the fuel (molten metal) is usually at a very high temperature, when it comes in contact with the coolant (usually liquid water), intense thermal exchanges happen and vapour is created, sometimes this evaporation could be so rapid and unstable that pressure shock waves are generated, which may endanger the surrounding structures. These pressure waves and the resulting velocities represent the mechanical interactions associated with VE.

In order to provide a model able to represent a FCI situation with VE occurrence, we studied in Chapter 1 [2] a barotropic three-phase flow model that allows to take into account the mechanical exchanges inside the mixture, while admitting well-defined shock wave structures. In Chapter 2 [3], on the basis of [6] the latter model was enriched to take energy equations into account, while considering only pressure and velocity relaxations.

In this chapter, we complete the model by considering thermal effects, namely temperature exchange, and mass transfer. In fact, in a FCI situation, once the fuel -initially at high temperature- comes in contact with the coolant, temperature exchanges happen and transform part of the coolant mass into vapour. These two effects are coupled, and are mandatory to obtain realistic simulation of a VE situation.

Thus, this chapter is organized as follows : in Section 2, we recall the PDE model [6], and we present the source terms that account for temperature exchange and mass transfer. The whole model's properties are checked in the continuous level. In Section 3, the discrete framework is studied, we present numerical schemes that give approximate solutions of the heat exchange and mass transfer. Afterwards, Section 4 focuses on the numerical results, where several test cases are provided : verification of the mass transfer, verification of heat exchange, two *flow in a box* test cases that study the combined effect of relaxations (mechanical and thermal) in the absence of convection, and finally a validation test case representative of VE scenario, on the basis of the KROTOS experiment presented in [8].

3.2 Governing equations and main properties of the three-dimensional three-phase flow model

3.2.1 Governing equations

As presented in Chapter 2, we consider the following system of partial differential equations (PDE) for the modeling of a three-phase flow. For $k = 1, .., 3$ and $t > 0$:

$$\begin{cases} \frac{\partial \alpha_k}{\partial t} + \mathbf{V}_i(\mathbf{W}).\nabla \alpha_k = S_k^{\alpha}(\mathbf{W}) \\ \frac{\partial m_k}{\partial t} + \nabla.(m_k \mathbf{U}_k) = S_k^{m}(\mathbf{W}) \\ \frac{\partial m_k \mathbf{U}_k}{\partial t} + \nabla.(m_k \mathbf{U}_k \otimes \mathbf{U}_k + \alpha_k p_k \mathbf{Id}) + \sum_{l=1, l\neq k}^{3} \Pi_{kl}(\mathbf{W}) \nabla \alpha_l = \mathbf{S}_k^{U}(\mathbf{W}) \\ \frac{\partial \alpha_k E_k}{\partial t} + \nabla.(\alpha_k E_k \mathbf{U}_k + \alpha_k p_k \mathbf{U}_k) - \sum_{l=1, l\neq k}^{3} \Pi_{kl}(\mathbf{W}) \frac{\partial \alpha_l}{\partial t} = S_k^{E}(\mathbf{W}) \end{cases} \tag{3.1}$$

The quantities $\alpha_k \in [0, 1]$, ρ_k, $m_k = \alpha_k \rho_k$, $\mathbf{U}_k$, p_k, $e_k(p_k, \rho_k)$ and E_k represent respectively the statistical fraction, the mean density, the partial mass, the mean velocity, the mean pressure, the mean internal energy and the mean total energy of phase k, $k = 1, 2, 3$, where :

$$E_k = \frac{1}{2} \rho_k \mathbf{U}_k.\mathbf{U}_k + \rho_k e_k(p_k, \rho_k) \tag{3.2}$$

The three involved phases are supposed to be non-miscible, this gives the following constraint on statistical fractions :

$$\alpha_1 + \alpha_2 + \alpha_3 = 1 \tag{3.3}$$

The state variable $\mathbf{W} \in \mathbb{R}^{17}$ denotes the following vector :

$$\mathbf{W} = (\alpha_2, \alpha_3, m_1, m_2, m_3, m_1 \mathbf{U}_1, m_2 \mathbf{U}_2, m_3 \mathbf{U}_3, \alpha_1 E_1, \alpha_2 E_2, \alpha_3 E_3)^t \tag{3.4}$$

Some additional thermodynamic variables need to be defined. We set :

$$c_k^2(p_k, \rho_k) = \left(\frac{p_k}{\rho_k^2} - \frac{\partial e_k(p_k, \rho_k)}{\partial \rho_k} \right) \left(\frac{\partial e_k(p_k, \rho_k)}{\partial p_k} \right)^{-1} \tag{3.5}$$

$s_k(p_k, \rho_k)$, the specific entropy of phase k, is defined such that :

$$c_k^2 \frac{\partial s_k(p_k, \rho_k)}{\partial p_k} + \frac{\partial s_k(p_k, \rho_k)}{\partial \rho_k} = 0 \tag{3.6}$$

The temperature is given by :

$$\frac{1}{T_k} = \frac{\partial s_k}{\partial p_k} \left(\frac{\partial e_k}{\partial p_k} \right)^{-1} \tag{3.7}$$

And μ_k denotes the Gibbs potential :

$$\mu_k = e_k + \frac{p_k}{\rho_k} - T_k s_k \tag{3.8}$$

We recall that the interface velocity that is chosen here is defined by :

$$\mathbf{V}_i(\mathbf{W}) = \mathbf{U}_1 \tag{3.9}$$

and the interface pressures are given by :

$$\left\{ \begin{array}{l} \Pi_{12}(\mathbf{W}) = \Pi_{21}(\mathbf{W}) = \Pi_{23}(\mathbf{W}) = p_2 \\ \Pi_{13}(\mathbf{W}) = \Pi_{31}(\mathbf{W}) = \Pi_{32}(\mathbf{W}) = p_3 \end{array} \right. \tag{3.10}$$

Source terms respond to the constraint :

$$\sum_{k=1}^{3} S_k^{\alpha}(\mathbf{W}) = \sum_{k=1}^{3} S_k^{m}(\mathbf{W}) = \sum_{k=1}^{3} S_k^{E}(\mathbf{W}) = 0 \quad ; \quad \sum_{k=1}^{3} \mathbf{S}_k^{U}(\mathbf{W}) = \mathbf{0}$$

Closure laws to account for the different relaxation effects involved in (3.1) are given by :

— Pressure relaxation :

$$S_k^{\alpha}(\mathbf{W}) = \sum_{l=1, l\neq k}^{3} K_{kl}^{P}(W)(p_k - p_l) \tag{3.11}$$

where : $K_{kl}^{P}(\mathbf{W}) = \frac{\alpha_k \alpha_l}{\tau_{kl}^{P}(\mathbf{W})\Pi_0}$, $\tau_{kl}^{P}(\mathbf{W}) = \tau_{lk}^{P}(\mathbf{W})$ is symmetric positive, and represents the pressure-relaxation time scale between phases k and l (see [5]), and Π_0 is a positive reference pressure.

— Mass transfer :

$$S_k^{m}(\mathbf{W}) = \sum_{l=1, l\neq k}^{3} \Gamma_{kl}(\mathbf{W}) = \sum_{l=1, l\neq k}^{3} K_{kl}^{m}(\mathbf{W}) \left(\frac{\mu_l}{T_l} - \frac{\mu_k}{T_k} \right) \tag{3.12}$$

where : $K_{kl}^{m}(\mathbf{W}) = \frac{1}{\tau_{kl}^{m}(\mathbf{W})\Gamma_0} \frac{m_k m_l}{m_k + m_l}$. The symmetric positive function $\tau_{kl}^{m}(\mathbf{W})$ represents the characteristic mass transfer time scale between phases k and l, and Γ_0 is a positive constant (with dimension μ/T).

— Momentum interfacial transfer term :

$$\mathbf{S}_k^{U}(\mathbf{W}) = \sum_{l=1, l\neq k}^{3} \mathbf{D}_{kl}(\mathbf{W}) + \sum_{l=1, l\neq k}^{3} \tilde{\mathbf{U}}_{kl} \Gamma_{kl}(\mathbf{W}) \tag{3.13}$$

where $\mathbf{D}_{kl}$ represents the drag effect between phases k and l :

$$\mathbf{D}_{kl}(\mathbf{W}) = e_{kl}(\mathbf{W})(\mathbf{U}_l - \mathbf{U}_k) \tag{3.14}$$

The terms e_{kl} are chosen under the form :

$$e_{kl}(\mathbf{W}) = \frac{m_k m_l}{\tau_{kl}^{U}(\mathbf{W}) M_0} \tag{3.15}$$

where $\tau_{kl}^{U}(\mathbf{W})$ is symmetric positive, and accounts for the velocity-relaxation time scale. $M_0 = m_1 + m_2 + m_3$ is the total mass.

The velocity $\tilde{\mathbf{U}}_{kl}$ is chosen under the symmetric form :

$$\tilde{\mathbf{U}}_{kl}(\mathbf{W}) = \frac{\mathbf{U}_k + \mathbf{U}_l}{2} \tag{3.16}$$

— Energy balance source term :

$$S_k^E(\mathbf{W}) = \sum_{l=1,l\neq k}^{3} \mathbf{V}_{kl}(\mathbf{W}).\mathbf{D}_{kl}(\mathbf{W}) + \sum_{l=1,l\neq k}^{3} \psi_{kl}(\mathbf{W}) + \sum_{l=1,l\neq k}^{3} \tilde{H}_{kl}\Gamma_{kl}(\mathbf{W}) \tag{3.17}$$

where :

$$\mathbf{V}_{kl} = \frac{1}{2}(\mathbf{U}_k + \mathbf{U}_l) \tag{3.18}$$

and $\tilde{H}_{kl}$ is given by :

$$\tilde{H}_{kl}(\mathbf{W}) = \frac{\mathbf{U}_k.\mathbf{U}_l}{2} \tag{3.19}$$

The term ψ_{kl} accounts for the heat transfer between phases k and l, it is defined by :

$$\psi_{kl}(\mathbf{W}) = K_{kl}^{T}(\mathbf{W})(T_l - T_k) \tag{3.20}$$

with :

$$K_{kl}^{T}(\mathbf{W}) = \frac{1}{\tau_{kl}^{T}(\mathbf{W})} \frac{m_k m_l C_{V,k} C_{V,l}}{m_k C_{V,k} + m_l C_{V,l}} \tag{3.21}$$

Here again $\tau_{kl}^{T}(\mathbf{W})$ is symmetric positive and accounts for the heat transfer characteristic time between phases k and l, and $C_{V,k}$ denotes the volumetric heat capacity of phase k.

3.2.2 Main properties

3.2.2.1 General properties

In view of the study presented in Chapter 2, the model (3.1) has the following properties :

✓ The smooth solutions of (3.1) agree with an entropy inequality, as a consequence of the choices made for the interface terms (3.9),(3.10) as well as the closures given in (3.11),(3.12),(3.13),(3.17) ;

✓ The convective subset of (3.1) is hyperbolic, and the system waves are either LD or VNL ;

✓ For each isolated GNL wave, exact jump conditions hold.

The details of these properties as well as their proofs were presented in Chapter 2. The convective subset of (3.1) was studied in both 3D and pure 1D framework. The structure of fields being proved for the general 3D case, the 1D case allows to push the study further, and give the Riemann invariants for a LD waves and the exact jump conditions for each GNL wave.

The entropy inequality was proved for the general 3D system but not including the mass transfer terms. In the presence of $\Gamma_{kl}(\mathbf{W})$, an additional term appears in the right-hand side of the entropy balance. In fact, we recall the definitions of the mixture entropy $\eta(\mathbf{W})$ and the mixture entropy flux $\mathbf{F}_\eta(\mathbf{W})$:

$$\begin{cases} \eta(\mathbf{W}) = -\sum_{k=1}^{3} m_k Log(s_k) \\ \mathbf{F}_\eta(\mathbf{W}) = -\sum_{k=1}^{3} m_k Log(s_k)\mathbf{U}_k \end{cases} \tag{3.22}$$

For regular solutions of (3.1), we have the following evolution equation :

$$\begin{aligned} \frac{\partial \eta(\mathbf{W})}{\partial t} + \nabla.\mathbf{F}_\eta(\mathbf{W}) = &-\sum_{k=1}^{3} \frac{1}{T_k}\left(p_k S_k^\alpha(\mathbf{W}) + \sum_{l\neq k} \Pi_{kl}(\mathbf{W}) S_l^\alpha(\mathbf{W})\right) \\ &-\sum_{k=1}^{3} \frac{1}{T_k} \sum_{l=1,l\neq k}^{3} ((\mathbf{V}_{kl}(\mathbf{W}) - \mathbf{U}_k).\mathbf{D}_{kl}(\mathbf{W}) + \psi_{kl}(\mathbf{W})) \\ &+\sum_{k=1}^{3} \frac{\mu_k}{T_k} \sum_{l=1,l\neq k}^{3} \Gamma_{kl}(\mathbf{W}) \end{aligned} \tag{3.23}$$

In the right-hand side of (3.23), each one of the two first terms account for the pressure, the velocity and the temperature relaxation, they have been studied in Chapter 2. Considering the closure (3.12), we have :

$$\begin{aligned} \sum_{k=1}^{3} \frac{\mu_k}{T_k} \sum_{l=1,l\neq k}^{3} \Gamma_{kl}(\mathbf{W}) &= \sum_{k=1}^{3} \frac{\mu_k}{T_k} \sum_{l=1,l\neq k}^{3} K_{kl}^m(\mathbf{W}) \left(\frac{\mu_l}{T_l} - \frac{\mu_k}{T_k}\right) \\ &= -\sum_{l<k} K_{kl}^m(\mathbf{W}) \left(\frac{\mu_l}{T_l} - \frac{\mu_k}{T_k}\right)^2 \leq 0 \end{aligned} \tag{3.24}$$

This allows to conclude that the entropy inequality holds for the global system including the mass transfer.

3.2.2.2 Mass transfer

In this paragraph, we focus on the mass transfer, or Gibbs potential relaxation. Concretely, we study what happens in the continuous framework when the space derivatives are null, and only the mass transfer source terms are at stake. The concerned PDE subsystem writes as follows :

$$\begin{cases} \partial_t \alpha_k = 0 \\ \partial_t m_k = \sum_{l=1,l\neq k}^{3} \Gamma_{kl}(\mathbf{W}) \\ \partial_t (m_k \mathbf{U}_k) = \sum_{l=1,l\neq k}^{3} \tilde{\mathbf{U}}_{kl} \Gamma_{kl}(\mathbf{W}) \\ \partial_t (\alpha_k E_k) = \sum_{l=1,l\neq k}^{3} \tilde{H}_{kl} \Gamma_{kl}(\mathbf{W}) \end{cases} \tag{3.25}$$

In the sequel of this work, only the mass transfer between phases 2 and 3 will be considered. This is driven by the fact that our objective is the simulation of vapour explosion, where a liquid metal gets in contact with liquid water, a part of which is eventually evaporated. The phase 1 in our study represents the liquid metal, while phases 2 and 3 represent respectively the liquid water and water vapour. Therefore, the mass transfer can happen only between phases 2 and 3.

In practice, this means that phase $k = 1$ state variables don't move within this step, the effective PDE system to solve is the following :

$$\begin{cases} \partial_t \alpha_k = 0 \ (k = 1, 2, 3) & \text{(3.26a)} \\ \partial_t m_2 = \Gamma_{23}(\mathbf{W}) & \text{(3.26b)} \\ \partial_t (m_2 \mathbf{U}_2) = \tilde{\mathbf{U}}_{23} \Gamma_{23}(\mathbf{W}) & \text{(3.26c)} \\ \partial_t (\alpha_2 E_2) = \tilde{H}_{23} \Gamma_{23}(\mathbf{W}) & \text{(3.26d)} \\ \partial_t (m_2 + m_3) = 0 & \text{(3.26e)} \\ \partial_t (m_2 \mathbf{U}_2 + m_3 \mathbf{U}_3) = \mathbf{0} & \text{(3.26f)} \\ \partial_t (\alpha_2 E_2 + \alpha_3 E_3) = 0 & \text{(3.26g)} \end{cases}$$

It is important to notice here that the mass transfer term $\Gamma_{23}(\mathbf{W})$ could be expressed only in function of the densities and internal energies :

$$\Gamma_{23}(\mathbf{W}) = \Gamma_{23}(\rho_2, e_2, \rho_3, e_3) \tag{3.27}$$

Moreover, considering the closures of $\tilde{\mathbf{U}}_{23}$ and $\tilde{H}_{23}$ given in (3.16) and (3.19), we can easily prove that :

$$\partial_t (m_2 e_2) = \partial_t (m_3 e_3) = 0 \tag{3.28}$$

The result (3.28) means that we can express Γ_{23} as a function of **one** variable m_2, since :

$$\begin{cases} \rho_2 = \frac{m_2}{\alpha_2(t=0)} \\ e_2 = \frac{(m_2 e_2)(t=0)}{m_2} \\ \rho_3 = \frac{(m_2+m_3)(t=0)-m_2}{\alpha_3(t=0)} \\ e_3 = \frac{(m_3 e_3)(t=0)}{(m_2+m_3)(t=0)-m_2} \end{cases} \tag{3.29}$$

Therefore :

$$\Gamma_{23}(\rho_2, e_2, \rho_3, e_3) = \frac{m_2(M - m_2)}{\tau_{23}^m M} \tilde{\Gamma}_{23}(m_2) \tag{3.30}$$

where $M = m_2 + m_3$ is constant, and noting :

$$\tilde{\Gamma}_{23}(m_2) = \frac{1}{\Gamma_0} \left(\frac{\mu_2}{T_2} - \frac{\mu_3}{T_3} \right)(m_2) \tag{3.31}$$

This approach is the one introduced in [4, 9].

3.2.2.3 Heat transfer

In this paragraph, we examine the heat transfer subsystem. Similarly to the mass transfer in the precedent paragraph, we consider only the time derivatives and the heat transfer source terms. The studied system writes :

$$\begin{cases} \partial_t \alpha_k = 0 \\ \partial_t m_k = 0 \\ \partial_t (m_k \mathbf{U}_k) = 0 \\ \partial_t (\alpha_k E_k) = \sum_{l=1, l\neq k}^{3} K_{kl}^T(\mathbf{W})(T_l - T_k) \end{cases} \tag{3.32}$$

Taking into account the invariance of the partial masses and the partial kinetic energies, the energy balance of (3.32) can be rewritten as :

$$m_k \partial_t e_k = \sum_{l=1, l\neq k}^{3} K_{kl}^T(\mathbf{W})(T_l - T_k) \tag{3.33}$$

For the *Stiffened Gaz EOS* we know that :

$$T_k = \frac{1}{C_{V,k}} \left(e_k - \frac{\Pi_k}{\rho_k} \right) \tag{3.34}$$

where Π_k is the constant such that : $p_k + \gamma_k \Pi_k = (\gamma_k - 1) e_k \rho_k$. This means that :

$$\partial_t e_k = C_{V,k} \partial_t T_k \tag{3.35}$$

Therefore, (3.33) becomes :

$$\partial_t T_k = \sum_{l=1, l\neq k}^{3} \frac{K_{kl}^T(\mathbf{W})}{m_k C_{V,k}} (T_l - T_k) \tag{3.36}$$

We apply the same process that we used in Chapter 2, Paragraph 2.2.5 (Velocity relaxation) ; by considering the temperature differences $T_1 - T_2$ and $T_1 - T_3$ we have :

$$\partial_t \begin{pmatrix} T_1 - T_2 \\ T_1 - T_3 \end{pmatrix} = -A(\mathbf{W}) \begin{pmatrix} T_1 - T_2 \\ T_1 - T_3 \end{pmatrix} \tag{3.37}$$

where the matrix $A(\mathbf{W})$ is defined by :

$$A(\mathbf{W}) = \begin{pmatrix} \frac{K_{12}^T}{m_1 C_{V,1}} + \frac{K_{12}^T}{m_2 C_{V,2}} + \frac{K_{23}^T}{m_2 C_{V,2}} & \frac{K_{13}^T}{m_1 C_{V,1}} - \frac{K_{23}^T}{m_2 C_{V,2}} \\ \frac{K_{12}^T}{m_1 C_{V,1}} - \frac{K_{23}^T}{m_3 C_{V,3}} & \frac{K_{13}^T}{m_1 C_{V,1}} + \frac{K_{13}^T}{m_3 C_{V,3}} + \frac{K_{23}^T}{m_3 C_{V,3}} \end{pmatrix} \tag{3.38}$$

We can then *formally* write :

$$\begin{pmatrix} T_1 - T_2 \\ T_1 - T_3 \end{pmatrix} (t) = exp \left(- \int_{t_0}^{t} A(s) ds \right) \begin{pmatrix} T_1 - T_2 \\ T_1 - T_3 \end{pmatrix} (t_0) \tag{3.39}$$

It should be noted that the determinant and the trace of the matrix A are positive :

$$\begin{cases} det(A) > 0 \\ tr(A) > 0 \end{cases}$$

A direct, though cumbersome, calculation proves it. This means that matrix A eigenvalues are either real positive, or complex with positive real part, which ensures that temperature differences decrease over time, their decrease is monotonous when eigenvalues are real, and oscillating when eigenvalues are complex.

3.3 Numerical method

The PDE model presented in the previous section consists of a hyperbolic convective subset and source terms accounting for different physical relaxation effects. In the spirit of [7], and in the continuity of [2] and Chapter 2, a fractional step method is adopted. The first step treats the pure convection effects, while the second step deals with the relaxation effects, the splitting is realized in agreement with the entropy inequality.

Concerning the convection, the choice was made to use the explicit Rusanov scheme in order to obtain approximate solutions of the hyperbolic subset. Chapter 2 gave the details of the scheme and its properties, especially the CFL constraint that is imposed on the time step.

Regarding the relaxation effects, two of them were studied in Chapter 2, namely the velocity and the pressure relaxations. Implicit schemes were considered, and their different properties were examined.

In this section, we present the numerical schemes that will be considered to find approximate solutions of the mass transfer and the temperature relaxation subsystems. This will allow to complete the study of the four relaxation effects, therefore it will be possible to consider full simulations of vapour explosion scenarios.

3.3.1 Mass transfer

For computing approximate solutions of (3.26), the numerical scheme that we consider is the one which was presented in [4, 9]. In each cell Ω_i, starting from a state $\mathbf{W}_i^*$, and for a given time step Δt_n, we compute $\mathbf{W}_i^{n+1}$ by following the sequence :

— Compute $(m_2)_i^{n+1}$, solution of :

$$(m_2)_i^{n+1} = (m_2)_i^* + \frac{\Delta t_n}{(M\tau_{23}^m)^*}(m_2)_i^{n+1}(M - (m_2)_i^{n+1})\tilde{\Gamma}_{23}((m_2)_i^{n+1}) \tag{3.40}$$

— Compute $(m_3)_i^{n+1}$:

$$(m_3)_i^{n+1} = ((m_2)_i^* + (m_3)_i^*) - (m_2)_i^{n+1} \tag{3.41}$$

— Compute $(\mathbf{U}_2)_i^{n+1}$ and $(\mathbf{U}_3)_i^{n+1}$ by solving the linear system wrt $(\mathbf{U}_2, \mathbf{U}_3)_i^{n+1}$:

$$\begin{cases} (m_2\mathbf{U}_2)_i^{n+1} = (m_2\mathbf{U}_2)_i^* + (\tilde{\mathbf{U}}_{23})_i^{n+1}\frac{\Delta t_n}{(M\tau_{23}^m)^*}(m_2)_i^{n+1}(M - (m_2)_i^{n+1})\tilde{\Gamma}_{23}((m_2)_i^{n+1}) \\ (m_3\mathbf{U}_3)_i^{n+1} = (m_2\mathbf{U}_2)_i^* + (m_3\mathbf{U}_3)_i^* - (m_2\mathbf{U}_2)_i^{n+1} \end{cases} \tag{3.42}$$

— Update the total energies :

$$\begin{cases} (\alpha_2 E_2)_i^{n+1} = (\alpha_2 E_2)_i^* + (\tilde{H}_{23})_i^{n+1}\frac{\Delta t_n}{(M\tau_{23}^m)^*}(m_2)_i^{n+1}(M - (m_2)_i^{n+1})\tilde{\Gamma}_{23}((m_2)_i^{n+1}) \\ (\alpha_3 E_3)_i^{n+1} = (\alpha_2 E_2)_i^* + (\alpha_3 E_3)_i^* - (\alpha_2 E_2)_i^{n+1} \end{cases} \tag{3.43}$$

Remark 1 :

— *For more details about the resolution of equation* (3.40) *and system* (3.42)*, we refer the reader to the previous works [4, 9]* ;

— *By construction, this scheme ensures the conservation of the total mass, the total momentum and the total energy.*□

3.3.2 Temperature relaxation

Taking into account the continuous framework study presented in the paragraph (3.2.2.3), we consider the following algorithm to compute approximate solutions of (3.32). In each cell Ω_i, starting from a state $\mathbf{W}_i^*$, and for a given time step Δt_n, we follow the sequence :

— Compute $(T_1 - T_2)_i^{n+1}$ and $(T_1 - T_3)_i^{n+1}$, the exact solutions of the ODE :

$$\partial_t \begin{pmatrix} T_1 - T_2 \\ T_1 - T_3 \end{pmatrix} = -A(\mathbf{W}^*) \begin{pmatrix} T_1 - T_2 \\ T_1 - T_3 \end{pmatrix} \tag{3.44}$$

at time $t_n + \Delta t_n$;

— Compute $(T_1)_i^{n+1}$, by solving the total energy conservation equation :

$$(T_1)_i^{n+1} = \frac{1}{\sum_{k=1}^{3}(m_k)_i^* C_{V,k}} \left(\sum_{k=1}^{3} (m_k)_i^* C_{V,k} (T_k)_i^* + \sum_{k=2}^{3} (m_k)_i^* C_{V,k} (T_1 - T_k)_i^{n+1} \right) \tag{3.45}$$

and deduct $(T_2)_i^{n+1}$ and $(T_3)_i^{n+1}$ by : $(T_k)_i^{n+1} = (T_1)_i^{n+1} - (T_1 - T_k)_i^{n+1}$, $k = 2, 3$;

— Update the total energies by :

$$(\alpha_k E_k)_i^{n+1} = \left(\frac{1}{2} m_k \mathbf{U}_k . \mathbf{U}_k \right)_i^* + (m_k e_k)_i^{n+1} \tag{3.46}$$

where : $(m_k e_k)_i^{n+1} = (m_k)_i^* e_k((\rho_k)_i^*, (T_k)_i^{n+1})$ as the masses and the densities are constant in the temperature relaxation step.

3.4 Numerical results

In Chapter 2, mechanical effects represented by pressure and velocity relaxation terms were studied. Several algorithms were given, and different test cases were considered, which highlight the impact of these source terms as well as the key role of the relaxation time scales τ_{kl}^P and τ_{kl}^U.

Here in this section, we present the different numerical results that were obtained using the schemes introduced in Section 3. We start by two verification test-cases given in subsection 4.1 and 4.2, which concern respectively the mass and the heat transfer schemes. Afterwards, in subsections 4.3 and 4.4 we consider two *flow in a box* test cases, that aim at emphasizing the combined relaxation effects. Subsection 4.3 studies the case of pressure relaxation and heat exchange, while subsection 4.4 examines what happens when the mass

	Phase $k=1$	Phase $k=2$	Phase $k=3$
u_k	0.00	0.00	0.00
p_k	7.0×10^5	7.0×10^5	4.0×10^5
ρ_k	998.1	5.0	20.0
α_k	0.3	0.5	0.2
γ_k	27.07	10.0	10.0
Π_k	$8.06\ 10^7$	0.00	0.00
$C_{V,k}$	10.58	700.0	700.0
q'_k	0.00	-1836.1	-1836.1

TABLE 3.1 – *Mass transfer verification test case : initialisation and EOS dataset*

transfer is included. Finally, in subsection 4.5 a more complete test-case representative of a vapour explosion scenario is presented. It consists in the simulation of a *KROTOS* facility [8], where some molten metal (at very high temperature) gets in contact with coolant liquid water (at ambient thermodynamic conditions), part of which turns into vapour, in the presence of pressure shock waves. This makes a particular three-phase flow configuration where mechanical and thermal effects are highly at stake.

3.4.1 Mass transfer : verification test case

The mass transfer scheme was studied previously in [4, 9]. For the analytical solution considered in this verification test-case, we refer the reader to [4] and its *Appendix A*. This test's EOS framework is the *Stiffened Gas* EOS :

$$\left\{ \begin{array}{l} p_k + \gamma_k \Pi_k = (\gamma_k - 1)\rho_k e_k \\ s_k = C_{V_k} log\left[\left(e_k - \frac{\Pi_k}{\rho_k}\right)\rho_k^{1-\gamma_k}\right] + q'_k \end{array} \right. \tag{3.47}$$

In order to be able to build the analytical solution, one possibility is that phases 2 and 3, that are really concerned by the mass transfer, must comply with :

$$\gamma_2 C_{V_2} = \gamma_3 C_{V_3} \tag{3.48}$$

Table 3.1 gives the numerical data that was used in the test case. We mention that the test's final time is $T_{final} = 1.0\ s$, and the mass transfer relaxation time scale is fixed to :

$$\tau_{23}^m = 5.0 \times 10^{+3}$$

We check also that EOS of phases 2 and 3 satisfy (3.48).

Turning to the results, figure 3.1 gives the error in function of the mesh size. We check that the expected h^1 convergence rate is retrieved.

3.4.2 Heat transfer : verification test case

In this paragraph, we implement a test-case that aims at the verification of the scheme introduced in subsection (3.3.2) to compute approximate solutions of (3.32). Appendix A1 provides the considered analytical solution, as well as the initial dataset that was used in the computations. Figure 3.2 shows that the variables converge at the expected h^1 rate.

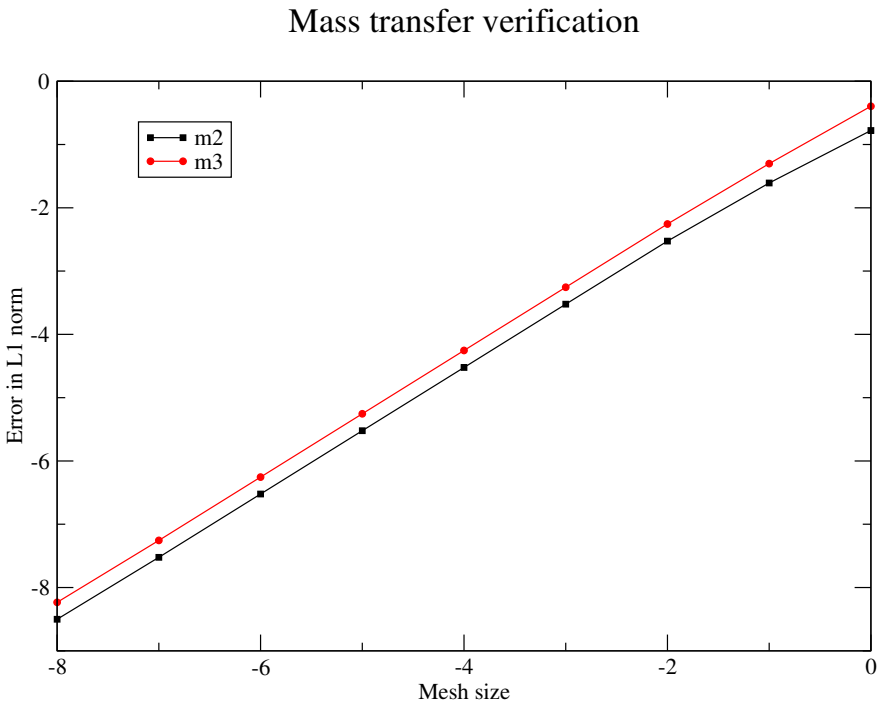

FIGURE 3.1 – *Mass transfer verification test-case*

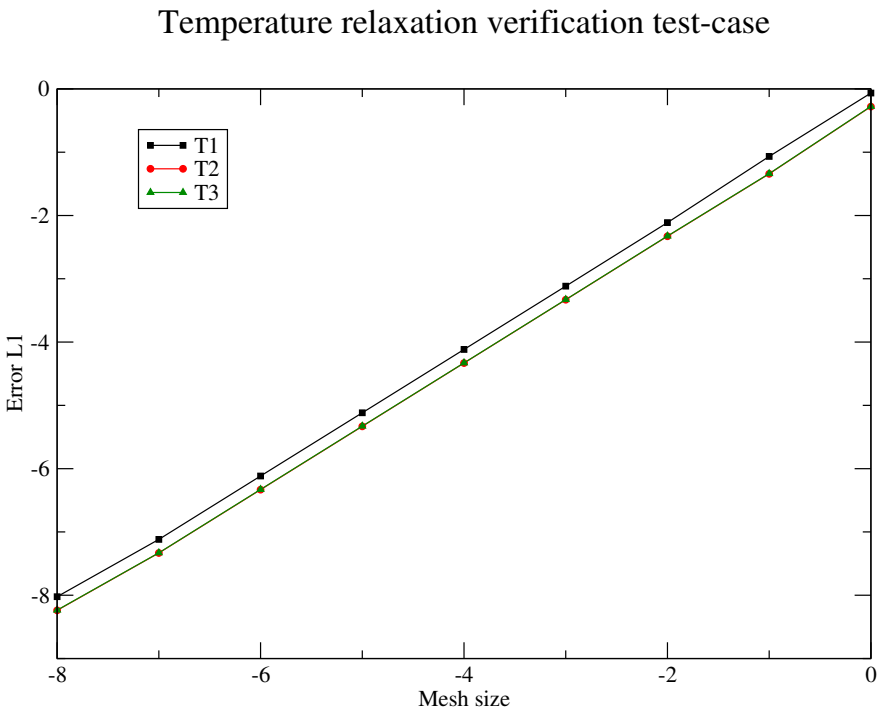

FIGURE 3.2 – *First heat transfer verification test-case*

3.4.3 Heat transfer : a second verification test case

In this paragraph, we examine the combined effect of temperature and pressure relaxations, by considering the case of a flow where no convection is included. Only the source terms are taken into account. The PDE system we are examining is the following :

$$\begin{cases} \partial_t \alpha_k = \sum_{l=1,l\neq k}^{3} K_{kl}^P(W)(p_k - p_l) \\ \partial_t m_k = 0 \\ \partial_t (m_k \mathbf{U}_k) = \sum_{l=1,l\neq k}^{3} \mathbf{D}_{kl}(\mathbf{W}) \\ \partial_t (\alpha_k E_k) - \sum_{l=1,l\neq k}^{3} \Pi_{kl}(\mathbf{W}) \partial_t \alpha_l = \sum_{l=1,l\neq k}^{3} \mathbf{V}_{kl}(\mathbf{W}).\mathbf{D}_{kl}(\mathbf{W}) + \sum_{l=1,l\neq k}^{3} K_{kl}^T(\mathbf{W})(T_l - T_k) \end{cases} \tag{3.49}$$

The idea of this test is to consider an initial state where the temperatures are unbalanced. Owing to the relaxation mechanisms, the system will evolve in such a way that an equilibrium is reached, and the temperature differences are null. The velocity relaxation has no effect on the results of this test case. In fact, since we set the velocities initially to 0, the velocity relaxation ensures that they remain null during the whole computation. Considering the total energy conservation, and the fact that the partial masses do not vary in this case, the final equilibrium temperature can be estimated depending on the chosen EOS.

We note that the pressure relaxation has a real impact, because of the presence of Π_{kl} terms in the energy balance. This connects the temperature variations to the statistical fractions, and therefore the pressures move. Concretely, we have chosen the instantaneous pressure relaxation algorithm (presented in the Chapter 2 Appendix A1) to run the simulations :

$$\tau_{kl}^P = 0 \tag{3.50}$$

We recall that the temperature relaxation coefficients K_{kl}^T are given by :

$$K_{kl}^T(\mathbf{W}) = \frac{1}{\tau_{kl}^T(\mathbf{W})} \frac{m_k m_l C_{V,k} C_{V,l}}{m_k C_{V,k} + m_l C_{V,l}} \tag{3.51}$$

In this test case, the characteristic times τ_{kl}^T that drives the relaxation pace are chosen to be identical for all the phases :

$$\tau_{kl}^T(\mathbf{W}) = \tau_0^T \tag{3.52}$$

with the choice :

$$\tau_0^T = 10^{-5} \tag{3.53}$$

The simulation's final time is $t = 2\ ms$ and the time-step dt is of the order of 10^{-6}. This configuration is therefore such that :

$$\frac{dt}{\tau_{kl}^T} < 1 \tag{3.54}$$

which allows to better observe the temperature's evolution, as the equilibrium is not reached very quickly.

In terms of EOS, we choose the *General Stiffened Gas* (GSG) framework, in which we have for each phase k :

$$\begin{cases} s_k = C_{V,k} log\left[\left(e_k - Q_k - \frac{\Pi_k}{\rho_k}\right)\frac{1}{\rho_k^{\gamma_k - 1}}\right] + q'_k \\ p_k + \gamma_k \Pi_k = (\gamma_k - 1)\rho_k(e_k - Q_k) \\ C_{V,k} T_k = e_k - Q_k - \frac{\Pi_k}{\rho_k} \end{cases} \tag{3.55}$$

Various numerical settings were considered (detailed below). In addition to the GSG case, the *Stiffened Gas* and *Perfect Gas* EOS cases were tested, by taking null the relevant thermodynamic parameters in each case (Q_k alone or Q_k and Π_k). For all the tests, the parameters q'_k that were chosen are :

$$\begin{cases} q'_1 = 0.00 \\ q'_2 = 10000.00000 \\ q'_3 = -1836.098569 \end{cases} \tag{3.56}$$

The Perfect Gas EOS case :

In this case, all the coefficients Π_k and Q_k are null, the internal energy is directly given in function of the temperature. The conservation of the total energy allows to explicitly determine the final theoretical temperature, which is nothing but the average of the initial temperatures weighted by coefficients $m_k C_{V,k}$:

$$T_{th}^{final} = \frac{m_1 C_{V,1} T_1^{in} + m_2 C_{V,2} T_2^{in} + m_3 C_{V,3} T_3^{in}}{m_1 C_{V,1} + m_2 C_{V,2} + m_3 C_{V,3}} \tag{3.57}$$

Numerically speaking, Tables 3.2 and 3.3 give the thermodynamic constants and the initial dataset :

Phase k	γ_k	$C_{V,k}$
1	22.83859097	1287.294826
2	1.655128030	1395.286166
3	1.401153242	713.1396320

TABLE 3.2 – Perfect Gas EOS parameters

Phase k	α_k	p_k	T_k	m_k
1	0.1	10^5	2500.0	$1.42284\ 10^{-4}$
2	0.8	10^5	363.0	$2.37473\ 10^{-1}$
3	0.1	10^5	1000.0	$3.49225\ 10^{-2}$

TABLE 3.3 – Perfect Gas case : initial dataset

In Figure 3.3 we can observe the evolution of the temperatures towards the final equilibrium state. The three temperatures do not vary in the same pace, due to the differences

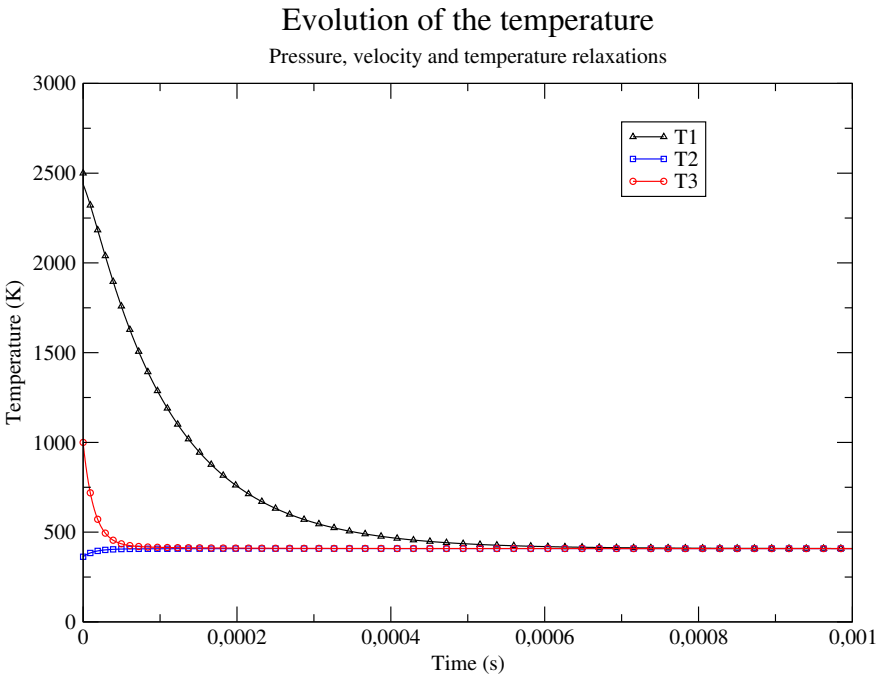

FIGURE 3.3 – *Second heat transfer verification test-case : Perfect Gas EOS*

of $m_k C_{V,k}$ as well as the initial $\Delta T_{kl} = T_k - T_l$. The final numerical value is verified to be in consistency with the theoretical estimation, at $t = 2\ ms$ the error is less than to 10^{-5}, as shown in (3.58).

$$T_{th}^{final} = 408.60\ K \quad \begin{cases} T_1^{num}(t = 2\ ms) = 408.60\ K \\ T_2^{num}(t = 2\ ms) = 408.60\ K \\ T_3^{num}(t = 2\ ms) = 408.60\ K \end{cases} \tag{3.58}$$

The Stiffened Gas EOS case :

In this case, the presence of non-null Π_k coefficients makes the computation of the final temperature more complicated. In fact, the final densities ρ_k^{final} can be expressed in terms of the final statistical fractions α_k^{final}, hence :

$$T_{th}^{final} = \frac{\sum_{k=1}^{3} m_k C_{V,k} T_k^{in}}{\sum_{k=1}^{3} m_k C_{V,k}} - \sum_{k=1}^{3} m_k \frac{\Pi_k}{\rho_k^{final}} \tag{3.59}$$

In practice, we take the final numerical values of the densities $\rho_k(t = 2\ ms)$, and we inject them in equation (3.59) to obtain a temperature estimation. Tables 3.4 and 3.5 give the thermodynamic parameters and initial dataset of this test case.

Figure 3.4 presents the temperature evolution. We notice that T_1 and T_3 curves are superimposed, due to the fact that m_3 is small compared with m_1 and m_2, and also due to the fact that phase $k = 3$ is represented by a *Perfect Gas* EOS ($\Pi_3 = 3$).

In (3.60) we give the numerical values of the temperatures at $t = 2\ ms$ as well as the *theoretical* value T_{th}^{final}. A match is established between the *theoretical* value and numerical

Phase k	γ_k	Π_k	$C_{V,k}$
1	22.83859097	188447923.6	128.7294826
2	1.655128030	37258761.46	13.95286166
3	1.401153242	0.00	71313.96320

TABLE 3.4 – Stiffened Gas parameters

Phase k	α_k	P	T_k	m_k
1	0.2	10^5	2500.0	$5.36382\ 10^{+1}$
2	0.4	10^5	363.0	$4.42517\ 10^{+4}$
3	0.4	10^5	1000.0	$1.39690\ 10^{-4}$

TABLE 3.5 – Stiffened Gas case : initial dataset

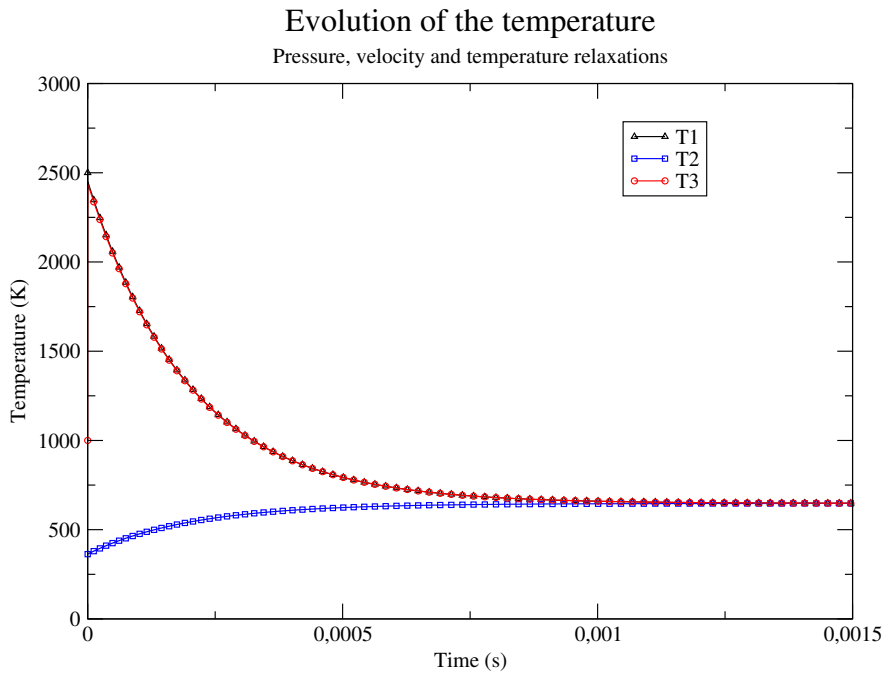

FIGURE 3.4 – *Second heat transfer verification test-case : Stiffened Gas EOS*

results, the observed error is of the order of 10^{-4}.

$$T_{th}^{final} = 647.22\ K \quad \begin{cases} T_1^{num}(t = 2\ ms) = 647.34\ K \\ T_2^{num}(t = 2\ ms) = 647.22\ K \\ T_3^{num}(t = 2\ ms) = 647.34\ K \end{cases} \tag{3.60}$$

The General Stiffened Gas EOS case :

In this case, similarly to the *Stiffened Gas* configuration, the equilibrium temperature's value T_{th}^{final} cannot be computed without the use of a part of the numerical result, as equation (3.61) below shows. Nevertheless, the interest of this case lays in the used EOS combination :

General Stiffened Gas for phase 1, *Stiffened Gas* for phase 2 and *Perfect Gas* for phase 3. This represents the set of EOS that will be considered for the simulation of the the three-phase flow composed of : molten metal (phase 1), liquid water (phase 2) and water vapour (phase 3), as paragraph 4.5 will explain.

$$T_{th}^{final} = \frac{\sum_{k=1}^{3} m_k C_{V,k} T_k^{in}}{\sum_{k=1}^{3} m_k C_{V,k}} - \sum_{k=1}^{3} m_k \left(\frac{\Pi_k}{\rho_k^{final}} + Q_k \right) \tag{3.61}$$

In Tables 3.6 and 3.7 we give the EOS parameters and the initial dataset.

Phase k	γ_k	Π_k	Q_k	$C_{V,k}$
1 (GSG)	22.83859097	188447923.6	-13316.20000	12.87294826
2 (SG)	1.655128030	37258761.46	0.00	1395.286166
3 (PG)	1.401153242	0.00	0.00	713.1396320

TABLE 3.6 – General Stiffened Gas parameters

Phase k	α_k	p_k	T_k	m_k
1	0.4	10^5	2500.0	$1.07276\ 10^{+3}$
2	0.2	10^5	363.0	$2.21258\ 10^{+2}$
3	0.4	10^5	1000.0	$1.39690\ 10^{-1}$

TABLE 3.7 – General Stiffened Gas case : initial dataset

In Figure 3.5 we give the temperatures' evolution, and in (3.62) we present the comparison of the *theoretical* temperature and the final numerical values.

$$T_{th}^{final} = 1175.77\ K \quad \begin{cases} T_1^{num}(t = 2\ ms) = 1175.80\ K \\ T_2^{num}(t = 2\ ms) = 1175.70\ K \\ T_3^{num}(t = 2\ ms) = 1175.78\ K \end{cases} \tag{3.62}$$

3.4.4 Mass transfer combined with heat exchange

In this paragraph we focus on an other *flow in a box* test case which is dedicated to examine the combined effect of temperature relaxation and mass transfer. The PDE system we examine is the following :

$$\begin{cases} \partial_t \alpha_k = S_k^{\alpha}(\mathbf{W}) \\ \partial_t m_k = S_k^{m}(\mathbf{W}) \\ \partial_t (m_k \mathbf{U}_k) = \mathbf{S}_k^{U}(\mathbf{W}) \\ \partial_t (\alpha_k E_k) - \sum_{l=1, l\neq k}^{3} \Pi_{kl}(\mathbf{W}) \partial_t \alpha_l = S_k^{E}(\mathbf{W}) \end{cases} \tag{3.63}$$

where the source terms are given by closures (3.11-3.20). We initialize the problem as follows :

For the EOS, we stick to the *General Stiffened Gas* framework (3.55), and we adopt the following numerical parameters :

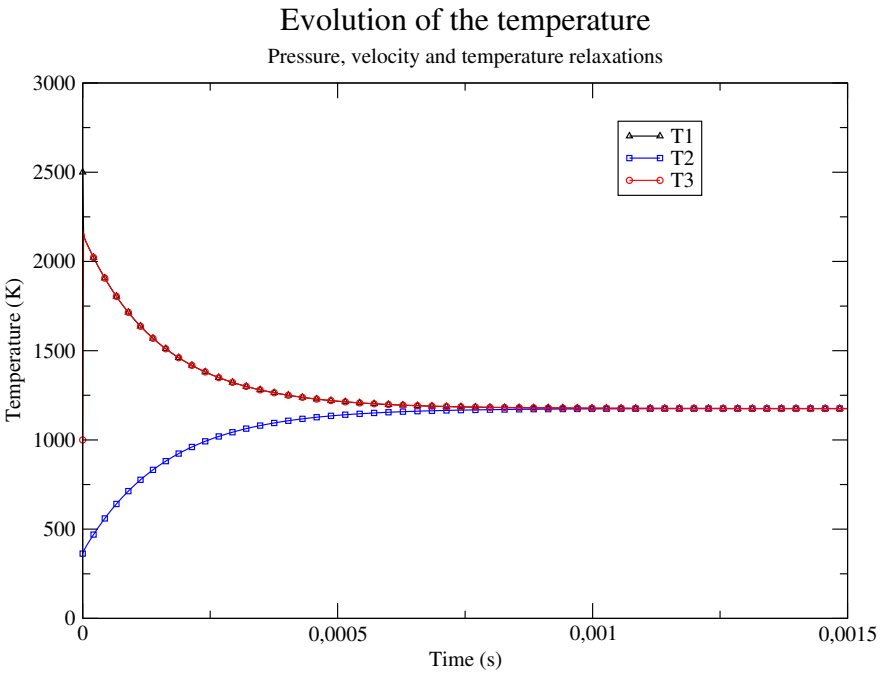

FIGURE 3.5 – *Second heat transfer verification test-case : General Stiffened Gas EOS*

Phase k	α_k	p_k	T_k	u_k
1	0.02	10^5	2500.0	0.00
2	0.88	10^5	363.0	0.00
3	0.10	10^5	1000.0	0.00

TABLE 3.8 – Mass and heat exchange test case - initial dataset

In terms of relaxation algorithms, similarly to paragraph 3.4.3 we maintain the choice of the instantaneous pressure relaxation algorithm, we also choose the instantaneous velocity relaxation :

$$\left\{ \begin{array}{l} \tau_{kl}^P = 0 \\ \tau_{kl}^U = 0 \end{array} \right. \tag{3.64}$$

Turning to heat and mass transfers, we choose the algorithms given in subsections (3.3.2) and (3.3.1) respectively, for which we adopt the following relaxation time scales :

$$\left\{ \begin{array}{l} \tau_{23}^m = 5.0 \times 10^{-5} \\ \tau_{kl}^T = \tau_0^T = 10^{-5} \end{array} \right. \tag{3.65}$$

Using these numerical parameters, two simulations are performed : one without mass transfer (where only the pressure and temperature relaxations are at stake), and one including the mass transfer (which means that all the three thermodynamical relaxations are involved).

Figure 3.6 gives the comparison of the two simulations in terms of partial mass m_3, as well as the mixture pressure defined by :

$$P_{mix} = \alpha_1 p_1 + \alpha_2 p_2 + \alpha_3 p_3 \tag{3.66}$$

Phase k	γ_k	Π_k	Q_k	$C_{V,k}$	q'_k
1 (GSG)	22.83859097	188447923.6	-13316.20000	12.87294826	0.00
2 (SG)	6.636214111	334850824.3	0.00	165.9732071	10000.00000
3 (PG)	1.083834328	0.00	0.00	6626.564746	-86464.79253

TABLE 3.9 – Mass and heat exchange test case - EOS parameters

We notice that when the mass transfer is not included, m_3 remains -as expected- constant and equal to its initial value $m_3 = 1.80 \times 10^{-2}$ during the whole simulation. When the mass transfer is taken into account, the Gibbs potential imbalance leads to a rapid increase of m_3, which reaches a maximum value of $m_{3,max} \approx 0.11$ around $t = 0.5\ ms$, after which it witnesses a less rapid decrease down to a final value of $m_3(t = 2\ ms) \approx 0.07$. We have checked that this m_3 evolution is compensated at each time instant by m_2 in a way such that $M = m_2 + m_3$ remains constant during the simulation. The transferred mass is significantly small in comparison with the initial value of m_2 and thus cannot be clearly seen on the scale of the figure.

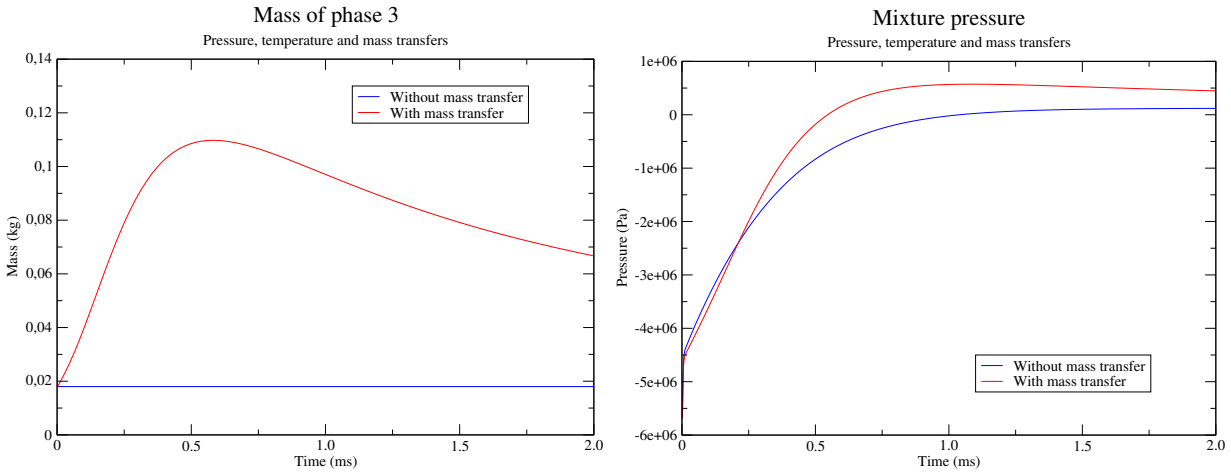

FIGURE 3.6 – *Effect of the mass transfer : on partial mass m_3 (left) and mixture pressure P_{mix} (right). Blue colour : without mass transfer, red colour : with mass transfer*

Figure 3.6 also presents the evolution of the pressure P_{mix} resulting from the mass transfer, which is also an important point to highlight. In fact, it has to be put in the physical context represented by EOS given in table 3.9 :

— Phase 1 : the corium, a high density-high temperature liquid, represented by the *Generalized Stiffened Gas* EOS ;

— Phase 2 : liquid water, represented by the *Stiffened Gas* EOS ;

— Phase 3 : water vapour, represented by the *Perfect Gas* EOS.

Therefore, negative P_{mix} values seen in figure 3.6 (right) are not abnormal, since EOS of phases 1 and 2 admit such values.

With this in mind, the increase of m_3 observed when the mass transfer is included is nothing but the partial evaporation of liquid water that happens under the thermodynamic

circumstances of this test case. And the resulting overpressure observed between the red and blue P_{mix} curves translates the compression that occurs when more and more vapour is created. This also explains why the mass m_3 is significantly smaller than m_2, it is linked to the fact that vapour's density is very low when compared to the liquid's one, and this is fairly represented by the set of EOS given in Table 3.8.

In figure 3.7 we provide the temperatures' evolution associated with the latter two simulations : without mass transfer in blue, and with mass transfer in red. We check that, in both cases, a state of temperature equilibrium is reached, and a slight difference in the temperature's evolution occurs, as observed in the time range $t \in [0, 0.5]$.

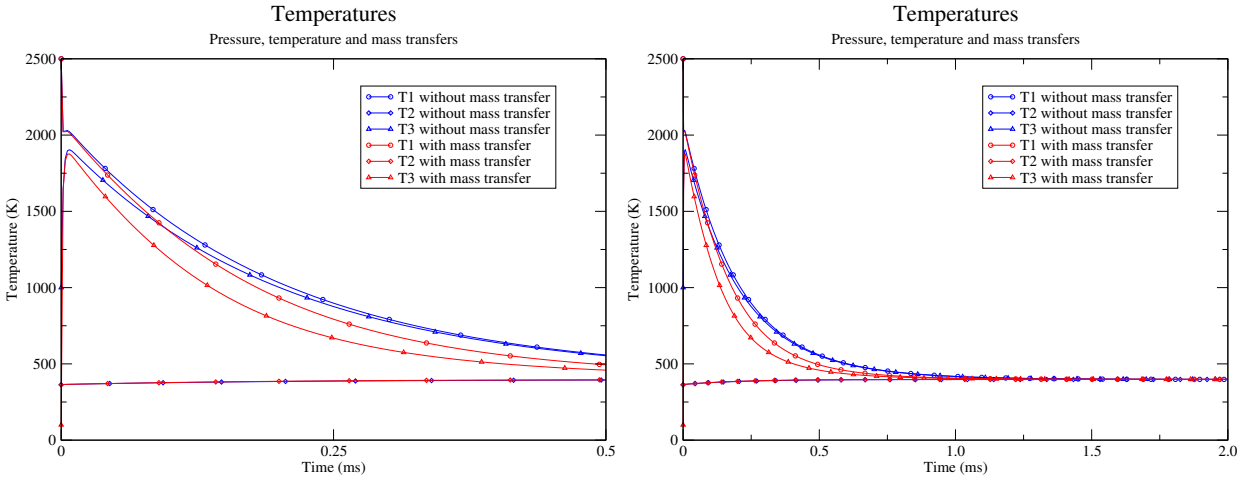

FIGURE 3.7 – *Effect of the mass transfer : evolution of the temperatures T_k, without mass transfer (blue) and with mass transfer (red). Zoom on the time range* $[0, 0.5]$ *(left).*

Knowing that the relaxation time scales play a key role in the transfers between phases, we have run several numerical tests with different values of τ_{kl}^T, while keeping :

$$\tau_{23}^m = 5.0 \times 10^{-5}$$

The temperature relaxation time scale was taken under the form :

$$\tau_{kl}^T = \tau_0^T = 10^{-N}$$

Figure 3.8 gives the comparison between the case $N = 4$ (called case 2 in the figure's caption), and the case $N = 5$ already presented above (called case 1). We observe that the created mass in case 2 is significantly higher, its maximum value is almost eight times greater than the maximum m_3 value of case 1. The expected effect on P_{mix} is checked : the more phase 3 (water vapour) is created the more P_{mix} increases. Nevertheless, we note that this correlation between the relaxation time scale and the increase of P_{mix} is a non linear process ; other simulations with $\tau_{kl}^T = 10^{-N}$, $N = 1, 2, 3$ did not show a significant rise of m_3 and P_{mix}, the results were of the same order of case 1 ($N = 5$).

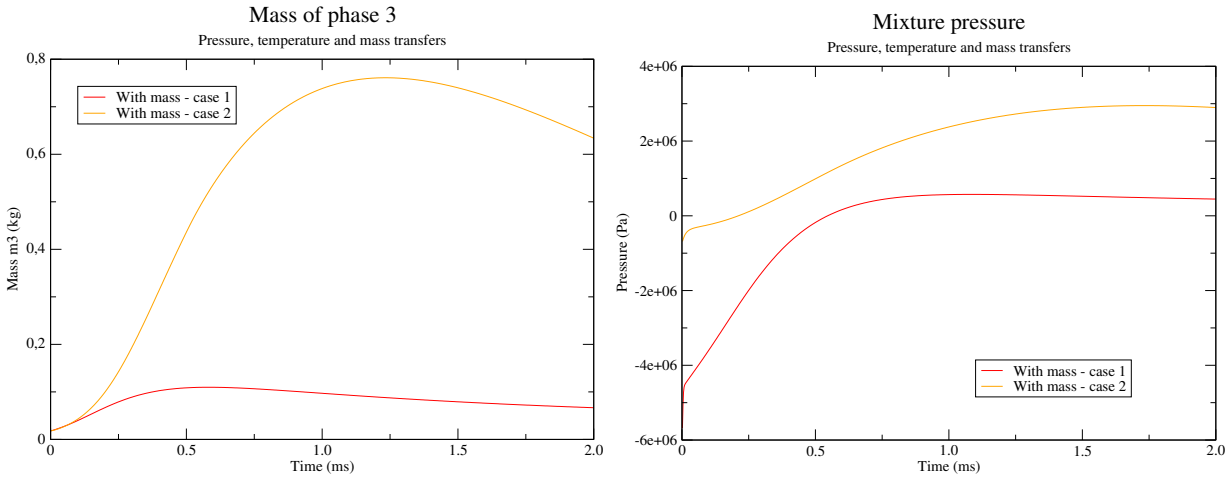

FIGURE 3.8 – *Effect of the mass transfer : on partial mass m_3 (left) and mixture pressure P_{mix} (right). Red colour : $\tau_{kl}^T = 10^{-5}$ (case 1), orange colour : $\tau_{kl}^T = 10^{-4}$ (case 2)*

3.4.5 Validation test case : the KROTOS experimental setup

The KROTOS experimental program was conducted in order to study some aspects of *fuel coolant interactions* (FCI), by performing research tests on specific phenomena involved in a FCI scenario. *Vapour explosion* is one of the aspects that the KROTOS experiment examined, by considering several fuel-coolant mixtures where different types of nuclear reactor prototypic materials were involved (zirconium dioxide, aluminium oxide, uranium dioxide, tin, etc.), the liquid water served as a standard coolant. Various conditions have been tested, including fuel masses between 1 kg and 10 kg at temperatures around 3000 K, while the liquid water was taken either at the saturation temperature, or with low subcooling (≈ 10 K less than the saturation temperature). For more details about these tests, we refer the reader to [8] where detailed descriptions and results are given.

The particular configuration that we focus on is the KROTOS-44 test, where alumina melt was poured into water with low subcooling, melt droplets are formed and progress slowly inside the water volume. An external pressure pulse was used to trigger the explosion before the first droplet hits the bottom of the water pool, at the triggering instant we consider that all the melt droplets are located inside the water volume. This configuration was identified as a numerical benchmark to test and compare different FCI codes, including MC3D [10] which is commonly used in France for *vapour explosion* simulations. [11] gives the details of the imposed geometry and the melt-coolant distribution, at the explosion's initiation instant.

In figure 3.9, we give a schematic representation of the geometry that we have considered in our numerical simulations. The phases distribution in the low pressure chamber is identical to what is given in [11] : the chamber is filled of liquid water at 363 K which is present as a pure phase between $x = 2.00$ and $x = 2.15$, then there is a 70 cm thick mixed zone called the *interaction zone*, where the three phases (melt droplets, liquid water and its vapour) are present, after which there is the *plug* composed of liquid and vapour water, and finally for $x > 3.23$ a pure gaseous volume covering the whole. The low pressure chamber was equipped

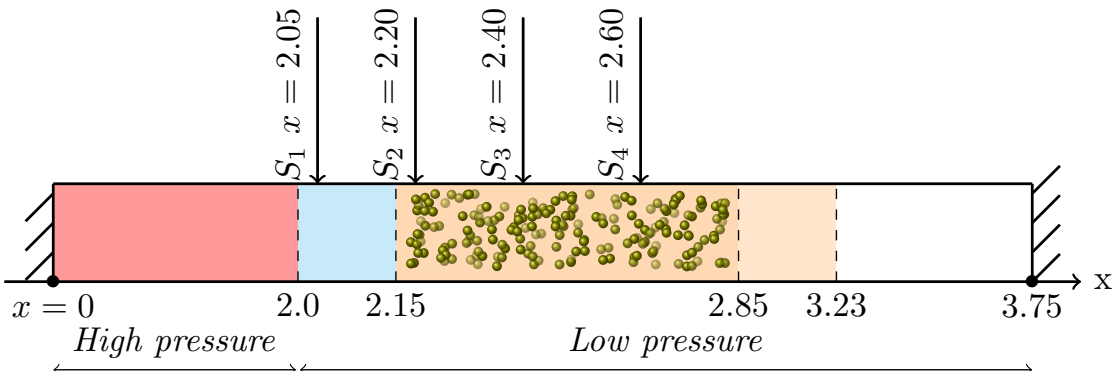

FIGURE 3.9 – *KROTOS-44 - Scheme of the shock tube*

with pressure stations at different positions, in order to record pressure histories over time and allow the examination of the pressure's evolution.

The experiment was realized in a vertical position, the latter layers' order is actually a bottom-top description of the KROTOS-44 tube right at the triggering instant. Nevertheless, in the model (3.1) the gravity effect is not taken into account. In fact, the gravity induced movement is too slow when compared to the explosion generated shock wave, that is why we considered the horizontal setup of figure 3.9.

The high pressure chamber, that triggers the shock wave, is represented in our numerical setup by a two meter thick water volume pressurized at 150 *bar*, which is the triggering pressure adopted in the experiment. However, while the experiment used a small pressurized gas volume (few centimetres thick) to trigger the shock wave, we have chosen the pressurized two meter thick water volume in order to avoid numerical difficulties that could arise from the reflection of rarefaction waves on the left side of the shock tube, once the explosion is triggered.

The dataset that was used to initialize the numerical simulations is :

High pressure chambre	Low pressure chamber			
	Pure liquid	*Interaction zone*	*Plug*	Cover gas
$\alpha_2 = 1 - 2 \times 10^{-6}$ $\alpha_1 = \alpha_3 = 10^{-6}$ $T_k = 1000.0\ K$ $p_k = 150 \times 10^5\ Pa$ $u_k = 0$	$\alpha_2 = 1 - 2 \times 10^{-6}$ $\alpha_1 = \alpha_3 = 10^{-6}$ $T_k = 363.0$	$\alpha_1 = 0.026$ $\alpha_2 = 0.884$ $\alpha_3 = 0.09$ $T_1 = 2500.0\ K$ $T_2 = 363.00\ K$ $T_3 = 1000.0\ K$	$\alpha_2 = 0.835 - 10^{-6}$ $\alpha_3 = 0.165$ $\alpha_1 = 10^{-6}$ $T_k = 363.00\ K$	$\alpha_3 = 1 - 2 \times 10^{-6}$ $\alpha_1 = \alpha_2 = 10^{-6}$ $T_3 = 700.00\ K$ $T_1 = T_2 = 363.00\ K$
	$u_k = 0$ and $p_k = 1.0 \times 10^5\ Pa$			

TABLE 3.10 – KROTOS-44 : shock tube initialization

The adopted EOS are those given in table 3.9, where, as mentioned in subsection 4.4, phases 1, 2 and 3 represent respectively the melt droplets, the liquid water and the vapour water. The initial droplets diameter is set to 15 *mm*, as stated in [11]. The heat transfer term K_{13}^T, defined initially in (3.21), is modified to account of the heat transfer between melt

droplets and water vapour, it is written as :

$$K_{13}^{T} = \frac{A}{A_0}\frac{1}{\tau_{13}^{T}}\frac{m_1 m_3 C_{V,1} C_{V,3}}{m_1 C_{V,1} + m_3 C_{V,3}} \tag{3.67}$$

where : A is the interfacial area variable that translates the droplet break-up phenomenon, and A_0 its initial value (see Chapter 1 [2] for more details about the considered interfacial area equation).

In order to treat the relaxations effects, we have chosen instantaneous relaxation algorithms for both the pressure and the velocity (see Chapter 2), that is :

$$\begin{cases} \tau_{kl}^{P} = 0 \\ \tau_{kl}^{U} = 0 \end{cases}$$

while for heat exchange and mass transfer, we have considered algorithms of subsections 3.2 and 3.1 respectively, using time scales given in (3.65). We mention also that we set for all numerical tests $CFL = 1/2$.

Turning to numerical results, a first aspect to examine is the mesh refinement. In fact, for a final simulation time of less than 2 ms, several meshes were tested. Figure 3.10 provides the comparison between the different meshes results in term of velocity, at the same time $t = 0.7$ ms. From figure 3.10 we can tell that the discrepancies between the results are reduced as mesh is refined. Thus, in the sequel we will focus on the finest mesh (375000 cells) to examine the pressure and velocity results.

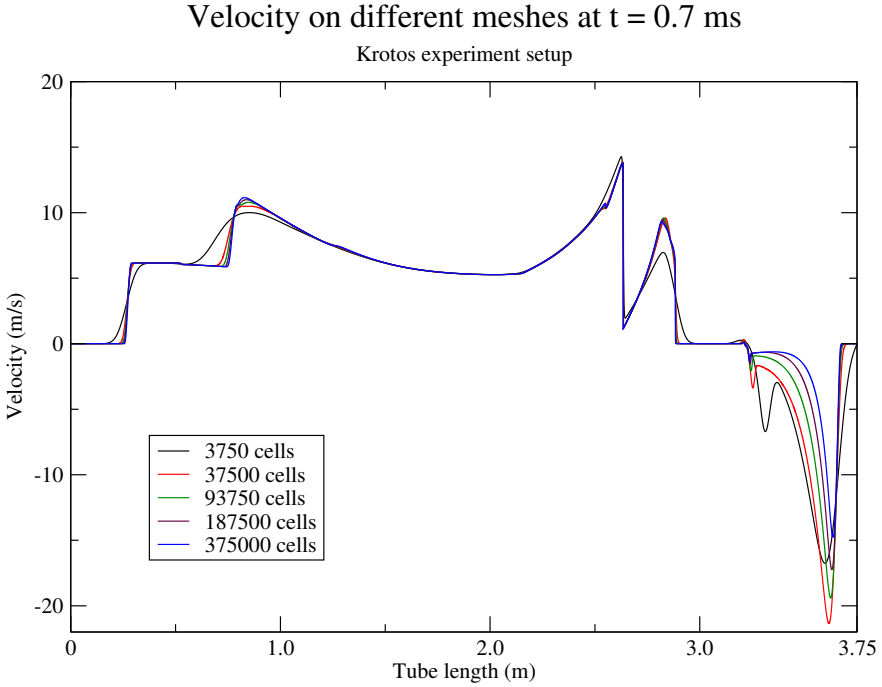

FIGURE 3.10 – *KROTOS-44 - Velocity at* $t = 0.7$ ms *on various meshes*

In figure 3.11, pressure histories in stations $S_1, .., S_4$ are given. It presents the variable P_{mix} (defined previously in (3.66)) wrt time at each station. For station S_1, we notice that the behaviour of the pressure signal at the early time instants, namely $t \approx 0.05\ ms$, is similar to what happens in the one-phase flow framework : a sudden pressure jump, followed by a plateau.

Turning to stations S_2, S_3 and S_4 located inside the *interaction zone*, we remark that after the shock wave is triggered, the pressure increases in a uniform way over the three stations, which is translated by the fact that the three pressure curves are superimposed for $t \in [0, 0.25]$. This is the signature of the occurring evaporation inside the *interaction zone*, which is a direct consequence of the initial thermodynamic setup of this zone. Actually, this behaviour is exactly what was highlighted in subsection 4.4, using the same three-phase mixture's initial data (statistical fractions, temperatures, and EOS). Mass transfer acts and creates more and more vapour, which drives the pressure to increase. At $t \approx 0.25\ ms$, station S_2 observes the arrival of the shock wave, while S_3 and S_4 continue the evaporation process.

At $t \approx 0.5\ ms$, the shock wave reaches station S_3, creating a significant pressure jump that gives $P_{mix} \approx 17\ MPa$, which is higher than the triggering initial pressure 15 MPa. This behaviour is retrieved at station S_4 as well, with even a higher pressure value $P_{mix} \approx 18\ MPa$. We recall that in Chapter 2 we have seen pressure jumps resulting from the dynamic effects (velocity and pressure relaxations) but without exceeding the triggering high pressure. Here, what is involved -in addition to dynamics- is thermal effects, namely thermal exchange and the resulting evaporation.

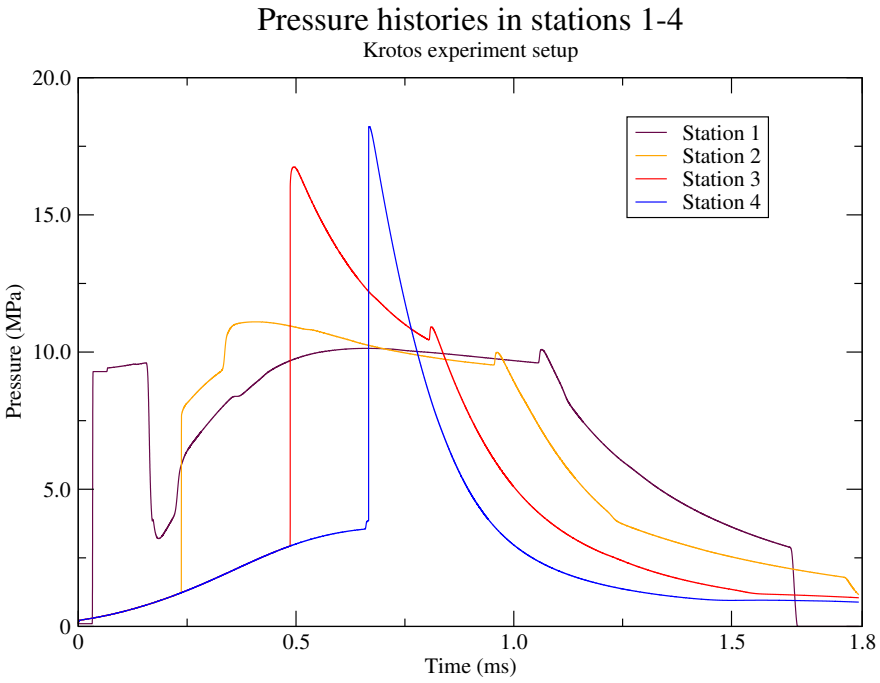

FIGURE 3.11 – *KROTOS-44 - Pressure histories in stations* $S_1, .., S_4$

We mention that the droplet break-up do not play a significant role in the presented numerical case. In fact, the interfacial area's evolution is proportional to the velocity difference

$U_1 - U_2$, since we consider the instantaneous velocity relaxation, the relative velocity remains almost null all the time, which does not allow A to evolute to higher values, as shown in figure 3.12.

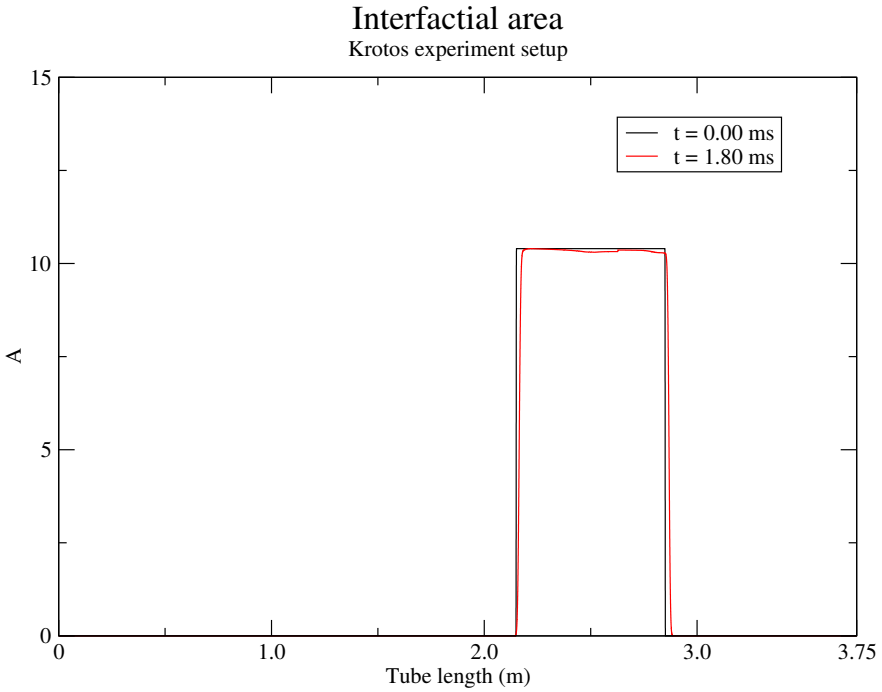

FIGURE 3.12 – *KROTOS-44 - Interfacial area at the start and the end of the computation*

In figure 3.13, we provide complementary results of this test case, by presenting the pressure and velocity at five distinct time instants. The progress of the right-going shock wave can be observed, at $t = 1.0\ ms$ the front of this wave is located around $x = 2.90\ m$, which means that at this time instant the shock wave has completely crossed the *interaction zone*. Pressure's values can be also checked, we notice that for $t = 0.55\ ms$ and $t = 0.70\ ms$ the reached pressure values are higher than 15 MPa, which confirms the observed result in the stations S_3 and S_4. In this figure, we can also see the progress of the left-going rarefaction wave, which -shortly before $t = 1.0\ ms$ reaches the left tube's boundary where it gets reflected.

Finally, it is relevant to draw a comparison between the numerical and experimental results concerning the KROTOS-44 setup. As provided in [8], the measured pressure around stations S_3 and S_4 locations is of the order of 50 MPa to 60 MPa, while our model's result is 18 MPa. Nevertheless, we mention that the numerical benchmark given in [11] shows an important dispersion between the different *vapour explosion* codes, pressure values vary from 10 MPa to more than 100 MPa. In turn, the code MC3D [10] gives an estimation of the order of 20 MPa [11].

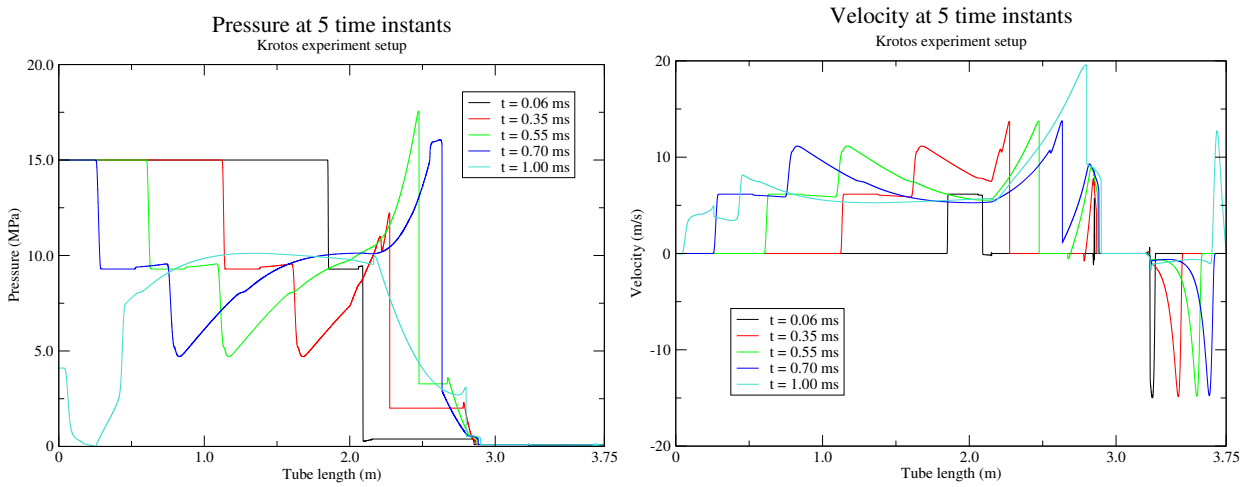

FIGURE 3.13 – *KROTOS-44 - Pressure (left) and velocity (right) at 5 time instants*

3.5 Conclusion

In this chapter, we have recalled the three-phase flow model that was presented in Chapter 2, which we have enriched to account for temperature relaxation and mass transfer. Closure laws to account for the latter thermodynamical effects were given, and properties of the whole model were examined.

On the continuous level, the new added sources terms were checked to be in agreement with the entropy balance. Afterwards, numerical schemes to find approximate solutions of relaxation subsystems were presented. Several test cases were performed to ensure that the numerical schemes provide accurate and physically relevant results ; this included pure verification test cases, *flow in a box* test cases to have a deeper look on the combined relaxation effects, and finally a more complete test case representative of a *vapour explosion* scenario.

However, a point that arose immediately from the numerical test cases is the necessity of investigating the stability of the non-instantaneous relaxation algorithms (for pressure and velocity). This would allow to consider a wider range of time scales (considered null in the presented test cases), and to better account for different physically relevant situations.

Bibliographie

[1] G. Berthoud, Vapor explosions, *Annual Review of Fluid Mechanics*, vol. 32, pp. 573–611, 2000.

[2] H. Boukili and J.M. Hérard, Relaxation and simulation of a barotropic three-phase flow model, *ESAIM : Mathematical Modelling and Numerical Analysis*, vol. 53, pp. 1031-1059, 2019.

[3] H. Boukili and J.M. Hérard, Simulation and validation of a three-phase flow model with energy, Preprint submitted to *Computers and Fluids*.

[4] F. Crouzet, F. Daude, P. Galon, J.-M. Hérard, O. Hurisse and Y. Liu, Validation of a two-fluid model on unsteady water-vapour flows, *Computers and Fluids*, vol. 199, pp.131-142, Elsevier 2015.

[5] S. Gavrilyuk, The structure of pressure relaxation terms : the one-velocity case, *EDF report H-I83-2014-0276-EN*, 2014.

[6] J.M. Hérard, A three-phase flow model, *Mathematical and Computer Modelling*, vol. 45, pp. 732-755, 2007.

[7] J.M. Hérard and O. Hurisse, A fractional step method to compute a class of compressible gas-liquid flows, *Computers and Fluids*, vol. 55, pp.57-69, 2012.

[8] I. Huhtiniemi, H. Hohmann, R. Faraoni, M. Field, R. Gambaretti and K. Klein, KROTOS 38 to KROTOS 44 : Data Report, *Technical Note No. I.96.37, Joint Research Centre Ispra*, February 1996.

[9] O. Hurisse, Simulation des écoulements industriels diphasiques compressibles, *Université de Strasbourg*, Thèse d'habilitation à diriger les recherches, https ://hal.archives-ouvertes.fr/tel-01570985, 2017.

[10] R. Meignen, B. Raverdy, S. Picchi and J. Lamome, The challenge of modelling fuel-coolant interaction. Part II : steam explosion, *Nuclear Engineering and Design*, vol. 280, pp.528-541, 2014.

[11] Nuclear Energy Agency Committee on the Safety of Nuclear Installations, OECD research programme on fuel-coolant interaction steam explosion resolution for nuclear applications - SERENA, *Organisation for Economic Co-operation and Development*, https ://www.oecd-nea.org/nsd/docs/2007/csni-r2007-11.pdf, 2007.

3.6 Appendix A1 - Analytical solution for the heat transfer sub-system

We recall the heat transfer sub-system (3.32) :

$$\begin{cases} \partial_t \alpha_k = 0 \\ \partial_t m_k = 0 \\ \partial_t (m_k \mathbf{U}_k) = 0 \\ \partial_t (\alpha_k E_k) = \sum_{l=1, l\neq k}^{3} K_{kl}^T(\mathbf{W})(T_l - T_k) \end{cases}$$

We focus particularly on the energy balances that have been written under the form (3.36) :

$$\partial_t T_k = \sum_{l=1, l\neq k}^{3} \frac{K_{kl}^T(\mathbf{W})}{m_k C_{V,k}}(T_l - T_k)$$

We expand the three equations, and replace the last one by the total conservation of the internal energies, this gives :

$$\begin{cases} \partial_t T_1 = \frac{K_{12}^T(\mathbf{W})}{m_1 C_{V,1}}(T_2 - T_1) + \frac{K_{13}^T(\mathbf{W})}{m_1 C_{V,1}}(T_3 - T_1) \\ \partial_t T_2 = \frac{K_{12}^T(\mathbf{W})}{m_2 C_{V,2}}(T_1 - T_2) + \frac{K_{23}^T(\mathbf{W})}{m_2 C_{V,2}}(T_3 - T_2) \\ \partial_t (m_1 C_{V,1} T_1 + m_2 C_{V,2} T_2 + m_3 C_{V,3} T_3) = 0 \end{cases} \tag{3.68}$$

We define :

$$E_0 = m_1 C_{V,1} T_1(t=0) + m_2 C_{V,2} T_2(t=0) + m_3 C_{V,3} T_3(t=0) \tag{3.69}$$

We can therefore write :

$$T_3(t) = \frac{1}{m_3 C_{V,3}} \left[E_0 - m_1 C_{V,1} T_1(t) - m_2 C_{V,2} T_2(t) \right] \tag{3.70}$$

We then replace in the first two equations of (3.68) to get :

$$\begin{cases} \partial_t T_1 + \left(\frac{K_{12}^T}{m_1 C_{V,1}} + \frac{K_{13}^T}{m_1 C_{V,1}} + \frac{K_{13}^T}{m_3 C_{V,3}} \right) T_1 + \left(\frac{m_2 C_{V,2} K_{13}^T - m_3 C_{V,3} K_{12}^T}{m_1 C_{V,1} m_3 C_{V,3}} \right) T_2 = \frac{K_{12}^T E_0}{m_1 C_{V,1} m_3 C_{V,3}} \\ \partial_t T_2 + \left(\frac{K_{12}^T}{m_2 C_{V,2}} + \frac{K_{23}^T}{m_2 C_{V,2}} + \frac{K_{23}^T}{m_3 C_{V,3}} \right) T_2 + \left(\frac{m_1 C_{V,1} K_{23}^T - m_3 C_{V,3} K_{12}^T}{m_2 C_{V,2} m_3 C_{V,3}} \right) T_1 = \frac{K_{23}^T E_0}{m_2 C_{V,2} m_3 C_{V,3}} \end{cases} \tag{3.71}$$

Here we introduce the following assumption :

$$m_1 C_{V,1} K_{23}^T = m_2 C_{V,2} K_{13}^T = m_3 C_{V,3} K_{12}^T \tag{3.72}$$

This allows to fully decouple the equations in (3.71), and their resolution becomes easier. Practically, we choose a set of time-dependent coefficients K_{kl}^T such that :

$$m_1 C_{V,1} K_{23}^T = m_2 C_{V,2} K_{13}^T = m_3 C_{V,3} K_{12}^T = t + 1 \tag{3.73}$$

	Phase $k=1$	Phase $k=2$	Phase $k=3$
u_k	2.00	3.00	7.00
p_k	7.10^3	1.10^4	4.10^3
ρ_k	5.20	2.70	0.30
α_k	0.30	0.35	0.35
γ_k	27.07	1.40	2.40
Π_k	$8.06\ 10^7$	0.00	0.00

TABLE 3.11 – *Heat transfer initialisation dataset*

Therefore, if we denote :

$$\begin{cases} \alpha = \frac{1}{m_1 C_{V,1} m_2 C_{V,2}} + \frac{1}{m_1 C_{V,1} m_3 C_{V,3}} + \frac{1}{m_2 C_{V,2} m_3 C_{V,3}} \\ \beta = \frac{E_0}{m_1 C_{V,1} m_2 C_{V,2} m_3 C_{V,3}} \end{cases} \tag{3.74}$$

The system (3.71) becomes :

$$\begin{cases} \partial_t T_1 + \alpha(t+1) T_1 = \beta(t+1) \\ \partial_t T_2 + \alpha(t+1) T_2 = \beta(t+1) \end{cases} \tag{3.75}$$

The solution is then given by :

$$\begin{cases} T_1(t) = \frac{\beta}{\alpha} + \left(T_1^0 - \frac{\beta}{\alpha}\right) exp(-\alpha(t^2/2 + t)) \\ T_2(t) = \frac{\beta}{\alpha} + \left(T_2^0 - \frac{\beta}{\alpha}\right) exp(-\alpha(t^2/2 + t)) \end{cases} \tag{3.76}$$

$T_3(t)$ is given by (3.70). This determines completely the analytical solution. In practice, we considered the following initial dataset :

Chapitre 4

Conclusion et perspectives

Ce travail de thèse se focalise sur l'étude théorique et numérique des écoulements à trois phases, pour application à la simulation de l'*explosion vapeur* (EV), phénomène qui a beaucoup intéressé les chercheurs dans le domaine de la sûreté nucléaire pendant ces dernières décennies.

L'occurrence d'EV est liée à un mélange de trois fluides : le *corium*, liquide chaud apportant l'énergie, l'eau en tant que liquide de refroidissement, et la vapeur d'eau. D'où la nécessité d'un modèle d'écoulement à trois phases afin de pouvoir décrire un tel scénario. Le modèle recherché doit également être capable de décrire les transitoires rapides, en présence d'ondes de choc, tout en prenant en compte les échanges dynamiques et thermiques. L'ensemble de ces éléments est obligatoire pour une représentation réaliste de l'EV.

Dans un premier temps, un modèle d'écoulement triphasique barotrope est présenté. Cela fait l'objet du chapitre 1 [10, 40] et de son annexe. Ce modèle permet de décrire les transitoires rapides d'un mélange à trois phases. L'une des difficultés liées à ce genre de modèles est la nécessité de proposer des lois de fermeture, afin de donner une description des échanges physiques ayant lieu à l'interface entre les phases, et également pour que le modèle soit *bien posé*, au sens mathématique du terme. Un choix de lois de fermeture est proposé. Le modèle résultant est tel que sa structure convective est hyperbolique avec des relations de saut uniques, ce qui permet de bien définir les ondes de choc dans le mélange. Des fermetures pour les termes sources sont également présentées, pour prendre en compte les effets dynamiques de relaxation vitesse et pression, tout en respectant une contrainte d'inégalité d'entropie sur le système global, ce qui permet de s'assurer que l'on retient bien des solutions physiques du modèle.

Ce modèle est complété d'une équation d'aire interfaciale, afin de pouvoir représenter ce qui se passe dans le cas de présence de gouttes dispersées dans une phase continue. Cela correspond typiquement à des gouttes d'eau réparties dans de l'air, ou encore des gouttes de *corium* qui se retrouvent au milieu d'un volume d'eau. L'équation d'aire interfaciale considérée s'intègre dans le formalisme mathématique expliqué ci-dessus, et elle permet, du point de vue physique, de rendre compte du phénomène de fragmentation des gouttes sous l'impact d'une onde de choc [6, 56].

Pour la résolution numérique, la stratégie de *pas fractionnaires* est mise en œuvre. Elle permet de résoudre étape par étape le système d'EDP global, tout en étant consistant avec

l'inégalité d'entropie. Le système global est découpé en trois sous-systèmes : la convection, la relaxation vitesse et la relaxation pression. Des cas tests de vérification des schémas numériques sont présentés, et un cas test de validation globale sur la base de [11, 12] est également étudié.

Dans le chapitre 2, le modèle du chapitre 1 est étendu au cadre non barotrope [39], en prenant en compte les bilans d'énergie des trois phases. Cela a pour conséquence immédiate l'introduction de plus d'interdépendance entre les variables thermodynamiques du système, ainsi que le couplage des étapes de relaxation vitesse et pression, qui étaient indépendantes dans le formalisme barotrope. Dans ce chapitre, la stratégie de résolution par *pas fractionnaires* est maintenue. De nouveaux schémas numériques sont mis en place pour résoudre les différents sous-systèmes (convection et relaxations), et des cas tests de vérification sont réalisés. Ensuite, le cas test de validation [11, 12] est réexaminé. On constate notamment que le formalisme non barotrope permet de retrouver des niveaux de pression plus proches de l'expérience. Enfin, plusieurs annexes donnent des résultats et détails techniques complémentaires aux résultats présentés dans le chapitre, notamment en ce qui concerne l'impact des temps caractéristiques de relaxation (vitesse et pression) sur les résultats du modèle, dans une configuration d'écoulement à trois phases.

Le chapitre 3 vient compléter le modèle du chapitre 2, en y rajoutant les termes sources pour tenir compte du transfert thermique et de l'échange de masse. En effet, ces deux effets sont d'une importance capitale dans la simulation d'EV, leur prise en compte est indispensable. On vérifie que les termes sources choisis sont en accord avec l'inégalité d'entropie globale, et on propose ensuite des schémas numériques pour leur approximation. Sur le plan numérique, des cas tests de vérification sont considérés, afin de s'assurer de la précision de résolution des étapes de transfert thermique et échange de masse. Ensuite, des cas tests d'*écoulement en boite* sont analysés, afin de mieux comprendre l'action couplée des effets de relaxation en l'absence de termes de convection. Finalement, un cas test complet représentatif d'un scénario d'EV est examiné. Il s'agit du cas proposé dans le benchmark numérique [58] sur la base de l'expérience KROTOS-44 [45], où l'interaction entre une masse de métal fondu avec de l'eau liquide, en présence d'ondes de choc, est étudiée. La comparaison entre les résultats numériques et expérimentaux est établie.

Globalement, ce qui ressort des résultats présentés dans les différents chapitres est la capacité du modèle d'EDP à rendre compte, de façon assez satisfaisante, des effets dynamiques liés au mélanges diphasiques et triphasiques étudiés. Cela se traduit notamment par des estimations correctes des amplitudes d'ondes de pression, ainsi que l'observation de l'impact du phénomène de fragmentation de gouttes. Cela est d'autant plus satisfaisant que la convergence en maillage sur tous les calculs instationnaires a été vérifiée, sachant que l'on calcule des structures de choc pertinentes, au vue de l'unicité des relations de saut dans le système convectif considéré. Par ailleurs, les effets thermiques sont également retrouvés, toutefois en l'absence de données expérimentales détaillées sur ces effets (évolution des températures et/ou des masses partielles lors d'une EV), et à défaut d'une connaissance précise des échelles de temps de transfert thermique et échange de masse, on est contraint à ce jour à se satisfaire des aspects qualitatifs uniquement.

Néanmoins, les aspects suivants peuvent être considérés, afin de rendre le modèle plus riche, plus robuste et mieux adapté aux scénarios d'EV :

1. Sur le plan numérique, pour l'approximation du sous-système convectif on a considéré le schéma de Rusanov [64] à la fois pour le modèle barotrope et non barotrope. Le développement d'un solveur de Riemann plus robuste et surtout plus précis aurait un impact positif sur la précision du modèle global (voir [65] par exemple).

2. Dans le chapitre 3, on a choisi les algorithmes de relaxation instantanée pour les étapes de vitesse et pression. Or, d'après l'analyse présentée dans le chapitre 2, les temps caractéristiques de relaxation ont un impact significatif sur les solutions du modèle. Il est donc nécessaire d'examiner la combinaison des algorithmes de relaxation vitesse et pression **non instantanée** avec les effets thermiques (relaxation de température et transfert de masse), afin de voir l'impact sur les résultats numériques, et permettre l'analyse d'un large spectre de temps de relaxation.

   En particulier, considérer un temps de relaxation non nul pour la vitesse permettra d'autoriser la variable d'aire interfaciale à évoluer en fonction de l'écoulement (en admettant des écarts de vitesse non nuls). On rappelle que cette variable est ce qui permet de suivre la fragmentation des gouttes, phénomène important dans la dynamique d'une EV, et qui -pour l'instant- n'a pas été pris en compte dans le cas test KROTOS (voir le chapitre 3), à cause de la relaxation vitesse instantanée.

3. Les lois d'états choisies sont du type *gaz parfait* ou *gaz raide*. Certains algorithmes mis en place reposent sur ces lois deux d'état pour garantir l'existence et unicité de solutions admissibles. Certes, les ordres de grandeur des solutions obtenues sont en accord assez satisfaisant avec les mesures expérimentales, mais il serait pertinent de considérer des lois d'état plus riches, afin de représenter de façon plus fidèle la physique des fluides réellement mis en jeu en cas d'EV.

Chapitre 5

Bibliographie générale

Bibliographie

[1] M.E. Ahamadi, H.T. Rakotondramiarana and Rakotonindrainy, Modeling and Simulation of Compressible Three-Phase Flows in an Oil Reservoir : Case Study of Tsimiroro Madagascar, *American Journal of Fluid Dynamics*, vol. 4, pp. 181-193, 2014.

[2] A. Ambroso , C. Chalons, F. Coquel and T. Galié, Relaxation and numerical approximation of a two-fluid two-pressure diphasic model, *ESAIM : Mathematical Modelling and Numerical Analysis*, vol. 43, pp. 1063-1097, 2009.

[3] A. Ambroso , C. Chalons and P.-A. Raviart, A Godunov-type method for the seven-equation model of compressible two-phase flow, *Comput. and Fluids*, vol. 54, pp. 67-91, 2012.

[4] M.R. Baer and J.W. Nunziato, A two phase mixture theory for the deflagration to detonation transition (DDT) in reactive granular materials, *Int. J. Multiphase Flow*, vol. 12-6, pp. 861-889, 1986.

[5] C. Berthon, Contribution à l'analyse numérique des equations de Navier-Stokes compressibles à deux entropies spécifiques. Applications à la turbulence compressible, *PhD thesis*, Université Paris 6, 1999.

[6] G. Berthoud, Vapor explosions, *Annual Review of Fluid Mechanics*, vol. 32, pp. 573-611, 2000.

[7] Z. Bilicki and J. Kestin, Physical aspects of the relaxation model in two-phase flow, *Proceedings of the Royal Society of London A : Mathematical, Physical and Engineering Sciences*, vol. 428, pp. 379-397, 1990.

[8] W. Bo, H. Jin, D. Kim, X. Liu, H. Lee, N. Pestiau, Y. Yu, J. Glimm and J.W. Grove, Comparison and validation of multiphase closure models, *Computers and Mathematics with Applications*, vol. 56, pp. 1291-1302, 2008.

[9] M. Bonizzi and R.I. Issa, On the simulation of three-phase slug flow in nearly horizontal pipes using the multi-fluid model, *Int. J. Multiphase Flow*, vol. 29-11, pp. 1719-1747, 2003.

[10] H. Boukili and J.M. Hérard, Relaxation and simulation of a barotropic three-phase flow model, *ESAIM : Mathematical Modelling and Numerical Analysis*, vol. 53, p. 1031-1059, 2019.

[11] A. Chauvin, Étude expérimentale de l'atténuation d'une onde de choc par un nuage de gouttes et validation numérique, *PhD thesis*, Université Aix Marseille, https ://www.theses.fr/2012AIXM4732.pdf, 2012.

[12] A. Chauvin, G. Jourdan, E. Daniel, L. Houas and R. Tosello, Experimental investigation of the propagation of a planar shock wave through a two-phase gas-liquid medium, *Physcis of Fluids*, vol.23, 113301, 2011.

[13] S. Clerc, Numerical simulation of the homogeneous equilibrium model for two-phase flows, *Journal of Computational Physics*, vol. 161, pp. 354-375, 2000.

[14] F. Coquel, T. Gallouët, J.M. Hérard and N. Seguin, Closure laws for a two fluid two-pressure model, *C. R. Acad. Sci. Paris*, vol. I-334, pp. 927-932, 2002.

[15] F. Coquel, J.M. Hérard and K. Saleh, A positive and entropy-satisfying finite volume scheme for the Baer Nunziato model, *Journal of Computational Physics*, vol. 330, pp. 401-435, 2017.

[16] F. Coquel, J.M. Hérard, K. Saleh and N. Seguin, A robust entropy-satisfying finite volume scheme for the isentropic Baer Nunziato model, *ESAIM : Mathematical Modelling and Numerical Analysis*, vol. 48, pp. 165-206, 2014.

[17] F. Crouzet, F. Daude, P. Galon, J.-M. Hérard, O. Hurisse and Y. Liu, Validation of a two-fluid model on unsteady liquid-vapor water flows, *Computers and Fluids*, vol. 199, pp.131-142, Elsevier 2015.

[18] D. A. Drew and S. L. Passman Theory of Multicomponent Fluids, *Springer Verlag*, 2006.

[19] P. Downar-Zapolski, Z. Bilicki, L. Bolle, and J. Franco The non-equilibrium relaxation model for one-dimensional flashing liquid flow, *International journal of multiphase flow*, vol. 22, pp. 473-483, 1996.

[20] P. Embid and M. Baer, Mathematical analysis of a two-phase continuum mixture theory, *Continuum Mech. Thermodyn*, vol. 4, pp. 279-312, 1992.

[21] M. Essadki, Contribution to a unified modelling of fuel injection : from dense liquid to polydisperse evaporating spray, *PhD thesis*, Ecole polytechnique, https ://tel.archives-ouvertes.fr/tel-01928584, 2018.

[22] G. Faccanoni, S. Kokh and G. Allaire, Modelling and simulation of liquid-vapor phase transition in compressible flows based on thermodynamical equilibrium, *ESAIM : Mathematical Modelling and Numerical Analysis*, vol. 46, pp. 1029-1054, 2012.

[23] I. Faille and E. Heintze, A rough finite volume scheme for modeling two-phase flow in a pipeline, *Computers and Fluids*, vol. 28, pp. 213-241, 1999.

[24] T. Flätten and H. Lund, Relaxation two-phase flow models and the subcharacteristic condition, *Mathematical Models and Methods in Applied Sciences*, vol. 21(12), pp. 2379-2407, 2011.

[25] D. Furfaro and R. Saurel, A simple HLLC-type Riemann solver for compressible non-equilibrium two-phase flows, *Computers & Fluids*, vol. 111, pp. 159-178, 2015.

[26] J. Gale, I. Tiselj, and A. Horvat, Two-fluid model of the WAHA code for simulations of water hammer transients, *Multiphase Science and Technology*, vol .20 (3-4), pp. 291-322, 2008.

[27] T. Gallouët, P. Helluy, J.M. Hérard and J. Nussbaum, Hyperbolic relaxation models for granular flows, *ESAIM : Mathematical Modelling and Numerical Analysis*, vol. 44 (2), pp. 371-400, 2010.

[28] T. Gallouët, J.M. Hérard and N. Seguin, Numerical modeling of two-phase flows using the two-fluid two-pressure approach, *Mathematical Models and Methods in Applied Sciences, World Scientific Publishing*, vol. 14(15), pp. 663-700, 2004.

[29] S. Gavrilyuk, The structure of pressure relaxation terms : the one-velocity case, *EDF report H-I83-2014-0276-EN*, 2014.

[30] S. Gavrilyuk and R. Saurel, Mathematical and numerical modelling of two-phase compressible flows with micro inertia, *Journal of Computational Physics*, vol. 175, pp. 326-360, 2002 .

[31] B.E Gelfand, Droplet breakup phenomena in flows with velocity lag, *Progress in Energy and Combustion Science*, vol. 22 , pp. 201-265 , 1996.

[32] H.Guillard and F.Duval, A Darcy law for the drift velocity in a two-phase flow model, *Journal of Computational Physics*, vol. 224, pp. 288-313, 2007.

[33] V. Guillemaud, Modéisation et simulation numérique des écoulements diphasiques par une approche bifluide à deux pressions, *Ph.D. thesis*, Université de Provence - Aix-Marseille I, https ://tel.archives-ouvertes.fr/tel-00169178/document, 2007.

[34] L. Haar, J.S. Gallagher and G.S. Kell, NBS/NRC Steam Tables : Thermodynamic and Transport Properties and Computer Programs for Vapor and Liquid States of Water in SI Units, *Taylor & Francis*, 1984.

[35] E. Han, M. Hantke and S. Müller, Efficient and robust relaxation procedures for multi-component mixtures including phase transition, *Journal of Computational Physics*, vol. 338, pp. 217-239, 2017.

[36] M. Hantke and S. Müller, Closure conditions for a one temperature non-equilibrium multi-component model of Baer-Nunziato type, *ESAIM proceedings*, vol. 66, pp. 42-60, 2019.

[37] P. Helluy and H. Mathis, Pressure laws and fast Legendre transform, *Mathematical Models and Methods in Applied Sciences*, vol. 21, pp. 745-775, 2011.

[38] P. Helluy and N. Seguin, Relaxation models of phase transition flows, *ESAIM : Mathematical Modelling and Numerical Analysis*, vol. 40, pp. 331-352, 2006.

[39] J.M. Hérard, A three-phase flow model, *Mathematical and Computer Modelling*, vol. 45, pp. 732-755, 2007.

[40] J.M. Hérard, A class of compressible multiphase flow models, *Comptes Rendus Mathématique*, vol. 354, pp. 954-959, 2016.

[41] J.M. Hérard and O. Hurisse, A simple method to compute standard two-fluid models, *International Journal of Computational Fluid Dynamics*, vol. 19 (7), pp. 475-482, 2005.

[42] J.M. Hérard and O. Hurisse, A fractional step method to compute a class of compressible gas-liquid flows, *Computers and Fluids*, vol. 55, pp. 57-69, 2012.

[43] J.M. Hérard, H. Mathis, A three-phase flow model with two miscible phases, *ESAIM : Mathematical Modelling and Numerical Analysis*, vol. 53, pp. 1373-1389, 2019,

[44] T.Y. Hou and P.G. LeFoch, Why nonconservative schemes converge to wrong solutions : error analysis, *Mathematics of computation*, vol. 62(206), pp. 497-530, 1994.

[45] I. Huhtiniemi, H. Hohmann, R. Faraoni, M. Field, R. Gambaretti and K. Klein, KROTOS 38 to KROTOS 44 : Data Report, *Technical Note No. I.96.37, Joint Research Centre Ispra*, February 1996.

[46] O. Hurisse, Simulation des écoulements industriels diphasiques compressibles, *Université de Strasbourg*, Thèse d'habilitation à diriger les recherches, https ://hal.archives-ouvertes.fr/tel-01570985, 2017.

[47] O. Hurisse, L. Quibel, A homogeneous model for compressible three-phase flows involving heat and mass transfer, *ESAIM proceedings*, vol. 66, pp. 84-108, 2019.

[48] M. Ishii, Thermo-fluid dynamic theory of two-phase flows, *Collection de la Direction des Études et Recherches d'Électricité de France*, 1975.

[49] A. K. Kapila, R. Menikoff, J. B. Bdzil, S. F. Son, and D. S. Stewart, Two-phase modeling of deflagration-to-detonation transition in granular materials : Reduced equations, *Physics of Fluids*, vol. 13 (10), pp. 3002-3024, 2001.

[50] A.K. Kapila, S.F. Son, J.B. Bdzil, R. Menikoff and D.S. Stewart, Two phase flow modeling of DDT : structure of the velocity relaxation zone, *Physics of Fluids*, vol. 9 (12), pp. 3885-3897, 1997.

[51] D. Lhuillier, C.-H. Chang and T. G. Theofanous, On the quest for a hyperbolic effective-field model of disperse flows, *Journal of Fluid Mechanics*, vol. 731, pp. 184-194, 2013.

[52] B. Li, H. Yin, C. Zhou and F. Tsukihashi, Modeling of Three-phase Flows and Behavior of Slag/Steel Interface in an Argon Gas Stirred Ladle, *ISIJ International*, vol. 48, pp. 1704-1711, 2008.

[53] S. Liang, W. Liu, and L. Yuan, Solving seven-equation model for compressible two-phase flow using multiple GPUs, *Computers & Fluids*, vol. 99, pp. 156-171, 2014.

[54] H. Mathis, A thermodynamically consistent model of a liquid-vapor fluid with a gas, *ESAIM : Mathematical Modelling and Numerical Analysis*, vol. 53, pp. 63-84, 2018.

[55] M. Massot, F. Laurent, D. Kah and S. de Chaisemartin, A robust moment method for evaluation of the disappearance rate of evaporating sprays, *SIAM Journal of Applied Mathematics*, vol. 70, pp. 3203-3234, 2010.

[56] R. Meignen, B. Raverdy, S. Picchi and J. Lamome, The challenge of modelling fuel-coolant interaction. Part II : steam explosion, *Nuclear Engineering and Design*, vol. 280, pp. 528-541, 2014.

[57] S. Müller, M. Hantke and P. Richter, Closure conditions for non-equilibrium multi-component models, *Continuum Mechanics and Thermodynamics*, vol. 28, pp. 1157-1190, 2016.

[58] Nuclear Energy Agency Committee on the Safety of Nuclear Installations, OECD research programme on fuel-coolant interaction steam explosion resolution for nuclear applications - SERENA, *Organisation for Economic Co-operation and Development*, https ://www.oecd-nea.org/nsd/docs/2007/csni-r2007-11.pdf, 2007.

[59] Nuclear Energy Agency Committee on the Safety of Nuclear Installations, Reactivity Initiated Accident (RIA) Fuel Codes Benchmark Phase-II, https ://www.oecd-nea.org/nsd/docs/2016/csni-r2016-6-vol1.pdf.

[60] M. Pelanti, K.M. Shyue and T. Flåtten, A Numerical Model for Three-Phase Liquid-Vapor-Gas Flows with Relaxation Processes, *Theory, Numerics and Applications of Hyperbolic Problems II. Springer Proceedings in Mathematics & Statistics*, vol. 237, pp. 423-435, 2018.

[61] V. H. Ransom and D. L. Hicks, Hyperbolic two-pressure models for two-phase flow, *Journal of Computational Physics*, vol. 53, pp. 124-151, 1984.

[62] X. Rogue, G. Rodriguez, J.F. Haas and R. Saurel, Experimental and numerical investigation of the shock induced fluidization of a particles bed, *Shock Waves*, vol. 8, pp. 29-45, 2014.

[63] E. Romenski, A. A. Belozerov and I. M. Peshkov, Conservative formulation for compressible multiphase flows, *http ://arxiv.org/abs/1405.3456*, 2014.

[64] VV. Rusanov, Calculation of interaction of non steady shock waves with obstacles, *Journal of Computational Mathematics and Physics*, vol. 1, pp. 267-279, 1961.

[65] K. Saleh, A relaxation scheme for a hyperbolic multiphase flow model. Part I : barotropic EOS, *ESAIM : Mathematical Modelling and Numerical Analysis*, vol. 63, pp. 1763-1795, 2019, DOI : https ://doi.org/10.1051/m2an/2019034.

[66] K. Saleh, N. Seguin, Some mathematical properties of a barotropic multiphase flow model, *HAL preprint available on https : https ://hal.archives-ouvertes.fr/hal-01921027v2*, 2018.

[67] A.B. Soprano, A.F.C. da Silva and C.R. Maliska, Numerical Solution of the Multiphase Flow of Oil, Water and Gas in Horizontal Wells in Natural Petroleum Reservoirs, *Mecánica Computacional*, vol. XXXI, pp. 683-693, 2012.

[68] R. Saurel and R. Abgrall, A Multiphase Godunov Method for Compressible Multifluid and Multiphase Flows, *Journal of Computational Physics*, vol. 150 (2), pp. 425-467, 1999.

[69] R. Saurel, F. Petitpas, and R. A. Berry, Simple and efficient relaxation methods for interfaces separating compressible fluids, cavitating flows and shocks in multiphase mixtures, *Journal of Computational Physics*, vol. 228 (5), pp. 1678-1712, 2009.

[70] I. Tiselj and S. Petelin, Modelling of two-phase flow with second-order accurate scheme, *Journal of Computational Physics*, vol. 136 (2), pp. 503-521, 1997.

[71] S. Tokareva and E. Toro, HLLC-type Riemann solver for the Baer-Nunziato equations of compressible two-phase flow, *Journal of Computational Physics*, vol. 229 (10), pp. 3573-3604, 2010.

[72] U.S. NRC Glossary, Loss of coolant accident (LOCA), https ://www.nrc.gov/reading-rm/basic-ref/glossary/loss-of-coolant-accident-loca.html.

[73] U.S. NRC Glossary, Departure from nucleate boiling (DNB), https ://www.nrc.gov/reading-rm/basic-ref/glossary/departure-from-nucleate-boiling-dnb.html.

[74] W. Wagnerand and H.J. Kretzschmar, IAPWS industrial formulation 1997 for the thermodynamic properties of water and steam, *International Steam Tables : Properties of Water and Steam Based on the Industrial Formulation IAPWS-IF97*, pp. 7-150, 2008.

Résumé

Dans ce travail de thèse, on étudie la problématique de modélisation d'écoulement à trois phases non miscibles. L'application visée est le phénomène d'explosion vapeur, qui risque de se produire lorsqu'un constituant liquide (S) (métal liquide à très haute température) rentre en contact avec un deuxième constituant (relativement froid) qui est en général de l'eau présente sous forme liquide (L) et vapeur (V). Les transferts principaux au sein de ce milieu bi-constituant sont de type dynamique (vitesse et pression) et thermodynamique (échanges de chaleur et de masse). Plus précisément, les transferts de chaleur apparaissent entre les phases S, L et V, tandis que le transfert de masse ne peut survenir qu'entre les phases L et V du constituant eau. Les applications de type explosion vapeur (EV) génèrent des ondes de choc se propageant au sein du milieu et allant impacter des structures. Il est enfin essentiel de noter que les temps de simulation réels, et les différentes échelles de temps, sont courts. Il s'agit donc de simuler un modèle d'EDP avec lois de fermeture, qui permette de traiter des écoulements fortement instationnaires à trois phases immiscibles, avec génération d'ondes de choc et forts transferts thermiques et de masse, et qui soit conforme au second principe de la thermodynamique. Une fois le modèle d'EDP fermé donné, l'attention est portée sur la méthode numérique d'approximation de ce modèle. La technique des Volumes Finis est adoptée, et une stratégie à pas fractionnaires est mise en place, afin de permettre de traiter un à un les différents effets de relaxation inclus dans le modèle. Des cas-tests numériques de différents degrés de complexité ont été réalisés, afin de s'assurer des propriétés des schémas considérés, et valider la cohérence entre les résultats numériques et le comportement physique attendu de l'écoulement simulé.

Mots-clés : systèmes hyperboliques, convection, relaxation, triphasique.

Abstract

This PhD work consists of modeling a three-phase flow : liquid (L), gas (V) for the same component (water) and liquid (S) for a second component (high temperature liquid metal). Such a mix is characterized by the risk of occurrence of vapour explosion, where major transfers happen : in this bi-component environment dynamic transfers are important (speed / pressure) and thermodynamic exchanges (heat and mass transfers) also are at stake. More specifically, heat transfers occur between phases S, L and V, while the mass transfer can only occur between the phases L and V. The vapour explosion type applications (EV) generate shock waves propagating within the medium and can impact the structures. Finally, it is essential to note that the actual simulation time, and different time scales are short. The mission is, therefore, to compute an EDP model with closure laws, capable of dealing with strongly unsteady three-phase non-miscible flows, with generation of shock waves and high thermal and mass transfer, and consistent with the second principle of thermodynamics. The second step is to propose a Finite Volume numerical method adapted to the approximation of this model, and in the presence of shock waves. Numerical test cases are given in order to verify the properties of the considered schemes, attention is paid to the consistency between the numerical results and the expected physical behavior of the simulated flow.

Keywords : hyperbolic systems, convection, relaxation, three-phase flow.